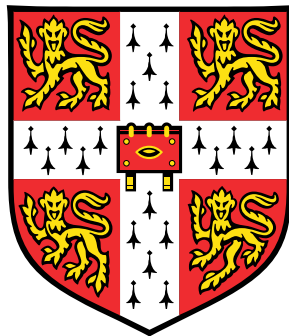


On the generation of waves during frontogenesis



Callum James Shakespeare

Department of Applied Mathematics and Theoretical Physics
University of Cambridge

This dissertation is submitted for the degree of
Doctor of Philosophy

Trinity College

June 2015

“Essentially, all models are wrong, but some are useful.”

— George Box

Declaration

This dissertation is an account of research undertaken between October 2012 and April 2015 at the Department of Applied Mathematics and Theoretical Physics, University of Cambridge, United Kingdom. This dissertation is the result of my own work and includes nothing which is the outcome of work done in collaboration except as specified below. It is not substantially the same as any that I have submitted, or, is being concurrently submitted for a degree or diploma or other qualification at the University of Cambridge or any other University or similar institution. I further state that no substantial part of my dissertation has already been submitted, or, is being concurrently submitted for any such degree, diploma or other qualification at the University of Cambridge or any other University or similar institution.

Much of the content of this thesis also appears in papers either published or currently in review, in many cases with my PhD supervisor John R. Taylor as co-author. I list these papers below, along with the chapters to which they correspond:

1. **Chapters 2 & 3.** Shakespeare, C. J and Taylor, J. R. 2013. A generalized mathematical model of geostrophic adjustment and frontogenesis. *J. Fluid Mech.*
2. **Chapters 2 & 4.** Shakespeare, C. J and Taylor, J. R. 2014. The spontaneous generation of inertia-gravity waves during frontogenesis forced by large strain: theory. *J. Fluid Mech.*
3. **Chapter 5.** Shakespeare, C. J and Taylor, J. R. 2015. The spontaneous generation of inertia-gravity waves during frontogenesis forced by large strain: numerical solutions. *J. Fluid Mech.*
4. **Chapters 6 & 7.** Shakespeare, C. J. Accepted. Non-hydrostatic wave generation at strained fronts. *J. Atmos. Sci.*
5. **Chapters 6 & 8.** Shakespeare, C. J and Taylor, J. R. In review. Spontaneous wave generation at strongly strained density fronts. *J. Phys. Oceanogr.*

Callum James Shakespeare

June 2015

Acknowledgements

As with any work of this kind, a great number of people merit recognition.

Firstly, a huge thank you to my PhD supervisor John Taylor for the work, effort and time he has put into assisting me with this thesis and the associated papers. He is a pleasure to work with and I have learnt a great deal from the experience!

Secondly, to the rest of the Atmosphere-Ocean Dynamics group at DAMTP including Peter Haynes, Alexis Kaminski, Megan Stamper, Dan Whitt and Scott Bachman. Thanks for the fascinating work you do and making DAMTP such an academically stimulating place to be.

I have also been privileged to collaborate at various stages with folks at other institutions including Leif Thomas at Stanford University, and John Methven and Ben Harvey at Reading University — and I thank them for these opportunities. Thanks also to Riwal Plougonven of Ecole Polytechnique for many helpful comments and discussions.

Lastly, I thank my parents for their support during my PhD. Knowing the sun was still shining somewhere on Earth was a great comfort during those miserable English winters!

Abstract

Density fronts are ubiquitous features of the ocean and atmosphere boundary layers. Boundary layers are characterised by strong surface fluxes of heat, water and momentum, and exhibit intense eddy fields that are associated with strong horizontal strains. Such boundary layer phenomena can drive the generation and sharpening of frontal density gradients in a process known as *frontogenesis*. Analytic models of frontogenesis have typically employed the ‘two-dimensional front’ configuration where the density front is assumed to be infinitely long and straight, such that gradients along the front may be neglected, and the mathematical problem reduced to two spatial dimensions. Hoskins & Bretherton (1972) used this configuration to demonstrate how a weak background strain flow, associated with a large scale weather system, can drive the collapse of a boundary front to a discontinuity in the inviscid equations in finite time. More recently, Blumen (2000) has used the same configuration to demonstrate how an unbalanced initial state — associated with a rapidly applied boundary flux — can trigger an adjustment process which drives frontogenesis on the boundary. These two types of frontogenesis are known as ‘forced’ and ‘spontaneous’, respectively. Forced and spontaneous frontogenesis have typically been studied in isolation, despite it being well established that they can and do occur simultaneously. Furthermore, neither the Hoskins & Bretherton (1972) nor Blumen (2000) models include propagating inertia-gravity waves, despite recent observations and numerical simulations showing that these waves are often generated during active frontogenesis.

Here we formulate a generalised mathematical model for the classical two-dimensional density front subject to a simple background strain flow, as studied by Hoskins & Bretherton (1972). This model firstly unifies the disparate frontogenesis theories of Hoskins & Bretherton (1972) and Blumen (2000). Secondly, the model extends these theories by permitting arbitrary initial conditions, stratification and strong strains. Thirdly, the model incorporates non-hydrostatic effects and unbounded domains. An important novel feature of the model is the accurate description of inertia-gravity wave generation during frontogenesis. We show that these waves can be generated both by the geostrophic adjustment of initial imbalances in a stratified ambient, and spontaneously due to the acceleration of the strain flow around the front. The generalised model thus provides a unified theory capable of describing

frontogenesis and wave generation in the atmosphere and ocean boundary layers on a vast range of scales. In particular, the inclusion of strong strains permits the description of frontogenesis on the ocean submesoscale. The predictions of the generalised model are confirmed by comparison with a suite of fully non-linear numerical simulations.

Table of contents

List of figures	xv
List of tables	xxxi
1 Introduction	1
1.1 Fronts in the ocean and atmosphere	1
1.2 The equations	8
1.2.1 The background flow equations	8
1.2.2 The 2D frontogenesis problem	10
1.3 Analytic models of fronts	13
1.3.1 Boundary dynamics	14
1.3.2 The HB model	16
1.3.3 The QG model	19
1.3.4 The Blumen model	19
1.4 Objectives and outline	23
2 The non-linear uniform PV generalised model	25
2.1 Model configuration and non-dimensionalisation	25
2.2 The generalised momentum coordinate	28
2.3 The generalised model	30
2.4 Summary	34
3 Geostrophic adjustment and frontogenesis	37
3.1 Introduction	38
3.2 Inertial oscillations and frontogenesis in zero PV flow	40
3.3 Geostrophic adjustment and frontogenesis in uniform PV flow	49
3.3.1 Uniform PV flow with no deformation field	50
3.3.2 Uniform PV flow with a deformation field	59
3.4 Numerical comparison	68

3.5	Discussion	72
4	Spontaneous wave generation during frontogenesis: analytic solutions	75
4.1	Introduction	75
4.2	Scaling analysis	79
4.2.1	Limits of the generalised model	81
4.3	'Spontaneous' inertial oscillations in zero PV flow	85
4.4	Constant strain	87
4.4.1	Impulse response solution	89
4.4.2	Full solution	96
4.5	Time-dependent strain	101
4.6	Discussion	107
5	Spontaneous wave generation during frontogenesis: numerical solutions	111
5.1	Introduction	111
5.2	Numerical setup	114
5.3	Comparison of numerical and analytical solutions	116
5.3.1	Weak strain	119
5.3.2	Strong strain	123
5.4	Equilibrated fronts	130
5.5	Discussion	134
6	The linear non-uniform PV model	137
6.1	Model formulation	137
6.2	Analytic solution: constant strain and stratification	141
6.2.1	Green's Functions	142
6.3	Solutions in three domains	149
6.3.1	Fully infinite domain	149
6.3.2	Semi-infinite domain	149
6.3.3	Dual rigid lid domain	149
6.4	Summary	151
7	Non-hydrostatic wave generation at a tropospheric front	153
7.1	Introduction	153
7.2	Analytic solution	155
7.3	Numerical solution	158
7.4	Non-uniform stratification	163

7.5	Discussion	165
8	Semi-infinite domain solutions with application to the ocean submesoscale	169
8.1	Introduction	169
8.2	Analytic model results	172
8.2.1	Strain dependence	173
8.2.2	Frontal scale dependence	176
8.2.3	Comparison with lee waves	179
8.2.4	Energy budgets	183
8.3	Numerical model comparison	187
8.4	Discussion	192
9	Conclusion	195
9.1	Summary of key results	199
9.1.1	Wave generation	199
9.1.2	Frontogenesis	200
9.1.3	Strong strain dynamics	201
9.2	Model limitations and future work	202
	References	205
	Appendix A Green's function solution of the non-linear generalised model	211
A.1	Green's function differential equation	211
A.2	Boundary conditions on the Green's function	212
	Appendix B Numerical solution to the linear frontogenesis problem	215
	Appendix C Ray-tracing in a background strain flow	217

List of figures

- 1.1 Density fronts in the ocean and atmosphere. (a) Near-infrared satellite image of a weather front that passed over the United Kingdom on November 24 2009 (from figure 3 of Knippertz *et al.*, 2010). (b) Submesoscale fronts in a wind-forced simulation of the ocean mixed layer: (left) relative surface density ($\sigma = \rho - \rho_0$; kg m^{-3} , where ρ is the density and ρ_0 a reference value) and (right) vertical velocity (mm s^{-1}) at 15 m depth (from figure 5 of Mahadevan *et al.*, 2012). The surface density fronts are associated with bands of intense downwelling. 2
- 1.2 Schematic of a frontal region at an upper boundary such as the ocean surface. Colours indicate the buoyancy with warm colours (red) denoting light fluid and cool colours (blue) denoting dense fluid. The pressure gradient across the front is balanced by the Coriolis force (rotation is denoted by the f) and drives an along-front jet (labelled 1). In the absence of active frontogenesis there is no other flow (although instabilities are possible for sharp enough fronts). In the case of active frontogenesis a secondary circulation is forced. Here frontogenesis is induced due to the confluent flow (shown by black arrows) generated by a pair of eddies shown schematically at the surface (not to scale). The secondary circulation consists of an intense downwelling (labelled 2) on the cold side of the front and a broader, weaker upwelling (labelled 3) on the warm side of the front. 3

- 1.3 Parameterisation of submesoscale phenomena. Results from the submesoscale resolving simulations of Rosso *et al.* (2015) — see figures 1 and 5 therein. (a,b) Horizontal density gradient magnitude at a particular instant in time for (a) the high-resolution simulated sector of the Southern Ocean and (b) a smaller area denoted by the red box in (a). The observed fronts are submesoscale (order 1 to 10 km in width). (c, d) The submesoscale vertical velocity (m day^{-1}) as a function of the (c) mesoscale eddy kinetic energy and (d) the mesoscale strain rate. 4
- 1.4 UK Met Office simulations of the weather front shown in figure 1.1a, for 4pm on 24 November 2009. (a) Rainfall rate (mm hr^{-1}). Land shown by black contours. (b) Vertical velocity (m s^{-1}) at 4.5km height. Note the intense band of vertical flow, corresponding to an inertia-gravity wave, propagating ahead of the front. (c) Cross section of the PV ($1 \text{ PVU} = 10^{-6} \text{ K m}^2\text{kg}^{-1}\text{s}^{-1}$) along the black line shown in (a). (d) Cross section of the potential temperature (K, colour) and stratification (10^{-4} s^{-2} , black contours) along the black line shown in (a). (Plots provided courtesy of J. Methven and B. Harvey, personal communication). 6
- 1.5 Ocean fronts and wave generation. (a) The Subtropical Front on the northern edge of the North Pacific Subtropical Gyre. Colours indicate surface Chlorophyll concentration (K. McMahon, Woods Hole Oceanographic Institution). (b, c) Observations of the Subtropical Front in the North Pacific by Alford *et al.* (2013) — see figures 1 and 7 therein. (c) Plan view of the observed sea surface temperature (SST, $^{\circ}\text{C}$), corresponding approximately to the region shown by the red box in (a). (b) The cross-frontal (meridional) vertical shear along the line shown in (c). Note the banded structure in the observed shear characteristic of inertia-gravity waves. 7
- 1.6 Vector plot of the idealised strain flow $\vec{\psi} = -\alpha xy$ where $\alpha > 0$ 11
- 1.7 The effect of the strain flow $\vec{\psi} = -\alpha xy$ on an initially circular ‘blob’ of passive tracer. A tracer C in this strain flow will evolve as $C = C_0(xe^{\beta}, ye^{-\beta})$ where $C_0(x, y)$ is the initial distribution and β is defined by (1.11). 13
- 1.8 The solution to the uniform PV Hoskins & Bretherton (1972) model (1.30) for parameter values typical of an atmospheric front ($\alpha = 0.1f$, $N = 33.3f$) at the initial time, and at the time of discontinuity formation. Buoyancy contours are shown as thick black lines. Vertical velocity contours (spacing: 0.3 cm s^{-1}) are shown as thin lines: grey = down, black = up. 18

- 1.9 The solution to the QG model of frontogenesis for parameter values typical of an atmospheric front (as in the previous figure) at $t = 0, 26$ and 52 hours. Buoyancy contours are shown as thick black lines. Vertical velocity contours are shown as thin lines: grey = down, black = up. Contour levels are the same as for the previous figure (1.8). 20
- 1.10 The non-dimensional solution to the Blumen (2000) model of unbalanced frontogenesis for a critical buoyancy profile, i.e. $\max |b_0''(\chi)| = f^2/H$ from (1.37). Buoyancy contours are shown as thick black lines. Vertical velocity contours are shown as thin lines: grey = down, black = up. Time is in units of $1/f$ 22
- 2.1 Schematic of the dual rigid lid, uniform PV frontogenesis problem. The cross-frontal xz plane is shown, with the y direction into the page. The fluid is trapped between rigid lids at the top ($z = H$) and bottom ($z = 0$) of the domain, but unbounded in the cross-frontal (x) direction. The constraint of uniform PV requires that the stratification, N^2 , is uniform and that the buoyancy difference across the front, ΔB_0 , is the same for all z . It follows that if $b = b_0(X)$ on the lower rigid lid, then $b = b_0(X) + N^2H$ on the upper rigid lid, as shown. Parameter X is the generalised momentum coordinate described in §2.2. 26
- 3.1 The time evolution of the buoyancy field during frontogenesis as predicted by the general zero PV solution (3.5) for a typical B00 case ($Ro = 3, \delta = 0, \mathcal{I} = 1$, left panel) and a typical HB case ($Ro = 0.4, \delta = 0.1, \mathcal{I} = 0$, right panel) at times from top to bottom of $0, t_c/3, 2t_c/3$ and t_c . The critical time is $t_c = 1.49$ in the B00 case and $t_c = 19.8$ in the HB case. The contour interval is 0.1 46
- 3.2 Time series of the frontal width d and the perturbation velocity magnitudes (u, v, w) at the x position of the buoyancy gradient maximum (the front) for parameter values of $\delta = 0.1$ and $Ro = 0.4$. The vertical position is $z = 0$ for the horizontal velocities u and v , and $z = 1/2$ for the vertical velocity w . The general solution (3.5) is shown for a full mass imbalance $\mathcal{I} = 1$ (solid) and zero initial imbalance $\mathcal{I} = 0$ (dotted). The HB solution given by (3.8) is also shown (dashed). 48

- 3.3 The limiting curve (solid) evaluated from (3.34) for the error function profile (3.15) dividing frontogenetic (above) and non-frontogenetic (below) regions. The limiting curve (dashed) found empirically by Neves (1996, equation 41) from numerical simulations is also shown (rescaled appropriately to match the buoyancy profile given by 3.15). The two specific cases of ($Ro = 4, F = 0.4$, non-frontogenetic) and ($Ro = 4, F = 1$, frontogenetic) considered in the text are represented by a circle and '+', respectively. The critical Rossby and Froude numbers, $Ro_c = 2.03$ and $F_c = 0.31$ respectively, are labelled. The shading indicates the parameter values for which an adjusted state (with non-vanishing inverse Jacobian) exists. 54
- 3.4 Geostrophic adjustment of the buoyancy (thin contours) and along-front velocity (thick contours) fields towards a steady state for (non-frontogenetic) initial parameter values of $Ro = 4$ and $F = 0.4$ ($\delta = 0$), as predicted by general solution for uniform PV flow (3.26). Inertia-gravity waves propagate outward from the imbalance region leaving behind flatter isopycnals. Negative contours, denoting a velocity directed out of the page, are coloured grey. Contour intervals are 0.338 for the buoyancy and 0.1 for the velocity. 56
- 3.5 Time evolution of the streamfunction for initial parameter values of $Ro = 4$ and $F = 0.4$ ($\delta = 0$), as predicted by general solution for uniform PV flow (3.26). Inertia-gravity waves propagate outwards leaving a progressively weaker overturning cell in the initial imbalance region. Positive values (black) correspond to anticlockwise flow, and negative values (grey) to clockwise flow. Contour intervals are 0.01. 57
- 3.6 The (a) initial buoyancy field for parameter values of $Ro = 4$ and $F = 0.4$ ($\delta = 0$), and the (b,c,d) corresponding geostrophically adjusted steady state as predicted by (3.28). The isopycnals are flattened in the steady state (b) relative to the initial configuration and in balance with a steady geostrophic out-of-plane jet (d). The buoyancy anomaly pertaining to the geostrophically adjusted state is also shown (c). Negative contours are coloured grey. Contour intervals are 0.338 for the buoyancy, 0.06 for the buoyancy anomaly and 0.061 for the velocity. 58

- 3.7 Hovmöller plot of the streamfunction at mid-depth $z = 0.5$ during the course of geostrophic adjustment for initial parameter values of $Ro = 4$ and $F = 0.4$ ($\delta = 0$), as predicted by general solution for uniform PV flow (3.26). The unbalanced initial conditions generate inertia-gravity waves which propagate outwards at a constant speed given by their group velocity, with the highest horizontal mode numbers propagating most rapidly. Group velocities for modes $n = 1$ and $k = 0.1, 0.3$ and $k \rightarrow \infty$ are indicated by dashed lines. 59
- 3.8 Time evolution of the buoyancy field for initial parameter values of $Ro = 4$ and $F = 1$ ($\delta = 0$), as predicted by general solution for uniform PV flow (3.26). An infinite horizontal buoyancy gradient develops on the upper and lower boundaries. The streamfunction (anticlockwise) at each time is represented by grey shading. Contour intervals are 0.075 for the buoyancy and 0.024 for the streamfunction. 60
- 3.9 Time evolution of the along-front (out-of-plane) velocity field for initial parameter values of $Ro = 4$ and $F = 1$ ($\delta = 0$), as predicted by general solution for uniform PV flow (3.26). The baroclinic jet intensifies with time and develops an infinite horizontal gradient on the upper and lower boundaries as frontogenesis occurs. Negative contours are coloured grey. The contour intervals is 0.1. 61
- 3.10 Time series of the (a) frontal width d and (b) frontal position x (the position of the buoyancy gradient maximum on the lower boundary), for the non-frontogenetic ($Ro = 4, F = 0.4, \delta = 0$ solid) and frontogenetic ($Ro = 4, F = 1, \delta = 0$, dashed) cases, as predicted by the uniform PV solution (3.26). The steady state frontal width and position predicted by (3.28) are also shown as dotted lines for the non-frontogenetic case. 62
- 3.11 Time series of the velocity magnitudes (u, v, w) at the position of the buoyancy gradient maximum on the lower boundary for three vertical heights, for the non-frontogenetic ($Ro = 4, F = 0.4, \delta = 0$, left panel) and frontogenetic ($Ro = 4, F = 1, \delta = 0$, right panel) cases. For the horizontal velocities u and v the heights are $z = 0$ (solid), $z = 0.5$ (dashed) and $z = 1$ (dot-dashed). For the vertical velocity w the heights are $z = 0.1$ (solid), $z = 0.5$ (dashed) and $z = 0.9$ (dot-dashed). Also shown (dotted) is the steady state maximum value of v on the lower boundary, as predicted by (3.28). 63

- 3.12 The scaled time taken δT_{HM} for the propagating wave components of the solution (3.41), $J_\sigma(\eta)$ and $Y_\sigma(\eta)$, to decay to half their initial magnitude in the small strain limit, $\sigma = \iota/\delta$, in terms of the parameter $a = kBu/(n\pi)$. In the limit of large a the time taken δT_{HM} converges to $2\ln 2$, corresponding to a decay rate of $\delta/2$ 66
- 3.13 The buoyancy field and streamfunction at the critical time $t_c \approx 26$ for parameter values of $Ro = 0.4$, $F = 0.8$ and $\delta = 0.1$, as computed from the differential equation (3.20). Both unbalanced (a,b) and balanced (c,d) initial conditions are shown, with the same contour levels. The inertia-gravity wave field is substantially more intense for the unbalanced initial conditions. Positive values of the streamfunction (black) correspond to anticlockwise flow and negative values (grey) to clockwise flow. Contour intervals are 0.103 for the buoyancy and 0.002 for the streamfunction. 67
- 3.14 Time series of the (a) frontal width d and (b) frontal position x (the position of the buoyancy gradient maximum on the lower boundary), for parameter values of $Ro = 0.4$, $F = 0.8$ and $\delta = 0.1$, as computed from the HB solution (3.38, dashed) and the differential equation (3.20) for both unbalanced (black solid) and balanced (grey solid) initial conditions. 68
- 3.15 Hovmöller plot of the streamfunction difference $\psi - \psi_{HB}$ for parameter values of $Ro = 0.4$, $F = 0.8$ and $\delta = 0.1$, and unbalanced initial conditions, at height $z = 0.5$ in Eulerian coordinates (left) and momentum coordinates (right). Waves generated by the initial conditions are initially trapped until the release time $T_R \sim 7$ (shown as a horizontal dashed line) as non-decaying inertial oscillations. Once released the waves propagate towards a stagnation point $x_s = \pm 1.6$ shown by the vertical dashed line (left) and the dashed curve (right, $X_s = \pm x_s \exp \delta T$). 69
- 3.16 Numerical solution to the fully non-linear equations for the unstrained non-frontogenetic case ($Ro = 4$, $F = 0.4$, $\delta = 0$) studied in §3.3.1. (a) Hovmöller of the streamfunction at $z = 0.5$ from the numerical model is shown in colour. The corresponding contours from the analytical solution (as in figure 3.7) are overlaid in black. (b) The maximum along-front velocity v as a function of time from the numerical (solid) and analytical (dashed) models. 70

- 3.17 Numerical solution to the fully non-linear equations for the unstrained fronto-genetic case ($Ro = 4, F = 1, \delta = 0$) studied in §3.3.1. Left: Time series of (a) maximum along-front velocity v and (c) maximum vertical velocity w from the numerical (solid) and analytic (dashed) models, up to the critical time in each model. (b) The buoyancy field (lines) and streamfunction (shaded) from the numerical model just prior to the critical time (the equivalent plot for the analytic model is shown in figure 3.8). 71
- 3.18 Numerical solution to the fully non-linear equations for the strained fronto-genetic case ($Ro = 0.4, F = 0.8, \delta = 0.1$) studied in §3.3.2. Left: Time series of (a) maximum along-front velocity v and (c) maximum vertical velocity w from the numerical (solid) and analytic (dashed) models, up to the critical time in each model. (b) The buoyancy field (lines) and streamfunction (shaded) from the numerical model just prior to the critical time (the corresponding fields for the analytic model are shown in figure 3.13a&b). 72
- 3.19 The variation of the non-dimensional critical time with Rossby number Ro for Froude numbers of (a) $F \rightarrow \infty$ and (b) $F = 1$ for a strains of $\delta = 0.1$, as derived from the generalised model. The critical times predicted by the HB model (dashed) and B00 model (dot-dashed) are also shown. The assumed initial conditions are zero motion ($u = v = w = 0$) and an error function buoyancy profile (3.15) with critical Rossby number $Ro_c = 2.03$. The Rossby number at which the error in the HB prediction of the critical time first exceeds 10% is shown by a vertical dashed line. Since the size of the Rossby number controls the magnitude of the (near-inertial) oscillations in the frontal zone, a small increase in the Rossby number can cause the critical time to decrease by an entire inertial period, giving rise to the step-like features seen in the figure. 73
- 4.1 The geostrophic and ageostrophic responses to a pulse of strain in zero PV flow. The strain $\delta(T)$ (left) is defined by (4.30) with $\delta_0 = 0.2$ and $\tau = 8\pi$. The time variation of the strain drives ageostrophic flow $\zeta(T)$ in the form of an oscillation about the geostrophic solution, $e^{\beta(T)}$ 86
- 4.2 (a) The relative amplitude r (4.43) of the ‘wave’ term in the generalised model solution (4.42), and the relative strength of wave generation \mathcal{R} (4.50), as a function of the strain δ . (b) The fraction of amplitude from an impulse forcing going into the wave, \mathcal{R} , and GSC, $1 - \mathcal{R}$, components of the flow for a given value of strain. 91

- 4.3 Streamfunction impulse response ψ_I evaluated at $Z = 0.5$ for the generalised secondary circulation (GSC) and wave components of the general solution (4.45), and the HB solution (4.47, HB), for strains of (a) $\delta = 0.2$ and (b) $\delta = 0.9$. The impulse forcing is located at $\chi = 0$, and the spread of energy away from this point is indicated by arrows for the first two non-zero modes $n = 1$ and $n = 3$. Energy can only spread over the region $\chi \leq Bu/(n\pi\delta)$ for each mode. The parameter values used are $Bu = 1.5$ and $Ro = 0.6$, consistent with other examples considered later in this chapter. 94
- 4.4 The vertical velocity field from the generalised model w , Hoskins & Bretherton (1972) model w_{HB} , and the difference between the two, evaluated just prior to the critical time for parameter values of $Ro = 0.6$, $Bu = 1.5$, and $\delta = 0.2$. Black denotes positive and grey denotes negative velocities. Contours of buoyancy are overlaid on the top plot (thick grey lines). 98
- 4.5 The (a) generalised secondary circulation (ψ_{GSC}) and (b) wave streamfunction (ψ_W), for parameter values of $Ro = 0.6$, $Bu = 1.5$, and $\delta = 0.2$. The GSC and wave impulse response functions from figure 4.3a have been overlaid in grey. 99
- 4.6 The time evolution of the wave ψ_W (left) and GSC ψ_{GSC} (right) streamfunctions for parameter values of $Ro = 0.6$, $Bu = 1.5$, and $\delta = 0.9$, at times of $t = 0, 1.3, 2$ and 2.7 (just prior to the critical time) with time increasing down the page. Buoyancy contours are overlaid in black in each case. Grey contours enclose the region $|X| \leq 1$, demonstrating the convergent action of the strain field, and the simultaneous slumping of the front. 100
- 4.7 The solution of the time dependent model (2.29) with $\mathcal{N} \equiv 0$, computed numerically, for parameter values of $Ro = 0.1$ and $Bu = 1$. The imposed strain field (b) is defined in (4.30) with $\delta_0 = 0.2$ and $\tau = 8\pi$. The boundary profile of buoyancy is $b_0(X) = 1/2 \operatorname{erf}(X/\sqrt{2})$. (a) Hovmöller of the streamfunction evaluated at mid-depth. Contour spacing is logarithmic from 1% to 100% of the maximum value, with grey contours indicating negative (clockwise) overturning. (c) The maximum value of the along-front velocity v . (d) The frontal width $d = J^{-1}$ 103

- 4.8 The solution of the time dependent model (2.29) with $\mathcal{N} \equiv 0$, computed numerically, for parameter values of $Ro = 0.1$ and $Bu = 1$, as in figure 4.7. Hovmöller plots of the generalised secondary circulation (GSC) and wave components of the vertical velocity (top) and streamfunction (bottom) are displayed, evaluated at mid-depth ($z = 0.5$). The stagnation lines for the first vertical mode are shown on the top-right plot (black-dashed lines; from (4.22) with $\chi_0 = 0$). The family of characteristics χ_+ and χ_- defined by (4.22) for the first vertical mode are shown on the bottom left plots (solid black lines). Streamfunction contours for the unstrained adjustment of the maximum GSC for $T > \tau = 8\pi$ (shown by a dashed black line) are overlaid on the bottom-left plot, with black denoting positive (anticlockwise) and grey negative (clockwise) overturning. 106
- 5.1 A comparison of the streamfunctions from the numerical model when initialised in the state predicted by the generalised model forced solution, GM, (a: GM_I) and semigeostrophic balance, HB, (c: HB_I) for parameter values $Ro = 0.6$, $Bu = 1.5$, $\delta = 0.2$, and $A = 100$. Buoyancy contours are overlaid in grey. The difference between the initial states is shown in (e). The streamfunctions just prior to the critical time ($t = 14.5$) for the GM- and HB-initialised runs, GM_F and HB_F , are shown in (b) and (d), respectively. The difference between the final states is shown in (f). The time evolution of the difference at mid-depth ($z = -0.5$) is shown in (g). Positive (anticlockwise) values are represented by black contours, and negative by grey. The contour interval in (e-g) is 10% of that in (a-d). 118
- 5.2 Time series of the (a) frontal width $d = \min J^{-1}$ and (b) maximum vertical velocity w , from the generalised model (wide-dash), HB model (narrow-dash) and numerical model (solid). The colours correspond to different values of Rossby number Ro and uniform strain δ as indicated in (a). The Burger number is $Bu = 1.5$ in each case. The time axis is in units of δt ; that is, time is normalised by the strain rate rather than the inertial frequency. The evolution of the frontal width, $d(\delta t)$, from the HB model is independent of strain, meaning that the red/magenta lines and green/black lines in (a) are overlaid. 119

- 5.3 Case (i): The vertical velocity field from the (a) generalised (GM), (b) numerical (NUM), and (c) semigeostrophic (HB) models, just prior to the time of discontinuity formation in each model, for parameter values of $Ro = 0.6$, $Bu = 1.5$, and constant strain $\delta = 0.2$. Contours of buoyancy from each model are overlaid in grey. 121
- 5.4 Case (ii): The vertical velocity field from the (a) generalised (GM), (b) numerical (NUM), and (c) semigeostrophic (HB) models, just prior to the time of discontinuity formation in each model, for parameter values of $Ro = 1.5$, $Bu = 1.5$, and constant strain $\delta = 0.2$. Contours of buoyancy from each model are overlaid in grey. 122
- 5.5 Case (iii): The vertical velocity field from the (a) generalised (GM), (b) numerical (NUM), and (c) semigeostrophic (HB) models, just prior to the time of discontinuity formation in each model, for parameter values of $Ro = 0.6$, $Bu = 1.5$, and constant strain $\delta = 0.9$. Contours of buoyancy from each model are overlaid in grey. 124
- 5.6 Case (iv): The vertical velocity field from the (a) generalised (GM), (b) numerical (NUM), and (c) semigeostrophic (HB) models, just prior to the time of discontinuity formation in each model, for parameter values of $Ro = 1.0$, $Bu = 1.5$, and constant strain $\delta = 0.9$. Contours of buoyancy from each model are overlaid in grey. 125
- 5.7 Case (v): The streamfunction, buoyancy field, and net velocity vectors from the numerical model numerical model at times (a) 0, (b) 0.5 and (c) 1.0 (critical time), for parameter values of $Ro = 1.5$, $Bu = 1.5$, and constant strain $\delta = 0.9$. The net cross-front velocity vectors, $(u - \delta x/Ro, w)$, are displayed as black arrows. The locations of the surface fronts, defined as the maximum of $\partial_x b$ on the boundary, are denoted by red circles. Three momentum coordinates contours, $\chi = x + Ro v = 0, \pm Bu/(\pi\delta)$, are displayed on each plot as thick black lines. 126
- 5.8 Hovmöller plot of the vertical velocity just below the surface, at $z = -0.25$, from the (a) generalised (GM) and (b) numerical (NUM) models for the time dependent strain defined by (5.9), and parameter values of $Ro = 0.6$, $Bu = 1.5$, $\delta_0 = 0.9$ and $A = 100$. Contours of surface ($z = 0$) buoyancy are overlaid in black, showing the collapse of the front with time. The strain field $\delta(T)$ is overlaid at $x = -4$, and time series of the maximum of the velocities u, v and w near $x = 4$. The characteristics predicted from the analytical model (4.22) for vertical modes $n = 1$ to 3 are overlaid in grey. 129

- 5.9 Numerical solution for parameter values of $Ro = 1.5$, $Bu = 1.5$, $\delta = 0.2$ and $A = 100$, as in figure 5.4, but with horizontal hyperdiffusion of $|Re_h| = 10^7$. (a) The steady state vertical velocity field with buoyancy contours overlaid (thin grey lines). The presence of diffusion modifies the PV from the background value of $q = F^{-2}$; the PV contours for 90% and 110% of the background value are displayed (thick grey lines). PV is reduced along the boundary between the fronts and increased in the interior along the frontal axis. (b) Hovmöller of the vertical velocity at mid-depth. (c) The diffusive analytical prediction from (5.12) for the vertical velocity at mid-depth. (d) The difference between (b) and (c). 132
- 6.1 Schematic of the non-uniform PV 2D frontogenesis problem for a semi-infinite domain, $z \leq 0$, with a single rigid lid at the top, representing the ocean surface. The domain is unbounded in the cross-frontal (x) direction, and the front is assumed to be infinitely long into the page (y). The width L and depth scale H of the front are set by the choice of PV anomaly, $q_0(xe^\beta, z)$. The background stratification can be an arbitrary function of depth, $N^2(z)$. The surface buoyancy b_0 is then set by (6.3) and collapses with time in the presence of a confluent background strain flow. 139
- 6.2 (Normalised) Green's functions from the three limits of the constant strain and stratification linear model: quasigeostrophic (QG, red; (6.18)), hydrostatic (H, blue; (6.20)) and non-hydrostatic (NH, black; (6.21)). The plots are for parameter values of $\alpha/f = 0.2$ and $N/f = 61$. (a,c,e) The modulus of the spectral Green's function for the (a) along-front shear $\widehat{\partial_z v}_G$, (c) cross-front shear/streamfunction $l^2 \widehat{\psi}_G = -\widehat{\partial_z u}_G$ and (e) divergence $\widehat{\partial_z w}_G$, as a function of the mode slope $\varepsilon = Nk/(fl)$. The high wavenumber oscillations in the H and NH models are associated with waves. (b,d,f) The cross-frontal structure of the Green's function for a single vertical wavenumber l for (b) along-front shear $\partial_z v_G$, (d) cross-front shear/streamfunction $l^2 \widehat{\psi}_G = -\widehat{\partial_z u}_G$ and (f) divergence $\partial_z w_G$. The non-dimensional horizontal coordinate x' is defined as $x' = flx/N$ 147
- 6.3 Normalised cross-frontal shear Green's function $|\partial_z u_G|$ as a function of N/f for a strain of $\delta = \alpha/f = 0.4$ and single vertical wavenumber l . The amplitude is almost entirely confined within the region where the maximum hydrostatic group speed, $\max c_g = N/l$, exceeds the strain flow speed, αx , or equivalently the region where $N/f > \delta xl$ 148

- 6.4 Fully infinite domain solution (vertical velocity field) for a ‘blob’ buoyancy anomaly of $b_0(x, z) = \Delta B_0 \exp(-(z/H)^2 - (x/L_R)^2)$ — where $L_R = NH/f$ is the Rossby radius — and strain $\alpha = 0.4f$ from the (a) QG model and (b) hydrostatic model. The perturbation PV q is contoured on (a) with grey contours implying negative PV and black positive. The buoyancy field is contoured in blue. The action of the background strain on the region of perturbation PV gradient near $z = 0$ and associated ‘blob’ of increased buoyancy drive a secondary flow. The vertical velocity associated with this secondary flow is shown in units of $\Delta B_0 f / N^2$. The hydrostatic model (b) also predicts the radiation of waves away from the PV anomaly. Note the different vertical axes in the two plots. 150
- 7.1 Vertical velocity w (cm s^{-1}) at the critical time, $t = 10\text{hrs}$, from the various non-linear models. (a) Semigeostrophic model (SG) of Hoskins & Bretherton (1972). (b) The hydrostatic generalised model (GM) of Chapters 2 through 5. (c) The difference between the hydrostatic generalised and semigeostrophic models, GM-SG. Contours of buoyancy are overlaid in black in each case. . . 157
- 7.2 Time evolution of the vertical velocity, w (cm s^{-1}), from the various linear models. (a) The vertical velocity from the QG model at $t = 72$ hours, with isotherms overlaid in black. Cross-front velocity $u(x = 0, z)$ is indicated by grey arrows. If advection by this velocity, $u \partial_x$, is included in the model, the surface front slumps outwards in the direction of the arrows, stabilising the isotherms (as in figure 7.1a). (b) The vertical velocity from the non-hydrostatic (NH) model at $t = 72$ hours, with isotherms overlaid in black. (c) The time evolution of the vertical velocity from the non-hydrostatic (NH) model at $z = 4.5 \text{ km}$, from $t = 0$ up to 72 hours. (d) The vertical velocity from the hydrostatic (H) model at $t = 72$ hours, with isotherms overlaid in black. (e) The time evolution of the vertical velocity from the hydrostatic (H) model at $z = 4.5 \text{ km}$, from $t = 0$ up to 72 hours. 159

- 7.3 Time evolution of the vertical velocity, w (cm s^{-1}), in the numerical model for the parameter values discussed in the text. Plots (a,c,e,g) correspond to the low resolution run with $\Delta x = 7 \text{ km}$ and diffusivity $\kappa_h = 232 \text{ m}^2 \text{ s}^{-1}$, and (b,d,f,h) to the high resolution run with $\Delta x = 0.45 \text{ km}$ and diffusivity $\kappa_h = 58 \text{ m}^2 \text{ s}^{-1}$. (a,b) The vertical velocity at $t = 72$ hours, with isotherms overlaid in black. (c,d) The time evolution of the vertical velocity at $z = 4.5 \text{ km}$, from $t = 0$ up to 120 hours. (e,f) The time evolution of the slow-time (low-pass filtered) vertical velocity at $z = 4.5 \text{ km}$, from $t = 0$ up to 120 hours. The low-pass filter applied is $F = \exp(-(2\omega/f)^4)$, i.e. a cut-off frequency of $\omega = 0.5f$. (g,h) The time evolution of the residual fast-time vertical velocity at $z = 4.5 \text{ km}$, from $t = 0$ up to 120 hours. The fast time part contains frequencies $\omega > 0.5f$ and thus contains the propagating wave part of the flow. These propagating waves are generated due to an imbalance in the initial condition. The propagating wave packets follow the paths predicted by ray-tracing (7.3), plotted as black lines for parameters of $x_0 = 0$ and $L_0 = \pi/k_0 = 1000 \text{ km}$ 161
- 7.4 Numerical solution to the non-hydrostatic linear frontal model (6.9) for a variable stratification that increases above 9 km . (a) The vertical velocity (cm s^{-1}) after 60 hours. (b) The vertical profile of stratification ratio $N(z)/f$. (c) Hovmöller plot of the vertical velocity at $z = 5 \text{ km}$ (dashed line in (a)). (d) The strain as a function of time, $\alpha(t)/f$ 164
- 7.5 Numerical solution to the non-hydrostatic linear frontal model (6.9) for a variable stratification that initially decreases with height, then increases above 9 km . (a) The vertical velocity (cm s^{-1}) after 60 hours. (b) The vertical profile of stratification ratio $N(z)/f$. (c) Hovmöller plot of the vertical velocity at $z = 5 \text{ km}$ (dashed line in (a)). (d) The strain as a function of time, $\alpha(t)/f$ 166
- 8.1 Non-dimensional hydrostatic Green's function for the cross-front shear, $f \widehat{\partial_z u_G}$ (6.22), as a function of slope $\varepsilon = Nk/(fl)$ and strain $\delta = \alpha/f$. Local extrema in the Green's function correspond to wave packets of frequency $\omega = f\sqrt{1+\varepsilon^2}$ 173
- 8.2 Comparison of vertical velocity field (in units of $\Delta B_0 f/N^2$) for strains of (a) $\alpha = 0.1f$, (b) $\alpha = 0.3f$, and (c) $\alpha = f$, and a frontal anomaly defined by (8.3). Straight grey lines indicate the slopes of secondary circulation and first three wave packets (if they exist), as predicted from the Green's function (see figures 8.3 and 8.4). 174

- 8.3 (a) Slope of the frontal jets as a function of strain $\delta = \alpha/f$, in units of f/N . (b) Vertical velocity magnitude as a function of strain, in units of $\Delta B_0 H/(NL)$. The results from the small (8.1) and large (8.2) strain limits are shown as dashed lines. The slope is nearly constant at small strain and increases linearly at large strain. The vertical velocity increases linearly at small strain and quadratically at large strain. 176
- 8.4 Frequencies of the six lowest frequency distinct wavepackets as a function of strain $\delta = \alpha/f$, derived from computing the local extrema of the non-dimensional cross-front shear Green's function, $f\widehat{\partial_z u_G}$, shown in figure 8.1. The lowest frequency distinct wavepacket is $\omega = 1.93f$, for a strain of $\alpha = 0.29f$ 177
- 8.5 Vertical velocity fields for a strain of $\alpha = 0.4f$ and buoyancy anomaly defined by (8.3), for various frontal Burger numbers $\varepsilon_F = L_R/L$. The velocities are in units of $\varepsilon_F \Delta B_0 f/N^2$. Contours are logarithmically spaced from 3 to 100% of the maximum value (0.03). Grey-dashed lines indicate the predicted slope of the frontal jets and wave packets. The figure can also be viewed as a sequence of snapshots in time, $\alpha t = \ln(\varepsilon_F/0.1)$: (a) $\alpha t = 0$, (b) $\alpha t = 0.69$, (c) $\alpha t = 1.61$, (d) $\alpha t = 2.30$, and (e) $\alpha t = 3$ 178
- 8.6 Comparison of perturbation vertical velocity (colour, units of fH) and buoyancy (black contours) fields associated with (a,c) a strain flow, $\bar{U} = -\alpha x$, acting across a front/filament and (b,d) a uniform flow, $U_0 = \alpha L_R$, across a topographic ridge. The topographic ridge has profile $h(x) = H/(1 + (x/L_R)^2)$, and the front has a surface buoyancy profile $b_0(x) = -N^2 h(x)$, such that the geostrophic buoyancy fields are identical for the two flows. Plots (a,b) show the solutions for Rossby number $Ro_L = \delta = 0.2$, and plots (c,d) for $Ro_L = \delta = 0.9$. The background flow in each case is indicated by vectors (not to scale). 182
- 8.7 The energy budget for the linearised problem. The four energy reservoirs are the potential energy (PE), cross-front kinetic energy (CFKE), along-front kinetic energy (AFKE) and the strain field (STRAIN). Energy fluxes between the reservoirs are indicated by black/grey arrows. The grey arrow denotes an energy flux that is negligible (order δ^3) for small strains. Double-headed arrows (\leftrightarrow) on some energy pathways indicate that the direction of those fluxes reverse for sufficiently large strains and sharp fronts. The dashed box indicates the total energy E of the perturbation flow. 185

- 8.8 Time evolution of the energy reservoirs and fluxes for various strains, in units of $H^2\Delta B_0^2/N$. The frontal width at a given time is $L/L_R = 10e^{-\alpha t}$ where L_R is the Rossby radius. (a) The net energy input: $\partial_t E$. (b) The change in net kinetic energy with time: $\partial_t \langle (u^2 + v^2)/2 \rangle$. (c) The change in potential energy with time: $\partial_t \langle \Delta b(\Delta b + 2b_0)/(2N^2) \rangle$. (d) Potential energy to kinetic energy flux: $\langle wb \rangle$. (e) Kinetic energy to strain flux: $\alpha \langle -u^2/2 + 3v^2/2 \rangle$. (f) Strain to potential energy flux: $\langle -\alpha \Delta b(\Delta b + 2b_0)/(2N^2) \rangle$ 186
- 8.9 The time evolution of the strain magnitude, $\alpha(t)/f$, and the surface buoyancy field, $b(x, 0, t)$, in the numerical model for the initial condition defined by (8.18). A steady state is reached after about 45 hours. 189
- 8.10 Comparison of the numerical and analytical solutions. (a) The steady state numerical vertical velocity (m day^{-1}) field. (b) The analytical vertical velocity field (m day^{-1}) for the same frontal structure (see text for details). The grey lines on each plot are the wave and jet slopes predicted from the Green's function. 190
- 8.11 Comparison of the numerical and analytical solutions near the surface front. (a) The vorticity Rossby number $Ro = f^{-1}\partial_x v$ in the numerical model steady state. (b) The vertical velocity field [m day^{-1}] and buoyancy contours in the numerical model steady state. (c) The vertical velocity field (m day^{-1}) and buoyancy contours predicted by the analytical model. (d) The vertical velocity field (m day^{-1}) and buoyancy contours of the ad-hoc non-linear analytical model (see text for detailed description). 191

List of tables

2.1	Non-dimensional parameters and variable scales employed herein. The fundamental physical scales are the inertial frequency f , buoyancy difference across the front δB , buoyancy frequency N , strain α , horizontal length L , and height H . The geostrophic Rossby and Froude numbers, defined in terms of the geostrophic velocity scale $V_g \sim \Delta B_0 H / (fL)$, are also shown to assist in comparison of the present work with other studies.	27
2.2	Quantities of interest expressed in generalised momentum coordinates in both dimensional and non-dimensional forms. The effective velocities were defined by Blumen (2000) and have been generalised here to include the deformation field. The definition of the potential vorticity is taken as $q = (\mathbf{k} + f^{-1} \nabla \times \mathbf{U}) \cdot \nabla b$ where \mathbf{k} is a unit vector in the z -direction.	29
2.3	The non-dimensional, non-linear generalised model: coordinates, governing equation, and field relations. The model describes the response of a uniform PV fluid trapped between two rigid lids to certain initial conditions and/or a background strain flow, $\delta(T)$	35
3.1	Comparison of forced and spontaneous singularity formation on the lower boundary from the B00 and HB models of frontogenesis, where $\gamma = -b''_0(X_f) > 0$. Note that the maximum jet velocity scales inversely with Ro in the B00 model, and is independent of Ro in the HB model. In contrast, the Eulerian frontal position is independent of Ro in the B00 model, and proportional to Ro in the HB model. The Eulerian (real space) position of frontogenesis on the lower boundary is related to the momentum coordinate (GMC) position by $x_f = \exp(-\delta t_c) X_f - Ro v_f$	45

- 5.1 Parameter values for cases (i) to (v) shown in figure 5.2 and discussed in §5.3. The strain is constant in time, and $Bu = 1.5$ for each case. The structure of the generalised, HB and numerical model solutions for each case are shown in the figure listed in the ‘Fig.’ column. The table lists the fractional error expected from scaling arguments for the HB model, $(Ro^2 + 1)\delta^2$, and the GM model, $Ro^2\delta^2$, in addition to the RMS error (in the vertical velocity field) computed from comparison of the analytic solutions at their critical times with the numerical solutions at their critical times, as shown in each of the figures. 120
- 6.1 Linear forced solutions in spectral space for the flow about a 2D strained front with constant strain α and uniform stratification N^2 from the quasi-geostrophic, hydrostatic and non-hydrostatic models. The horizontal and vertical wavenumbers are k and l , respectively. The Coriolis frequency is f and the non-dimensional strain is $\delta = \alpha/f$. The solution at any instant in time can be determined if the PV anomaly at that time $q_0(xe^{\alpha t}, z)$ is known. 152
- 9.1 Solutions of the classical two-dimensional strained front problem defined by (1.12). The front is assumed to infinitely long and straight such that along-front gradients may be neglected. A simple background strain flow $\bar{\Psi} = -\alpha xy$ acts across the front. Models in the table are listed in chronological order. Models 1 through 4 are ‘balance’ models that omit waves, whereas models 5 through 7 include waves. Parameter $Ro_g = \Delta B_0 H / (f^2 L^2)$ is the geostrophic Rossby number, with L the frontal width, H the height, f the Coriolis parameter, and ΔB_0 the buoyancy difference across the front. Parameter N^2 is the buoyancy frequency. †The theory of Hoskins & Bretherton (1972) includes non-uniform PV but analytic solutions are only presented for uniform PV. 198

Chapter 1

Introduction

1.1 Fronts in the ocean and atmosphere

Density fronts are ubiquitous features in both the atmosphere and ocean. A broad definition of a ‘front’ is a region of fluid with a sharp density gradient in one horizontal direction, but a relatively weak density gradient in the orthogonal direction (Hoskins, 1982). Sharp fronts tend to form near boundaries where vertical flow is constrained (Levy *et al.*, 2012). Fronts can form via many different mechanisms and exhibit a vast range of behaviours and scales. For example, baroclinic instability of the atmosphere leads to the growth of global baroclinic waves. Synoptic fronts develop in regions of convergence between low and high pressure systems within these waves (Hoskins, 1982) and extend over thousands of kilometres, affecting weather on a continental scale. The elevated vertical velocities associated with these fronts drive the vertical transport of moisture and thus lead to cloud formation, and severe weather events such as heavy rain or snowfall. Figure 1.1a shows a satellite image of a synoptic-scale weather front that passed over the United Kingdom on 24 November 2009. An elongated band of cloud is evident in this image, indicating the band of intense upwelling directly ahead of the surface front. Smaller atmospheric fronts associated with local topography or cloud cover can also effect weather on a more local scale (Ostdiek & Blumen, 1997).

For the ocean, global-scale surface forcing via wind stresses and buoyancy fluxes drives large scale flow including western boundary currents such as the Gulf Stream and Kuroshio, and the Antarctic Circumpolar Current. These current systems are associated with strong density fronts and are barotropically and baroclinically unstable. This instability drives the formation of mesoscale eddies — the ocean equivalent of atmospheric highs and lows — with horizontal scales of 10km to 300km. As in the atmosphere, smaller scale fronts can develop in regions of convergence between these eddies. An example of such *frontogenesis*

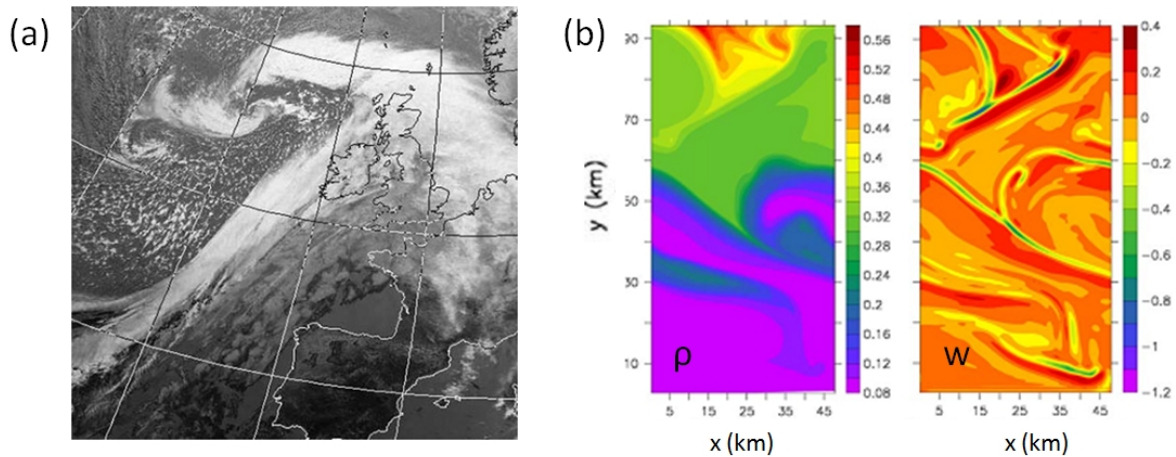


Fig. 1.1 Density fronts in the ocean and atmosphere. (a) Near-infrared satellite image of a weather front that passed over the United Kingdom on November 24 2009 (from figure 3 of Knippertz *et al.*, 2010). (b) Submesoscale fronts in a wind-forced simulation of the ocean mixed layer: (left) relative surface density ($\sigma = \rho - \rho_0$; kg m^{-3} , where ρ is the density and ρ_0 a reference value) and (right) vertical velocity (mm s^{-1}) at 15 m depth (from figure 5 of Mahadevan *et al.*, 2012). The surface density fronts are associated with bands of intense downwelling.

is shown in figure 1.1b which displays a snapshot of the surface density and vertical velocity associated with a simulation of baroclinic instability in the ocean mixed layer. Squeezing by the mesoscale eddies drives the formation of sharp fronts with widths of order 1km or smaller — known as *submesoscale fronts* — which are associated with very large vertical velocities. These elevated vertical velocities increase the transport of tracers such as heat, carbon dioxide and nutrients into the ocean interior, and are thus of fundamental importance to ocean circulation and biology (Ferrari, 2011; Thomas *et al.*, 2008). Ocean fronts can also form due to localised surface buoyancy fluxes such as river outflows or wind-driven mixing by storms (Tandon & Garrett, 1994).

Fronts in the atmosphere and ocean often exist as relatively steady, long-lived flow features due to a *geostrophic balance* between the frontal density gradient — and associated pressure force — and the Coriolis force arising from the rotation of the Earth, which leads to a horizontal jet orthogonal to the frontal density gradient. As an example, a schematic of an ocean surface front is shown in figure 1.2. A frontal jet (labelled 1) is present on the warm side of the sloping density front. If the front remains in exact geostrophic balance then there will be no circulation about the density front. However, fronts tend to be continually displaced from balance by background flows such as eddies (as represented in the schematic) and surface fluxes of buoyancy and momentum. In these cases, a *secondary circulation*

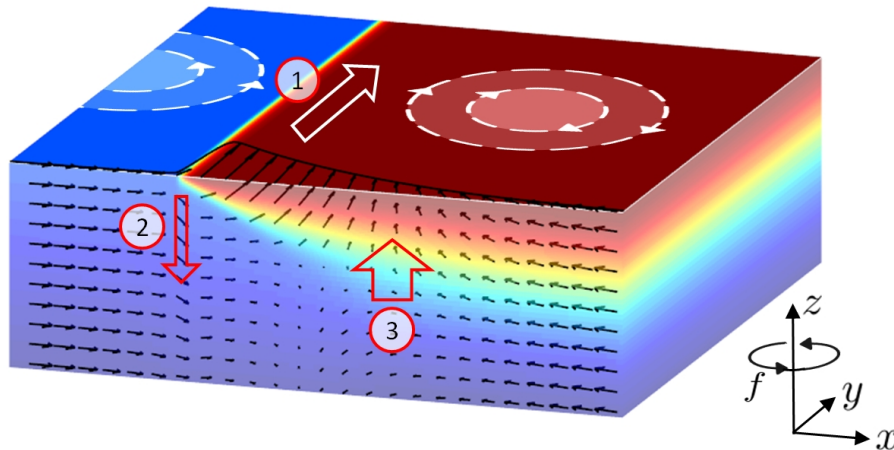


Fig. 1.2 Schematic of a frontal region at an upper boundary such as the ocean surface. Colours indicate the buoyancy with warm colours (red) denoting light fluid and cool colours (blue) denoting dense fluid. The pressure gradient across the front is balanced by the Coriolis force (rotation is denoted by the f) and drives an along-front jet (labelled 1). In the absence of active frontogenesis there is no other flow (although instabilities are possible for sharp enough fronts). In the case of active frontogenesis a secondary circulation is forced. Here frontogenesis is induced due to the confluent flow (shown by black arrows) generated by a pair of eddies shown schematically at the surface (not to scale). The secondary circulation consists of an intense downwelling (labelled 2) on the cold side of the front and a broader, weaker upwelling (labelled 3) on the warm side of the front.

will be generated about the front. During frontogenesis — that is, where the front is being sharpened — this circulation is thermally direct, meaning fluid upwells on the warm side (labelled 2 in the schematic) and downwells on the cool side of the front (labelled 3). As shown in the schematic, the flow directed away from the boundary is typically more intense than that directed toward the boundary, owing to non-linear dynamics that will be discussed later (e.g. Eliassen, 1962). These frontal dynamics are also visible in the submesoscale simulations shown in figure 1.1. The density fronts in figure 1.1b (left panel) are undergoing active frontogenesis, and so are collocated with intense downward flow (right panel).

Quantifying the strength of the secondary circulation associated with frontogenesis in terms of bulk fluid properties has — and continues to be — a major objective of research in this area (e.g. Eliassen, 1962; Hoskins & Bretherton, 1972; Rosso *et al.*, 2015). While synoptic scale atmospheric fronts can now be well resolved in numerical models (something that was certainly not true when Eliassen (1962) first considered this problem), small scale phenomena such as submesoscale ocean fronts remain difficult to resolve in even regional numerical ocean models (Boccaletti *et al.*, 2007), and virtually impossible to resolve in global ocean and climate models. Rosso *et al.* (2015) recently conducted submesoscale

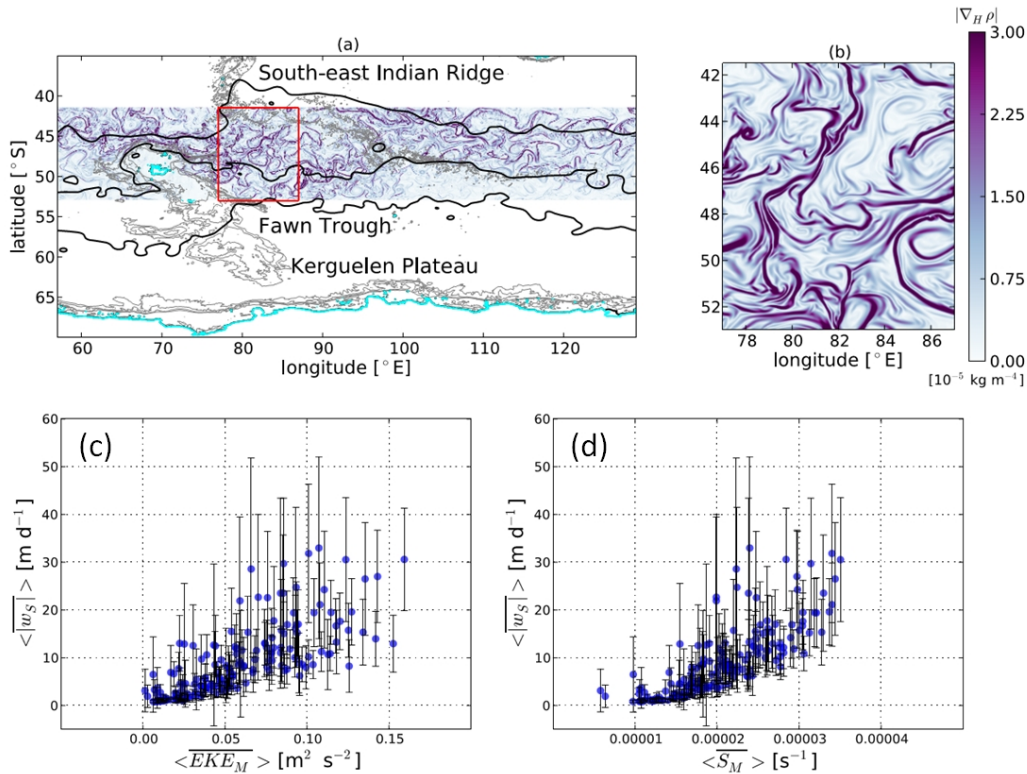


Fig. 1.3 Parameterisation of submesoscale phenomena. Results from the submesoscale resolving simulations of Rosso *et al.* (2015) — see figures 1 and 5 therein. (a,b) Horizontal density gradient magnitude at a particular instant in time for (a) the high-resolution simulated sector of the Southern Ocean and (b) a smaller area denoted by the red box in (a). The observed fronts are submesoscale (order 1 to 10 km in width). (c, d) The submesoscale vertical velocity (m day^{-1}) as a function of the (c) mesoscale eddy kinetic energy and (d) the mesoscale strain rate.

resolving simulations of a sector of the Southern Ocean, showing the vast network of submesoscale fronts that develop (figure 1.3a,b). These submesoscale fronts are associated with the most intense vertical velocities in the model, and are strongly correlated with the mesoscale eddy kinetic energy and strain, as shown in figure 1.3c and 1.3d, respectively. However, a dynamical model describing frontogenesis in the submesoscale regime does not yet exist. Thus, the theoretical basis for these correlations is unclear, making parameterisation difficult. Given the significance of submesoscale fronts to the global ocean (e.g. Ferrari, 2011), it is vital that their dynamics are well understood so that their effects can be correctly parameterised in global circulation models. The present work is intended as a first step in this direction.

As well as the driving vertical circulation, fronts and their associated jets are of immense research interest as potentially very significant sources of inertia-gravity wave (IGW) gen-

eration (Plougonven & Zhang, 2014). In the atmosphere, IGWs have the ability to initiate and modulate tropospheric convection (Zhang, 2004) and influence the circulation of the stratosphere (Plougonven & Zhang, 2014). One visible manifestation of wave generation in the atmosphere is the formation of lines of clouds and precipitation, called squall lines, ahead of advancing cold fronts (e.g. Ley & Peltier, 1978). The accurate parametrisation of non-orographic atmospheric IGWs, such as those generated at jets and fronts, is vital to the robustness of the next generation of climate models (Plougonven & Zhang, 2014). In the ocean, IGWs provide a mechanism for energy transport from the surface to the deep ocean and can drive significant vertical mixing in the interior (e.g. Polzin, 2010). While most ocean IGW energy is associated with forcing by tides and surface wind stresses (Wunsch & Ferrari, 2004), wave generation in frontal regions may provide an important contribution to energy loss from large scale flows (e.g. Alford *et al.*, 2013; Williams *et al.*, 2008). However, wave generation at fronts is not yet well understood or quantified, and thus its relative importance vis-a-vis other mechanisms of wave generation is difficult to determine.

Since inertia-gravity waves are typically characterised by relatively short time and length scales, they can be difficult to observe directly in the atmosphere and ocean. Fortuitously, Knippertz *et al.* (2010) were able to observe a very distinct wave generated at the weather front shown in figure 1.1a. For comparison with the observations, Knippertz *et al.* ran a regional simulation of the same front, the results of which are shown in figure 1.4. The frontal cloud bands noted in the previous figure 1.1a are associated with heavy rainfall (figure 1.4a). A cross-section of the frontal structure in terms of its potential vorticity (PV) and potential temperature is shown in figures 1.4c and 1.4d, respectively. The structure is typical of atmospheric cold fronts: a sharply sloping frontal interface with elevated PV divides the cold air on the left from the warm on the right. The tropopause — the line which separates the high-PV stratosphere from the low-PV troposphere — is pulled downwards on the cooler side of the surface front. This sloping tropopause can itself undergo so-called ‘upper-level frontogenesis’ (e.g. Griffiths & Reeder, 1996). However, of particular interest here is the vertical velocity field shown in figure 1.4b, and in particular the thin band of intensified vertical flow sitting ahead of, and parallel to, the front. This band appears to be an IGW generated at the surface front (Knippertz *et al.*, 2010), but the precise mechanism of generation is unclear.

Recently, IGW generation has also been observed at an ocean front by Alford *et al.* (2013). Alford *et al.* made observations in a region of the North Pacific Subtropical Front (NPSF), located on the northern edge of the North Pacific Subtropical Gyre, indicated by the red box in figure 1.5a. A plan view of the observed sea surface temperature in this region is shown in figure 1.5c. Figure 1.5a&c are good examples of where a large scale front (the

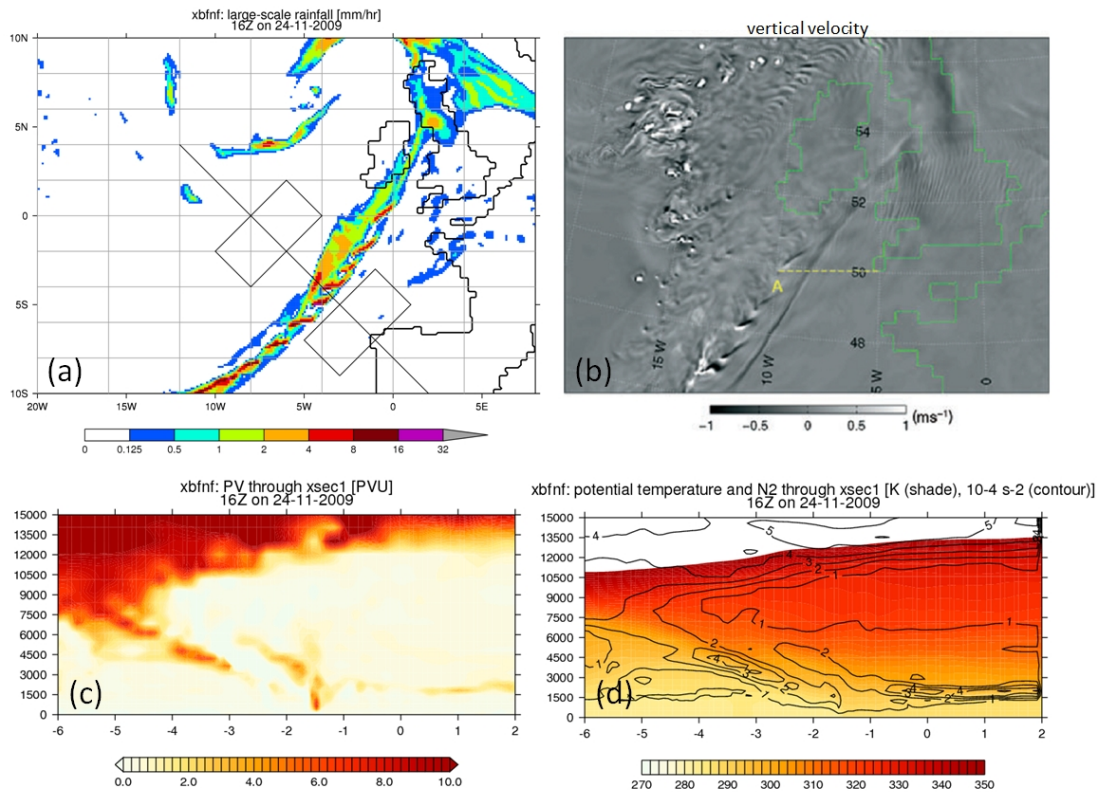


Fig. 1.4 UK Met Office simulations of the weather front shown in figure 1.1a, for 4pm on 24 November 2009. (a) Rainfall rate (mm hr^{-1}). Land shown by black contours. (b) Vertical velocity (m s^{-1}) at 4.5km height. Note the intense band of vertical flow, corresponding to an inertia-gravity wave, propagating ahead of the front. (c) Cross section of the PV ($1 \text{ PVU} = 10^{-6} \text{ K m}^2 \text{ kg}^{-1} \text{ s}^{-1}$) along the black line shown in (a). (d) Cross section of the potential temperature (K, colour) and stratification (10^{-4} s^{-2} , black contours) along the black line shown in (a). (Plots provided courtesy of J. Methven and B. Harvey, personal communication).

NPSF as shown in 1.5a) has been deformed by the action of eddies to generate smaller scale fronts and filaments, one of which is shown in the 1.5c. Figure 1.5b displays the vertical shear measured beneath the surface front along the cross-section shown in 1.5c. The shear shows a distinct banded structure characteristic of inertia-gravity waves. Once again, the precise mechanism of generation is unclear.

The examples introduced above emphasise two significant deficiencies in our current understanding of fronts in the ocean and atmosphere. Firstly, that relatively little is known about the dynamics of frontogenesis in ‘extreme’ parameter regimes such as the ocean submesoscale, and secondly, that the mechanisms of wave generation at fronts are not well understood. In the present work we seek to address these deficiencies. Our methodology is

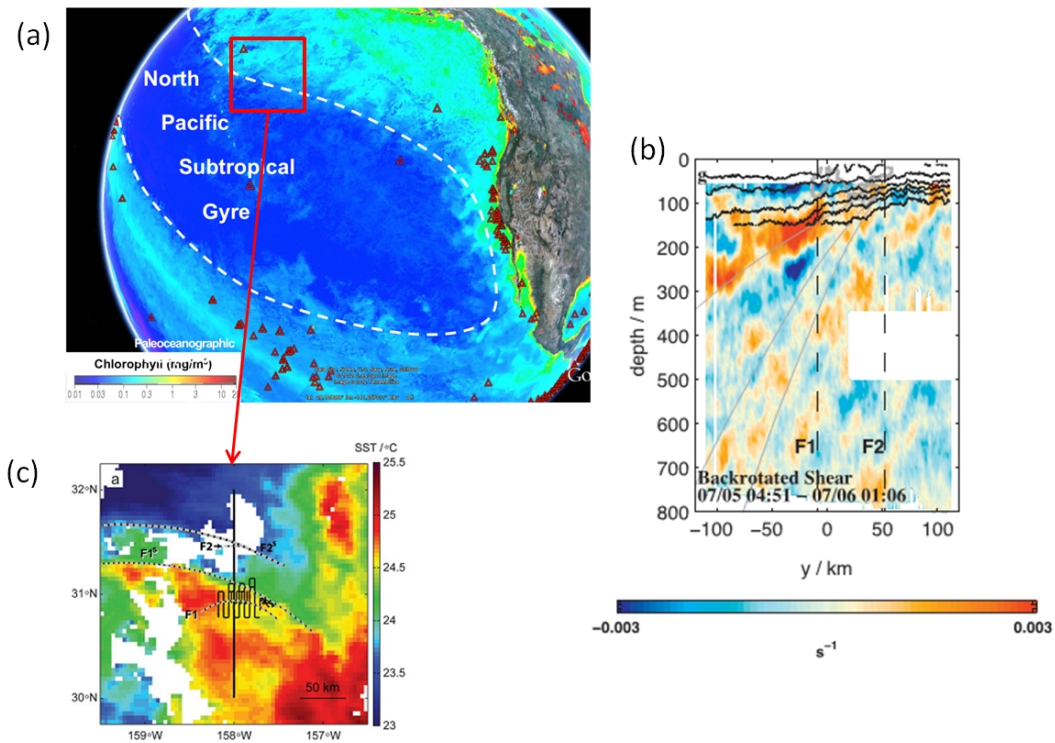


Fig. 1.5 Ocean fronts and wave generation. (a) The Subtropical Front on the northern edge of the North Pacific Subtropical Gyre. Colours indicate surface Chlorophyll concentration (K. McMahon, Woods Hole Oceanographic Institution). (b, c) Observations of the Subtropical Front in the North Pacific by Alford *et al.* (2013) — see figures 1 and 7 therein. (c) Plan view of the observed sea surface temperature (SST, °C), corresponding approximately to the region shown by the red box in (a). (b) The cross-frontal (meridional) vertical shear along the line shown in (c). Note the banded structure in the observed shear characteristic of inertia-gravity waves.

as follows. Firstly, we will seek to generalise present analytic models of frontogenesis which only apply in limited parameter regimes and do not describe inertia-gravity waves. Secondly, we will employ numerical simulations to verify the analytic results and furthermore, to study the dynamics of fronts in highly non-linear parameter regimes not well described by analytic models. The underlying motivation of this work is to build a dynamical basis for the parametrisation of fluxes of mass, momentum and tracers, and wave generation, associated with unresolved fronts in numerical global ocean and/or atmosphere models.

In the next section (§1.2) we discuss the equations relevant to frontogenesis. Following this, in §1.3 we introduce the present analytic models of fronts that are derived as solutions for particular limits of these equations.

1.2 The equations

Here we will employ the incompressible Boussinesq equations on an f -plane to study fronts. An f -plane model is appropriate given the relatively small scales of the fronts of interest. The assumption of incompressibility and small variation of density with vertical height (Boussinesq) are standard in ocean modelling, but less satisfactory for the atmosphere where the air density varies greatly with height. Nonetheless, the Boussinesq equations are a reasonable first order approximation and have been widely used in the study of fronts in the atmospheric literature (e.g. Hoskins & Bretherton, 1972). In Cartesian coordinates the f -plane, incompressible, inviscid, Boussinesq equations are

$$\frac{DU}{Dt} - fV = -\frac{1}{\rho_0} \frac{\partial P}{\partial x}, \quad (1.1a)$$

$$\frac{DV}{Dt} + fU = -\frac{1}{\rho_0} \frac{\partial P}{\partial y}, \quad (1.1b)$$

$$\frac{DW}{Dt} = B - \frac{1}{\rho_0} \frac{\partial P}{\partial z}, \quad (1.1c)$$

$$\frac{DB}{Dt} = 0, \quad (1.1d)$$

$$0 = \frac{\partial U}{\partial x} + \frac{\partial V}{\partial y} + \frac{\partial W}{\partial z}, \quad (1.1e)$$

where (U, V, W) are the velocities in the (x, y, z) directions, B is the buoyancy and P the pressure. The material derivative in (1.1) is defined by

$$\frac{D}{Dt} = \frac{\partial}{\partial t} + U \frac{\partial}{\partial x} + V \frac{\partial}{\partial y} + W \frac{\partial}{\partial z} = \frac{\partial}{\partial t} + \mathbf{U} \cdot \nabla. \quad (1.2)$$

The constant f is the Coriolis parameter and ρ_0 is the reference density of the fluid. The full density ρ is related to the buoyancy via $B = -g(\rho - \rho_0)/\rho_0$ where g is the acceleration due to gravity.

1.2.1 The background flow equations

Fluids often exhibit many different scales of flow, with the largest scales forcing the smaller scales. A common example is baroclinic instability, as in the classical Eady problem, where a large scale horizontal density gradient in geostrophic balance with a vertical shear, forces the generation of smaller scale baroclinic eddies. If the generated smaller scale flow has minimal feedback on the larger scale, then it is often convenient to represent the large scale flow as an imposed ‘background flow’.

Here we will consider a purely horizontal, non-divergent background flow $\bar{\mathbf{U}} = (\bar{U}, \bar{V}, 0)$ defined by a background flow streamfunction $\bar{\psi}$ where

$$\bar{U} = \frac{\partial \bar{\psi}}{\partial y}, \text{ and } \bar{V} = -\frac{\partial \bar{\psi}}{\partial x}. \quad (1.3)$$

The net flow is composed of the background and perturbation parts,

$$U = \bar{U} + u, \quad (1.4a)$$

$$V = \bar{V} + v, \quad (1.4b)$$

$$W = w, \quad (1.4c)$$

$$P = \bar{P} + p, \quad (1.4d)$$

$$B = \bar{B} + b, \quad (1.4e)$$

with the perturbation part denoted by lower case symbols. The background flow is chosen such that in the absence of perturbations it is a valid solution to the inviscid equations of motion (1.1). Thus, we find that the background pressure and buoyancy satisfy

$$\frac{\partial \bar{U}}{\partial t} + \bar{U} \frac{\partial \bar{U}}{\partial x} + \bar{V} \frac{\partial \bar{U}}{\partial y} - f\bar{V} = -\frac{1}{\rho_0} \frac{\partial \bar{P}}{\partial x}, \quad (1.5a)$$

$$\frac{\partial \bar{V}}{\partial t} + \bar{U} \frac{\partial \bar{V}}{\partial x} + \bar{V} \frac{\partial \bar{V}}{\partial y} + f\bar{U} = -\frac{1}{\rho_0} \frac{\partial \bar{P}}{\partial y} \quad (1.5b)$$

$$\bar{B} = \frac{1}{\rho_0} \frac{\partial \bar{P}}{\partial z}, \quad (1.5c)$$

$$\frac{\partial \bar{B}}{\partial t} + \bar{U} \frac{\partial \bar{B}}{\partial x} + \bar{V} \frac{\partial \bar{B}}{\partial y} = 0. \quad (1.5d)$$

We now substitute (1.4) and (1.5) into the Boussinesq equations (1.1) and thereby derive equations for the evolution of the perturbation flow:

$$\frac{Du}{Dt} + \mathbf{u} \cdot \nabla \bar{U} - fv = -\frac{1}{\rho_0} \frac{\partial p}{\partial x}, \quad (1.6a)$$

$$\frac{Dv}{Dt} + \mathbf{u} \cdot \nabla \bar{V} + fu = -\frac{1}{\rho_0} \frac{\partial p}{\partial y}, \quad (1.6b)$$

$$\frac{Dw}{Dt} = b - \frac{1}{\rho_0} \frac{\partial p}{\partial z}, \quad (1.6c)$$

$$\frac{Db}{Dt} + \mathbf{u} \cdot \nabla \bar{B} = 0, \quad (1.6d)$$

$$0 = \frac{\partial u}{\partial x} + \frac{\partial v}{\partial y} + \frac{\partial w}{\partial z}. \quad (1.6e)$$

We call (1.6) the *background flow equations*. Note that the material derivative in (1.6) includes advection by the full (i.e. both background and perturbation) flow as defined by (1.2). The background flow acts on some initial velocity or buoyancy perturbation through the material advection terms, and thus drives a flow response. These equations will form the basis for all theory and numerical simulations developed henceforth. Note that in the absence of a background flow (1.6) collapses back to the regular Boussinesq equations (1.1).

1.2.2 The 2D frontogenesis problem

The classical two-dimensional (2D) forced frontogenesis problem (e.g. Hoskins & Bretherton, 1972; Snyder *et al.*, 1993; Williams & Plotkin, 1968, etc.) considers the effect of a pure strain background flow field on a density perturbation (front). The strain streamfunction is

$$\bar{\psi} = -\alpha xy, \quad (1.7)$$

where the strain magnitude is defined here as $\alpha = -\partial_x u = -\partial_{xy} \bar{\psi}$, and may be a function of time, $\alpha = \alpha(t)$. This strain flow is displayed in figure 1.6. It is the first order representation of the strain associated with *any* purely horizontal flow near a given point (as may be shown via a Taylor expansion). Here the background strain is intended to represent the flow confluence in regions of the atmosphere and ocean boundary layers such as between ocean gyres, eddies and within large scale baroclinic waves (e.g. atmospheric weather systems). The characteristic magnitude of the strain will differ in each of these situations owing to the different length and velocity scales. To quantify this variation, it is convenient to define a

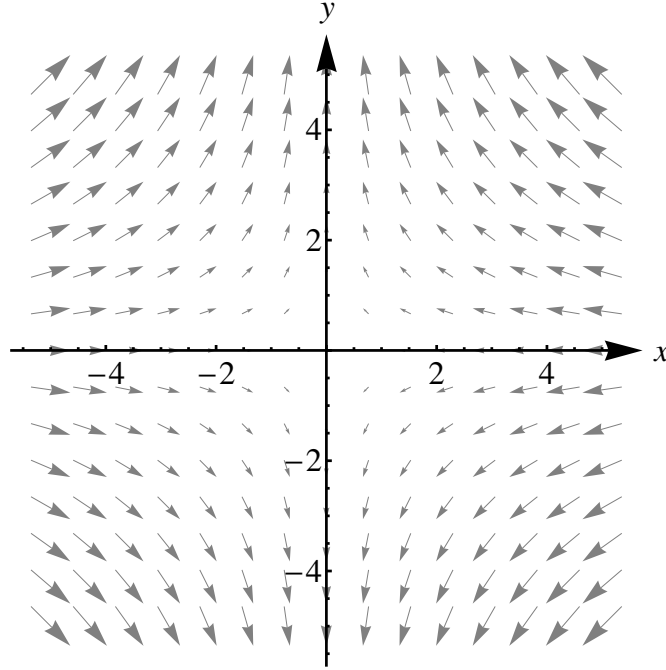


Fig. 1.6 Vector plot of the idealised strain flow $\bar{\psi} = -\alpha xy$ where $\alpha > 0$.

strain Rossby number

$$\delta = \left| \frac{1}{f} \frac{\partial u}{\partial x} \right| = \frac{\alpha}{f}. \quad (1.8)$$

As an example, a typical synoptic scale weather system has a length scale of order 1000 km , velocity scale of order 10 m s^{-1} and assuming $f \sim 10^{-4} \text{ s}^{-1}$, the corresponding Rossby number is $\delta \sim 0.1$. By contrast, a submesoscale eddy field in the ocean might have length scales of order 10 km and velocities of order 1 m s^{-1} , yielding $\delta \sim 1$. Given this difference in Rossby number, we anticipate that the dynamics of the flow in these two cases will be substantially different. The classical models of frontogenesis described in the next section (§1.3) all make the assumption of small strain Rossby number, or $\alpha \ll f$. A major objective of the present work is to investigate the effect of larger strains.

The background pressure and buoyancy fields corresponding to the pure strain flow defined by (1.7) are, from (1.5),

$$\bar{P} = -\rho_0 \left(\frac{\alpha^2}{2} (x^2 + y^2) + \frac{\partial_t \alpha}{2} (y^2 - x^2) - \alpha f xy - \int \bar{B}(z) dz \right), \quad (1.9a)$$

$$\bar{B} = \bar{B}(z). \quad (1.9b)$$

Here, without loss of generality, we will assume $\bar{B} = 0$ and include any background stratification (i.e. $\bar{B} = N^2(z)$) as part of the perturbation buoyancy b . With the above definitions

(1.9), the background flow equations (1.6) become

$$\frac{Du}{Dt} - \alpha u - f v = -\frac{1}{\rho_0} \frac{\partial p}{\partial x}, \quad (1.10a)$$

$$\frac{Dv}{Dt} + \alpha v + f u = -\frac{1}{\rho_0} \frac{\partial p}{\partial y}, \quad (1.10b)$$

$$\frac{Dw}{Dt} = b - \frac{1}{\rho_0} \frac{\partial p}{\partial z}, \quad (1.10c)$$

$$\frac{Db}{Dt} = 0, \quad (1.10d)$$

$$0 = \frac{\partial u}{\partial x} + \frac{\partial v}{\partial y} + \frac{\partial w}{\partial z}. \quad (1.10e)$$

At this point it is useful to note that the effect of the strain flow (1.7) on an initial buoyancy anomaly (or any tracer) in the xy plane will be to squeeze it in the x -direction, and stretch it out along the y -axis. Specifically, a passive tracer field will evolve as $C = C_0(xe^\beta, ye^{-\beta})$, where $C_0(x, y)$ is the initial distribution and β is the non-dimensional *time-integrated strain*,

$$\beta = \int_0^t \alpha(t') dt'. \quad (1.11)$$

The tracer field will therefore become increasingly elongated and uniform in the y -direction with time, as shown in figure 1.7. Given this behaviour, it is useful to simplify the system by making the assumption *a priori* that the perturbation is uniform and the buoyancy front ‘infinitely long’ in the y -direction. The y derivatives of the perturbation variables in (1.10) then vanish and the equations become,

$$\frac{Du}{Dt} - \alpha u - f v = -\frac{1}{\rho_0} \frac{\partial p}{\partial x}, \quad (1.12a)$$

$$\frac{Dv}{Dt} + \alpha v + f u = 0, \quad (1.12b)$$

$$\frac{Dw}{Dt} = b - \frac{1}{\rho_0} \frac{\partial p}{\partial z}, \quad (1.12c)$$

$$\frac{Db}{Dt} = 0, \quad (1.12d)$$

$$0 = \frac{\partial u}{\partial x} + \frac{\partial w}{\partial z}, \quad (1.12e)$$

where the material derivative is now

$$\frac{D}{Dt} = \frac{\partial}{\partial t} + (u - \alpha x) \frac{\partial}{\partial x} + w \frac{\partial}{\partial z}. \quad (1.12f)$$

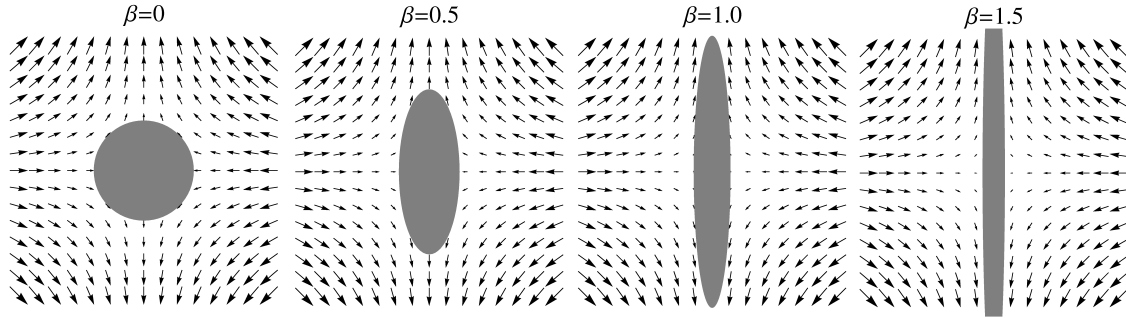


Fig. 1.7 The effect of the strain flow $\bar{\psi} = -\alpha xy$ on an initially circular ‘blob’ of passive tracer. A tracer C in this strain flow will evolve as $C = C_0(xe^\beta, ye^{-\beta})$ where $C_0(x, y)$ is the initial distribution and β is defined by (1.11).

Equations (1.12) are the *2D strained front equations* and form the basis for virtually all analytic — and many numerical — studies of strain-forced frontogenesis. The infinitely long y direction is called the ‘along-front direction’ and x the ‘cross-front direction’.

Potential vorticity (PV) conservation may be derived from the strained front equations (1.12) as,

$$\frac{Dq}{Dt} = 0, \quad (1.13)$$

where the PV, q , is here defined as

$$q = \left(1 + \frac{1}{f} \frac{\partial v}{\partial x}\right) \frac{\partial b}{\partial z} - \frac{1}{f} \frac{\partial v}{\partial z} \frac{\partial b}{\partial x}. \quad (1.14)$$

The background PV, away from the front, is simply $q_0 = N^2$, where N^2 is the background stratification. As will be seen below, many analytic models of frontogenesis are based on the principle of PV conservation.

1.3 Analytic models of fronts

The classical frontogenesis mechanism of a horizontal strain field, as introduced in the previous section, was first suggested almost a century ago (Bergeron, 1928). A large variety of conceptual and analytic models of this system have since been developed including Sawyer (1956), Eliassen (1962), Stone (1966), Williams & Plotkin (1968), Hoskins & Bretherton (1972) and Davies & Muller (1988). The early conceptual models (Eliassen, 1962; Sawyer, 1956) emphasised the importance of horizontal boundaries in constraining the vertical flow and thereby driving rapid frontogenesis via a non-linear self-advection mechanism — these boundary dynamics will be discussed in §1.3.1 below. Linear models of frontogenesis,

such as the quasigeostrophic solution to (1.12) derived by Williams & Plotkin (1968) and discussed in §1.3.3, were unable to capture these dynamics and thus produced unrealistic frontal structures. In §1.3.2 we discuss how Hoskins & Bretherton (1972) applied the results of Eliassen (1962) to formulate an analytic non-linear solution to (1.12) that produces realistic frontal structures. We note that both the Williams & Plotkin (1968) and Hoskins & Bretherton (1972) models were derived with application to synoptic-scale atmospheric fronts in mind and as such, consider only the weak strain limit, $\alpha \ll f$.

More recently, it has been recognised that the system described by (1.12) can exhibit ‘spontaneous frontogenesis’ in the absence of a background flow (i.e. $\alpha = 0$), if it is somehow displaced from geostrophic balance (e.g. Blumen, 2000; Blumen & Williams, 2001; Blumen & Wu, 1995; Ou, 1984). The mechanism is closely related to classical geostrophic adjustment (Blumen, 1972; Rossby, 1938). As an archetype, the Blumen (2000) analytic model of spontaneous frontogenesis will be discussed in §1.3.4.

1.3.1 Boundary dynamics

Following the work of Eliassen (1962), it is insightful to consider what the strained front equations (1.12) say about the evolution of a conservative tracer on a solid boundary. Assuming the boundary is a rigid lid, the vertical flow must vanish, $w = 0$, and thus material conservation of some conservative tracer C (for example, the PV or the buoyancy) on the boundary becomes

$$\frac{\partial C}{\partial t} + (u - \alpha x) \frac{\partial C}{\partial x} = 0. \quad (1.15a)$$

Similarly, conservation of along-front momentum (1.12b) becomes

$$\frac{\partial v}{\partial t} + (u - \alpha x) \frac{\partial v}{\partial x} + \alpha v + f u = 0. \quad (1.15b)$$

Equations (1.15) are coupled through the cross-front flow, u , which may be eliminated by rearranging the equations,

$$u \left(f + \frac{\partial v}{\partial x} \right) = - \frac{\partial v}{\partial t} - \alpha v + \alpha x \frac{\partial v}{\partial x}, \quad (1.16a)$$

$$u \left(\frac{\partial C}{\partial x} \right) = - \frac{\partial C}{\partial t} + \alpha x \frac{\partial C}{\partial x}, \quad (1.16b)$$

and then cross-multiplying to obtain,

$$\left(f + \frac{\partial v}{\partial x} \right) \frac{\partial C}{\partial t} - \left(\frac{\partial v}{\partial t} + \alpha(v + f x) \right) \frac{\partial C}{\partial x} = 0. \quad (1.17)$$

Equation (1.17) is readily solved to obtain an expression for the time evolution of the tracer on the boundary,

$$C = C_0 \left(e^{\beta} \left(x + \frac{v}{f} \right) \right), \quad (1.18)$$

where the *function* C_0 corresponds to the initial profile and β is defined by (1.11). As shown previously (e.g. figure 1.7), the effect of the strain is to squeeze the tracer profile with time and therefore amplify x gradients. This is an entirely linear effect associated with advection by the background strain flow. However, according to (1.18) the boundary tracer field is also translated to the left by v/f due to advection by the perturbation flow u . This is the non-linear effect noted by Eliassen (1962) that can give rise to very rapid frontogenesis. For instance, the tracer gradient $\partial_x C$ computed from (1.18) is proportional to the absolute vorticity, $(f + \partial_x v)$, and thus is amplified in regions of cyclonic vorticity and weakened in regions of anticyclonic vorticity.

Furthermore, the non-linear contraction of the front in cyclonic regions provides the possibility of discontinuity formation. This process is most readily described through the introduction of a new coordinate, motivated by the structure of the boundary solution (1.18). Following Eliassen (1962) we define

$$\chi = x + \frac{v}{f}, \quad (1.19)$$

which is called the *momentum coordinate*. Transforming to this coordinate we have that $C = C_0(e^{\beta} \chi)$ on the boundary — that is, tracer boundary conditions in momentum coordinates possess the special property of having no explicit reference to the interior flow. The derivative transforms between regular Eulerian coordinates (x, z, t) and momentum coordinates $(\chi = x + v/f, Z = z, T = t)$ may be derived as

$$\frac{\partial}{\partial x} = J \frac{\partial}{\partial \chi}, \quad (1.20a)$$

$$\frac{\partial}{\partial z} = \frac{\partial}{\partial Z} + \frac{1}{f} \frac{\partial v}{\partial Z} J \frac{\partial}{\partial \chi}, \quad (1.20b)$$

$$\frac{\partial}{\partial t} = \frac{\partial}{\partial T} + \frac{1}{f} \frac{\partial v}{\partial T} J \frac{\partial}{\partial \chi}, \quad (1.20c)$$

where J is the Jacobian of the transformation,

$$J = \frac{\partial \chi}{\partial x} = 1 + \frac{1}{f} \frac{\partial v}{\partial x} = \left(1 - \frac{1}{f} \frac{\partial v}{\partial \chi} \right)^{-1}, \quad (1.20d)$$

and is equal to the vertical vorticity of the fluid. Discontinuities in the solution occur if/when the Jacobian becomes infinite; that is, $\partial_\chi v$ grows sufficiently large. For a constantly strained front with $\alpha > 0$ the formation of a discontinuity is inevitable, as will be seen in the next section.

1.3.2 The HB model

The Hoskins & Bretherton (1972, hereafter, HB) model of frontogenesis utilises the momentum coordinate (1.19) to solve the 2D strained front equations (1.12) in the limit of a weak background strain flow, defined by $\alpha \ll f$. A key innovation of Hoskins & Bretherton (1972) was to show that PV takes a remarkably simple form when expressed in momentum coordinates. Applying the derivative transformations (1.20) to the PV equation (1.14) results in

$$q = \frac{\partial b}{\partial Z} \left(1 - \frac{1}{f} \frac{\partial v}{\partial \chi} \right)^{-1}. \quad (1.21)$$

For an initial PV, q_0 , conservation of PV can be expressed as

$$q = q_0 \left(\chi e^\beta, b \right), \quad (1.22)$$

since both the buoyancy b and quantity χe^β are conserved in the 2D flow,

$$\frac{D}{Dt} \left(\chi e^\beta \right) = \frac{Db}{Dt} = 0. \quad (1.23)$$

Combining the above results, PV conservation in momentum coordinates may be written as (e.g. equation 3.3 of Hoskins & Bretherton, 1972)

$$\left(1 - \frac{1}{f} \frac{\partial v}{\partial \chi} \right) q_0 \left(\chi e^\beta, b \right) = \frac{\partial b}{\partial Z}. \quad (1.24)$$

This result is a generic property of the 2D strained front equations (1.12) and does not rely on any additional assumptions.

Returning to the strained front equations (1.12), Hoskins & Bretherton (1972) made the assumption that the frontal system is ‘balanced’ in the sense that time evolution occurs on the timescale of the background flow, $D/Dt \sim \alpha$. Thus (1.12b) implies that $u \sim (\alpha/f)v$ and the cross-front flow, u , is therefore negligible compared to the along-front flow, v , in the limit of weak strain. Equations (1.12a) thus reduces to geostrophic balance in this limit,

$$\mathcal{O} \left(\frac{\alpha^2}{f} v \right) - f v = -\frac{1}{\rho_0} \frac{\partial p}{\partial x}. \quad (1.25)$$

Since $w \sim (H/L)u$ from continuity (1.12e), following similar reasoning reduces (1.12c) to hydrostatic balance,

$$\mathcal{O}\left(\frac{H^2\alpha^2}{L^2f}v\right) = b - \frac{1}{\rho_0}\frac{\partial p}{\partial z}, \quad (1.26)$$

Eliminating the pressure in (1.25) and (1.26) we have the usual thermal wind equation,

$$\frac{\partial v}{\partial z} = \frac{1}{f}\frac{\partial b}{\partial x}. \quad (1.27)$$

Transforming (1.27) to momentum coordinates using the derivative relations (1.20) yields simply

$$\frac{\partial v}{\partial Z} = \frac{1}{f}\frac{\partial b}{\partial \chi}. \quad (1.28)$$

Taking a Z derivative of the PV relation derived above (1.24) and substituting $\partial_Z v$ from (1.28) and $\partial_\chi v$ from (1.24), it is straightforward to write down an equation for the buoyancy (e.g. equation 3.39 of Hoskins & Bretherton (1972))

$$\left[\frac{\partial^2}{\partial \chi^2} + \frac{\partial}{\partial Z} \left(\frac{f^2}{q_0(\chi e^\beta, b)} \frac{\partial}{\partial Z} \right) \right] b = 0. \quad (1.29)$$

For an arbitrary PV that depends on the buoyancy b , (1.29) is difficult to solve.

However, Hoskins & Bretherton (1972) presented an analytic solution for the case of uniform PV, $q_0 = N^2$, where N^2 is the background stratification. In this limit (1.29) becomes

$$\left[\frac{\partial^2}{\partial \chi^2} + \frac{f^2}{N^2} \frac{\partial^2}{\partial Z^2} \right] b = 0. \quad (1.30)$$

Equation (1.30) must be solved subject to the tracer boundary condition derived previously (1.18) — that is, $b = b_0(e^\beta \chi)$ on the boundaries. Time only enters the solution as a parameter in this boundary condition and the time-evolving interior flow is thus forced entirely by the strain-driven collapse of the boundary buoyancy profile. Hoskins & Bretherton (1972) solved (1.30) for a domain with two rigid lids at $z = 0$ and $z = H$. An example solution of the uniform PV Hoskins & Bretherton (1972) model is displayed in figure 1.8 for parameter values typical of an atmospheric front. The assumption of uniform PV constrains the model to have fronts on both the upper and lower rigid lid boundaries. The circulation about these fronts is described as ‘thermally direct’, meaning vertical velocities are upward on the warm side and downward on the cool side of the front. The vertical velocity field in figure 1.8 is initially weak, but the self-advection of the cross-frontal circulation leads to the formation of discontinuities (or buoyancy ‘steps’) on the boundaries on a timescale of days (26 hours for

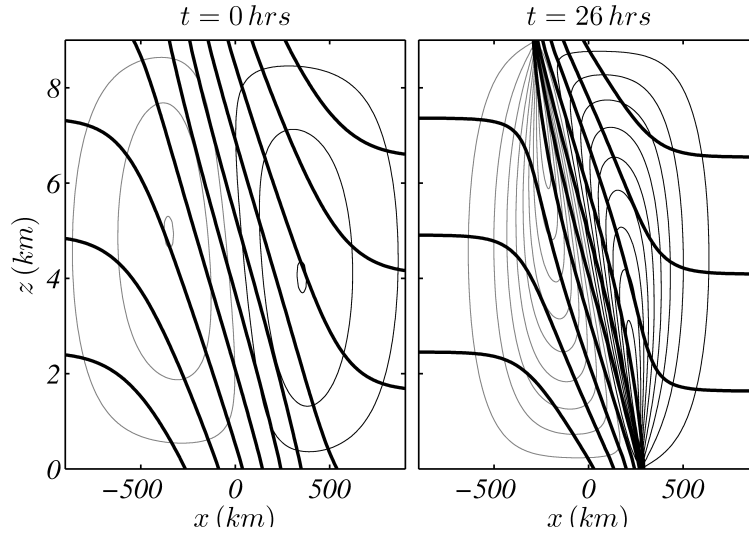


Fig. 1.8 The solution to the uniform PV Hoskins & Bretherton (1972) model (1.30) for parameter values typical of an atmospheric front ($\alpha = 0.1f$, $N = 33.3f$) at the initial time, and at the time of discontinuity formation. Buoyancy contours are shown as thick black lines. Vertical velocity contours (spacing: 0.3 cm s^{-1}) are shown as thin lines: grey = down, black = up.

the example in the figure). The formation of such discontinuities implies a breakdown of inviscid dynamics and the analytic model is formally invalid beyond this point — although efforts have been made to extend it (e.g. see Cullen & Purser, 1984).

The uniform potential vorticity HB model (1.30) has also been considered in a *semi-infinite domain*, rather than the dual rigid lid configuration (e.g. Davies & Muller, 1988). In this case, the rigid lid constraint, $b = b_0(e^\beta \chi)$, is imposed on a single boundary at $Z = 0$ and it is also required that $b \rightarrow N^2 Z$ as $Z \rightarrow \infty$. However, for an isolated front, the class of solutions satisfying these criteria have velocity fields that do not vanish at infinity and are thus somewhat unrealistic. The finite velocities at infinity result from the fact that the frontal buoyancy and pressure gradient at the boundary cannot be compensated by variations in stratification in the interior (owing to the assumption of uniform PV), and thus still drive flow at infinity. Nonetheless, the Davies & Muller (1988) semi-infinite model exhibits some notable dynamical differences to the Hoskins & Bretherton (1972) rigid lid model that may be physically relevant. In particular, in the semi-infinite model the vertical scale of the flow is no longer fixed and instead contracts at the same rate as the horizontal scale, such that the characteristic slope of the circulation is constant.

The HB model (1.29) is often described as a state of ‘semigeostrophic balance’. This nomenclature arises since the along-front velocity v is in geostrophic balance, but the cross-frontal flow (u, w) is non-zero, unlike true geostrophic balance. The fact that $v =$

v_g also implies that the solution contains no waves. The absence of waves is intriguing since the system is continually accelerating due to the forcing by the strain flow. In fact, ‘semigeostrophic balance’ can only be maintained as a direct result of the assumption of weak strain, $\alpha \ll f$, which implies that this acceleration is vanishingly small. As we will see later, in reality any finite strain — and therefore acceleration — will give rise to waves, but the amplitude of these waves is exponentially small for weak strains.

1.3.3 The QG model

The quasigeostrophic (QG) model (e.g. Williams & Plotkin, 1968) describes 2D frontogenesis in the limit of strong rotation and weak strain. While the QG model originated earlier than the HB model, it is readily derived directly from the HB model as the strongly-rotating limit; that is, the vorticity Rossby number,

$$Ro_g = \frac{1}{f} \frac{\partial v}{\partial x} \ll 1. \quad (1.31)$$

In this limit the momentum coordinate, $\chi = x + v/f$, becomes equal to the Eulerian coordinate, $\chi \simeq x$. The equations describing the HB model (1.29) therefore also describe the QG model, but with the momentum coordinate replaced by the Eulerian coordinate. Thus, the non-linearity seen in the HB model is no longer present, and a discontinuity only evolves in the limit of infinite time.

A QG model solution is shown in figure 1.9 for the same parameter values as the previous HB model solution (figure 1.8). The front in the QG solution remains vertically oriented, rather than slumping under the effect of gravity as seen in the HB solution. As a result, whereas the HB model forms a discontinuity at $t = 26$ hours, the QG solution remains smooth, with a much weaker circulation at this time. The front in the QG solution gradually sharpens with time until the isopycnals eventually overturn near the boundaries (e.g. $t = 52$ hours). The development of such static instabilities is characteristic of QG models of frontogenesis (e.g. also see the QG model of Stone, 1966), and implies that the small Rossby number assumption (1.31) has broken down at the front.

1.3.4 The Blumen model

In the previous sections we have considered so-called *balanced* frontogenesis — that is, frontogenesis that does not involve inertia-gravity waves. In those models, sharp fronts formed due to the squeezing by the background strain flow and self-advection by the perturbation flow. In contrast, the Blumen (2000) model considers the 2D frontal system (1.12) in the

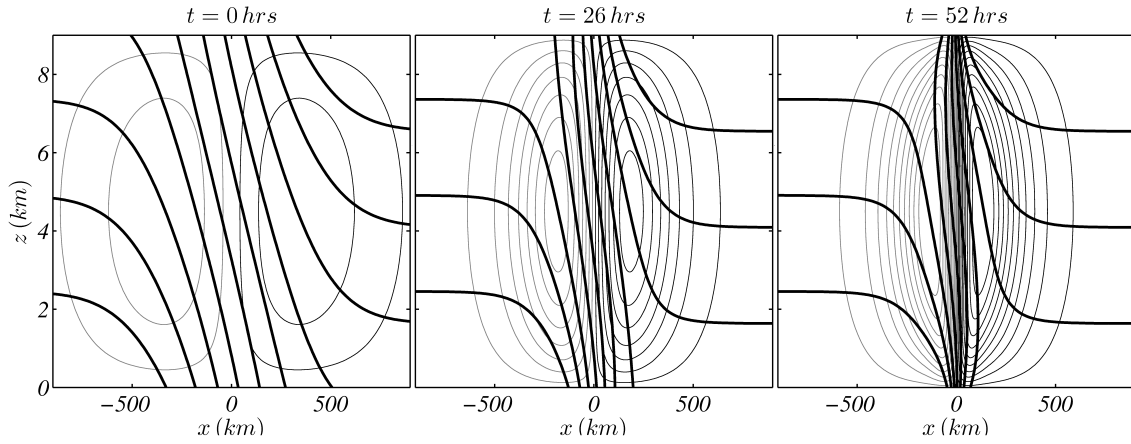


Fig. 1.9 The solution to the QG model of frontogenesis for parameter values typical of an atmospheric front (as in the previous figure) at $t = 0, 26$ and 52 hours. Buoyancy contours are shown as thick black lines. Vertical velocity contours are shown as thin lines: grey = down, black = up. Contour levels are the same as for the previous figure (1.8).

absence of strain, but with an unbalanced initial condition. Waves are generated due to geostrophic adjustment of this initial condition, and the self-advection of the wave drives frontogenesis. Once again, the non-linear frontal sharpening can be captured using the momentum coordinate.

Blumen (2000) consider the special case of an unstratified fluid with uniformly zero PV, $q = 0$, trapped between dual rigid lids. Referring to the expression for PV in momentum coordinates (1.21) implies that $\partial_z b = 0$ is everywhere zero when $q = 0$ and thus the buoyancy b is a function of χ only, $b = b_0(\chi)$. Thus, the zero strain, zero PV, hydrostatic frontal equations can be derived from (1.12) as

$$\frac{Du}{Dt} - fv = -fv_g, \quad (1.32a)$$

$$\frac{Dv}{Dt} + fu = 0, \quad (1.32b)$$

$$\frac{\partial v_g}{\partial z} = \frac{1}{f} \frac{\partial b}{\partial x}, \quad (1.32c)$$

$$b = b_0(\chi), \quad (1.32d)$$

$$0 = \frac{\partial u}{\partial x} + \frac{\partial w}{\partial z}, \quad (1.32e)$$

where the material derivative is now

$$\frac{D}{Dt} = \frac{\partial}{\partial t} + u \frac{\partial}{\partial x} + w \frac{\partial}{\partial z}, \quad (1.32f)$$

or

$$\frac{D}{Dt} = \frac{\partial}{\partial T} + w \frac{\partial}{\partial Z}, \quad (1.32g)$$

in momentum coordinates ($\chi = x + v/f, Z = z, T = t$). The geostrophic velocity v_g in (1.32) is defined in terms of the pressure as

$$v_g = \frac{1}{\rho_0 f} \frac{\partial p}{\partial x}. \quad (1.33)$$

To derive the Blumen (2000) model we take the material derivative of (1.32b) and substitute Du/Dt from (1.32a) to yield,

$$\frac{D^2 v}{Dt^2} + f^2 v = f^2 v_g. \quad (1.34)$$

Thus, the motion is forced by the geostrophic velocity (or buoyancy gradient). The geostrophic velocity can be determined from thermal wind (1.32c), which upon transformation to momentum coordinates, yields the expression

$$\frac{\partial v_g}{\partial Z} - \frac{1}{f} \frac{\partial b}{\partial \chi} = \frac{1}{f} \left(\frac{\partial v}{\partial \chi} \frac{\partial v_g}{\partial Z} - \frac{\partial v}{\partial Z} \frac{\partial v_g}{\partial \chi} \right). \quad (1.35)$$

Equation (1.35) demonstrates that while some relations, such as PV, are greatly simplified by transformation to momentum coordinates, others are made significantly more complex (another example is continuity, (1.32e)).¹ Blumen (2000) assumed that the vertical advection term, $w \partial_Z$, in the material derivative (1.32g) may be neglected at first order, or equivalently $D/Dt = \partial_T$. Under this assumption (1.34) and (1.35) may be solved directly. Blumen (2000) examined this problem for the initial condition of zero motion, $u = v = 0$, for which the solution is

$$v(\chi, Z, T) = v_g(\chi, Z) (1 - \cos(fT)), \quad (1.36a)$$

$$u(\chi, Z, T) = v_g(\chi, Z) \sin(fT), \quad (1.36b)$$

with the geostrophic velocity defined by

$$v_g(\chi, Z) = \frac{1}{2f} b'_0(\chi) (2Z - H). \quad (1.36c)$$

Primes denote derivatives and the constant of integration is chosen to maintain the symmetry of the system (although other choices are also valid). Equations (1.36) show that fluid

¹Note that Blumen & Williams (2001) erroneously neglected the non-linear term in (1.35) — for example, see their equation 3.3.

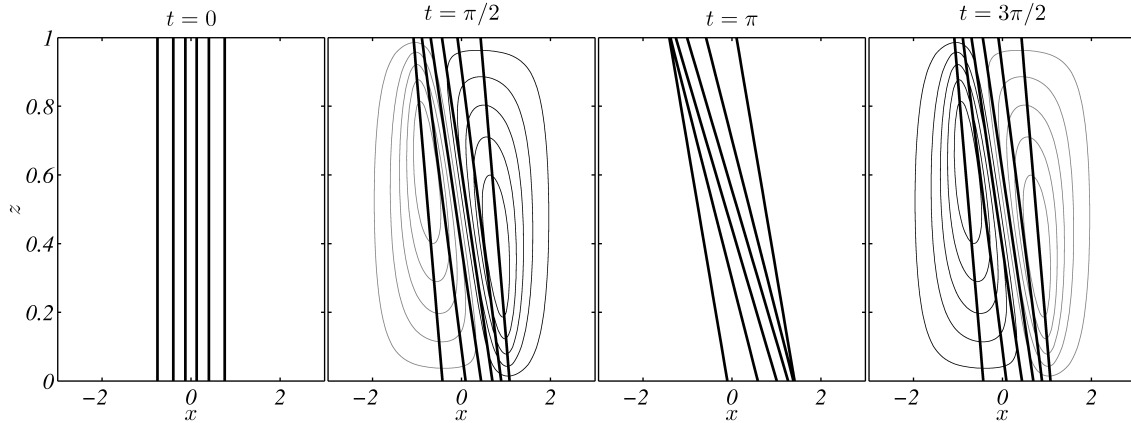


Fig. 1.10 The non-dimensional solution to the Blumen (2000) model of unbalanced frontogenesis for a critical buoyancy profile, i.e. $\max |b_0''(\chi)| = f^2/H$ from (1.37). Buoyancy contours are shown as thick black lines. Vertical velocity contours are shown as thin lines: grey = down, black = up. Time is in units of $1/f$.

undergoes a non-decaying inertial oscillation (i.e. an oscillation at frequency f) around the geostrophically balanced state. Frontogenesis occurs due to self-advection by the inertial wave, and if the amplitude is large enough a discontinuity can form. The discontinuity emerges via a breakdown of the coordinate transformation or,

$$J^{-1} = 1 - \frac{1}{f} \frac{\partial v}{\partial \chi} < 0 \implies \max \left(\frac{1}{f} \frac{\partial v}{\partial \chi} \right) = \frac{H \max |b_0''(\chi)|}{f^2} > 1. \quad (1.37)$$

Thus, discontinuities tend to occur for large buoyancy gradients and/or weak rotation (i.e. large Rossby numbers). Figure 1.10 displays an example solution of the Blumen (2000) for the so-called ‘critical case’ where the buoyancy gradient is just strong enough to drive the formation of a discontinuity, or $\max |b_0''(\chi)| = f^2/H$ from (1.37). The unbalanced buoyancy gradient at time zero collapses under the influence of gravity, generating a thermally direct secondary circulation. At $ft = \pi/2$ the system oscillates through the geostrophically balanced state ($v = v_g$ at this time), and the secondary circulation gradually reduces until it reaches zero at $ft = \pi$. The boundary buoyancy gradient is maximum at this time. The system then oscillates back towards the initial state ($ft = 3\pi/2$), and the process repeats.

The Blumen (2000) model is a physically insightful model of the particular special case of zero PV or equivalently, an unstratified ambient. This assumption prohibits loss of energy from the front via the generation and propagation of waves as per the classical geostrophic adjustment problem (e.g. Rossby, 1938). One objective of the present work is to expand the Blumen (2000) model to examine unbalanced frontogenesis in a stratified ambient.

1.4 Objectives and outline

As described in §1.1, fronts in the ocean and atmosphere are of great importance to local weather, ocean circulation and biology, and the climate system more generally. In §1.2 we introduced the equations (1.12) that have been used to study fronts in an idealised context by many authors including Blumen (2000); Blumen & Wu (1995); Eliassen (1962); Hoskins & Bretherton (1972); Sawyer (1956); Williams & Plotkin (1968), among many others. Despite such work, the dynamics of this idealised two-dimensional front, subject to a depth-independent cross-frontal strain flow, are not fully understood. In particular, the effects of large strain and the possibility of unbalanced motions (waves) have not been explored in detail. As we observed above, such dynamics are expected to be relevant to fronts in both the atmosphere and ocean, particularly at smaller scales, and may help explain observations of wave generation events such as those pictured in figures 1.4 and 1.5. Thus, in the present study our objective is to fully explore the dynamics of the idealised two-dimensional (2D) strained front described by (1.12). This work will be roughly divided into two sections.

In the first section (Chapters 2 through 5) we restrict ourselves to the classical configuration used by most previous authors of a uniform PV flow trapped between two rigid lids. This configuration is mathematically convenient in that it allows a non-linear analytic solution to the problem, as detailed in Chapter 2, where we will unify present models of the 2D frontal system — namely the strain-forced frontogenesis theory of Hoskins & Bretherton (1972) and the imbalance frontogenesis theory of Blumen (2000) — into a single consistent theory. We will then investigate the predictions of this theory regarding geostrophic adjustment and frontogenesis (Chapter 3) and spontaneous wave generation during frontogenesis (Chapter 4). In Chapter 5 we will compare the theory with numerical simulations of the same system, and examine dynamics not captured by the theory.

In the second section (Chapters 6 through 8) we take an alternative approach of linearising the governing equations (1.12) and obtaining a generalised linear solution for any domain of interest (whether dual rigid lid, semi-infinite or fully infinite) and arbitrary non-uniform potential vorticity. While less accurate in a strict sense, the linearised model derived in Chapter 6 is arguably more useful in describing real fronts in the ocean and atmosphere. In Chapter 7 we will use the linear model to detail a potential mechanism for the formation of finescale cloud banding around atmospheric fronts, which depends vitally on non-hydrostatic dynamics. Similarly, in Chapter 8 we will use the linear model to describe the dependence of frontal vertical velocities on strain (e.g. figure 1.3d) as well as the conditions necessary for, and frequencies of, waves generated spontaneously at ocean fronts.

Lastly, in Chapter 9, we will draw together the above results and comment on the future directions for work in this area.

Chapter 2

The non-linear uniform PV generalised model

In this chapter we derive a non-linear analytic model of the two-dimensional strained front defined by (1.12) for the special case of uniform PV flow confined between two rigid lids. The objective is to make a minimum of approximations and thereby obtain the most general model possible of the system. In particular, unlike previous models we will include unbalanced flow and permit large strains, $\alpha \sim f$. The generalised model derived in this chapter will be applied in Chapters 3 through 5 to describe geostrophic adjustment, frontogenesis and wave generation in a unified framework.

2.1 Model configuration and non-dimensionalisation

Here we consider the classical idealised configuration used by Hoskins & Bretherton (1972, hereafter, HB), Blumen (2000, hereafter, B00) and many other authors to study the 2D strained front problem (1.12). The fluid is assumed to be trapped between rigid lids at the top and bottom of the domain, $z = 0$ and $z = H$, but unbounded in the cross-frontal (x) direction. Furthermore, it is assumed that the fluid has an initially uniform potential vorticity (PV). Since the flow is inviscid, the PV will remain uniform for all time. The uniform PV constraint requires that the buoyancy difference across the front ΔB_0 is the same for all depths, since otherwise the stratification (and thus the PV) in the far field on the left and right would differ. This requirement imposes a symmetry on the system (e.g. as discussed in §1.3.2) whereby fronts appear on both the upper and lower boundaries. A schematic of the configuration is shown in figure 2.1.

buoyancy scale		ΔB_0
horizontal velocity scale		$\sqrt{\Delta B_0 H}$
vertical velocity scale		$\sqrt{\frac{\Delta B_0 H^3}{L^2}}$
time scale		$\frac{1}{f}$
Rosby number	Ro	$\frac{\sqrt{\Delta B_0 H}}{fL}$
Froude number	F	$\sqrt{\frac{\Delta B_0}{N^2 H}}$
strain	δ	$\frac{\alpha}{f}$
aspect ratio	A	$\frac{L}{H}$
Burger number (Ro/F)	Bu	$\frac{NH}{fL}$
geostrophic Rossby number	Ro_g	Ro^2
geostrophic Froude number	F_g	RoF

Table 2.1 Non-dimensional parameters and variable scales employed herein. The fundamental physical scales are the inertial frequency f , buoyancy difference across the front δB , buoyancy frequency N , strain α , horizontal length L , and height H . The geostrophic Rossby and Froude numbers, defined in terms of the geostrophic velocity scale $V_g \sim \Delta B_0 H / (fL)$, are also shown to assist in comparison of the present work with other studies.

in Chapter 7. Another dependent non-dimensional number that will prove useful is the Froude number,

$$F = \sqrt{\frac{(U/H)^2}{N^2}} = \sqrt{\frac{\Delta B_0}{N^2 H}}. \quad (2.5)$$

The scales and non-dimensional parameters are listed in 2.1 for reference.

Of the three independent non-dimensional parameters (Ro , Bu , δ) the buoyancy difference ΔB_0 across the front only appears in the Rossby number. Ro thus provides a non-dimensional measure of the size of the buoyancy step $b_0(X)$ imposed on the rigid lids. Indeed the parameter Ro is equivalent to the ‘non-linearity parameter’ governing the relative surface height displacement in shallow water step-adjustment problems (e.g. Kuo & Polvani, 1997). We observe that while the convergent strain will act to increase horizontal gradients (i.e. by reducing the frontal width with time), it will not alter the net magnitude of buoyancy transition ΔB_0 across the front. A small Ro therefore implies an *initially* weak front, but does not preclude the formation of a sharp/strong front with time as the frontal width contracts.

The background stratification N^2 only appears in the Burger number Bu , and thus Bu is the non-dimensional scale that governs the speed of wave propagation and adjustment in the

system, or equivalently the background PV (dimensionally, $q_0 = N^2$). The non-dimensional strain $\delta(T)$ governs the magnitude of the imposed large scale convergent flow field. In fact, $\delta(T)$ may be interpreted as a *large scale Rossby number* Ro_L characterising the large scale strain flow,

$$Ro_L = \left| \frac{1}{f} \frac{\partial U}{\partial x} \right| = \alpha(T)/f = \delta(T). \quad (2.6)$$

A small strain δ thus implies that the large scale phenomena that is responsible for generating the strain field (such as a baroclinic eddy field or wave) is characterised by a small Rossby number.

2.2 The generalised momentum coordinate

Motivated by the boundary dynamics discussed in §1.3.1, to study frontogenesis in a general framework we introduce a new coordinate system defined by

$$X = e^\beta \left(x + \frac{v}{f} \right) = e^\beta \chi, \quad Z = z, \quad T = t, \quad (2.7)$$

where x is the regular Eulerian coordinate and χ is the *momentum coordinate* as used by B00 (§1.3.4) and HB (§1.3.2). As noted previously, for the B00 case in the absence of strain, the χ coordinate is conserved, while in the HB case the χ coordinate is not conserved. The key feature of the new coordinate X (2.7) is that it is conserved for any time-varying strain α , or

$$\frac{DX}{Dt} = 0, \quad (2.8)$$

and hence we will refer to X as the *generalised momentum (GM) coordinate*. Since X is conserved, the material derivative in generalised momentum coordinates (2.7) reduces to

$$\frac{D}{Dt} = \frac{\partial}{\partial T} + w \frac{\partial}{\partial Z}, \quad (2.9)$$

which greatly simplifies the analysis. Employing these coordinates allows us to simultaneously study the mass imbalance frontogenesis problem of B00 and the deformation frontogenesis problem of HB — but without the latter's assumption of thermal wind balance. The partial derivatives and Jacobian of the coordinate transformation, as well as other useful relations, are given in table 2.2. In non-dimensional form the generalised momentum coordinate is

$$X = e^\beta (x + Ro v), \quad (2.10)$$

	symbol	dimensional	non-dimensional
x coordinate	X	$e^\beta \left(x + \frac{v}{f} \right)$	$e^\beta (x + Ro v)$
Jacobian	J	$e^\beta \left(1 - e^\beta \frac{1}{f} \frac{\partial v}{\partial X} \right)^{-1}$	$e^\beta \left(1 - e^\beta Ro \frac{\partial v}{\partial X} \right)^{-1}$
t derivative	$\frac{\partial}{\partial t}$	$\frac{\partial}{\partial T} + \left(\alpha X e^\beta + \frac{1}{f} \frac{\partial v}{\partial T} \right) J \frac{\partial}{\partial X}$	$\frac{\partial}{\partial T} + \left(\delta X e^\beta + Ro \frac{\partial v}{\partial T} \right) J \frac{\partial}{\partial X}$
x derivative	$\frac{\partial}{\partial x}$	$J \frac{\partial}{\partial X}$	$J \frac{\partial}{\partial X}$
z derivative	$\frac{\partial}{\partial z}$	$\frac{\partial}{\partial Z} + \frac{1}{f} \frac{\partial v}{\partial Z} J \frac{\partial}{\partial X}$	$\frac{\partial}{\partial Z} + Ro \frac{\partial v}{\partial Z} J \frac{\partial}{\partial X}$
potential vorticity	q	$\frac{\partial b}{\partial Z} \left(1 - e^\beta \frac{1}{f} \frac{\partial v}{\partial X} \right)^{-1}$	$\frac{\partial b}{\partial Z} \left(1 - e^\beta Ro \frac{\partial v}{\partial X} \right)^{-1}$
effective u	u_*	$u + \frac{w}{f} \frac{\partial v}{\partial Z}$	$u + Ro w \frac{\partial v}{\partial Z}$
effective w	w_*	$w J^{-1}$	$w J^{-1}$
continuity equation		$\frac{\partial u_*}{\partial X} + \frac{\partial w_*}{\partial Z} = 0$	$\frac{\partial u_*}{\partial X} + \frac{\partial w_*}{\partial Z} = 0$

Table 2.2 Quantities of interest expressed in generalised momentum coordinates in both dimensional and non-dimensional forms. The effective velocities were defined by Blumen (2000) and have been generalised here to include the deformation field. The definition of the potential vorticity is taken as $q = (\mathbf{k} + f^{-1} \nabla \times \mathbf{U}) \cdot \nabla b$ where \mathbf{k} is a unit vector in the z -direction.

using the scales described in §2.1. Similarly, the material derivative is

$$\frac{D}{Dt} = \frac{\partial}{\partial T} + Ro w \frac{\partial}{\partial Z}. \quad (2.11)$$

The other non-dimensional expressions are also shown in 2.2 alongside their dimensional counterparts. Henceforth, non-dimensionality should be assumed unless otherwise stated.

We now transform the 2D strained front equations developed in the introduction (1.12) to generalised momentum coordinates. Here, as in previous frontogenesis models, we consider the hydrostatic limit. In this limit the vertical momentum balance (1.12c) reduces to the thermal wind equation, $\partial_z v_g = f^{-1} \partial_x b$, with the geostrophic velocity v_g defined as previously (1.33). In generalised momentum coordinates thermal wind takes the form

$$\frac{\partial v_g}{\partial Z} - Ro e^\beta \left(\frac{\partial b}{\partial X} + \frac{\partial v}{\partial X} \frac{\partial v_g}{\partial Z} - \frac{\partial v}{\partial Z} \frac{\partial v_g}{\partial X} \right) = 0, \quad (2.12)$$

and the horizontal momentum and buoyancy equations from (1.12) may be written as

$$\frac{\partial u}{\partial T} + Row \frac{\partial u}{\partial Z} - v - \delta u + v_g = 0, \quad (2.13a)$$

$$\frac{\partial v}{\partial T} + Row \frac{\partial v}{\partial Z} + u + \delta v = 0, \quad (2.13b)$$

$$\frac{\partial b}{\partial T} + Row \frac{\partial b}{\partial Z} = 0. \quad (2.13c)$$

One further equation is required to complete the system. As noted in the discussion of the HB model (§1.3.2), while the expression for volume conservation is rather complicated in momentum coordinates (e.g. see table 2.2), conservation of PV is relatively simple. In generalised momentum coordinates, PV conservation may be written as

$$\frac{\partial q}{\partial T} + Row \frac{\partial q}{\partial Z} = 0, \quad q = \frac{\partial b}{\partial Z} \left(1 - e^\beta Row \frac{\partial v}{\partial X} \right)^{-1}. \quad (2.14)$$

Here, consistent with prior work, we will consider the special case of uniform PV, whereupon (2.14) reduces to the linear relation

$$\frac{\partial b}{\partial Z} - q_0 \left(1 - e^\beta Row \frac{\partial v}{\partial X} \right) = 0. \quad (2.15)$$

2.3 The generalised model

Without loss of generality, here we define the buoyancy field as

$$b(X, Z, T) = b_0(X) + F^{-2} Z + \Delta b(X, Z, T). \quad (2.16)$$

In B00 the field $b_0(X)$ constitutes the initial imposed mass imbalance to which the system must adjust, while in HB the field $b_0(X)$ corresponds to the imposed surface ($Z = 0, 1$) distribution of buoyancy. Consistent with both these interpretations, we require that the buoyancy anomaly Δb vanishes on the rigid lid boundaries at time zero. Applying buoyancy conservation (2.13c) on the boundaries where $w = 0$ we obtain

$$\left. \frac{Db}{Dt} \right|_{Z=0,1} = \left. \frac{\partial b}{\partial T} \right|_{Z=0,1} = \left. \frac{\partial \Delta b}{\partial T} \right|_{Z=0,1} = 0, \quad (2.17)$$

and thus the buoyancy anomaly remains identically zero on the boundaries for all time. The buoyancy on the rigid lids in momentum coordinates is therefore independent of time with

$$b(Z = 0) = b_0(X) \quad (2.18a)$$

on the lower boundary, and

$$b(Z = 1) = b_0(X) + F^{-2}, \quad (2.18b)$$

on the upper boundary, as shown in the schematic (figure 2.1). Hence, buoyancy fronts are present on both boundaries. In the case where the buoyancy anomaly Δb is initially everywhere zero, the system is completely unbalanced at time zero (as in the B00 model). We can also consider cases where Δb is non-zero in the interior in the initial state and the system is balanced (or partially balanced) at time zero (as in the HB model), as long as the constraint of uniform potential vorticity holds in the initial state.

The PV relation (2.15) may be rearranged to relate the buoyancy anomaly Δb to the along-front velocity v ,

$$\frac{\partial \Delta b}{\partial Z} = -Ro F^{-2} e^\beta \frac{\partial v}{\partial X}, \quad (2.19)$$

where we have required that the buoyancy anomaly and velocity field vanish as $X \rightarrow \pm\infty$ and hence $q_0 \equiv F^{-2}$. The buoyancy anomaly field may thus be uniquely determined from knowledge of the along-front velocity $v(X, Z, T)$ by integration of (2.19) and application of the boundary condition (2.17):

$$\Delta b(X, Z, T) = -Ro F^{-2} e^\beta \int_0^Z \frac{\partial v}{\partial X} dZ'. \quad (2.20)$$

The total buoyancy field (in terms of v) is obtained by substitution of the anomaly (2.20) into (2.16):

$$b(X, Z, T) = b_0(X) + F^{-2} Z - Ro F^{-2} e^\beta \int_0^Z \frac{\partial v}{\partial X} dZ'. \quad (2.21)$$

Next, we substitute the buoyancy (2.21) into the buoyancy conservation equation (2.13c) to yield an expression for the vertical velocity,

$$\frac{Db}{Dt} = 0 \Rightarrow w = \frac{D}{Dt} \left(e^\beta \int_0^Z \frac{\partial v}{\partial X} dZ' \right). \quad (2.22)$$

Expanding the total derivative on the right-hand side, we obtain an expression for an effective vertical velocity w_* (as listed in table 2.2),

$$w_* = wJ^{-1} = w \left(1 - Ro e^\beta \frac{\partial v}{\partial X} \right) e^{-\beta} = e^{-\beta} \int_0^Z \frac{\partial}{\partial T} \left(e^\beta \frac{\partial v}{\partial X} \right) dZ', \quad (2.23)$$

from which the actual vertical velocity w may be readily obtained. This is a very useful expression. For example, (2.23) generates the vertical velocity field for both the B00 and HB models from their specified along-front velocity fields. Also using (2.23), the cross-front streamfunction may be derived as

$$\begin{aligned} \psi &= - \int w dx = - \int_{-\infty}^X w J^{-1} dX' = - \int_{-\infty}^X \int_0^Z \frac{\partial}{\partial T} \left(e^\beta \frac{\partial v}{\partial X'} \right) e^{-\beta} dZ' dX' \\ &= -e^{-\beta} \frac{\partial}{\partial T} \left(e^\beta \int_0^Z v dZ' \right), \end{aligned} \quad (2.24)$$

by substitution of the Jacobian from table 2.2 and assuming that v vanishes far from the front, at $X = -\infty$. The cross-front velocity u may be expressed using (2.24) as

$$\begin{aligned} u &= \frac{\partial \psi}{\partial z} = \frac{\partial \psi}{\partial Z} + Ro \frac{\partial v}{\partial Z} J \frac{\partial \psi}{\partial X} \\ &= -\frac{\partial v}{\partial T} - \delta v - Ro w \frac{\partial v}{\partial Z} \end{aligned} \quad (2.25)$$

by substitution of the appropriate derivatives from table 2.2. Note that equation (2.25) is merely a restatement of the non-dimensional y-momentum equation (2.13b).

The above expressions for buoyancy anomaly (2.20), vertical velocity (2.23) and streamfunction (2.24) all involve the vertical integral of the along-front velocity v . It is therefore convenient to define this quantity as a new field ϕ where

$$\phi(X, Z, T) = \int_0^Z v(X, Z', T) dZ', \quad (2.26)$$

such that,

$$v(X, Z, T) = \frac{\partial}{\partial Z} \phi(X, Z, T) \quad (2.27a)$$

$$b(X, Z, T) = b_0(X) + F^{-2} Z - Ro F^{-2} e^\beta \frac{\partial}{\partial X} \phi(X, Z, T), \quad (2.27b)$$

$$\psi(X, Z, T) = \left(-\delta - \frac{\partial}{\partial T} \right) \phi(X, Z, T). \quad (2.27c)$$

The entire time evolution of the system is thus known if $\phi(X, Z, T)$ can be determined subject to boundary conditions of $\phi(\pm\infty, Z, T) = \phi(X, 0, T) = \phi(X, 1, T) = 0$ to enforce $w = -\partial_x \psi = 0$ on the rigid lids. We now form an equation for ϕ .

The horizontal momentum equations (2.13a, 2.13b) comprise a set of two first-order differential equations (in the material derivative) which may be reduced to a single second order equation by eliminating u :

$$\frac{D^2 v}{Dt^2} + (1 - \delta^2 + \partial_T \delta) v = v_g. \quad (2.28)$$

Next, the geostrophic velocity v_g as defined by this equation (2.28) and b as defined by (2.21) are substituted into the thermal wind equation (2.12) to obtain an equation for the evolution of ϕ :

$$\left[\left(\frac{\partial^2}{\partial T^2} + 1 - \delta^2 + \partial_T \delta \right) \frac{\partial^2}{\partial Z^2} + Bu^2 e^{2\beta} \frac{\partial^2}{\partial X^2} \right] \phi(X, Z, T) = \mathcal{F} + \mathcal{N}. \quad (2.29)$$

The function \mathcal{F} on the right-hand side of (2.29) is the linear forcing defined by

$$\mathcal{F} = Ro e^\beta \frac{\partial}{\partial X} b_0(X), \quad (2.30)$$

where $b'_0(X) = \partial_X b|_{Z=0,1}$ (from 2.21) is the imposed buoyancy gradient at the rigid lids that forces motion in the interior. The function \mathcal{N} on the right-hand side of (2.29) is the sum of the explicit non-linear terms¹,

$$\mathcal{N} = Ro \frac{\partial}{\partial Z} \left[w \frac{\partial u}{\partial Z} + \left(\delta - \frac{\partial}{\partial T} \right) \left(w \frac{\partial v}{\partial Z} \right) \right] - Ro e^\beta \left[\frac{\partial v}{\partial X} \frac{\partial v_a}{\partial Z} - \frac{\partial v}{\partial Z} \frac{\partial v_a}{\partial X} \right], \quad (2.31)$$

where $v_a \equiv v - v_g$ is the ageostrophic along-front velocity. Clearly, the analytic model is only readily soluble in cases where these explicit non-linear terms may be neglected. We call (2.29) with the non-linear terms set to zero, $\mathcal{N} \equiv 0$, the *generalised model of frontogenesis*. This model will form the basis for our analytic solutions in Chapters 3 and 4. In Chapter 3 we discuss unbalanced initial conditions and geostrophic adjustment. In this case \mathcal{N} is initially zero, and the generalised model is valid for an initial period of time. In Chapter 4 we focus on balanced initial conditions, where \mathcal{N} is non-zero at time zero, in which case the neglect of \mathcal{N} is valid for certain parameter regimes (see §4.2)

¹We use the term ‘explicit non-linear’ here since some of the non-linearity in the problem is included implicitly through the momentum coordinate transformation.

The equations and relations pertaining to the generalised model are summarised in table 2.3 for easy reference.

2.4 Summary

Here we have developed a generalised model of frontogenesis accommodating both unbalanced initial conditions and a background strain flow. The solutions to — and validity of — the generalised model in various limits will be derived and discussed in the following chapters. In Chapter 3 the generalised model will be used to describe geostrophic adjustment and frontogenesis in a stratified ambient with both strain-forced and spontaneous frontogenesis occurring simultaneously. Only weak strains ($\alpha \ll f$) will be considered. In Chapter 4 we will discuss the spontaneous generation of inertia-gravity waves predicted by the model for larger strains ($\alpha \sim f$). Then, in Chapter 5 fully non-linear numerical simulations will be employed to verify these results and investigate more extreme parameter regimes.

Description	Eqn.	Definition
generalised momentum coordinate	(2.7)	$X = e^\beta (x + Ro v)$
time-integrated strain	(1.11)	$\beta(T) = \int_0^T \delta(T') dT'$
model equation	(2.29)	$\left[\left(\frac{\partial^2}{\partial T^2} + 1 - \delta^2 + \partial_T \delta \right) \frac{\partial^2}{\partial Z^2} + Bu^2 e^{2\beta} \frac{\partial^2}{\partial X^2} \right] \phi(X, Z, T) = Ro e^\beta \frac{\partial}{\partial X} b_0(X)$
boundary conditions		$\phi(\pm\infty, Z, T) = \phi(X, 0, T) = \phi(X, 1, T) = 0$
along-front velocity	(2.27a)	$v(X, Z, T) = \frac{\partial}{\partial Z} \phi(X, Z, T)$
buoyancy	(2.27b)	$b(X, Z, T) = b_0(X) + F^{-2} Z - Ro F^{-2} e^\beta \frac{\partial}{\partial X} \phi(X, Z, T)$
cross-frontal streamfunction	(2.27c)	$\psi(X, Z, T) = \left(-\delta - \frac{\partial}{\partial T} \right) \phi(X, Z, T)$

Table 2.3 The non-dimensional, non-linear generalised model: coordinates, governing equation, and field relations. The model describes the response of a uniform PV fluid trapped between two rigid lids to certain initial conditions and/or a background strain flow, $\delta(T)$.

Chapter 3

Geostrophic adjustment and frontogenesis

In this chapter we unify the theory of deformation frontogenesis (e.g. Hoskins & Bretherton, 1972) with the theory of spontaneous frontogenesis (e.g. Blumen, 2000). To do this, we examine the generalised model solution derived in Chapter 2 in three distinct cases. Firstly, for a zero potential vorticity (PV) flow bounded by rigid lids, a general solution is derived for the transient response of the fluid to an arbitrary initial mass imbalance and deformation field strength. The deformation frontogenesis solution of Hoskins & Bretherton (1972) and the mass imbalance solution of Blumen (2000) emerge as two limits of this general solution. Secondly, the problem of geostrophic adjustment of an initial mass imbalance in the absence of strain is considered for a uniform (non-zero) PV flow. The general solution is derived, composed of an adjusted state (matching that derived by Blumen & Wu, 1995) and a transient component describing the propagation of inertia-gravity waves. The criteria for the occurrence of a frontal discontinuity is determined in terms of the Rossby and Froude numbers. The uniform PV solution reduces identically to the zero PV solution of Blumen (2000) in the limit of vanishing background stratification. Thirdly, we examine the more general case of uniform PV flow with a (weak and temporally constant) deformation field and unbalanced initial conditions. In this case the solution is composed of a time-varying mean state matching the Hoskins & Bretherton (1972) solution and a propagating inertia-gravity wave field. The dynamics of these waves are examined in detail. Our analysis provides a unifying framework capable of describing frontal formation and geostrophic adjustment in a wide variety of settings.

3.1 Introduction

As already noted, frontogenesis is the process by which relatively weak horizontal density gradients are intensified. Two dynamical mechanisms driving this intensification which have received considerable attention in the literature are forcing by large scale strain fields, and the geostrophic adjustment of fluid from an initially unbalanced state. We will refer to these two mechanisms as ‘forced’ and ‘spontaneous’ frontogenesis, respectively.

Geostrophic adjustment refers to the adaptation of a rotating fluid system to an imposed force and/or set of initial conditions. This adjustment process is ubiquitous in the surface layers of both the atmosphere and ocean which are subject to rapid (compared to the inertial period) inputs of buoyancy and momentum. For example, in the adjustment problem considered by Rossby (1938), wind stress applied to the ocean causes a rapid acceleration of the surface layer resulting in an unbalanced Coriolis force (a momentum imbalance), and thus driving a change in the free surface height. In a related problem, a sudden change in the buoyancy of a fluid layer, for example in response to an air-sea flux of heat or fresh water, or a river outflow, will cause an unbalanced pressure field and thereby generate a flow that smooths the buoyancy anomaly and restratifies the layer (Tandon & Garrett, 1994). For a relatively weak imbalance, the final state is in geostrophic balance. However, for larger imbalances significant questions arise as to whether (a) a geostrophically balanced state exists, and (b) if it does exist, whether it is attainable (Plougonven & Zeitlin, 2005). For example, sufficiently large imbalances may lead to the spontaneous formation of a sharp front during the adjustment process (hence the name *spontaneous* frontogenesis). These issues have been the focus of significant research since Rossby’s 1938 paper and yet remain largely unresolved in the general case.

Frontogenesis can also be triggered when an initially balanced flow is subject to an external force or acceleration. This process may be considered as one of *continuous geostrophic adjustment* (Plougonven & Zeitlin, 2005) whereby the imposed force continually pushes the system away from geostrophic balance, and a secondary circulation acts to continually maintain geostrophic balance (and thus the system remains close to a balanced state throughout the process, if the imposed force is sufficiently small). An example of such a force is the horizontal convergence of flow in the region between weather systems or ocean eddies (e.g. Hoskins & Bretherton, 1972, hereafter, HB). The convergent flow amplifies pre-existing buoyancy gradients and thus drives the flow away from geostrophic balance. The resulting change in the pressure gradient generates a smaller-scale secondary circulation acting to restore geostrophic balance. However, non-linear self-advection of this ageostrophic flow drives additional frontogenesis. In the model constructed by HB, the combination of large

scale strain and secondary circulation lead to the formation of a discontinuity in the (inviscid) momentum and buoyancy fields in a finite period of time — as shown in §1.3.2.

Frontogenesis driven by large scale forcing has largely been studied in isolation from the parallel problem of spontaneous frontogenesis associated with an initial mass or momentum imbalance. This is at least in part due to the analytical intractability of the latter problem, since the unbalanced initial conditions prohibit the use of quasi- or semigeostrophy which both implicitly assume a degree of balance to the flow. The first attempts at solving the spontaneous frontogenesis problem mostly dealt with one dimensional flow (see the review paper of Blumen, 1972) until Ou (1984) who demonstrated that, in the case of initially motionless two dimensional flow trapped between rigid boundaries, a continuous geostrophically adjusted state will not exist if the initial buoyancy gradient (mass imbalance) is sufficiently large. This result was further developed by Blumen & Wu (1995) who applied the Eliassen (1962) momentum coordinates to the mass imbalance problem to determine a general solution for the adjusted steady state in the special case of uniform potential vorticity (PV) flow. The similarity of their mathematical approach to that of HB emphasises the connection between the spontaneous mass imbalance and forced frontogenesis problems (a fact also reflected on by Plougonven & Zeitlin, 2005, and further explored in this chapter). Blumen & Wu (1995) did not use their result to determine the values of the Rossby and Froude numbers required for the existence of the adjusted state, or consider the temporal evolution. Here, we will examine both of these aspects in detail.

Plougonven & Zeitlin (2005) applied a Lagrangian approach to the problem of geostrophic adjustment to a frontal imbalance, with particular emphasis on the existence and attainability of an adjusted state. They found that the non-existence of the adjusted state is a generic property of bounded domains and that (expanding upon the results of Wu & Blumen, 1995) frontogenesis is enhanced by the presence of an initial cyclonic horizontal shear. Thus, smaller imbalances can lead to spontaneous frontogenesis, meaning that the formation of mesoscale fronts in the atmosphere is likely to be a more common process than previously believed. The Plougonven & Zeitlin (2005) Lagrangian approach also illustrates the dynamical splitting of the fluid response into balanced (adjusted state) and unbalanced (inertia-gravity waves) motions. They emphasised the importance of the fully non-linear unbalanced motions in determining whether the system can attain the adjusted state.

As observed by Blumen (2000, hereafter B00), most previous models have either not considered the transient motion but retained non-linearity (e.g. Blumen & Wu, 1995; Ou, 1984), or included transient motion but neglected non-linear effects (e.g. Tandon & Garrett, 1994). While the time-independent equations can be used to determine the existence (or otherwise) of a geostrophically adjusted state, they cannot describe the transient adjustment

process and hence the attainability of the adjusted state. For example, transient phenomena such as hydrodynamic instabilities, trapped waves, and propagating inertia-gravity waves may prevent the adjusted state from being reached. As a case in point, the model of B00 was the first to include both non-linearity and time dependence to derive a general solution for the rigid lid mass imbalance problem in the special case of zero PV flow. As shown in §1.3.4, the B00 solution consists of a non-decaying inertial oscillation about a steady adjusted state — but the system never attains this adjusted state. The waves are effectively trapped, since the absence of a free surface or background stratification eliminates possible propagation mechanisms. The addition of density stratification will fundamentally alter the dynamics by permitting the propagation of inertia-gravity waves away from the frontal zone and hence allow the system to attain a steady state. However, no solution for the transient response to a mass imbalance in uniform PV flow (that is, the time dependent motion pertaining to the attainment of the adjusted state determined by Blumen & Wu, 1995) as yet exists.

The chapter is set out as follows. In §3.2 we derive the generalised zero PV solution for a flow with both strain and unbalanced initial conditions. In §3.3 we determine the full transient solution to the uniform PV mass imbalance problem (e.g. Blumen, 2000; Blumen & Wu, 1995). The physical behaviour of the uniform PV solution will be investigated for both the frontogenetic case, where a frontal discontinuity forms, and the non-frontogenetic case, where the system undergoes geostrophic adjustment to a steady state. In §3.3.2 we derive the uniform PV solution of HB as a late-time and small-strain limit of the general solution. Furthermore, we demonstrate that the full solution for *weakly* strain-forced frontogenesis in non-zero uniform PV flow is composed of a time-varying mean state given by the HB solution, plus an inertia-gravity wave field, and we describe the dynamics of these waves. In §3.4 we investigate the error associated with approximations made in the derivation of the generalised model and to what extent the model captures the fully non-linear dynamics of geostrophic adjustment.

3.2 Inertial oscillations and frontogenesis in zero PV flow

The generalised model provides a unified framework for analysing frontogenesis and geostrophic adjustment in a 2D flow of uniform (but arbitrary) potential vorticity. Before considering the system more generally, it is enlightening to discuss the special case of zero potential vorticity which corresponds to vanishingly small background stratification N^2 and Burger number Bu . In addition to being more tractable analytically, this special subset of uniform PV flows is commonly studied in its own right since the boundary layers where fronts form in the atmosphere and ocean often have very weak stratification. For example, an estimate of the

Burger number in the ocean mixed layer, using typical values (e.g. see Boccaletti *et al.*, 2007) of $N \sim 10^{-3} s^{-1}$, $f \sim 10^{-4} s^{-1}$ and aspect ratio $L/H \sim 100$, yields $Bu = NH/(fL) = 0.1$. The neglect of the term involving the Burger number in the governing differential equation (2.29) will therefore introduce error of only about 1% in this situation, and hence the zero PV model is a very good approximation.

Setting the Burger number to zero and the strain to be constant (such that $\beta = \delta T$), the generalised model equation (2.29) becomes simply

$$\left[\frac{\partial^2}{\partial T^2} + (1 - \delta^2) \right] \frac{\partial^2 \phi}{\partial Z^2} = e^{\delta T} Rob'_0(X), \quad (3.1)$$

where ϕ is required to vanish on the rigid lids at $Z = 0, 1$. Integrating (3.1) with respect to Z yields

$$\left[\frac{\partial^2}{\partial T^2} + (1 - \delta^2) \right] v = e^{\delta T} Rob'_0(X) \left(Z - \frac{1}{2} \right), \quad (3.2)$$

where the constant of integration has been chosen to satisfy the boundary conditions on ϕ . We now need to select appropriate initial conditions. Here we will consider initial conditions of zero perturbation flow in the cross-front plane, $u = w = 0$, and an along-front velocity of

$$v = (1 - \mathcal{I}) v_g, \quad (3.3)$$

where $0 \leq \mathcal{I} \leq 1$. The imbalance fraction \mathcal{I} allows us to control to degree of initial imbalance: if $\mathcal{I} = 0$ the system begins in its geostrophically adjusted state and there is no mass imbalance, while for greater \mathcal{I} there exists an initial thermal wind that *partially* balances the imposed horizontal buoyancy gradient. The initial conditions match those of B00 when $\mathcal{I} = 1$, corresponding to no initial motion and a fully unbalanced initial state. The initial conditions do not match those of HB — the initial conditions in that model correspond to a geostrophic along-front velocity but with additional cross-frontal flow ($u, w \neq 0$) implied by the assumption of (semigeostrophic) balance. One of the limitations of the HB model is that the initial conditions in a given geophysical context are unlikely to be in exact semigeostrophic balance. We examine the case of geostrophic balance ($v = v_g$) but semigeostrophic imbalance ($u = w = 0$) as a convenient set of initial conditions to investigate the presence of inertial oscillations in the solution. Such oscillations appear to be a common feature of frontal systems (e.g. Ostdiek & Blumen, 1997; Snyder *et al.*, 1993).

Substitution of the initial conditions $u = w = 0$ into the expression for u (2.25) results in a second initial condition on v of

$$\frac{\partial v}{\partial T} + \delta v = 0. \quad (3.4)$$

Solving (3.2) with initial conditions (3.3, 3.4) yields

$$v = Rob'_0(X) \left(Z - \frac{1}{2} \right) \left(e^{\delta T} - \mathcal{I} \cos \sqrt{1 - \delta^2 T} + \frac{\delta(\mathcal{I} - 2)}{\sqrt{1 - \delta^2}} \sin \sqrt{1 - \delta^2 T} \right). \quad (3.5a)$$

The cross-front velocity may now be generated from (2.25) as

$$u = -Rob'_0(X) \left(Z - \frac{1}{2} \right) \left(2\delta \left(e^{\delta T} - \cos \sqrt{1 - \delta^2 T} \right) + \frac{\mathcal{I} - 2\delta^2}{\sqrt{1 - \delta^2}} \sin \sqrt{1 - \delta^2 T} \right) - Row \frac{\partial v}{\partial Z}, \quad (3.5b)$$

and the vertical velocity from (2.23) as

$$w = \frac{Rob''_0(X) Z(Z - 1) e^{\delta T} \left(\delta \left(e^{\delta T} - \cos \sqrt{1 - \delta^2 T} \right) + \frac{\mathcal{I} - 2\delta^2}{2\sqrt{1 - \delta^2}} \sin \sqrt{1 - \delta^2 T} \right)}{1 - Ro e^{\delta T} \frac{\partial v}{\partial X}}. \quad (3.5c)$$

The general solution (3.5) depends on only two non-dimensional parameters: Ro and δ . The solution is composed of (a) an exponential growth driven by the large scale strain field and (b) near-inertial (presuming $\delta \ll 1$) oscillations resulting from both the initial conditions (with relative amplitude \mathcal{I}) and the deformation forcing (with relative amplitude δ). Previous solutions have either considered the exponentially growing part (e.g. HB, balanced) or the oscillatory part (e.g. B00, unbalanced) in isolation. However, the two effects are known to occur simultaneously. For example, in Ostdiek & Blumen (1997) observations pertaining to the movement of an atmospheric front over the central United States are described and compared with HB theory. A significant feature of the observed wind fields in the frontal zone is the presence of strong inertial oscillations that cause a departure from the HB prediction (see also Blumen, 1997).

The zero PV solutions of HB and B00 may now be obtained as limits of the general solution given above. Setting the initial imbalance to zero ($\mathcal{I} = 0$) yields a modified version of the HB solution that additionally satisfies the condition of no flow in the x and z directions at time zero. If we additionally suppose that $T \gg 1$ such that the oscillations are negligible in comparison to the directly forced part of the flow, we recover the *exact* HB solution in

non-dimensional form:

$$u = -e^{\delta T} Ro b'_0(X) (Row + (2Z - 1) \delta), \quad (3.6)$$

$$v = v_g = e^{\delta T} Ro b'_0(X) \left(Z - \frac{1}{2} \right), \quad (3.7)$$

$$w = Ro \delta b''_0(X) Z(Z - 1) e^{2\delta T} \left(1 - Ro e^{\delta T} \frac{\partial v}{\partial X} \right)^{-1}. \quad (3.8)$$

We emphasise that this HB solution is in general only valid at times of $O(\alpha^{-1})$, where α is the dimensional strain. In particular, the neglect of the initial conditions (and their corresponding oscillations) in this HB solution places a constraint on the size of the Rossby number (see below). Returning to the general solution, if we instead set $\delta = 0$ and $\mathcal{I} = 1$, we obtain a non-dimensional version of the B00 solution:

$$u = -Ro b'_0(X) \left(\left(Z - \frac{1}{2} \right) \sin T + Row (1 - \cos T) \right), \quad (3.9a)$$

$$v = Ro b'_0(X) \left(Z - \frac{1}{2} \right) (1 - \cos T), \quad (3.9b)$$

$$w = \frac{1}{2} Ro b''_0(X) Z(Z - 1) \sin T \left(1 - Ro \frac{\partial v}{\partial X} \right)^{-1}. \quad (3.9c)$$

This solution (3.9c) is valid for all time, with no restrictions on the size of the Rossby number.

The criterion for the formation of a frontal discontinuity is that the inverse Jacobian of the coordinate transformation (from table 2.2),

$$J^{-1} = e^{-\delta T} - Ro \frac{\partial v}{\partial X}, \quad (3.10)$$

vanishes. In the B00 case (3.9b) it is the initial imbalance that drives frontogenesis through the inertial oscillatory response of the system and thus a singularity will only occur for a sufficiently large Rossby number,

$$Ro^2 \max |b''_0(X)| \geq 1. \quad (3.11)$$

The *critical* Rossby number is the minimum value required for a singularity to occur,

$$Ro_c = \frac{1}{\sqrt{\max |b''_0(X)|}}, \quad (3.12)$$

and is $O(1)$, although the exact value depends on the initial profile $b_0(X)$. In this case frontogenesis occurs on an *inertial* timescale f^{-1} with the critical time (i.e. the time taken for a singularity to form) given by

$$ft_c = \arccos \left(1 - 2 \left(\frac{Ro_c}{Ro} \right)^2 \right). \quad (3.13)$$

In contrast, in the HB case the along-front velocity (3.7) grows exponentially in time, and thus *any* arbitrarily weak buoyancy gradient is squeezed into a front by the large scale convergent field. In this case frontogenesis occurs on the (much longer) deformation field *forcing* timescale α^{-1} , with critical time

$$\alpha t_c = \frac{1}{2} \ln 2 - \ln \left(\frac{Ro}{Ro_c} \right). \quad (3.14)$$

As noted above, the neglect of the initial conditions in this HB model places a constraint on the size of the Rossby number Ro , as measured in momentum coordinates.¹ An extreme limit is given by the values of the Rossby number, $Ro \geq \sqrt{2}Ro_c$, that make $t_c \leq 0$ in (3.14), and consequently the implied initial state invalid (i.e. discontinuous or double valued).

In both the B00 and HB cases the singularity forms at the location where $|b_0''(X)|$ is maximised. These and other characteristics of forced and spontaneous frontogenesis are listed in table 3.1. To visualise these results, the time evolution of the buoyancy field is shown in figure 3.1 for a (scaled) error function initial buoyancy profile,

$$b_0(X) = \frac{1}{2} \operatorname{erf} \left(\frac{X}{\sqrt{2}} \right), \quad (3.15)$$

having critical Rossby number $Ro_c = 2.03$, for a typical B00 imbalance case ($Ro = 3$, $\delta = 0$, $\mathcal{I} = 1$) and a typical HB-type forced frontogenesis case ($Ro = 0.4$, $\delta = 0.1$, $\mathcal{I} = 0$). The isopycnal slope at time T in zero PV flow may be derived from the derivatives in table 2.2 as

$$\text{slope} = \frac{-\frac{\partial b}{\partial x}}{\frac{\partial b}{\partial z}} = -\frac{1}{Ro \frac{\partial v}{\partial z}}, \quad (3.16)$$

which is only infinite at time zero if the vertical gradient of v is zero. Hence, in the HB case the initial condition of geostrophic balance ($\mathcal{I} = 0$) imposes a non-zero stratification in the imbalance region at time zero — as may be observed by the slight tilt of the isopycnals in

¹Note that the Rossby number in Eulerian coordinates is $Ro_E = JRo$ where J is the Jacobian of the coordinate transformation. Hence the maximum value of Ro equates to a discontinuity in the initial state and $Ro_E \rightarrow \infty$.

	symbol	spontaneous; B00	forced; HB
critical Ro	Ro_c	$\frac{1}{\sqrt{\gamma}}$	always frontogenetic
position (GMC)	X_f	$b_0'''(X_f) = 0$	$b_0'''(X_f) = 0$
critical time	t_c	$\frac{1}{f} \arccos\left(1 - \frac{2}{Ro^2\gamma}\right)$	$\frac{1}{2\alpha} \ln\left(\frac{2}{Ro^2\gamma}\right)$
max jet velocity	v_f	$-\frac{b_0'(X_f)}{Ro\gamma}$	$-\frac{b_0'(X_f)}{\sqrt{2\gamma}}$
position (Euler)	x_f	$X_f + \frac{b_0'(X_f)}{\gamma}$	$Ro \frac{1}{\sqrt{2\gamma}} (X_f\gamma + b_0'(X_f))$

Table 3.1 Comparison of forced and spontaneous singularity formation on the lower boundary from the B00 and HB models of frontogenesis, where $\gamma = -b_0''(X_f) > 0$. Note that the maximum jet velocity scales inversely with Ro in the B00 model, and is independent of Ro in the HB model. In contrast, the Eulerian frontal position is independent of Ro in the B00 model, and proportional to Ro in the HB model. The Eulerian (real space) position of frontogenesis on the lower boundary is related to the momentum coordinate (GMC) position by $x_f = \exp(-\delta t_c)X_f - Ro v_f$.

the top right plot of figure 3.1. Substitution of v (3.5a) into (3.16) yields the result that the isopycnal slope is a function of only $X = X_0$ and T , and thus the isopycnals are straight lines for all time. Referring to the figure, we observe that in the B00 case the initially vertical isopycnals rapidly tilt towards the horizontal as frontogenesis proceeds. The length scale of the imbalance region remains $O(1)$ during frontogenesis, with the location of the singularity in Eulerian coordinates, x_f , defined in table 3.1. The location of the singularity is independent of Rossby number, and using (3.15), may be evaluated as $x_f = 2$. In contrast, in the HB case the large scale convergent field squeezes the imbalance region to a length scale of $O(Ro)$ by critical time. The initially near-vertical isopycnals are tilted through a far smaller angle and therefore the isopycnal slopes at the critical time (from 3.16) are substantially larger than in the B00 case (or equivalently the stratification is almost an order of magnitude smaller).

One major application of the general solution derived above is as a generalisation of the HB theory that correctly accounts for arbitrary initial conditions, thus providing a check on the applicability of the semigeostrophic approximation. With this in mind, we compare the general solution (3.5) with the semigeostrophic HB solution (3.8) for the specific initial buoyancy profile defined by (3.15) and parameter values of $Ro = 0.4$ and $\delta = 0.1$ (as for the right-hand panel of figure 3.1). Figure 3.2 displays time series of the normalised minimum

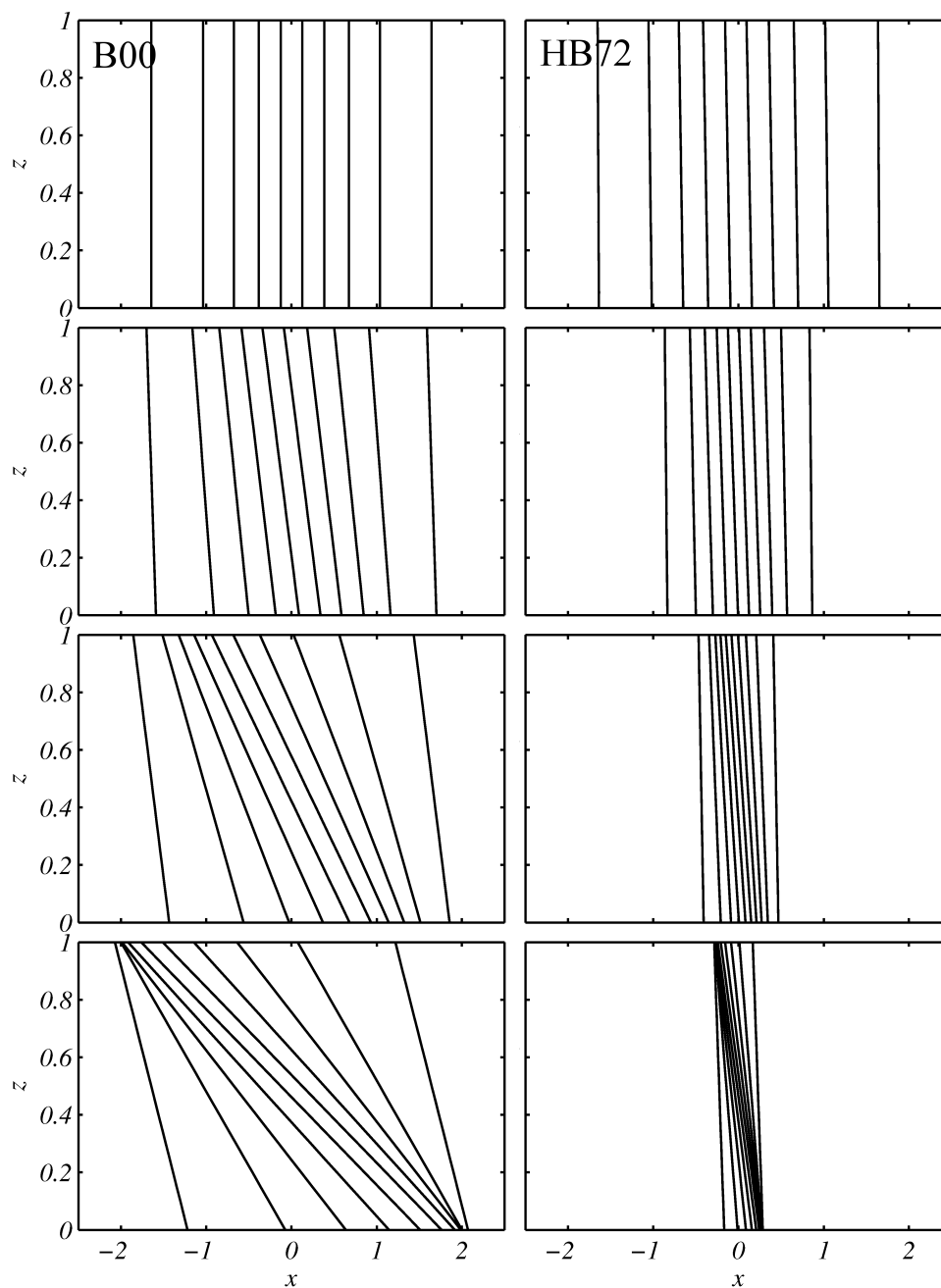


Fig. 3.1 The time evolution of the buoyancy field during frontogenesis as predicted by the general zero PV solution (3.5) for a typical B00 case ($Ro = 3$, $\delta = 0$, $\mathcal{I} = 1$, left panel) and a typical HB case ($Ro = 0.4$, $\delta = 0.1$, $\mathcal{I} = 0$, right panel) at times from top to bottom of 0 , $t_c/3$, $2t_c/3$ and t_c . The critical time is $t_c = 1.49$ in the B00 case and $t_c = 19.8$ in the HB case. The contour interval is 0.1 .

frontal width, d , defined similarly to Blumen & Williams (2001),

$$d = \frac{\max \left| \frac{\partial b_0}{\partial X} \right|}{\max \left| \frac{\partial b}{\partial x} \right|}, \quad (3.17)$$

and the magnitudes of the three velocity components at the position of the buoyancy gradient maximum. The solid line corresponds to the general solution with initial conditions of no motion ($\mathcal{I} = 1$), the dotted line to the general solution with initial conditions of (baroclinic) geostrophic balance ($\mathcal{I} = 0$), and the dashed line to the HB solution. The frontal width is almost indistinguishable in all three cases, implying that the HB prediction of the critical time (i.e. the time when d vanishes), and the buoyancy field at time T , are both accurate.

This close agreement between the models is readily explained as follows. The buoyancy field at a given time is determined from $b_0(X)$ with the momentum coordinate given by $X = x + Ro v$, and thus the difference in the buoyancy field of the HB solution with respect to the general solution at some x is given by

$$\Delta b \sim \frac{\partial b}{\partial X} \Delta X \sim \frac{\partial b}{\partial X} Ro (v - v_{\text{HB}72}) = \frac{\partial b}{\partial X} Ro v_a. \quad (3.18)$$

The ageostrophic velocity v_a (from 3.5a) is at most $Ro/2$ and thus Δb is at most $Ro^2/2$. Therefore the maximum error in d and the buoyancy field for $Ro = 0.4$ is less than 10%. Referring to the figure, the agreement in the along-front velocity itself is also very strong for the initially balanced case (since $v_a \sim \delta v_g$ initially), whereas in the case of zero initial motion the oscillations in v triggered by the mass imbalance are significant ($v_a \sim v_g$ initially). More generally, the oscillation amplitude for all field variables for an arbitrary mass imbalance \mathcal{I} is a factor of \mathcal{I}/δ larger than for the initially balanced case.

The effect of the initial conditions on the in-plane flow (u, w) is greater than on the along-front flow for both balanced and unbalanced initial conditions. This may be understood by observing that while the oscillation amplitudes in u (3.5b) and w (3.5c) are of a similar order to those in v , the in-plane flow from the HB solution is a factor of δ smaller than the along-front flow (this is true regardless of the size of the Rossby number). Furthermore, in figure 3.2 the oscillations in the vertical velocity grow up until about $T = 15$ as a result of the deformation field amplifying the vertical flow (including the oscillatory component, see the expression for the vertical velocity 3.5c). This effect is far less noticeable (but still present) when the system starts in a geostrophically balanced state. Given these results we conclude that the HB model is a good predictor of the buoyancy field for even quite large Rossby numbers ($Ro^2/2 \ll 1$) regardless of the initial conditions, but is substantially

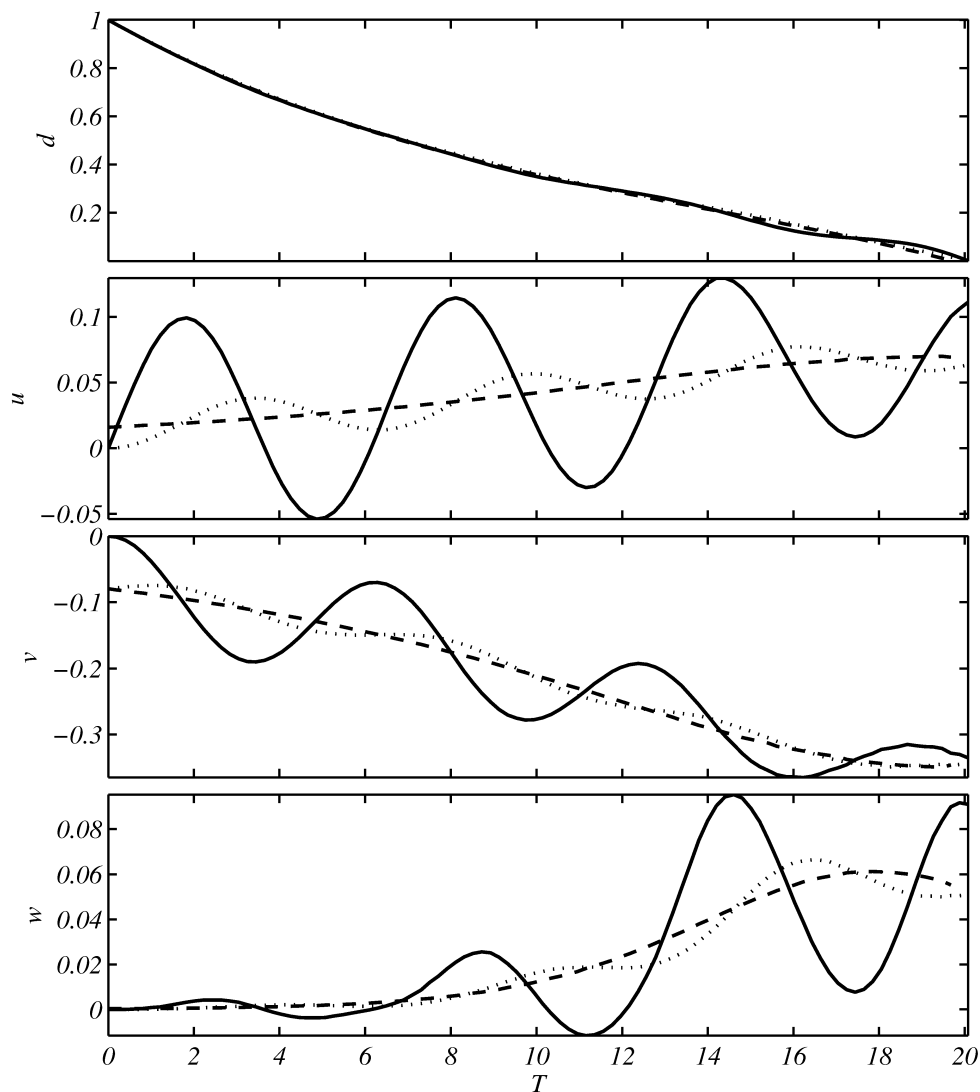


Fig. 3.2 Time series of the frontal width d and the perturbation velocity magnitudes (u, v, w) at the x position of the buoyancy gradient maximum (the front) for parameter values of $\delta = 0.1$ and $Ro = 0.4$. The vertical position is $z = 0$ for the horizontal velocities u and v , and $z = 1/2$ for the vertical velocity w . The general solution (3.5) is shown for a full mass imbalance $\mathcal{I} = 1$ (solid) and zero initial imbalance $\mathcal{I} = 0$ (dotted). The HB solution given by (3.8) is also shown (dashed).

poorer at describing the velocity fields — particularly when the initial state is unbalanced. Specifically, the semigeostrophic assumption of a geostrophic along-front velocity (i.e. $v \simeq v_g$) is reasonable only for (a) small initial imbalances ($\mathcal{I} \ll 1$), and (b) sufficiently small Rossby numbers ($Ro \ll Ro_c/\sqrt{2}$) such that the inertial oscillations do not themselves cause frontogenesis.

3.3 Geostrophic adjustment and frontogenesis in uniform PV flow

We now use the generalised model developed in Chapter 2 to analyse the fully time-dependent adjustment and frontogenesis problem in uniform PV flow with initial conditions of zero motion. In §3.3.1 we examine the unforced system, $\delta = 0$, before moving on to the more general case of $\delta \neq 0$ in §3.3.2. To simplify the analysis it is useful to take the (complex) Fourier transform in X and sine transform in Z (to satisfy the rigid lid boundary conditions) of the generalised model equation (2.29). Here we define the Fourier transform and its inverse by

$$F(k) = \int_{-\infty}^{\infty} f(\chi) e^{ik\chi} d\chi, \quad (3.19a)$$

and

$$f(\chi) = \frac{1}{2\pi} \int_{-\infty}^{\infty} F(k) e^{-ik\chi} dk, \quad (3.19b)$$

respectively. Transforming (2.29), and writing in terms of the along-front velocity v , we obtain

$$\frac{\partial^2 \hat{v}}{\partial T^2} + \left(1 - \delta^2 + \left(\frac{kBu}{n\pi} e^{\delta T} \right)^2 \right) \hat{v} = \frac{-ikA_n Ro \hat{b}_0 e^{\delta T}}{-n\pi}, \quad (3.20)$$

where k is the horizontal wavenumber, n the vertical wavenumber, hats denote Fourier mode amplitudes and A_n is defined by the Fourier series,

$$\sum_{n=1}^{\infty} A_n \sin n\pi Z = 1 \Rightarrow A_n = -\frac{2(-1 + (-1)^n)}{n\pi}. \quad (3.21)$$

Similarly transforming the equations for the other field variables (e.g. 2.20, 2.23, 2.24) yields

$$\widehat{w}_* = \frac{-ik}{n\pi} \left(\delta \widehat{v} + \frac{\partial \widehat{v}}{\partial T} \right), \quad (3.22a)$$

$$\widehat{\psi} = \frac{-1}{n\pi} \left(\delta \widehat{v} + \frac{\partial \widehat{v}}{\partial T} \right), \quad (3.22b)$$

$$\widehat{u}_* = - \left(\delta \widehat{v} + \frac{\partial \widehat{v}}{\partial T} \right), \quad (3.22c)$$

$$\widehat{\Delta b} = \frac{ikRo}{n\pi F^2} e^{\delta T} \widehat{v}, \quad (3.22d)$$

noting that $\widehat{v} = -n\pi\widehat{\phi}$. The (effective) horizontal velocities (u_* and v) involve cosine modes in the vertical, while the effective vertical velocity (w_*), cross-front streamfunction (ψ) and buoyancy anomaly (Δb) involve sine modes.

Equation (3.20) is a simple constant coefficient ordinary differential equation (ODE) when $\delta = 0$ and is solved analytically below (§3.3.1). However when $\delta \neq 0$, (3.20) is a variable coefficient second order ODE in time, and is therefore solved numerically for the cases studied below (§3.3.2).

3.3.1 Uniform PV flow with no deformation field

For uniform PV flow in the absence of a deformation field the solution to the mass imbalance problem is given by (3.20) with δ set to zero,

$$\frac{\partial^2 \widehat{v}}{\partial T^2} + \omega^2 \widehat{v} = -ikA_n Ro \widehat{b}_0, \quad (3.23)$$

with frequency ω defined by

$$\omega(k, n) = \sqrt{1 + \left(\frac{kBu}{n\pi} \right)^2}. \quad (3.24)$$

Following B00, we apply initial conditions of zero motion, $u = v = w = 0$, or equivalently

$$v = \frac{\partial v}{\partial T} = 0, \quad (3.25)$$

via substitution into the expression for u (2.25). Solving (3.23) with these initial conditions results in

$$\widehat{v} = -\frac{ik\widehat{b}_0 A_n Ro}{\omega^2} (1 - \cos \omega T). \quad (3.26a)$$

The other fields are generated by substitution of (3.26a) into (3.22):

$$\widehat{u}_* = ik\widehat{b}_0 Ro \frac{A_n}{\omega} \sin \omega T, \quad (3.26b)$$

$$\widehat{w}_* = -\frac{k^2 \widehat{b}_0 A_n Ro}{n\pi\omega} \sin \omega T, \quad (3.26c)$$

$$\widehat{\Delta b} = \frac{k^2 \widehat{b}_0 A_n Bu^2}{n\pi\omega^2} (1 - \cos \omega T). \quad (3.26d)$$

As expected, the solution given by (3.26) reveals the existence of propagating inertia-gravity waves (IGWs). Equation (3.24) is equivalent to the usual hydrostatic IGW dispersion relation. The IGW group velocity,

$$c_g = \frac{d\omega}{dk} = \frac{Bu^2 k}{n^2 \pi^2 \omega}, \quad (3.27)$$

is finite for all wavenumbers $k \neq 0$ so long as Bu is non-vanishing. Given this group velocity in momentum coordinates, the position of a wave packet at time T (sourced from the origin at time zero) will be $X = c_g T$ in momentum coordinates and $x = c_g T - Ro v(c_g T, Z, T)$ in Eulerian coordinates. Since v is a sum of odd vertical cosine modes, it is always identically zero at mid-depth ($z = 0.5$) and consequently the propagation distance is the same (i.e. $x \equiv X$) in both coordinate systems at this vertical height. The only difference between the dynamics of wave propagation in the two coordinate systems is that in Eulerian coordinates a given wave packet is tilted about $z = 0.5$ according to the vertical shear in the local along-front velocity $v(c_g T, Z, T)$. Thus the finite group velocity for $Bu \neq 0$ as per (3.27) implies that all wavenumbers $k \neq 0$ will propagate away from the imbalance region in finite time. Higher wavenumbers will propagate most rapidly, while smaller wavenumbers will propagate only very slowly. Since $\omega \rightarrow 1$ and $c_g \rightarrow 0$ for small k , the solution will exhibit slowly decaying near-inertial oscillations in the imbalance region due to the low wavenumber modes. The IGW signal in the above solution (3.26) is given by the transient (T dependent) part. The steady or *geostrophically adjusted* final state, defined as the T independent part of the solution, is given by

$$\widehat{u}_{ss} = 0, \quad (3.28a)$$

$$\widehat{v}_{ss} = -\frac{ik\widehat{b}_0 A_n Ro}{\omega^2}, \quad (3.28b)$$

$$\widehat{w}_{ss} = 0, \quad (3.28c)$$

$$\widehat{\Delta b}_{ss} = \frac{k^2 \widehat{b}_0 A_n Bu^2}{n\pi\omega^2}. \quad (3.28d)$$

The steady state defined by (3.28) is identical to the steady state solution derived by Blumen & Wu (1995, their equations 32 and 33). As expected, the in-plane flow vanishes, leaving an out-of-plane geostrophic jet given by (3.28b) in balance with the steady state buoyancy field,

$$b_{ss}(X, Z) = b_0(X) + F^{-2}Z + \Delta b_{ss}(X, Z), \quad (3.29)$$

as may be confirmed by substitution of (3.28b) and (3.29) into the steady state thermal wind equation (from 2.12 with $v = v_g$),

$$\frac{\partial v_{ss}}{\partial Z} = Ro \frac{\partial b_{ss}}{\partial X}. \quad (3.30)$$

Given the above arguments with respect to wave propagation, the timescale for the geostrophic adjustment process may be estimated from the group velocity as the time taken for a typical mode ($k = n = 1$) to leave the imbalance region (roughly $|X| < 1$). Applying (3.27), the non-dimensional adjustment timescale is

$$\tau = \frac{1}{c_g} = \sqrt{1 + \left(\frac{\pi}{Bu}\right)^2}, \quad (3.31)$$

which is finite *unless* Bu is vanishingly small. The degree of geostrophic adjustment of the buoyancy field is also governed by the Burger number, with the steady state buoyancy anomaly (3.28d) becoming negligibly small for

$$Bu = \frac{NH}{Lf} \ll 1, \quad (3.32)$$

and thus the buoyancy field behaving similarly to the zero PV limit. In this limit the group velocity (3.27) approaches zero and the frequency (3.24) approaches one for all wavenumbers — that is, the solution becomes only weakly dispersive and near-inertial. In physical terms, the near absence of background stratification limits inertia-gravity wave propagation and consequently much of the energy associated with the mass imbalance remains localised in the frontal region as an oscillating near-inertial wave for a significant period of time. The condition (3.32) is equivalent to the requirement that the length scale L is very much greater than the Rossby radius $L_R = NH/f$, and thus (3.32) is often termed the *large scale limit*. In the extreme case of vanishing Burger number the solution collapses to the zero PV limit already considered in §3.2 with the buoyancy anomaly vanishing entirely. In contrast, in the opposite extreme small scale limit, the steady state velocity field vanishes ($v_{ss} = 0$) and the buoyancy anomaly exactly cancels the initial buoyancy field ($\Delta b_{ss} = -b_0$). One physical example of this limit is non-rotating flow ($f \rightarrow 0$) where the initial imbalance generates

outward propagating gravity currents, leaving behind a stably stratified, motionless region. There is a continuum of behaviours between the zero PV extreme large scale limit and this strongly dispersive extreme small scale limit.

Let us now consider the occurrence of frontal discontinuities in uniform PV flow using solution (3.26). The general condition for singularity formation is that the inverse Jacobian (see table 2.2) vanish, or

$$J^{-1} = 1 - Ro \frac{\partial v}{\partial X} \leq 0. \quad (3.33)$$

Hence for a singularity to occur at a given Rossby number, the X gradient in the along-front flow v (which is zero at time zero) must become sufficiently large, $\partial_X v > 1/Ro$. This gradient will obtain its maximum value in the frontal zone as the unbalanced initial conditions drive wave generation and oscillations about the steady state. In the zero PV case ($Bu = 0$) where there is no energy loss from the frontal zone, the maximum value of the $\partial_X v$ is obtained at half an inertial period ($T = \pi$) as seen in §3.2. For larger Bu the system becomes more dispersive and energy is lost from the frontal zone more rapidly, reducing the maximum gradient obtainable in the frontal zone and the time at which it occurs. Heuristically, we therefore expect that for larger Bu it becomes increasingly unlikely for $\partial_X v$ to exceed $1/Ro$ and thus for a singularity to form. More rigorously, (3.33) may be rewritten as

$$\mathcal{F}^{-1} \left[\sum_{n=1}^{\infty} (-ikRo\hat{v}) \right] \geq 1, \quad (3.34)$$

with \mathcal{F}^{-1} denoting the inverse Fourier transform as defined by (3.19) (and noting that $\cos n\pi Z = 1$ on the lower boundary). Equation (3.34) must be evaluated numerically for a given profile $b_0(X)$. We have evaluated (3.34) for the error function buoyancy profile defined by (3.15) and plotted the result in figure 3.3. We note that employing a different buoyancy profile does not significantly alter the result. With reference to figure 3.3, we now have a general description of how the formation of strong fronts (singularities) is controlled by stratification (Froude number) and rotation (Rossby number). The main features of figure 3.3 are:

- For a given Froude number there exists a critical Rossby number which must be exceeded for a singularity to occur and this critical value is minimum in the absence of stratification.
- As F is decreased and the system becomes increasingly stratified, the Rossby number required for singularity formation increases since energy is removed more rapidly from the imbalance region via inertia-gravity wave propagation.

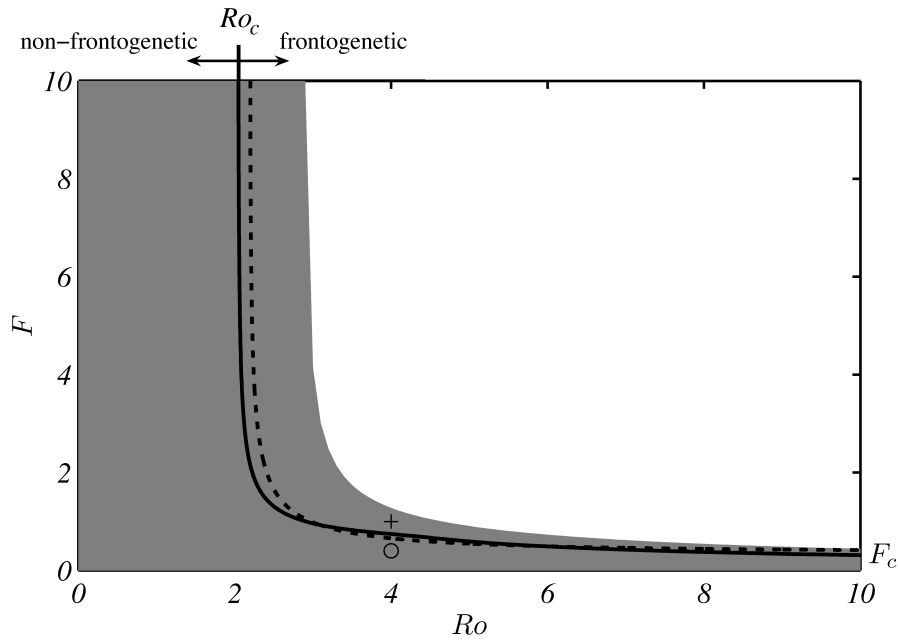


Fig. 3.3 The limiting curve (solid) evaluated from (3.34) for the error function profile (3.15) dividing frontogenetic (above) and non-frontogenetic (below) regions. The limiting curve (dashed) found empirically by Neves (1996, equation 41) from numerical simulations is also shown (rescaled appropriately to match the buoyancy profile given by 3.15). The two specific cases of $(Ro = 4, F = 0.4, \text{non-frontogenetic})$ and $(Ro = 4, F = 1, \text{frontogenetic})$ considered in the text are represented by a circle and '+', respectively. The critical Rossby and Froude numbers, $Ro_c = 2.03$ and $F_c = 0.31$ respectively, are labelled. The shading indicates the parameter values for which an adjusted state (with non-vanishing inverse Jacobian) exists.

- There exists a critical Froude number F_c below which singularity formation is impossible regardless of the Rossby number (within the scope of the approximations made in our model) — IGWs remove energy from the imbalance region too rapidly for a frontal singularity to form.

Also plotted in figure 3.3 is an empirical curve determined by Neves (1996), based on a suite of numerical simulations. The agreement between Neves (1996) result and our analytical prediction is remarkable.

The set of Rossby and Froude numbers for which a continuous adjusted state exists has also been indicated in figure 3.3 (shaded grey). The curve bounding this existence region may be computed by replacing the velocity in the frontogenesis condition (3.34) with the steady state velocity from (3.28b). It is immediately apparent from figure 3.3 that the existence of a steady state with non-vanishing inverse Jacobian does *not* imply attainability of that state. Indeed, all sets of Rossby and Froude numbers in the shaded region above the critical curve (solid line) have corresponding steady states, but these states are never reached. Instead a

singularity forms during the geostrophic adjustment process. The (Ro, F) parameter space is therefore divided into three regions based on the existence and attainability of an adjusted state: (1) for sufficiently small Rossby numbers a steady state does exist and is attainable, (2) for sufficiently large Rossby numbers a steady state does not exist, and (3) for intermediate Rossby numbers a steady state exists but is not attainable. In the case of zero PV flow ($F \rightarrow \infty$ in figure 3.3), it may be shown that the (critical) Rossby number required for singularity formation is a factor of $\sqrt{2}$ smaller than the Rossby number required for the non-existence of the adjusted state (this result was previously derived by Blumen & Williams, 2001). The three regions in the large Froude number limit are therefore as follows. For Rossby numbers in the range $Ro_c < Ro < \sqrt{2}Ro_c$ a steady state exists but is not attainable. For $Ro > \sqrt{2}Ro_c$ a steady state does not exist. For $Ro < Ro_c$ a steady state does exist and is attainable (at least in the limit of infinite time).

To illustrate the behaviour of the uniform PV solution (3.26) we examine the time evolution of the flow for the specific profile specified by (3.15) for two sets of parameters. Firstly, a *non-frontogenetic* case (i.e. no singularity forms) is considered ($Ro = 4, F = 0.4$, circle in figure 3.3) to demonstrate the dynamics of *small scale* (since $Bu = 10$, or $L/L_R = 0.1$) geostrophic adjustment to a steady state. We plot the time evolution of the buoyancy field and along-front velocity field (figure 3.4), and the streamfunction (figure 3.5). The isopycnals in figure 3.4 flatten as an IGW is generated ($T = 0.5\pi$) before steepening again as the IGW propagates out of the imbalance region ($T = 0.75\pi, \pi$), but remaining flatter than in the initial state. An along-front jet rapidly develops with its maximum coincident with the horizontal buoyancy gradient maximum on the boundary. The jet magnitude oscillates near-inertially with time (e.g. see $T = 0, \pi, 2\pi, 3\pi$) as IGWs are generated. After only an inertial period ($T = 2\pi$) the buoyancy field attains a near-steady state in the frontal zone. IGWs continue to be generated and propagate away from the imbalance region but are of significantly smaller amplitude than the initial wave and thus not noticeable in the large scale buoyancy field. The streamfunction in figure 3.5 initially ($T = 0.5\pi$) develops a single overturning cell in the imbalance region very similar to the zero PV case (for example, compare with figure 3 of B00). However, as IGWs are generated ($T \geq 0.75\pi$ in the figure) the strongest overturning is concentrated at the location of the outward propagating wavefronts, with a relatively weak (oscillating) overturning cell left behind in the imbalance region. The initial buoyancy field is plotted alongside the steady state buoyancy field, buoyancy anomaly, and geostrophic velocity in figure 3.6. The steady state fields are not substantially different from those at time $T = 9$ in figure 3.4.

A useful means to visualise the wave generation and propagation described above is through a Hovmöller plot of the streamfunction along $z = 0.5$, as shown in figure 3.7. As

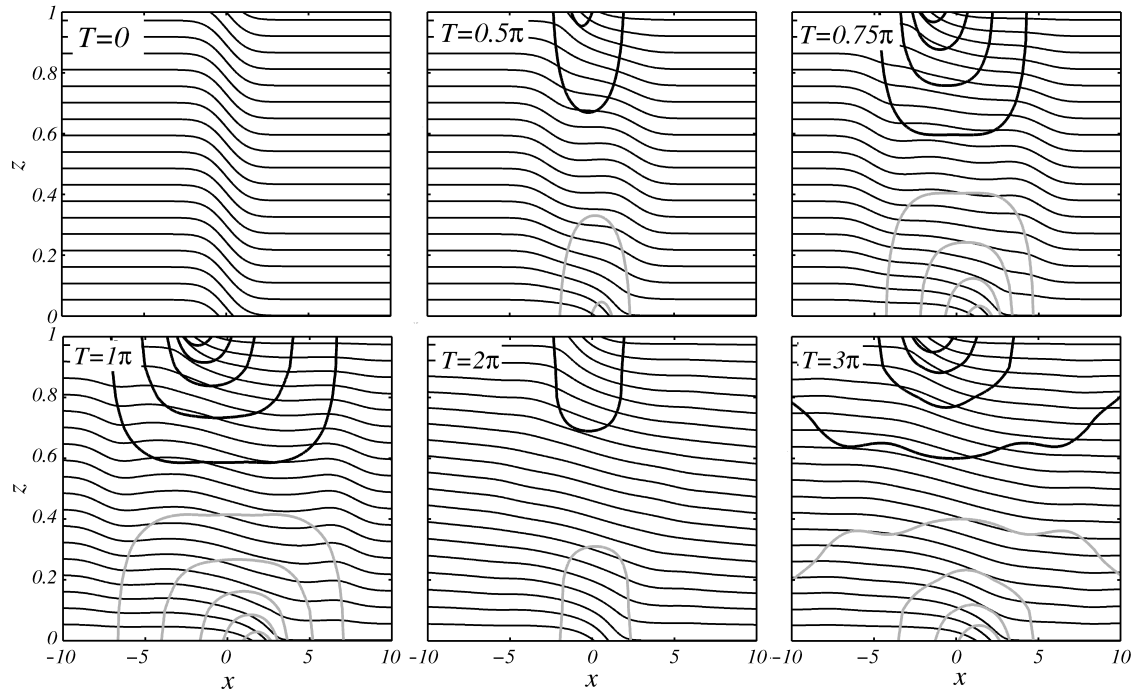


Fig. 3.4 Geostrophic adjustment of the buoyancy (thin contours) and along-front velocity (thick contours) fields towards a steady state for (non-frontogenetic) initial parameter values of $Ro = 4$ and $F = 0.4$ ($\delta = 0$), as predicted by general solution for uniform PV flow (3.26). Inertia-gravity waves propagate outward from the imbalance region leaving behind flatter isopycnals. Negative contours, denoting a velocity directed out of the page, are coloured grey. Contour intervals are 0.338 for the buoyancy and 0.1 for the velocity.

noted previously, this plot will look identical in momentum or Eulerian coordinates since $v = 0$ and $x = X$ along $z = 0.5$. Referring to figure 3.7, we observe that waves propagate away from the origin for all $T > 0$ with the smallest scales propagating most rapidly. The group velocity for waves with a vertical mode $n = 1$ and horizontal wavenumbers of $k = 0.1$, 0.3 and $k \rightarrow \infty$ are indicated by dashed lines. A given wave packet, seen as a coloured band in the figure, is composed of a range of wavenumbers and decays as it propagates outwards due to dispersion. This effect is also visible in the plots of the full streamfunction in figure 3.5. The propagation of the energy associated with the highest horizontal wavenumbers out of the frontal zone (approximately $|x| < 1$) rapidly leads (within an inertial period) to a decaying near-inertial oscillation in the frontal zone associated with the lowest horizontal wavenumbers.

For comparison with the above geostrophically adjusting case, the flow evolution for a frontogenetic case ($Ro = 4, F = 1$) is considered by way of the buoyancy field (figure 3.8) and along-front velocity field (figure 3.9). The key feature of these two figures (as

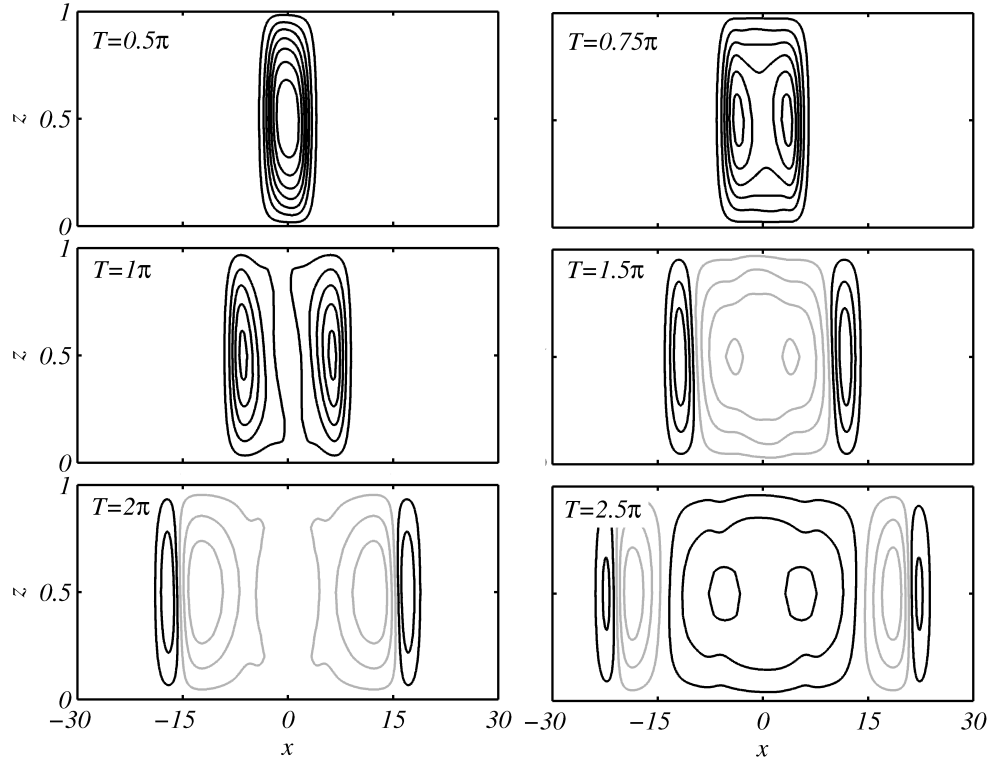


Fig. 3.5 Time evolution of the streamfunction for initial parameter values of $Ro = 4$ and $F = 0.4$ ($\delta = 0$), as predicted by general solution for uniform PV flow (3.26). Inertia-gravity waves propagate outwards leaving a progressively weaker overturning cell in the initial imbalance region. Positive values (black) correspond to anticlockwise flow, and negative values (grey) to clockwise flow. Contour intervals are 0.01.

compared with the non-frontogenetic case) is the rapid development of an infinite horizontal gradient (i.e. a frontal discontinuity) in the two fields. The increase in the Froude number as compared to the previous case (which had $F = 0.4$) decreases the propagation speed of IGWs, as previously discussed. Consequently energy cannot be dispersed away from the frontal zone sufficiently fast to prevent discontinuity formation. Note that the ‘+’ symbol denoting this frontogenetic case in figure 3.3 appears in the shaded region of the plot, implying that an adjusted state exists for the specified parameter values ($Ro = 4, F = 1$). However, the formation of a singularity during the geostrophic adjustment process, as seen in figures 3.8 and 3.9, prevents the system from attaining this steady state.

Figure 3.10 displays a time series of the frontal width d (as defined by 3.17) and the Eulerian position x where the buoyancy gradient maximum occurs (i.e. the frontal position at time T) for both the frontogenetic and non-frontogenetic cases. Frontogenesis occurs when the frontal width vanishes, as happens within the first oscillation for the frontogenetic case. In the non-frontogenetic case the frontal width adjusts towards the steady state value of d

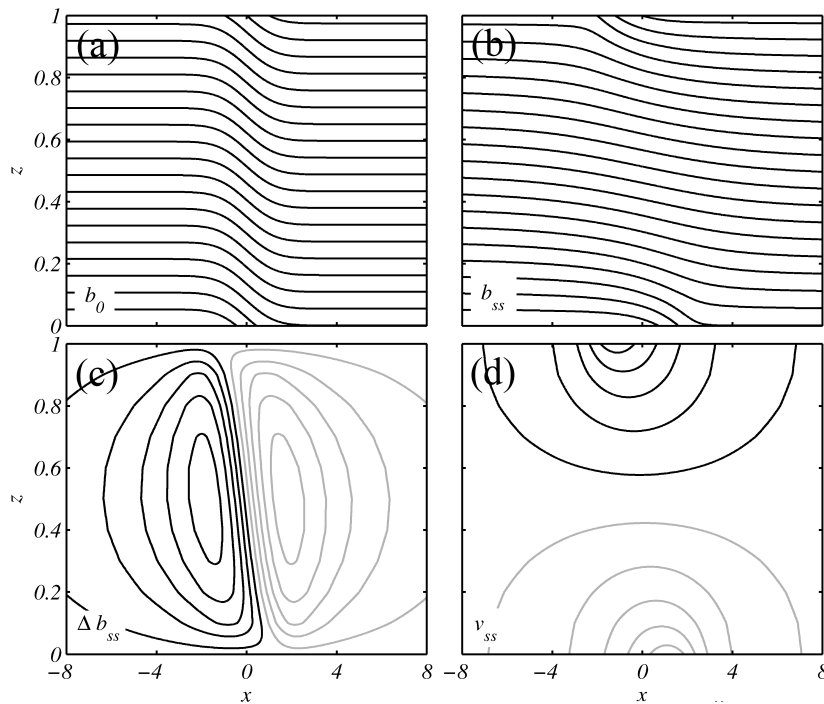


Fig. 3.6 The (a) initial buoyancy field for parameter values of $Ro = 4$ and $F = 0.4$ ($\delta = 0$), and the (b,c,d) corresponding geostrophically adjusted steady state as predicted by (3.28). The isopycnals are flattened in the steady state (b) relative to the initial configuration and in balance with a steady geostrophic out-of-plane jet (d). The buoyancy anomaly pertaining to the geostrophically adjusted state is also shown (c). Negative contours are coloured grey. Contour intervals are 0.338 for the buoyancy, 0.06 for the buoyancy anomaly and 0.061 for the velocity.

represented by a dotted line in the figure. However, we observe that the minimum value of the frontal width, occurring during the first oscillation at about $T = 2$, is smaller than this steady state value. Generalising this result, the sharpest front — and thus any discontinuity — will always occur during the first oscillation of the adjustment process, and can therefore prevent a system reaching the steady state (as previously discussed). Consistent with the Hovmöller plot above (figure 3.7), the oscillations in the frontal width and position are (except for the first oscillation) close to inertial and decay slowly in time. Lastly, in figure 3.11 we plot time series for the three velocity components at the position of the front (that is, the position x plotted in figure 3.10), at three vertical levels. The oscillations in horizontal velocities are near-inertial, with the upper and lower boundaries 180 degrees out of phase but with greater magnitudes at the lower boundary (where the front is located). As should be expected from the form of the solution (3.26), the velocities u and v are 90 degrees out of the phase on the boundaries. The vertical velocity w is maximum at the mid-level $z = 1/2$ and decays very

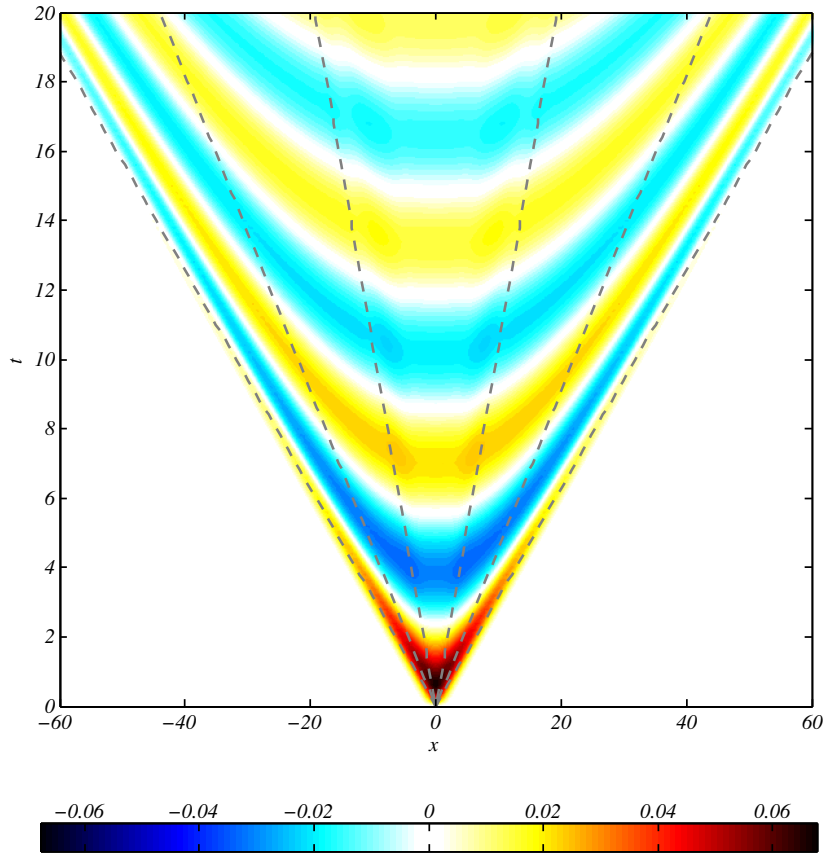


Fig. 3.7 Hovmöller plot of the streamfunction at mid-depth $z = 0.5$ during the course of geostrophic adjustment for initial parameter values of $Ro = 4$ and $F = 0.4$ ($\delta = 0$), as predicted by general solution for uniform PV flow (3.26). The unbalanced initial conditions generate inertia-gravity waves which propagate outwards at a constant speed given by their group velocity, with the highest horizontal mode numbers propagating most rapidly. Group velocities for modes $n = 1$ and $k = 0.1, 0.3$ and $k \rightarrow \infty$ are indicated by dashed lines.

rapidly in time in comparison to the horizontal velocities, although again oscillating with a near-inertial period.

3.3.2 Uniform PV flow with a deformation field

In this section we will consider frontogenesis *forced* by a background strain flow in the general case of uniform (non-zero) PV. The general linearised equation for uniform PV flow subject to a deformation field is given by (3.20). The generalised model permits arbitrary initial conditions for the buoyancy and along-front velocity, so long as they correspond to uniform PV. Here we will consider two particular initial conditions: (1) unbalanced initial

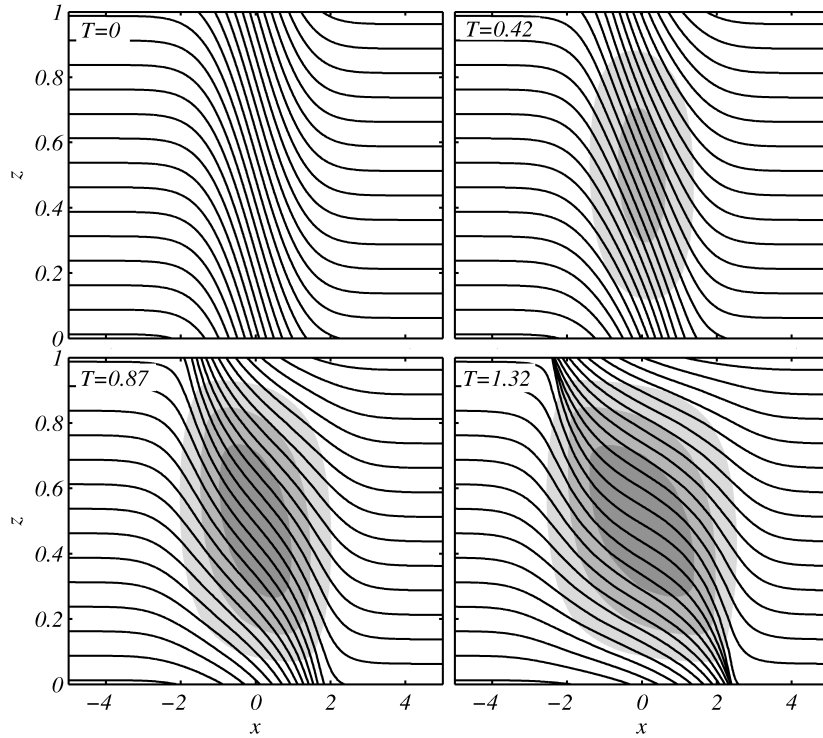


Fig. 3.8 Time evolution of the buoyancy field for initial parameter values of $Ro = 4$ and $F = 1$ ($\delta = 0$), as predicted by general solution for uniform PV flow (3.26). An infinite horizontal buoyancy gradient develops on the upper and lower boundaries. The streamfunction (anticlockwise) at each time is represented by grey shading. Contour intervals are 0.075 for the buoyancy and 0.024 for the streamfunction.

conditions, defined as

$$\hat{v}(0) = \frac{\partial \hat{v}(0)}{\partial T} = 0, \quad (3.35)$$

and (2) geostrophically balanced initial conditions, defined as

$$\hat{v}(0) = \hat{v}_{ss}, \quad \frac{\partial \hat{v}(0)}{\partial T} = -\delta \hat{v}_{ss}, \quad (3.36)$$

where the velocity \hat{v}_{ss} is given by (3.28b). Initial condition (1) implies no perturbation flow at time zero, $u = v = w = 0$, such that only the large scale strain flow is present. Initial condition (2) implies a geostrophically balanced along-front velocity, $v = v_g$, but zero in-plane perturbation flow (e.g. from 3.22b), $u = w = 0$. However, before considering the effect of initial conditions let us examine the long-time limit of (3.20) for small strain. At large times $T \gg 1$ we assume that the only time dependence in the along-front flow arises via the strain field (since all oscillations are presumed to have decayed away) and hence that

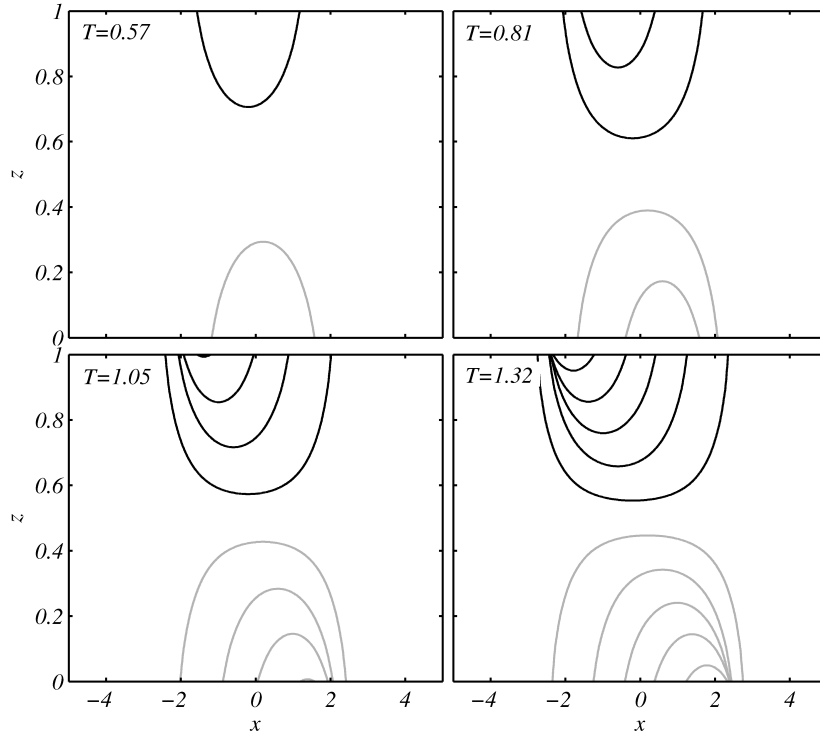


Fig. 3.9 Time evolution of the along-front (out-of-plane) velocity field for initial parameter values of $Ro = 4$ and $F = 1$ ($\delta = 0$), as predicted by general solution for uniform PV flow (3.26). The baroclinic jet intensifies with time and develops an infinite horizontal gradient on the upper and lower boundaries as frontogenesis occurs. Negative contours are coloured grey. The contour intervals is 0.1.

$\partial_{TT}v = O(\delta^2v)$. Further assuming that $\delta \ll 1$, we obtain a simplified version of (3.20),

$$\hat{v} \left(1 + \left(\frac{kBu}{n\pi} e^{\delta T} \right)^2 \right) = -ikA_n Ro \hat{b}_0 e^{\delta T}, \quad (3.37)$$

where A_n is defined by (3.21). The along-front flow is therefore

$$\hat{v} = -ikA_n Ro \hat{b}_0 e^{\delta T} \left(1 + \left(\frac{kBu}{n\pi} \right)^2 e^{2\delta T} \right)^{-1}. \quad (3.38a)$$

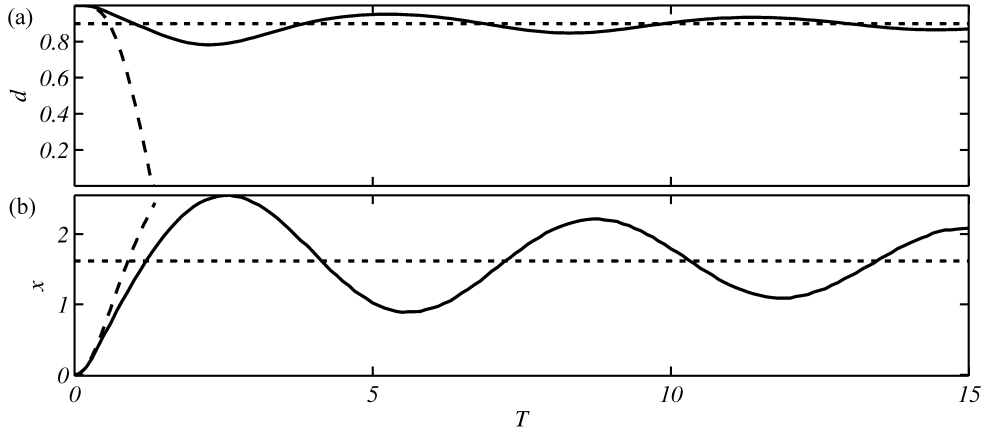


Fig. 3.10 Time series of the (a) frontal width d and (b) frontal position x (the position of the buoyancy gradient maximum on the lower boundary), for the non-frontogenetic ($Ro = 4, F = 0.4, \delta = 0$ solid) and frontogenetic ($Ro = 4, F = 1, \delta = 0$, dashed) cases, as predicted by the uniform PV solution (3.26). The steady state frontal width and position predicted by (3.28) are also shown as dotted lines for the non-frontogenetic case.

The cross-front streamfunction and buoyancy anomaly may be expressed using (3.22) as

$$\hat{\psi} = ikRo \frac{2A_n \delta \hat{b}_0}{n\pi} e^{\delta T} \left(1 + \left(\frac{kBu}{n\pi} \right)^2 e^{2\delta T} \right)^{-2}, \quad (3.38b)$$

$$\hat{\Delta b} = \frac{k^2 Bu^2 A_n \hat{b}_0}{n\pi} e^{2\delta T} \left(1 + \left(\frac{kBu}{n\pi} \right)^2 e^{2\delta T} \right)^{-1}. \quad (3.38c)$$

This solution (3.38) is equivalent to the uniform PV solution of HB (their equations 3.51, 3.52 and 3.54), although their solution is expressed differently. As discussed in the zero PV case, the assumption of a long-time solution and associated neglect of the oscillatory part of the flow in (3.37) constrains the range of parameter values for which the equation (and consequently the model of HB) is valid. A bounding constraint is that the initial state implied by the HB solution must be continuous with a non-vanishing inverse Jacobian. Since the initial condition implied by the HB (e.g. by evaluating 3.38a at $T = 0$) is that of geostrophic balance, the model can only be valid for parameter values (Ro, F) where this geostrophically balanced state exists as a uniform PV model solution. This region of existence was found in the previous section (§3.3.1) and shown as the shaded region on figure 3.3. Thus the uniform PV HB solution, like the zero PV HB solution (see §3.2), is only valid for sufficiently small (but still order 1) Rossby numbers. With reference to figure 3.3, the range of Rossby numbers for which the HB solution is valid increases for smaller Froude numbers (stronger stratification).

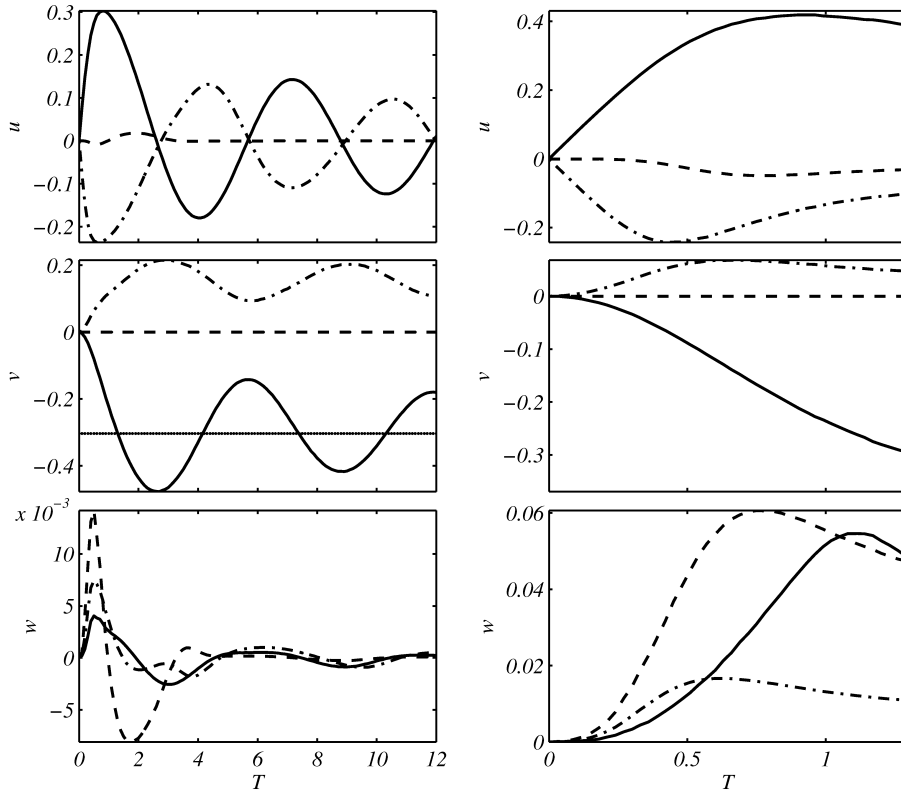


Fig. 3.11 Time series of the velocity magnitudes (u, v, w) at the position of the buoyancy gradient maximum on the lower boundary for three vertical heights, for the non-frontogenetic ($Ro = 4, F = 0.4, \delta = 0$, left panel) and frontogenetic ($Ro = 4, F = 1, \delta = 0$, right panel) cases. For the horizontal velocities u and v the heights are $z = 0$ (solid), $z = 0.5$ (dashed) and $z = 1$ (dot-dashed). For the vertical velocity w the heights are $z = 0.1$ (solid), $z = 0.5$ (dashed) and $z = 0.9$ (dot-dashed). Also shown (dotted) is the steady state maximum value of v on the lower boundary, as predicted by (3.28).

Let us now consider the full solution to the uniform PV deformation frontogenesis problem including wave motions. To do this it is convenient to rewrite the full linearised equation (3.20) for $\delta \neq 0$ and finite Bu with a change of variable, $T \rightarrow \eta$, with

$$\eta = \frac{kBu}{\delta n\pi} e^{\delta T}. \quad (3.39)$$

Equation (3.20) then becomes a forced Bessel equation,

$$\eta^2 \frac{\partial^2 \hat{v}}{\partial \eta^2} + \eta \frac{\partial \hat{v}}{\partial \eta} + \hat{v}(\eta^2 + \delta^{-2} - 1) = \frac{-iA_n Ron\pi \hat{b}_0}{\delta Bu} \eta, \quad (3.40)$$

the solution to which may be written as the sum of a forced part \widehat{v}_F and wave components,

$$\widehat{v} = \widehat{v}_F + c_1(k, n) J_\sigma(\eta) + c_2(k, n) Y_\sigma(\eta), \quad (3.41)$$

where $J_\sigma(\eta)$ and $Y_\sigma(\eta)$ are the Bessel functions of complex order $\sigma = \sqrt{1 - \delta^{-2}}$. The expression for the forced component \widehat{v}_F is somewhat complicated and will be discussed in Chapter 4. For present purposes, we observe that when $\delta \ll 1$ the leading order term in the forced component is simply given by the HB solution from (3.38a) and the order of the Bessel functions becomes $\sigma = \iota/\delta$. The constants c_1 and c_2 may be determined for each mode (k, n) for unbalanced or geostrophically balanced initial conditions using (3.35) or (3.36), respectively. As before, the other flow fields can then be calculated from v using (3.22). For either set of initial conditions, the flow is composed of an IGW field associated with the Bessel functions in (3.41) which drives oscillations about a time-varying mean state given by the HB solution.

Using the solution (3.41) we can describe the dynamics of the inertia-gravity waves. The mode number dependence of the Bessel functions may be fully described by a single parameter $a = kBu/(n\pi)$. We consider the two extreme limits of $\eta \rightarrow 0$ and $\eta \rightarrow \infty$ using the first term in a series expansion of $J_\sigma(\eta)$:

$$J_\sigma\left(\eta = \frac{a}{\delta} e^{\delta T}\right) \rightarrow \begin{cases} h(\delta, a) e^{\iota T} & \eta \rightarrow 0 \\ g(\delta, a) e^{-\frac{\delta}{2} T} \sin\left(\frac{a}{\delta} e^{\delta T} + \theta(a, \delta)\right) & \eta \rightarrow \infty \end{cases} \quad (3.42)$$

where h , g and θ are unspecified functions. Note that a similar result applies for the other Bessel function, $Y_\sigma(\eta)$. In the limit of small η the Bessel mode reduces to a non-propagating inertial wave ($\omega = 1$, $c_g = 0$) with constant amplitude. In contrast, for large η the Bessel function has an exponentially increasing frequency and group speed (in momentum coordinates) and its amplitude decays at a rate of $\delta/2$. The initial behaviour of a given wave packet will depend on the value of a associated with it, since the initial value of η is $\eta_0 = a/\delta$. Waves with $\eta_0 = kBu/(n\pi\delta) \gg 1$ will begin to both propagate and decay immediately. Waves with $\eta_0 \ll 1$ will be trapped in the frontal zone as oscillating inertial waves at early times. However, at some point in time (presuming a discontinuity does not occur first) η will grow sufficiently large that the waves will begin to propagate and decay (as per the large η limit). The time at which the waves are released may be estimated based on the time at which higher order terms in the small η series given in (3.42) become comparable to the first term. Using this method, the time at which a wave begins to propagate and decay is

$$\delta T_R \simeq \ln \frac{\sqrt{\delta}}{a} = \ln \frac{n\pi \sqrt{\delta}}{kBu}. \quad (3.43)$$

We call T_R the *release time*. Higher horizontal wavenumbers and smaller vertical wavenumbers are released more rapidly, and if $kBu/(n\pi\sqrt{\delta}) \geq 1$ the release is immediate ($T_R = 0$). Since wavenumbers $k < 1$ will be the most energetic for an appropriately scaled buoyancy gradient profile $b'_0(X)$, a good estimate for the earliest time of release for energetic (observable) waves is given by setting $k = n = 1$ and thus $T_R \sim \ln(\pi\sqrt{\delta}/Bu)$.

Now consider what happens to propagating waves in the limit of large time. Using (3.42) with $\eta \rightarrow \infty$, and interpreting the time-dependent argument of the sine function as the time integral of the frequency, $a \exp(\delta T)/\delta = \int \omega dT$, the frequency of the waves at time T is $\omega \approx Bu/(n\pi)k \exp \delta T$ in generalised momentum coordinates. In physical/Eulerian coordinates the frequency will be different since the mode number k_E increases exponentially due to the action of the strain field; that is, at mid-depth ($v = 0$),

$$x = e^{-\delta T} X \Rightarrow k_E = e^{\delta T} k \Rightarrow \omega = \frac{Bu k_E}{n\pi}. \quad (3.44)$$

The group (and phase) speed of the waves in Eulerian coordinates thus approaches a constant value for all horizontal scales, $c_g = Bu/(n\pi)$. Wave packets with this group speed will propagate outwards into the strain flow (which has a non-dimensional velocity $U = -\delta x$) until they reach a point where their outward group velocity equals the inward strain flow velocity and they become stationary. From this argument the location at which the waves stagnate, x_s , is

$$x_s = \frac{Bu}{\delta n \pi}. \quad (3.45)$$

The amplitude of the waves continues to decay, and their scale $1/k_E$ to shrink, during this process. The decay timescale of the waves as a function of the parameter a is shown in figure 3.12 in terms of the time taken for the waves to decay to half their initial magnitude. As predicted from the above series expansion, the decay timescale approaches $2/\delta$ for large a and infinity for small a . The damping of IGWs by the action of frontogenetic strain has been described in a similar context by Thomas (2012).

We now consider an explicit example of strain-forced frontogenesis with parameter values of $Ro = 0.4$, $F = 0.8$ (hence $Bu = 0.5$, or $L/L_R = 2$) and $\delta = 0.1$. The results presented are derived from a direct numerical solution to (3.20) for each mode. In figure 3.13 we display the buoyancy field and streamfunction at the critical time for this set of parameter values for both balanced and unbalanced initial conditions. The major difference is a significantly stronger wave field in the latter case, associated with the large initial imbalance and subsequent geostrophic adjustment. Figure 3.14 shows a time series of the frontal width and position. The frontal width arising from the full solution (unbalanced: solid, balanced: dotted) is almost indistinguishable from the HB solution (dashed). In contrast, the frontal position

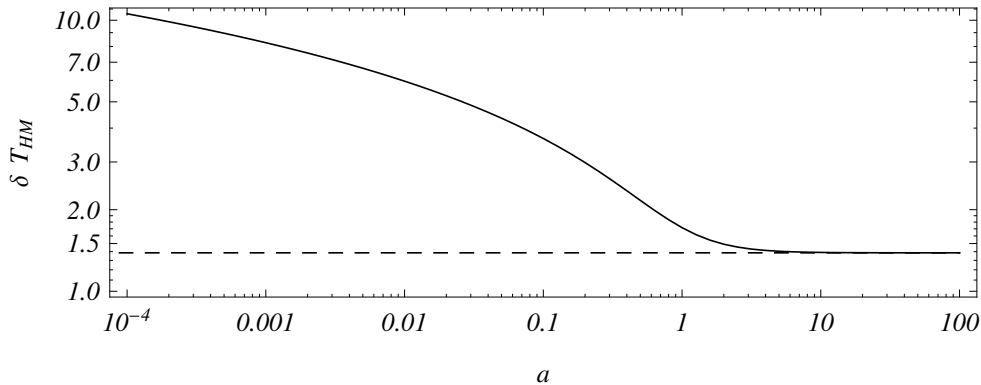


Fig. 3.12 The scaled time taken δT_{HM} for the propagating wave components of the solution (3.41), $J_\sigma(\eta)$ and $Y_\sigma(\eta)$, to decay to half their initial magnitude in the small strain limit, $\sigma = \nu/\delta$, in terms of the parameter $a = kBu/(n\pi)$. In the limit of large a the time taken δT_{HM} converges to $2 \ln 2$, corresponding to a decay rate of $\delta/2$.

exhibits slowly decaying near-inertial oscillations about a ‘mean state’, as in the previous section. In this case the mean state is time-varying, and for the above parameter values is well described by the HB solution. The amplitude of the oscillations about the HB solution is far larger for the unbalanced solution and there is a 90 degrees phase difference compared with the balanced solution. The balanced solution for the frontal position becomes visually indistinguishable from the HB solution at large time ($T \sim 20$).

The dynamics of the generated inertia-gravity waves seen in figure 3.13 are most transparent when the time-varying mean state (in this case the HB solution) is subtracted from the fields. Figure 3.15 displays a Hovmöller plot of the difference between the generalised model and the HB streamfunction, $\psi - \psi_{HB}$, at height $z = 0.5$ for unbalanced initial conditions. Using this figure we can trace the evolution of a given wave packet as seen in Eulerian coordinates (left-hand plot) and generalised momentum coordinates (right-hand plot). As predicted, the generated waves are trapped as inertial oscillations in the imbalance region until the release time ($T_R \simeq 7$ in this case, shown as a horizontal dashed line on the figure). The width of the oscillating region in Eulerian space begins to shrink due to the action of the strain field during this time, $T < T_R$. For $T > T_R$, waves begin to propagate outwards but with their propagation speed decreasing with time until they stagnate. The stagnation points x_s for the first vertical mode are shown by vertical dashed lines. The decay in wave amplitude with time predicted above is visible in both the Eulerian and momentum coordinate plots. Note that the horizontal scale of the waves in momentum coordinates (right) is approximately constant with time as they propagate, but shrinks in Eulerian coordinates (left) due to the squeezing effect of the strain field. Comparing the Hovmöller plot from §3.3.1 (figure 3.7)

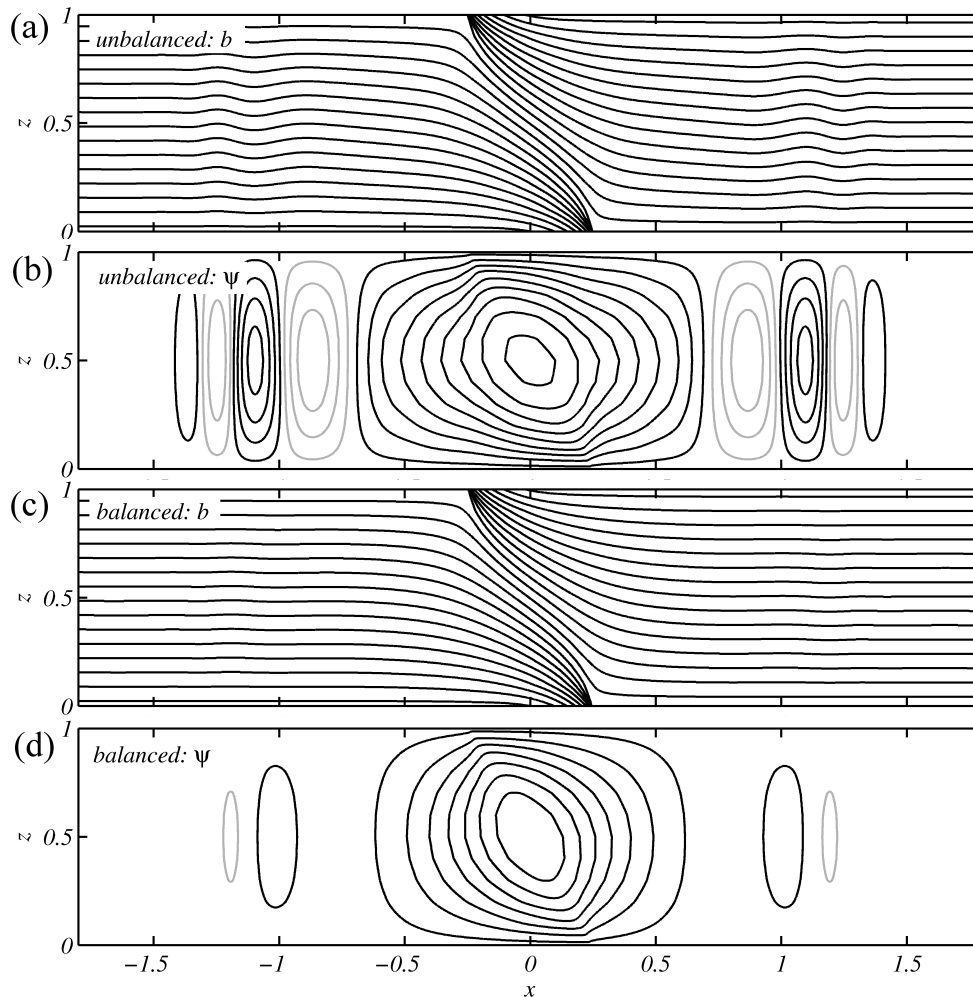


Fig. 3.13 The buoyancy field and streamfunction at the critical time $t_c \approx 26$ for parameter values of $Ro = 0.4$, $F = 0.8$ and $\delta = 0.1$, as computed from the differential equation (3.20). Both unbalanced (a,b) and balanced (c,d) initial conditions are shown, with the same contour levels. The inertia-gravity wave field is substantially more intense for the unbalanced initial conditions. Positive values of the streamfunction (black) correspond to anticlockwise flow and negative values (grey) to clockwise flow. Contour intervals are 0.103 for the buoyancy and 0.002 for the streamfunction.

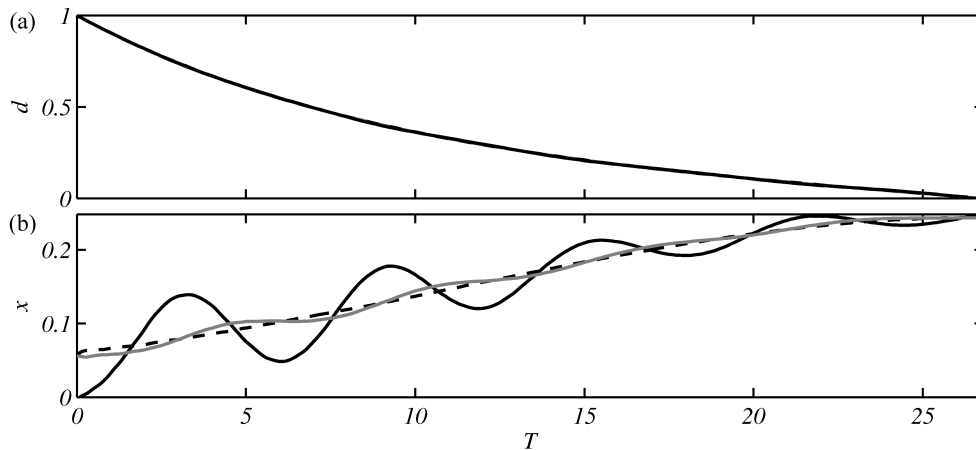


Fig. 3.14 Time series of the (a) frontal width d and (b) frontal position x (the position of the buoyancy gradient maximum on the lower boundary), for parameter values of $Ro = 0.4$, $F = 0.8$ and $\delta = 0.1$, as computed from the HB solution (3.38, dashed) and the differential equation (3.20) for both unbalanced (black solid) and balanced (grey solid) initial conditions.

with the current figure, note that there is no trapping effect in the unstrained case ($T_R \rightarrow 0$) and waves begin to propagate immediately at time zero. Also, in the absence of strain, the waves propagate freely towards $\pm\infty$ rather than stagnating at $\pm x_s$.

3.4 Numerical comparison

The derivation of the generalised model in Chapter 2 assumed that certain explicit non-linear terms could be neglected (i.e. \mathcal{N} in (2.29)). Here we assess the error made in the neglect of these non-linear terms and the validity of the analytical solution by comparison with a fully non-linear numerical solution to the problem. The full details of the numerical model employed will be described later in §5.2. For now we merely note that the model timesteps the two-dimensional strained front equations derived in Chapter 1 (1.12) in a 2D box from the specified unbalanced initial state. The model has no explicit diffusion (although inevitably there will be some numerical diffusion). Thus for frontogenetic cases the numerical model can only be iterated until the frontal width collapses to the grid scale, at which point the simulation is stopped. For non-frontogenetic cases, the model can be iterated indefinitely.

We compare the generalised model prediction with the numerical solution for the three cases studied in previous sections. Firstly, we consider the unstrained, non-frontogenetic case ($Ro = 4, F = 0.4, \delta = 0$, circle in figure 3.3) for which the analytical solution was shown in figures 3.4, 3.5, and 3.7, and the steady state in 3.6. Figure 3.16a compares the time evolution of the streamfunction at mid-depth in the numerical (colour) and analytical (contour lines)

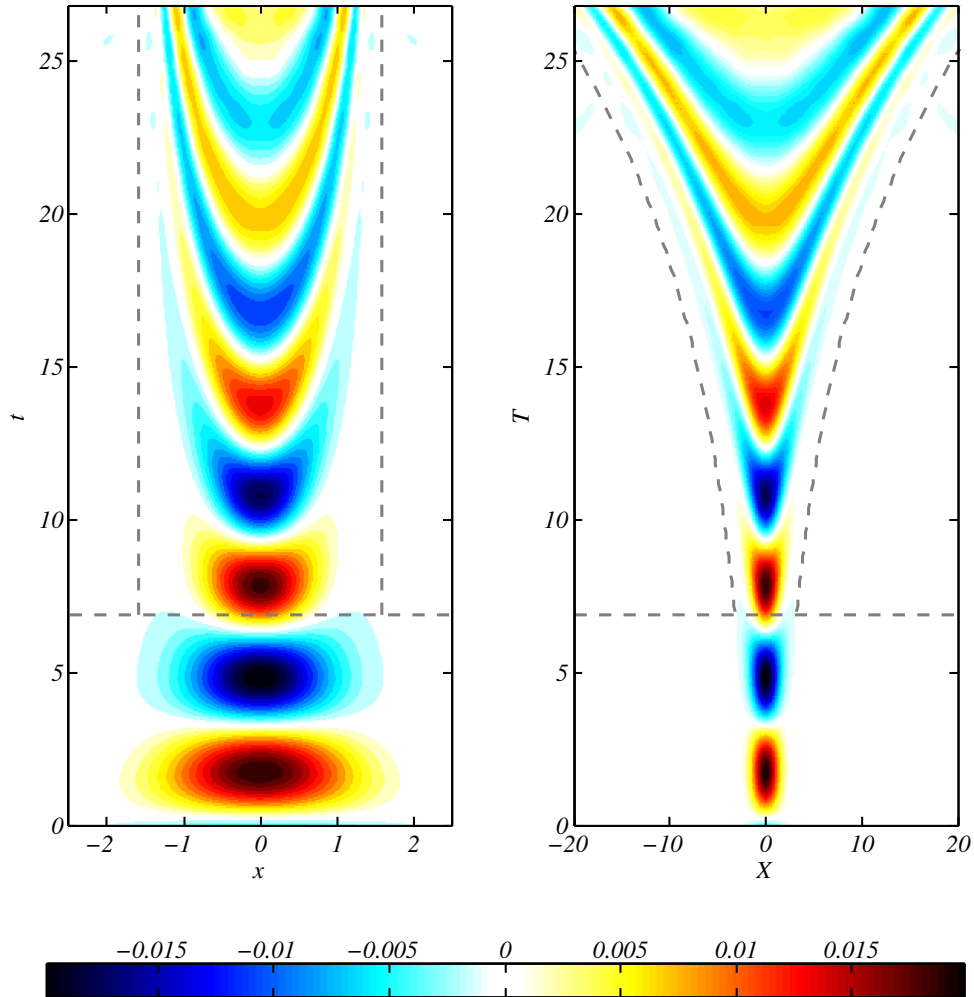


Fig. 3.15 Hovmöller plot of the streamfunction difference $\psi - \psi_{HB}$ for parameter values of $Ro = 0.4$, $F = 0.8$ and $\delta = 0.1$, and unbalanced initial conditions, at height $z = 0.5$ in Eulerian coordinates (left) and momentum coordinates (right). Waves generated by the initial conditions are initially trapped until the release time $T_R \sim 7$ (shown as a horizontal dashed line) as non-decaying inertial oscillations. Once released the waves propagate towards a stagnation point $x_s = \pm 1.6$ shown by the vertical dashed line (left) and the dashed curve (right, $X_s = \pm x_s \exp \delta T$).

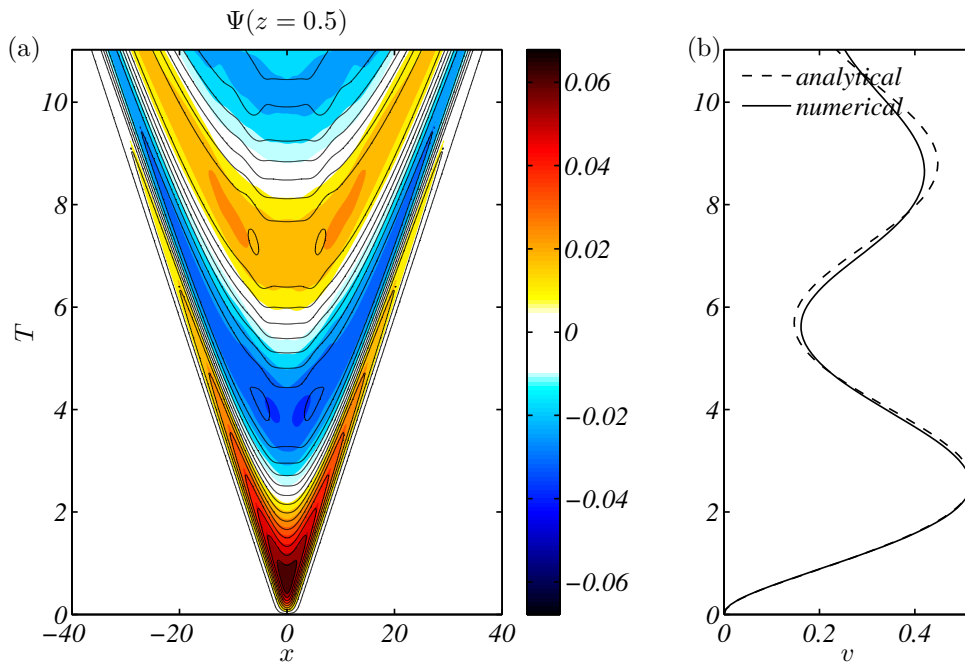


Fig. 3.16 Numerical solution to the fully non-linear equations for the unstrained non-frontogenetic case ($Ro = 4, F = 0.4, \delta = 0$) studied in §3.3.1. (a) Hovmöller of the streamfunction at $z = 0.5$ from the numerical model is shown in colour. The corresponding contours from the analytical solution (as in figure 3.7) are overlaid in black. (b) The maximum along-front velocity v as a function of time from the numerical (solid) and analytical (dashed) models.

models. Figure 3.16b displays a time series of the maximum along-front velocity in the two models. The agreement between the numerical and analytical solutions is excellent. The major difference in terms of the geostrophic adjustment process is that the near-inertial oscillations in the frontal zone (and thus in the along-front velocity) decay more rapidly in the numerical solution. In other words, energy is removed more rapidly from the frontal zone in the numerical solution, or equivalently, the generated waves have greater energy. Similar differences are observed for other parameter values, as will be described in Chapter 5.

Secondly, we consider the unstrained frontogenetic case ($Ro = 4, F = 1, \delta = 0$, ‘+’ in figure 3.3) for which the analytical solution was shown in figures 3.8 and 3.9. Figure 3.17 displays time series of the maximum along-front (v ; 3.17a) and vertical (w ; 3.17c) velocities from the analytical (dashed) and numerical (solid) models up to the critical time. The time taken to form a discontinuity is slightly longer ($T_c = 1.41$) in the numerical model compared with the analytical ($T_c = 1.32$) — something also noted by Blumen & Williams (2001) in their numerical study of the zero PV ($F \rightarrow \infty$) case. However, figure 3.17 indicates that the analytic solution remains accurate up until near to the critical time. The numerical

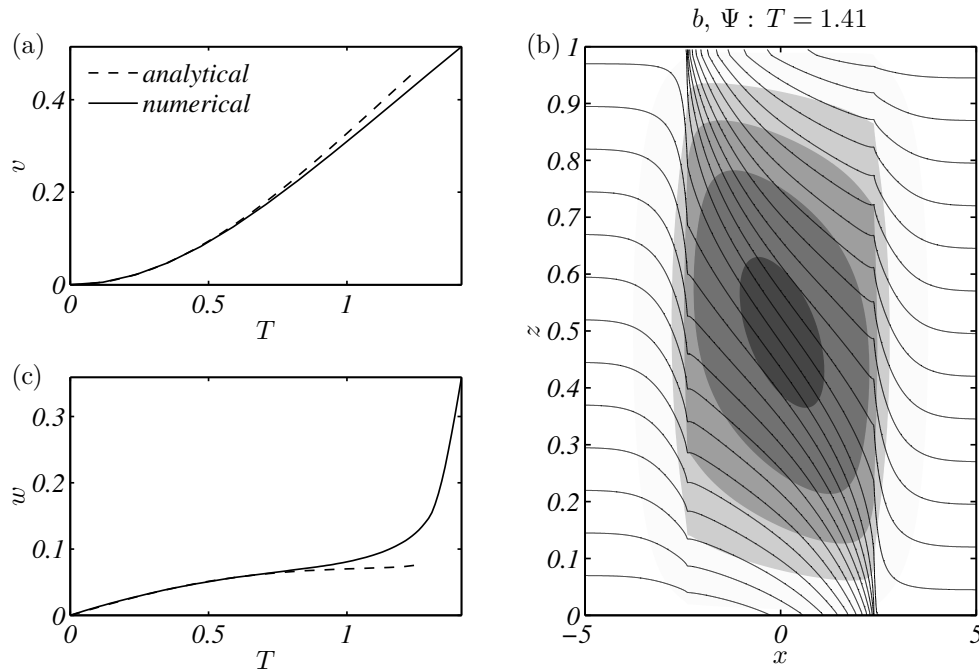


Fig. 3.17 Numerical solution to the fully non-linear equations for the unstrained frontogenetic case ($Ro = 4, F = 1, \delta = 0$) studied in §3.3.1. Left: Time series of (a) maximum along-front velocity v and (c) maximum vertical velocity w from the numerical (solid) and analytic (dashed) models, up to the critical time in each model. (b) The buoyancy field (lines) and streamfunction (shaded) from the numerical model just prior to the critical time (the equivalent plot for the analytic model is shown in figure 3.8).

buoyancy field and streamfunction just prior to the critical time are shown in figure 3.17b for comparison with the analytical solution in figure 3.8. The main difference is the formation of sharp ‘kinks’ in the buoyancy contours associated with intense vertical flow directly above the surface fronts — this effect will be discussed in more detail in Chapter 5.

Lastly, we consider the strained frontogenetic case ($Ro = 0.4, F = 0.8, \delta = 0.1$, unbalanced initial conditions) for which the analytical solution was shown in figures 3.13, 3.14 and 3.15. Figure 3.18 displays time series of the maximum along-front (v ; 3.18a) and vertical (w ; 3.18c) velocities from the analytical (dashed) and numerical (solid) models up to the critical time. The models are essentially indistinguishable up until about 80% of the critical time ($T \sim 20$), at which point the numerical model vertical velocity increases relative to the analytic. The numerical buoyancy field and streamfunction just prior to the critical time are shown in figure 3.18b for comparison with the analytical solution in figure 3.13 (upper two panels). Overall, the agreement is excellent.

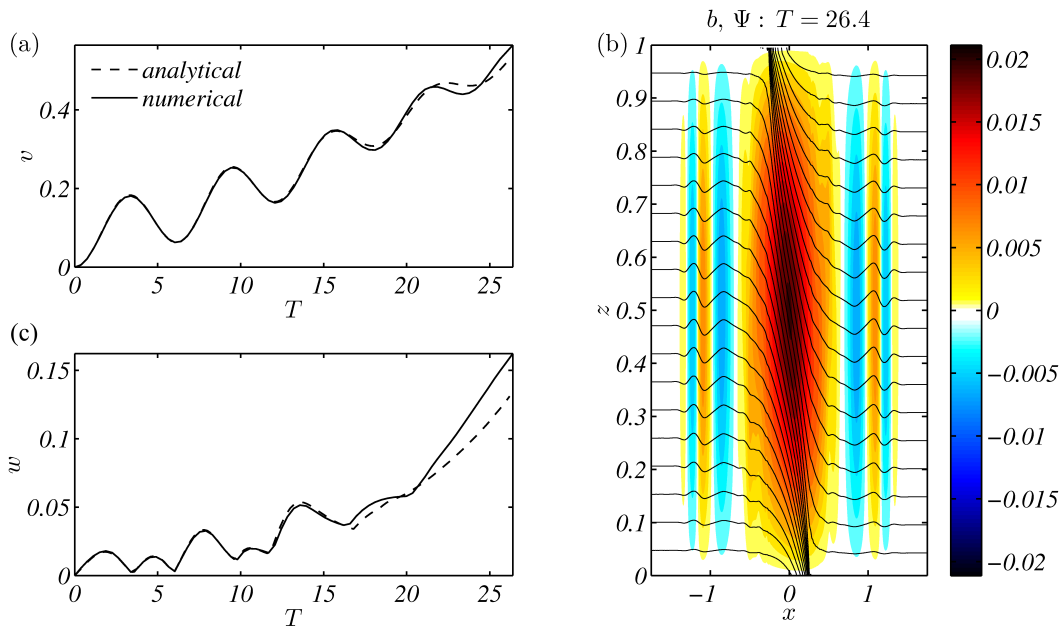


Fig. 3.18 Numerical solution to the fully non-linear equations for the strained frontogenetic case ($Ro = 0.4, F = 0.8, \delta = 0.1$) studied in §3.3.2. Left: Time series of (a) maximum along-front velocity v and (c) maximum vertical velocity w from the numerical (solid) and analytic (dashed) models, up to the critical time in each model. (b) The buoyancy field (lines) and streamfunction (shaded) from the numerical model just prior to the critical time (the corresponding fields for the analytic model are shown in figure 3.13a&b).

3.5 Discussion

While the problems of deformation-forced frontogenesis and spontaneous frontogenesis have previously been studied mostly in isolation, the solution presented herein emphasises the similarity of the two problems. The generalised model formulated in Chapter 2 unifies the HB model which applies at large time (or small Rossby numbers) where the strain-induced flow dominates, and the B00 model which applies at small time (or large Rossby numbers) where the oscillatory response of the system dominates. This generalisation of the two models is most apparent in the predictions of critical time emerging from each model. Figure 3.19 displays the predicted critical time as a function of Rossby number for two Froude numbers (figure 3.19a; $F = 1$, and 3.19b; $F \rightarrow \infty$) for the generalised model formulated herein (solid), the HB model (dashed) and the B00 model (dot-dashed). As expected, the generalised solution approaches the corresponding HB solution in the small Rossby number limit and the B00 solution in the large Rossby number limit. The transition between the two solutions occurs near the critical Rossby number ($Ro_c = 2.03$ in the case shown). The generalised model thus provides a framework to study forced frontogenesis beyond the limits

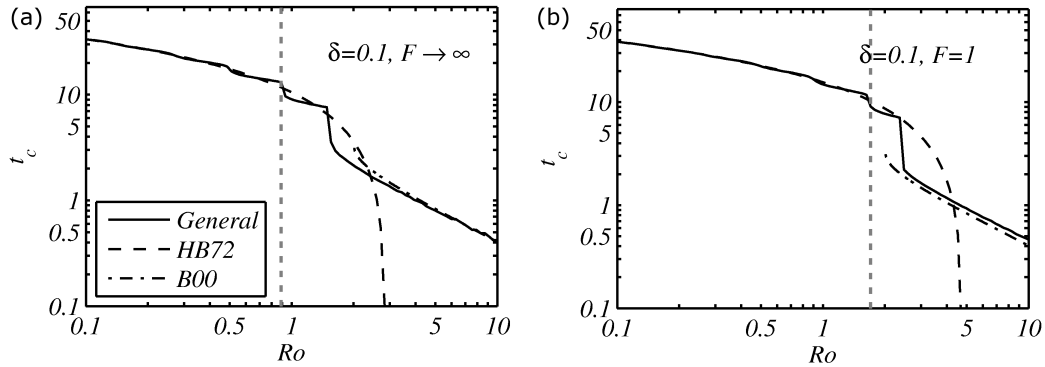


Fig. 3.19 The variation of the non-dimensional critical time with Rossby number Ro for Froude numbers of (a) $F \rightarrow \infty$ and (b) $F = 1$ for a strains of $\delta = 0.1$, as derived from the generalised model. The critical times predicted by the HB model (dashed) and B00 model (dot-dashed) are also shown. The assumed initial conditions are zero motion ($u = v = w = 0$) and an error function buoyancy profile (3.15) with critical Rossby number $Ro_c = 2.03$. The Rossby number at which the error in the HB prediction of the critical time first exceeds 10% is shown by a vertical dashed line. Since the size of the Rossby number controls the magnitude of the (near-inertial) oscillations in the frontal zone, a small increase in the Rossby number can cause the critical time to decrease by an entire inertial period, giving rise to the step-like features seen in the figure.

of the semigeostrophic approximation made by HB — that is, in cases where both strain and oscillatory effects are important.

In this chapter we also determined the non-linear, time-dependent, analytic solution for the response of an initially motionless, uniformly stratified, rotating fluid to an unbalanced horizontal buoyancy gradient — that is, the uniform PV mass imbalance problem. Previously, only the adjusted state for this problem had been analytically determined (Blumen & Wu, 1995). The key innovation allowing the solution to be found was the inclusion of an explicitly time dependent anomaly term in the buoyancy field which encapsulates the extra complexity of uniform PV as compared with zero PV flow — or more generally, it becomes significant when the scale of the flow is small compared with the Rossby radius. The buoyancy anomaly accounts for the interaction between the pressure and momentum fields (the interchange of potential and kinetic energies) that permits the propagation of inertia-gravity waves. These waves are responsible for the adjustment of the initial mass imbalance to a geostrophically balanced state (which agrees with that derived by Blumen & Wu, 1995). There are three major results emerging from this solution.

Firstly, the existence of an adjusted state does not imply attainability of that state, since the maximum flow gradients and minimum frontal width occur during the transient phase of

the motion prior to the generation of inertia-gravity waves and associated energy loss from the frontal zone (as suggested by Plougonven & Zeitlin, 2005). Second, we determined (see figure 3.3) whether a frontal discontinuity will result for a given set of flow parameters (i.e. a given Rossby and Froude number). Our criterion is consistent with previous frontogenesis predictions empirically determined from numerical simulations (Neves, 1996). Figure 3.3 demonstrates that the formation of a discontinuity is intrinsically linked to the propagation properties of inertia-gravity waves. Stronger background stratification (smaller Froude number) implies faster wave propagation and thus more rapid energy loss from the frontal zone, and a greater initial imbalance (larger Rossby number) is therefore required to generate a discontinuity.

Third, our model provides a useful description of the dynamics of small scale geostrophic adjustment. The key feature that emerges from this analysis is that an initial mass imbalance triggers the production of outward propagating inertia-gravity waves. The high wavenumber modes leave the imbalance region relatively quickly, leaving behind the near-inertial lower wavenumber modes and slowly decaying near-inertial oscillations (e.g. see the Hovmöller plot in figure 3.7). The extent and speed of geostrophic adjustment of the buoyancy field during this process is dependent on the size of the Burger number.

The dynamics of inertia-gravity wave generation and propagation in the presence of a strain field were also examined. In contrast to the unstrained case, where waves propagate freely out to infinity, in the strained case waves generated by the initial conditions are trapped for a finite period of time as non-decaying inertial oscillations in the frontal zone. The trapping time is greater for larger values of strain and smaller Burger numbers. Upon release the waves propagate away from the front with a decaying amplitude, shrinking horizontal scale, and ever-decreasing propagation speed. The waves become stationary at a fixed distance from the front, where their outward group velocity matches the inward strain flow velocity. These dynamics are graphically summarised by the Hovmöller plot shown in figure 3.15.

Here we have focussed on the small strain limit, $\alpha \ll f$. In the next chapter we will investigate the spontaneous generation of waves by the flow for larger values of strain.

Chapter 4

Spontaneous wave generation during frontogenesis: analytic solutions

Here we employ the generalised model developed in Chapter 2 to describe the spontaneous emission of inertia-gravity waves from an initially geostrophically balanced front subjected to a time-varying horizontal strain. Inertia-gravity waves are generated via two distinct mechanisms: acceleration of the large scale flow and frontal collapse. Wave emission via frontal collapse is predicted to be exponentially small for small values of strain but significant for larger strains. Time-varying strain can also generate finite amplitude waves by accelerating the cross-frontal flow and disrupting geostrophic balance. In both cases waves are trapped by the oncoming strain flow and can only propagate away from the frontal zone when the strain field weakens sufficiently, leading to wave emission that is strongly localised in both time and space.

4.1 Introduction

Inertia-gravity waves (IGWs) are of fundamental importance in both the atmosphere and ocean due to their ability to transfer significant amounts of energy, momentum and other tracer properties. For example, in the ocean IGWs provide a mechanism for energy loss from large scale flows (e.g. Williams *et al.*, 2008) and can drive significant vertical mixing (e.g. Polzin, 2010). In the atmosphere, these waves have the ability to initiate and modulate convection (Zhang, 2004). Substantial sources of IGWs include flows over topography and convection in both the atmosphere and ocean (e.g. Nikurashin *et al.*, 2014; Plougonven & Zhang, 2014; Waterman *et al.*, 2014), as well as direct forcing by wind stresses at the ocean surface (Wunsch & Ferrari, 2004). Recent work suggests that fronts and their associated geostrophic

jets are a further important source of IGWs (e.g. Alford *et al.*, 2013; Plougonven & Zhang, 2014). Despite the importance of IGWs, their generation mechanisms at fronts are still not fully understood. There are two broad mechanisms of IGW generation at fronts widely discussed in the literature: geostrophic adjustment (e.g. Blumen, 1972, 2000; Ou, 1984; Rossby, 1938; Tandon & Garrett, 1994, as discussed in Chapter 3 herein) and spontaneous emission (e.g. Danioux *et al.*, 2012; Ford *et al.*, 2000; Plougonven & Zhang, 2007; Viudez & Dritschel, 2006). In geostrophic adjustment, the system is instantaneously displaced from geostrophic balance and then adjusts back towards this state, releasing energy in the form of IGWs in the process (e.g. Blumen, 1972). On the other hand, spontaneous emission involves the generation of IGWs from an initially ‘balanced’ (i.e. long timescale, slow manifold) flow. Geostrophic adjustment relies on an imposed external influence or ‘initial condition’, whereas spontaneous emission is a fundamental transient feature of the dynamical equations. The process of spontaneous emission is therefore expected to be ubiquitous in the ocean and atmosphere and is arguably more important in terms of the global wave field and associated momentum fluxes (Plougonven & Zhang, 2014). Unfortunately, spontaneous wave emission is also far more difficult to quantify since, by definition, it involves the breakdown of the balanced approximations (e.g. geostrophy, quasigeostrophy, semigeostrophy, etc.) that form the basis of our understanding of most geophysical flows (Vanneste, 2013). Zhang (2004), among others, proposed that the mechanism of spontaneous emission can be considered as a generalisation of geostrophic adjustment, called ‘balance adjustment’. In this paradigm, departures from a suitably balanced state are treated as internally forced imbalances to which the system adjusts via the emission of waves, as per the classical geostrophic adjustment scenario. As such, the two mechanisms of wave generation at fronts, geostrophic adjustment and spontaneous emission, may be closely related — a topic investigated further in this chapter.

Baroclinic instability is a major source of spontaneous IGWs in both the atmosphere and ocean (Vanneste, 2013), which exhibit large scale baroclinic waves and eddy fields. Sharp horizontal buoyancy gradients (fronts) and strain flows are ubiquitous features of these fields. A convergent strain can act to drive frontogenesis (as described in prior chapters) and ultimately cause a breakdown of geostrophic balance (Juckes, 1994) and the generation of IGWs as the frontal scale collapses (Snyder *et al.*, 1993). In addition, the eddies are themselves naturally time-dependent according to a ‘baroclinic life-cycle’ and thus cause the surrounding strain field to accelerate and decelerate with time. Eddy fields consequently exhibit highly variable strains in time and space, and this variability can itself generate IGWs even in the absence of a sharp frontal gradient (Snyder *et al.*, 1993; Vanneste, 2013; Viudez & Dritschel, 2006). Williams *et al.* (2008) measured the generation of IGWs during

a baroclinic life-cycle in a rotating two-layer annulus experiment at small (~ 0.1) Rossby numbers. They found that the baroclinic eddies leak $\sim 1\%$ of their energy to IGWs each inertial cycle. Alford *et al.* (2013) obtained a similar order-of-magnitude result for the energy loss via wave emission from an actively-strained, mesoscale front observed in the ocean mixed layer. Collectively, these studies suggest that wave generation at strained fronts within eddy fields may provide a significant contribution to the ocean energy budget.

As discussed in Chapter 1, given the complexity of fully three dimensional baroclinic instability, it has proven useful to use two-dimensional (2D) models to examine small scale flow evolution within a large scale eddy field. Hoskins & Bretherton (1972, hereafter, HB) introduced a 2D, rigid lid model to study the effect of convergent strain within a baroclinic wave on the evolution of a smaller scale buoyancy gradient (a front). As shown in §1.3.2, they derived an analytical solution for the secondary flow in the limit of small strain, often called the ‘semigeostrophic model’. The assumption of small strain and associated neglect of time derivatives causes IGWs to be filtered from the solution. While the semigeostrophic model is valid (and IGW generation negligible) for many flows, it breaks down for unbalanced initial conditions (as studied in Chapter 3) and strongly strained flows where the horizontal strain rate α is of similar order to the inertial frequency f ; one example is at submesoscale fronts in the ocean mixed layer (Shcherbina *et al.*, 2013).

Among its various applications, the HB solution is a convenient balanced state for the study of spontaneous wave emission. Ley & Peltier (1978) computed the neglected ‘unbalanced’ ageostrophic flow arising from the model and used it to force a correction to the HB solution. This correction was found to take the form of a packet of IGWs, which produced a pressure minimum at a fixed distance ahead of the front. Ley & Peltier proposed that such wave emission provides a mechanism for the formation of squall lines in the warm sector ahead of an advancing cold front — such squall lines are a common feature of atmospheric weather systems (e.g. Karan *et al.*, 2010). Garner (1989) and Snyder *et al.* (1993) studied the difference between the HB solution and numerical primitive equation models, and found it to be dominated by a field of largely stationary IGWs. These waves were attributed to three mechanisms: generation via the geostrophic adjustment of initial conditions of semigeostrophic balance (mechanism 1), implying the existence of some more balanced primitive equation solution (Garner, 1989), generation via a time-dependent strain field (mechanism 2), and generation via frontal collapse (mechanism 3). Griffiths & Reeder (1996) and Reeder & Griffiths (1996) obtained similar results from their numerical model of upper-level frontogenesis, and in particular, found wave generation becomes more pronounced as frontogenesis varies rapidly. Despite these efforts, a theoretical model for

spontaneous wave generation from this idealised 2D system via the above mechanisms (2, 3) is still lacking.

The generalised model developed in Chapter 2 provides an ideal framework to formulate such a theoretical model since unlike HB, no assumption was made as to the smallness of the cross-front acceleration. In the previous chapter we focussed on the breakdown of the HB model due to unbalanced initial conditions at small strains, $\delta = \alpha/f = 0.1$, and the attendant wave generation via geostrophic adjustment (mechanism 1). We showed that in this limit the generalised model solution is composed of an IGW field driving oscillations about a time-varying mean state given by the HB solution. The strain flow traps the generated IGWs in the frontal zone and drives the decay of the wave amplitude with time.

Here we will instead consider the breakdown of semigeostrophy associated with larger strain fields, but purely balanced initial conditions. Since semigeostrophic balance breaks down for large strain, the requirement of balanced initial conditions will necessitate the use of a time-dependent strain field, such that the model can be initialised with zero strain in a geostrophically balanced state. The generalised model formulated in Chapter 2 also required an ad-hoc linearisation of the horizontal momentum equations. Here we will more rigorously consider the system via a scaling analysis of the governing equations, assuming balanced initial conditions, and determine the parameter values for which the neglect of the non-linear terms is valid. We find that the neglected non-linear terms are small compared to the leading order retained terms wherever the product of the Rossby number and non-dimensional strain, $Ro\delta$, is sufficiently small. Two subsets of the generalised model will be investigated. Firstly, the limit of small strain δ , corresponding to the semigeostrophic solution of HB which does not permit IGWs. Secondly, the limit of small Rossby number Ro , which permits large strain and accurately describes second order effects such as wave generation. However in contrast to Chapter 3, here we will only consider ‘spontaneously generated’ waves, which we define in the present context as waves generated at an initially balanced front subject to an imposed convergent strain. Such waves will arise both through time variation of the strain field even for an arbitrarily weak buoyancy gradient (mechanism 2), as well as for a constant strain in the limit of frontal collapse (mechanism 3). The spatial structure of the generated wave field in each case is strongly influenced by the effect of the large scale strain flow on wave propagation, as argued by Plougonven & Snyder (2005).

The layout of the chapter is as follows. In §4.2 we perform a scaling analysis to identify the parameter values for which the non-linear terms in the governing equations may be neglected. In §4.3 we consider the special case of zero potential vorticity (PV) to show that time variation in the large scale strain field drives inertial oscillations about the geostrophically balanced state. Then, in §4.4 the more general case of uniform PV flow is solved for constant

strain using a Green's function method. We demonstrate the tendency of the flow to develop a strong stationary wave field as the front collapses, and separate the flow into a wave and secondary circulation component. In §4.5 we consider the most general case of uniform PV and a time-dependent strain field, using the results from previous sections. Lastly, in §4.6 we discuss the implications of our results in terms of frontal evolution and energy loss from balanced flows.

4.2 Scaling analysis

As noted above, unlike Chapter 3 here we will only consider initial conditions that are appropriately 'balanced' such that the time variation in the solution is controlled by the strain forcing, implying that the time derivative ∂_T 'scales with' the strain δ — here denoted as $\partial_T \sim \delta$ — rather than the natural wave response of the system. Applying this result and relations (2.27) we can write scales for the velocity field and streamfunction as

$$v \sim \Phi, \quad \psi \sim \delta \Phi, \quad (4.1)$$

assuming $\phi \sim \Phi$. In determining further scales we will neglect any non-linear terms, and then employ the linearised scales to determine under what conditions the neglect is valid. Using (4.1), scales for the velocities $u = \partial_z \psi$ and $w = -\partial_x \psi$ may be written as

$$u \sim \delta \Phi, \quad w \sim \delta e^{\beta(T)} \Phi, \quad (4.2)$$

since $\partial_x \sim e^{\beta(T)}$. Substitution of (4.2) into the x -momentum equation (1.12a) yields a scale for the ageostrophic velocity,

$$v_a \sim \delta^2 \Phi, \quad (4.3)$$

neglecting the contribution of the non-linear advection term. Using these results it may be shown that the non-linear terms \mathcal{N} (2.31) scale as

$$\mathcal{N} \sim Ro \delta^2 e^{\beta(T)} \Phi^2, \quad (4.4)$$

the linear forcing \mathcal{F} (2.30) as

$$\mathcal{F} \sim Ro e^{\beta(T)}, \quad (4.5)$$

and the left-hand side (LHS) of (2.29) as

$$\text{LHS} \sim \Phi + \delta^2 \Phi + Bu^2 e^{2\beta(T)} \Phi. \quad (4.6)$$

Neglecting \mathcal{N} , the magnitude of ϕ must be determined by a balance between the linear forcing (4.5) and the LHS (4.6),

$$\Phi \sim \frac{Ro e^{\beta(T)}}{1 + \delta^2 + Bu^2 e^{2\beta(T)}}. \quad (4.7)$$

We can now determine under what conditions the neglect of the non-linear terms is valid. For a first estimate of model validity we require that the summed magnitude of the linear terms (LHS) greatly exceeds that of the neglected non-linear terms; that is,

$$(1 + \delta^2 + Bu^2 e^{2\beta(T)}) \Phi \gg Ro \delta^2 e^{\beta(T)} \Phi^2, \quad (4.8)$$

or substituting (4.7),

$$\mathcal{E} = \frac{Ro^2 \delta^2 e^{2\beta(T)}}{(1 + \delta^2 + Bu^2 e^{2\beta(T)})^2} \ll 1, \quad (4.9)$$

where \mathcal{E} is a measure of the relative fractional error in neglecting the non-linear terms. Thus, for the neglect of the non-linear terms to be valid at time zero, we must have

$$Ro^2 \delta^2 \ll (1 + \delta^2 + Bu^2)^2. \quad (4.10)$$

In other words, the product of Ro and δ must be sufficiently small the model to be valid at time zero. The relative error \mathcal{E} will be less for larger Bu . Equation (4.10) represents the weakest possible limit on model validity. If the leading order terms on the left hand side of (2.29) balance the forcing such that the scaling in (4.10) holds, then the large scale circulation predicted by the model should be accurate, but smaller amplitude features such as higher mode waves may not be well described by the model. A more stringent constraint on model validity can be obtained by requiring that the magnitude of the *smallest* linear term (i.e. in (4.6)) exceeds that of the largest neglected non-linear term:

$$\delta^2 \Phi \gg Ro \delta^2 e^{\beta(T)} \Phi^2, \quad (4.11)$$

or substituting the scale for ϕ (4.7),

$$\frac{Ro^2 e^{2\beta(T)}}{1 + \delta^2 + Bu^2 e^{2\beta(T)}} \ll 1. \quad (4.12)$$

Thus, for the neglect of the non-linear terms to be valid at time zero in this more stringent limit, we must have

$$Ro^2 \ll 1 + \delta^2 + Bu^2. \quad (4.13)$$

In other words, the Rossby number Ro must be sufficiently small for validity at time zero, where the term ‘validity’ in this more stringent limit implies that both the large scale circulation and smaller-scale features will be well described by the model.

We have derived constraints on the parameter values for the validity of the neglect of the non-linear terms *at time zero*, assuming suitably balanced initial conditions. We now consider the validity at later times. Firstly, note that the coordinate system (and model) breaks down when the inverse Jacobian J^{-1} of the momentum coordinate transformation (see table 2.2) vanishes:

$$J^{-1} = 1 - Ro e^{\beta(T)} \frac{\partial v}{\partial X}. \quad (4.14)$$

The vanishing of J^{-1} implies the formation of a discontinuity in velocity and buoyancy fields. The inverse Jacobian vanishes when ϕ grows sufficiently large; that is, from (4.14),

$$\Phi \sim Ro^{-1} e^{-\beta(T)}, \quad (4.15)$$

using the scales derived above. We observe that the constraint on model validity (4.11) in the more stringent limit discussed above may be rewritten as,

$$\Phi \ll Ro^{-1} e^{-\beta(T)}. \quad (4.16)$$

Thus, if (4.13) holds at $T = 0$, $\Phi \ll Ro^{-1}$, then the model is valid except near the time or location of discontinuity formation, when $e^{\beta(T)} \gg 1$. Similarly, the weak constraint on model validity (4.8) may be rewritten,

$$\Phi \ll Ro^{-1} e^{-\beta(T)} (1 + \delta^{-2} (1 + Bu^2)). \quad (4.17)$$

Thus, given the initial condition (4.10) is satisfied, the model is valid except near the time or location of discontinuity formation. Further, if δ is small, then the neglect of the non-linear terms will be valid even in the limit of discontinuity formation.

4.2.1 Limits of the generalised model

Given the above scaling analysis, for suitably balanced initial conditions the neglect of the non-linear terms in (2.29) is valid — in the sense that these terms are small compared to leading order linear terms — as long as the product $Ro \delta$ is sufficiently small, as defined by (4.10). A vital feature of the generalised model is that it permits the generation of inertia-gravity waves (as a result of the explicit time derivative in 2.29). The weak constraint on model validity (4.10) ensures that the large scale secondary circulation associated with

frontogenesis is well described, but second order effects, such as wave generation, may not be. The relative size of neglected effects may be estimated from (4.9). If we instead consider the limit of small Rossby number, defined by (4.13), both first and second order flow will be well described by the generalised model — neglected effects are strictly third order. The physical interpretation of this small Rossby limit is that of an initially weak front, somewhat analogous to small-step limit of shallow water free-surface height adjustment problems. The front is only weak at early times and will sharpen with time as the frontal width contracts (e.g. the Eulerian Rossby number is $Ro_E = Ro_J$, as discussed previously), although the above scaling arguments suggest that the generalised model may break down where $O(Ro_E) = 1$. Perhaps the most important feature of this small Rossby limit is that it permits an accurate analytical description of wave generation occurring at a strained front, since the included time derivative and strain terms in (2.29) that are associated with wave generation are guaranteed to exceed neglected terms in this limit.

One important subset of the generalised model is the limit of weak strain, $\delta^2 \ll 1$. In this limit, the generalised model equation (2.29) may be further simplified by the neglect of the $O(\delta^2)$ terms on the left-hand side, yielding

$$\left[\frac{\partial^2}{\partial Z^2} + Bu^2 e^{2\beta(T)} \frac{\partial^2}{\partial X^2} \right] \phi = \mathcal{F}, \quad (4.18)$$

where \mathcal{F} is given by (2.30), as previously. This derivation assumes that the time variation in the strain is also small, $\delta'(T) \ll 1$. Equation (4.18) is identical to the ‘HB model’ of frontogenesis (Hoskins & Bretherton, 1972). The neglect of the $O(\delta^2)$ terms (including the time derivative) in (2.29) filters inertia-gravity waves from the solution. As δ is small, the relative error \mathcal{E} associated with the neglected non-linear terms (4.9) will be small. Given this reduction of our model to the HB model in the limit of small strain, our model can be described as a generalisation of the HB model permitting large strain rates and IGWs. The physical interpretation of the weak-strain limit is that the large scale flow is strongly affected by rotation, or $Ro_L^2 \ll 1$, where Ro_L is the Rossby number of the large scale flow. While we model the (dimensional) large scale flow as $(-\alpha x, \alpha y, 0)$ in the region of the front, this is only an approximation to a flow that would have significant spatial and temporal variability. For instance, in the atmosphere the ‘large scale flow’ might be associated with locally convergent regions of a global-scale baroclinic wave (e.g. Hoskins, 1982). In the ocean, the ‘large scale flow’ could be associated with convergence within a mesoscale eddy field (e.g. Thomas *et al.*, 2008). In each case δ is the Rossby number describing the dynamics of that spatially and temporally varying larger scale flow field. For a global baroclinic wave in the atmosphere or a mesoscale ocean eddy field $Ro_L \sim 0.1$ and this $\delta^2 \ll 1$ limit is valid.

Given the influence of the Rossby number Ro on the validity of the generalised model, it is useful to consider the effect of the Rossby number on the dynamics. As already observed, a larger Rossby number Ro implies a stronger initial front and consequently more rapid discontinuity formation and model breakdown. Furthermore, the Rossby number appears in the governing equation (2.29) in two places: (i) in the momentum coordinate transformation, $X = e^{\beta(T)}(x + Ro v)$, and (ii) in the forcing \mathcal{F} on the right-hand side (defined by 2.30). As shown in Chapter 3, the appearance of the Rossby number in the coordinate transformation is related to the tilting/slumping of the front during frontogenesis; the position of the front on the boundary will be $O(Ro)$ by the time of model breakdown. A small Rossby number thus implies that the front remains relatively upright during frontogenesis due to rotational effects dominating over the gravity-driven tendency for frontal slumping. The Rossby number in the forcing term \mathcal{F} acts to scale the amplitude of the flow response to the applied strain. As expected, stronger fronts lead to a larger amplitude secondary circulation.

Before proceeding further and solving the generalised model in specific cases, we can gain significant insight into the dynamics from direct examination of the PDE (2.29) with $\mathcal{N} = 0$. Using the fact that ϕ must vanish on the boundaries at $Z = 0, 1$ we can write ϕ as a sum of vertical sine modes,

$$\phi(X, Z, T) = \sum_{n=1}^{\infty} \hat{\phi}(X, n, T) \sin n\pi Z. \quad (4.19)$$

Substituting (4.19) into (2.29) we obtain,

$$\left[\frac{\partial^2}{\partial T^2} + 1 - \delta(T)^2 + \delta'(T) - \left(\frac{Bu}{n\pi} \right)^2 e^{2\beta(T)} \frac{\partial^2}{\partial X^2} \right] \hat{\phi}(X, n, T) = Ro A_n e^{\beta(T)} b'_0(X), \quad (4.20)$$

with A_n defined as

$$A_n = \frac{2(-1 + (-1)^n)}{n^3 \pi^3}, \quad (4.21)$$

Equation (4.20) is hyperbolic (wave-like) for all n so long as $\delta \neq 0$ and $Bu \neq 0$. While we will not attempt to solve (4.20) analytically at this point, we can readily write down the equations for the characteristics,

$$\chi_{\pm} = e^{-\beta(T)} \left(\chi_0 \pm \frac{Bu}{n\pi} \int_0^T e^{\beta(T')} dT' \right), \quad (4.22)$$

defined here in terms of the regular momentum coordinate, $\chi = x + Ro v = e^{-\beta(T)} X$, which equals the Eulerian coordinate x at mid-depth (since $v = 0$ at $Z = 0.5$). The region between

the plus (χ_+) and minus (χ_-) characteristics is the *region of influence* of χ_0 , and indicates the area over which amplitude/energy associated with vertical mode n , and initially at location χ_0 , has spread by time T . In the case of a constant strain δ the characteristics from (4.22) become

$$\chi_{\pm}^{\delta=const.} = e^{-\delta T} \chi_0 \pm \frac{Bu}{n\pi\delta} (1 - e^{-\delta T}). \quad (4.23)$$

Thus, at constant strain, the region of influence of a given χ_0 is

$$\chi_0 e^{-\delta T} - \frac{Bu}{n\pi\delta} \leq \chi \leq \chi_0 e^{-\delta T} + \frac{Bu}{n\pi\delta}, \quad (4.24)$$

at time T . If we now consider the limit of infinite time, $T \rightarrow \infty$, then region of influence for χ_0 becomes

$$-\frac{Bu}{n\pi\delta} \leq \chi \leq \frac{Bu}{n\pi\delta}, \quad (4.25)$$

assuming that $\delta > 0$. Since (4.25) applies for any χ_0 , it implies that the solution ϕ is identically zero for $|\chi| > Bu/(n\pi\delta)$ in the limit $T \rightarrow \infty$ for an appropriate choice of boundary conditions (see Appendix A.2 for the detailed derivation). This ‘confinement’ result will prove important in formulating the general solution to (2.29) in §4.4.

The fact that at large enough time the frontal circulation is entirely confined within the region $|\chi| \leq Bu/(n\pi\delta)$, is a powerful result. It gives a fundamental scale for the width of frontal circulation at large time. This width decreases with increasing strain, δ , implying that for large strains we can expect significantly larger vertical velocities. The edge of the confinement region is equivalent to the points at which the group speed of the fastest inertia-gravity waves of vertical mode n , $\max c_g = Bu/(n\pi)$, equals the strain flow speed at mid-depth, $\delta\chi$. In other words, $\chi = \pm Bu/(n\pi\delta)$ are the points at which outward propagating wave packets are expected to stagnate in the strain flow. Thus, the convergent strain is effectively trapping the circulation within the region of possible wave propagation. By contrast, in the infinite time limit of the HB model, which doesn’t include waves, there is no equivalent confinement effect, and the amplitude of the solution is finite everywhere. We will discuss these differences between the generalised and HB models in more detail when we formulate the general solution in §4.4.

In the following sections we examine in detail the dynamics of frontogenesis and wave generation using the generalised model derived in Chapter 2. We focus on parameter values corresponding to the small Rossby limit (4.13) where the scaling analysis indicates the generalised model will be most accurate.

4.3 ‘Spontaneous’ inertial oscillations in zero PV flow

It is useful to first examine the limit of zero PV where the equations greatly simplify. The assumption of zero PV requires that the background stratification N^2 vanish and thus $Bu = (NH)/(fL) \rightarrow 0$. This limit allows the isolation of spontaneous wave generation via acceleration of the large scale flow from other mechanisms of generation that occur simultaneously at non-zero PV. The zero PV limit is also of practical interest since the PV in ocean and atmosphere boundary layers is often close to zero. With $Bu \rightarrow 0$, (2.29) with $\mathcal{N} \equiv 0$ becomes simply

$$\left[\frac{\partial^2}{\partial T^2} + 1 - \delta(T)^2 + \delta'(T) \right] \frac{\partial v}{\partial Z} = Ro b'_0(X) e^{\beta(T)}, \quad (4.26)$$

written here for convenience in terms of the along-front shear. The geostrophic component of this shear may be computed by substitution of the buoyancy ((2.21) with $Bu = 0$) into the thermal wind equation (2.12),

$$\frac{\partial v_g}{\partial Z} = Ro b'_0(X) e^{\beta(T)}. \quad (4.27)$$

Equation (4.27) represents the ‘directly forced’ part of the flow and is equivalent to the solution of the HB model (i.e. 4.18). Using (4.26) and (4.27) we can write down an equation for the time evolution of the ageostrophic part of the flow

$$\zeta''(T) + (1 - \delta(T)^2 + \delta'(T)) \zeta(T) = -2 \delta'(T) e^{\beta(T)}, \quad (4.28)$$

where,

$$\frac{\partial v_a}{\partial Z} = Ro b'_0(X) \zeta(T). \quad (4.29)$$

Consistent with the assumptions made in the model derivation (§4.2), we choose initial conditions of geostrophic balance with $v = v_g$ and $\partial_T v = 0$, or $\zeta(0) = \zeta'(0) = 0$. We therefore require a strain field with $\delta(0) = \delta'(0) = 0$ such that there is no forcing to the ageostrophic flow at time zero (i.e. the right-hand side of (4.28) vanishes). However, as the strain is turned on and $\delta'(T)$ becomes non-zero, ageostrophic flow is inevitably forced. As a simple example, consider applying a ‘pulse of strain’ to the system,

$$\delta(T) = \delta_0 \sin^2 \left(\frac{\pi T}{\tau} \right) H(\tau - T), \quad (4.30)$$

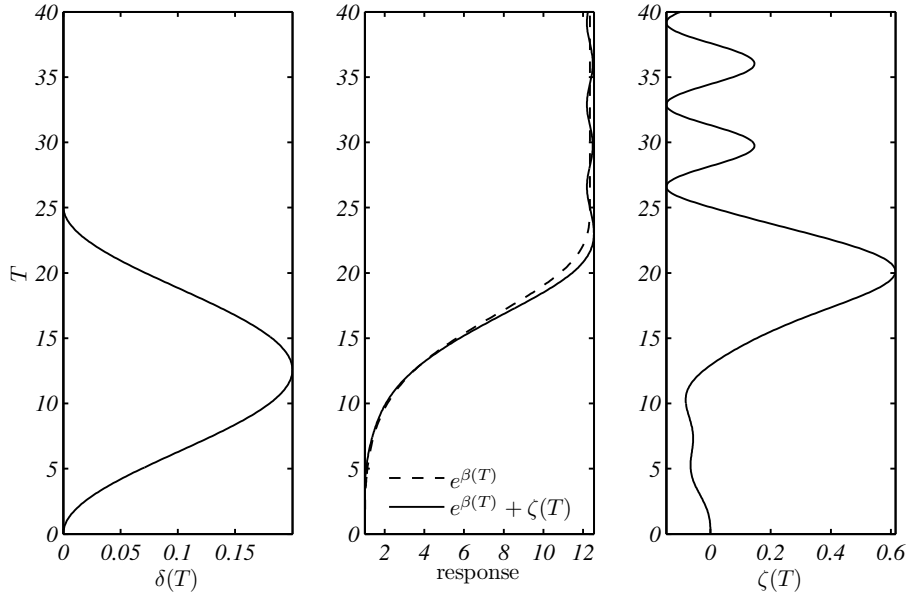


Fig. 4.1 The geostrophic and ageostrophic responses to a pulse of strain in zero PV flow. The strain $\delta(T)$ (left) is defined by (4.30) with $\delta_0 = 0.2$ and $\tau = 8\pi$. The time variation of the strain drives ageostrophic flow $\zeta(T)$ in the form of an oscillation about the geostrophic solution, $e^{\beta(T)}$.

where H is the Heaviside function. Such a strain profile could represent a region of convergence interior to an eddy field where the eddies evolve on a characteristic timescale τ . Figure 4.1 shows the time dependence of the solution for $\delta_0 = 0.2$ and $\tau = 8\pi$ (4 days) in terms of the ageostrophic part $\zeta(T)$, geostrophic part $e^{\beta(T)}$, and the full flow $e^{\beta(T)} + \zeta(T)$. The strain field from (4.30) is shown in the left-hand plot. The time variation in the strain forces ageostrophic flow (waves) which amplifies over time as the strain acts and the integrated strain $\beta(T)$ in (4.28) increases. The waves become exactly inertial and obtain a constant magnitude as the strain vanishes ($T = \tau$). In other words, for $T > \tau$ the net flow is composed of non-decaying inertial oscillations about the state of geostrophic balance — this end-state behaviour is identical to the behaviour of the Blumen (2000) zero PV model of frontogenesis. The key difference is that the Blumen (2000) model assumed *unbalanced* initial conditions, whereas here we have demonstrated a mechanism for the generation of inertial waves from purely balanced initial conditions.

The spatial and temporal separability of the solution (4.27, 4.29) implies that the generation of the inertial waves in this zero PV model is independent of the sharpness of the front; waves would be generated even with a linear buoyancy gradient (i.e. constant $b'_0(X)$). As such, the model provides an example of wave generation due to the acceleration (or transience) of the large scale flow (e.g. Vanneste, 2013; Viudez, 2007), rather than generation

via frontogenesis. Note that wave generation via this transience mechanism requires the imposed strain field to vary on a sufficiently fast timescale. Therefore, this mechanism by itself does not provide a complete model for spontaneous wave generation from a slowly varying balanced flow, since such a model would also require a description of the processes giving rise to the rapid time variation in the strain.

4.4 Constant strain

In the previous section we isolated the process of spontaneous IGW generation by acceleration of the large scale flow. In this section we wish to similarly isolate the process of spontaneous IGW generation via frontal sharpening, and as such will require δ to be constant here before returning to the more general case of time varying strain in §4.5.

The presence of a non-zero background stratification (non-zero PV) significantly complicates the situation compared with the zero PV case discussed above. As the strain field amplifies frontal gradients, the system is now able to adjust via the emission of inertia-gravity waves. Following Zhang (2004), the problem can be interpreted as one of continuous adjustment (on wave timescale $1/f$) to the applied strain (on timescale $1/\alpha$) and, unlike the zero PV case, geostrophic balance is no longer necessarily a sensible balanced state for the flow. Indeed, a balanced state may not even exist owing to the breakdown of timescale separation as $\delta = \alpha/f$ tends to 1 (e.g. McIntyre, 2009). We instead consider the flow field as being composed of two parts: a secondary circulation, as in HB, that is a directly forced response to the applied strain, and a wave field. In this section we have two main objectives. First, we seek to determine a generalised secondary circulation (GSC) that extends the HB secondary circulation to finite strain, and second, to quantify the size of the wave field in comparison to this ‘quasi-balanced’ secondary circulation.

The evolution of the frontal system in the generalised model is fully described by the PDE (2.29) with constant strain δ and $\mathcal{N} \equiv 0$. We seek a forced solution to the PDE of the form

$$\phi(X, Z, T) = \int_{-\infty}^{\infty} \phi_I((X - X_0) e^{-\delta T}, Z) b'_0(X_0) dX_0, \quad (4.31)$$

such that time-dependence in the solution only arises through the strain-driven contraction of the horizontal coordinate. This form of solution eliminates the propagating waves associated with initial conditions that were studied in Chapter 3. Equation (4.31) may be written more intuitively in terms of the regular momentum coordinate (e.g. as in Blumen, 2000),

$$\chi = X e^{-\delta T} = x + Ro v, \quad (4.32)$$

as

$$\phi(\chi, Z, T) = \int_{-\infty}^{\infty} \phi_I(\chi - \chi_0, Z) \frac{\partial}{\partial \chi_0} b_0(\chi_0 e^{\delta T}) d\chi_0, \quad (4.33)$$

The function $\phi_I(\chi, Z)$ in (4.33) is the time-independent impulse response, or Green's function, for the problem. We show in Appendix A.1 that the Green's function satisfies,

$$\left[\frac{\partial^2}{\partial Z^2} \left(\delta^2 \chi^2 \frac{\partial^2}{\partial \chi^2} + \delta^2 \chi \frac{\partial}{\partial \chi} + 1 - \delta^2 \right) + Bu^2 \frac{\partial^2}{\partial \chi^2} \right] \phi_I(\chi, Z) = Ro \underline{\delta}(\chi), \quad (4.34)$$

where $\underline{\delta}$ denotes the Dirac delta function. Given this impulse response is independent of time, time dependence only arises in the solution via the strain-driven contraction of the boundary buoyancy gradient. As indicated by (4.33), the solution at a given time is obtained by a convolution of the impulse response function with the boundary gradient at that time; time has thus been reduced to a parameter in the solution, as in the classical HB model. Note that the solution to the HB model of frontogenesis may be obtained from a similar convolution, where the HB impulse response $\phi_{I,HB}$ is defined by (4.34) with the $O(\delta^2)$ terms neglected:

$$\left[\frac{\partial^2}{\partial Z^2} + Bu^2 \frac{\partial^2}{\partial \chi^2} \right] \phi_{I,HB}(\chi, Z) = Ro \underline{\delta}(\chi). \quad (4.35)$$

In other words, (4.35) is equivalent to the classical Sawyer-Eliassen equation with the buoyancy gradient forcing set to a delta function. The generalised model equation (4.34), including the $O(\delta^2)$ terms, can thus be thought of as a large-strain generalisation of the Sawyer-Eliassen equation.

Apart from generating the full solution via (4.33), the impulse response functions defined by (4.34) also provide information about the long-time state of the system. As time progresses, any typical initially smooth boundary profile $b_0(\chi)$ will be squeezed towards a step, $b_0(\chi e^{\delta T}) \rightarrow H(\chi)$, where H is the Heaviside function. The gradient of the boundary profile therefore approaches a delta function, and thus the general solution from (4.33) will collapse towards the impulse response function. Specifically,

$$\begin{aligned} \lim_{T \rightarrow \infty} \phi(\chi, Z, T) &= \lim_{T \rightarrow \infty} \int_{-\infty}^{\infty} \phi_I(\chi - \chi_0, Z) \frac{\partial}{\partial \chi_0} b_0(\chi_0 e^{\delta T}) d\chi_0 \\ &= \int_{-\infty}^{\infty} \phi_I(\chi - \chi_0, Z) \underline{\delta}(\chi_0) d\chi_0 \\ &= \phi_I(\chi, Z). \end{aligned} \quad (4.36)$$

We will employ this result in §4.4.1 below to predict generic features of fronts at large-time from the impulse response functions.

4.4.1 Impulse response solution

Here we derive and physically interpret the impulse response $\phi_I(\chi, Z)$ defined by (4.34). The solution proceeds most readily if we consider ϕ_I as sum of vertical Fourier modes (similar to (4.19)) such that the homogeneous boundary conditions, $\phi_I(\chi, 0) = \phi_I(\chi, 1) = 0$, are satisfied. The PDE (4.34) in ϕ_I is then reduced to an ODE in $\widehat{\phi}_I$ for each vertical mode,

$$\left[(\chi^2 - \chi_s(n)^2) \frac{\partial^2}{\partial \chi^2} + \chi \frac{\partial}{\partial \chi} + \sigma^2 \right] \widehat{\phi}_I(\chi, n) = \frac{A_n Ro}{\delta^2} \underline{\delta}(\chi), \quad (4.37)$$

where A_n is defined as per (4.21),

$$\sigma = \frac{\sqrt{1 - \delta^2}}{\delta}, \quad \chi_s(n) = \frac{Bu}{n\pi\delta}, \quad (4.38)$$

and we assume that $\delta < 1$. It is further convenient to change the horizontal coordinate χ to

$$\varepsilon(\chi) = \sigma \arctan \frac{\chi}{\sqrt{\chi_s(n)^2 - \chi^2}}, \quad (4.39)$$

which transforms (4.37) to a very simple form,

$$\left[\frac{\partial^2}{\partial \varepsilon^2} - 1 \right] \widehat{\phi}_I(\chi(\varepsilon), n) = \frac{n\pi A_n Ro}{Bu\sqrt{1 - \delta^2}} \underline{\delta}(\varepsilon). \quad (4.40)$$

The boundary conditions on ϕ_I are that it must vanish infinitely far from the front, or $\widehat{\phi}_I \rightarrow 0$ as $\chi \rightarrow \pm\infty$. In Appendix A.2 we use the characteristics of the generalised model PDE (4.20) to show that, with these boundary conditions, the n^{th} vertical mode of $\phi(\chi, Z, T)$ vanishes in the region $|\chi| > Bu/(n\pi\delta)$ in the limit $T \rightarrow \infty$. Equation (4.36) implies that the same result must apply to the impulse response $\widehat{\phi}_I$. The boundary conditions on $\widehat{\phi}_I$ may also be verified by solving (4.37) in Fourier space (A.3) and taking the inverse Fourier transform numerically (e.g. see Chapter 6). The resulting $\widehat{\phi}_I$ is zero for $|\chi| > Bu/(n\pi\delta)$.

The physical reason for the sharp cut-off in amplitude at $\pm\chi_s(n)$ is associated with the dynamics of inertia-gravity waves (IGWs) in this strained, hydrostatic flow. The maximum energy propagation speed in the frontal system is the maximum group speed of IGWs, $\max c_g = Bu/(n\pi)$, as discussed earlier in the context of the characteristics (4.23). The waves responsible for the transfer of energy away from the source at the origin can only do so (at least approximately) in the region where their propagation speed exceeds the inwards strain flow speed. Since $\chi = \chi_s(n)$ is the location at which the strain flow magnitude first exceeds the maximum wave group speed for each mode n , the amplitude in vertical mode n can only spread out to this location. As in Chapter 3, we call the set of $\chi_s(n)$ the ‘stagnation

points' for each mode. The *sharp* cut-off in amplitude at these points is a result of us making the hydrostatic assumption in the derivation of the generalised model. If non-hydrostatic effects are included in the model, resulting in dispersion at high horizontal wavenumbers, then the sharp cut-off no longer occurs, and the impulse response tends smoothly to zero beyond the stagnation points. These non-hydrostatic dynamics will be discussed in more detail later (§6.2).

It is interesting to note that the problem in ε coordinates (4.40) is mathematically identical to that of calculating the geostrophically adjusted velocity for an initial step displacement in the free surface height in rotating shallow water, as studied by Gill (1976). Gill's equation 5.5 may be written as

$$\left(\frac{\partial^2}{\partial \varepsilon^2} - 1\right)v(\varepsilon) = v_0''(\varepsilon) - \eta_0'(\varepsilon), \quad (4.41)$$

where v is the steady state along-front flow, ε the horizontal coordinate, and v_0 and η_0 the initial velocity and height fields, respectively. With $v_0 = 0$ and η_0 equal to a unit-step, (4.41) is identical to (4.40), up to scaling by a constant. While Gill studied this problem in an infinite domain, the boundary conditions introduced above imply that the analogous shallow water flow is trapped between no-slip channel walls at $\varepsilon = \pm\sigma\pi/2$. The presence of a strain field in the frontogenesis problem may thus be thought of as constraining the flow between walls; as the strain tends to zero we have $\sigma \rightarrow \infty$ and so the 'walls' vanish.

Following Gill, it is straightforward to write down the exact solution to (4.40);

$$\widehat{\phi}_I(\chi, n) = \begin{cases} \frac{n\pi A_n Ro}{2Bu\sqrt{1-\delta^2}} \left[e^{-|\varepsilon|} - e^{-\frac{\pi\sigma}{2}} \frac{\cosh \varepsilon}{\cosh \frac{\pi\sigma}{2}} \right] & |\chi| < \chi_s(n) \\ 0 & |\chi| \geq \chi_s(n) \end{cases}. \quad (4.42)$$

The solution (4.42) is composed of two terms; the first, $e^{-|\varepsilon|}$, is the directly forced part (or particular solution) resulting from the applied impulse forcing and is the solution — vanishing at infinity in ε coordinates — that one would obtain in the absence of the constraint $|\varepsilon| \leq \sigma\pi/2$ (e.g. see equation 5.7 of Gill). However, with these 'walls' this part of the solution does not independently satisfy the boundary conditions. A second term, $\cosh \varepsilon$, corresponding to the wave (or homogeneous) solutions, must be introduced to satisfy the boundary conditions. We can understand the origin of this $\cosh \varepsilon$ term by consideration of the infinite domain shallow water problem where, as shown by Gill, the adjustment of the initial height displacement generates Poincare waves that propagate unimpeded away from the adjustment region. However, with the introduction of channel walls, the generated waves will instead reflect from the channel walls and set up a standing wave field in the channel. We can interpret the $\cosh \varepsilon$ part of the solution as corresponding to the time-averaged part of this standing wave field. The amplitude of this 'wave' term relative to the particular solution

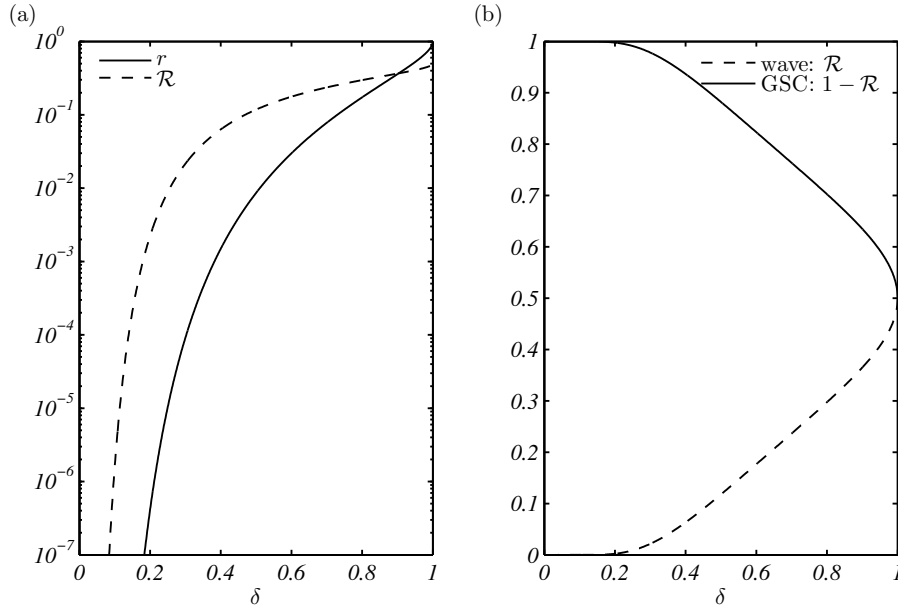


Fig. 4.2 (a) The relative amplitude r (4.43) of the ‘wave’ term in the generalised model solution (4.42), and the relative strength of wave generation \mathcal{R} (4.50), as a function of the strain δ . (b) The fraction of amplitude from an impulse forcing going into the wave, \mathcal{R} , and GSC, $1 - \mathcal{R}$, components of the flow for a given value of strain.

($e^{-|\varepsilon|}$) is

$$r = \frac{e^{-\frac{\pi\sigma}{2}}}{\cosh \frac{\pi\sigma}{2}}. \quad (4.43)$$

Equation (4.43) is a function only of the strain δ and is plotted in figure 4.2a. The figure shows that the ‘wave’ term is exponentially smaller than the particular solution for strains less than about $\delta = 0.2$, but becomes of comparable size for larger values of strain. This exponential smallness is an important feature which we will revisit below.

We now consider the problem of explicitly dividing the impulse response solution (4.42) into secondary circulation and wave components. The solution (4.42) is defined in terms of the function ϕ which, while mathematically useful, is difficult to physically interpret. However, using the relation between the streamfunction and ϕ (2.27c), and the definition of the impulse response solution (4.33), it may be shown that the streamfunction impulse response is defined by,

$$\psi_I(\chi, Z) = \delta \left(\chi \frac{\partial \phi_I}{\partial \chi} - \phi_I \right). \quad (4.44)$$

Substituting ϕ_I from the solution (4.42) into yields

$$\widehat{\psi}_I(\chi, n) = \frac{-\delta n\pi A_n Ro}{2Bu\sqrt{1-\delta^2}} \left[\underbrace{\left(e^{-|\varepsilon|} - r \cosh \varepsilon \right) (1 + |\chi| \varepsilon'(\chi))}_{\text{GSC}} + \underbrace{r \left(\chi \varepsilon'(\chi) \sinh \varepsilon + |\chi| \varepsilon'(\chi) \cosh \varepsilon \right)}_{\text{WAVE}} \right]. \quad (4.45)$$

Now consider dividing $\widehat{\psi}_I(\chi, n)$ into a generalised secondary circulation (GSC), accounting for the effects of finite strain, and a wave part. We require that the GSC part is finite everywhere in the domain and limits to the HB secondary circulation impulse response in the limit of small strain. We require that the wave component of streamfunction be proportional to r (4.50), as in the general solution for ϕ_I (4.42), such that it is exponentially small as $\delta \rightarrow 0$. The streamfunction impulse response in (4.45) has been divided into two components satisfying these requirements. Indeed, it may be shown that at small δ ,

$$\widehat{\psi}_{I,GSC}(\chi, n) = \widehat{\psi}_{I,HB}(\chi, n) + \mathcal{O}(\delta^3), \quad (4.46)$$

plus higher order terms, where

$$\widehat{\psi}_{I,HB}(\chi, n) = \frac{-\delta n\pi A_n Ro}{2Bu} e^{-\frac{n\pi}{Bu}|\chi|} \left(1 + \frac{n\pi}{Bu}|\chi| \right), \quad (4.47)$$

is the HB model impulse response (as may be determined from substituting the solution to (4.35) into (4.44)).

The exact separation of the circulation into GSC and wave components (4.45) is somewhat arbitrary, and the distinction between the components becomes more difficult to interpret at large values of δ . Nonetheless, the separation performed above has two important properties. First, in the limit of small strain, the GSC component limits to the secondary circulation from the HB model as indicated in (4.46), and as will be shown in §4.4.2, the wave component is well-described by stationary mode one inertia-gravity waves. Second, if the strain forcing turns off (i.e. a time-dependent strain, see §4.5), the propagating part of the resulting flow is entirely contained within the wave component. In light of these observations, the term ‘wave’ is invoked here to qualitatively describe the dynamical response of the system, even though the distinction between the wave and GSC parts of the flow may not be formally valid (particularly for large values of the strain).

The streamfunction impulse responses from the HB model, and the GSC and wave components from the generalised model, are shown in figure 4.3 for two values of strain δ . Firstly considering the small strain case, $\delta = 0.2$, we observe that differences between the GSC impulse response and the HB impulse response are relatively small, as should be expected. The major difference is that the GSC response is confined within the region $|\chi| < Bu/(\pi\delta)$ whereas the HB response is non-zero for all χ . This confinement of the secondary circulation in the generalised model is due the effect on strain on wave propagation; that is, waves can only propagate where their outwards group speed exceeds the incoming strain flow speed. By contrast, waves in the HB model are assumed to be ‘free’ and can thus propagate out to $\pm\infty$. As seen in figure 4.3a, the confinement of the GSC leads to an increased amplitude in the centre of the frontal zone (near $\chi = 0$) and a reduction on the flanks, compared to the HB secondary circulation.

Now consider the wave part of the streamfunction, $\psi_{I,W}$, as defined in (4.45). Since $\psi_{I,W}$ scales with r , which is exponentially small for small strains (see figure 4.2), we expect $\psi_{I,W}$ to be relatively small in comparison to the GSC for $\delta = 0.2$. Figure 4.3 shows that $\psi_{I,W}$ is close to zero everywhere except near the stagnation points, $\chi_s = \pm Bu/(n\pi\delta)$, where it becomes infinite. As with the GSC response, the wave response is identically zero for $\chi > \chi_s$. This structure of $\psi_{I,W}$ is consistent with the idea that inertia-gravity waves generated by the squeezing of the front are confined within $\chi < \chi_s$, and stagnate at $\chi = \chi_s$, and thus wave energy will accumulate at $\chi = \chi_s$. The infinities in the wave impulse response at the stagnation points require careful interpretation. We observe that the full time-dependent wave streamfunction ψ_W , which may be reconstructed from $\psi_{I,W}$ via

$$\psi_W(\chi, Z, T) = \int_{-\infty}^{\infty} \psi_{I,W}(\chi - \chi_0, Z) \frac{\partial}{\partial \chi_0} b_0(\chi_0 e^{\delta T}) d\chi_0, \quad (4.48)$$

will remain finite for all time for any smooth initial buoyancy profile b_0 . However, in the absence of the formation of a discontinuity at the front or viscous effects, the infinities in the impulse response imply that the magnitude of ψ_W at the stagnation points will continuously increase with time.

Figure 4.3b shows the streamfunction impulse responses for a larger value of strain, $\delta = 0.9$. The difference between the HB and generalised secondary circulations is now order one for all χ , due to the strong confinement of energy in the generalised model greatly intensifying the secondary circulation and localising it near the front. The wave component $\psi_{I,W}$ is an order one contribution to the overall streamfunction, and greatly exceeds the GSC near the first vertical mode stagnation points. The higher vertical mode signals ($n = 3, 5$ etc.) are also visible as large amplitude spikes near each of their stagnation

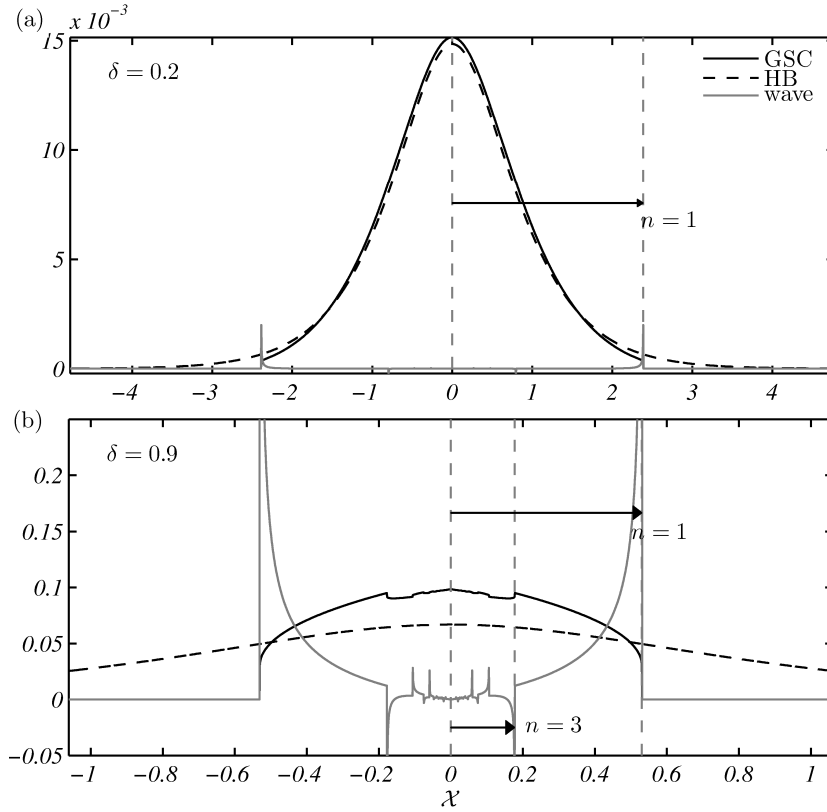


Fig. 4.3 Streamfunction impulse response ψ_I evaluated at $Z = 0.5$ for the generalised secondary circulation (GSC) and wave components of the general solution (4.45), and the HB solution (4.47, HB), for strains of (a) $\delta = 0.2$ and (b) $\delta = 0.9$. The impulse forcing is located at $\chi = 0$, and the spread of energy away from this point is indicated by arrows for the first two non-zero modes $n = 1$ and $n = 3$. Energy can only spread over the region $\chi \leq Bu/(n\pi\delta)$ for each mode. The parameter values used are $Bu = 1.5$ and $Ro = 0.6$, consistent with other examples considered later in this chapter.

points, $\chi_s = \pm Bu/(n\pi\delta)$, indicating the accumulation of wave energy from each mode at those locations.

The integral of the net streamfunction impulse responses (ψ_I) is equal for both the HB and generalised models, and is controlled by the magnitude of the impulse forcing in the original differential equation (4.37),

$$\int_{-\chi_s}^{\chi_s} \psi_I(X, n) d\chi = -2\delta \int_{-\chi_s}^{\chi_s} \phi_I(X, n) d\chi = -2\delta A_n Ro, \quad (4.49)$$

by substituting (4.44), followed by (4.42). For the generalised model, this ‘impulse of amplitude’ is split between the GSC and wave streamfunctions. As shown in figure 4.3, the relative size of the wave component varies significantly with strain δ . To quantify

this variation we compute the χ -integrated wave streamfunction, normalised by the total streamfunction amplitude from (4.49),

$$\mathcal{R} = \frac{\int_{-\chi_s}^{\chi_s} \Psi_{I,W}(X, n) d\chi}{-2\delta A_n Ro} = \frac{e^{-\frac{\pi\sigma}{2}} + \sigma}{e^{-\frac{\pi\sigma}{2}} + e^{\frac{\pi\sigma}{2}}} = \frac{r}{2} \left(1 + \sigma e^{\frac{\pi\sigma}{2}} \right). \quad (4.50)$$

The ratio \mathcal{R} can be interpreted as the relative strength of wave — as opposed to secondary circulation — generation associated with an element of horizontal buoyancy gradient acted on by convergent strain δ . The ratio is a function of δ only and is plotted in figure 4.2 (a; log scale, b; linear scale). Unsurprisingly, given the definition of the wave streamfunction in (4.45), the ratio \mathcal{R} is exponentially small for small strains, but finite for larger strains. Indeed for $\delta \rightarrow 0$ (4.50) implies that $\mathcal{R} \rightarrow 1/\delta e^{-\pi/(2\delta)}$, meaning that virtually all the energy supplied by the impulse forcing goes into the secondary circulation, consistent with the Hoskins & Bretherton (1972) paradigm. In contrast, for a forcing frequency approaching the inertial, $\delta \rightarrow 1$, (4.50) implies that $\mathcal{R} \rightarrow 1/2$, such that the impulse forcing is evenly split between the wave and GSC streamfunctions. We will see in §4.5 that the scale given by (4.50) provides a useful upper limit on the amplitude of propagating frontogenesis waves generated by a time-dependent strain field acting on a front — this is despite the separation of the wave and GSC streamfunctions in (4.45) being somewhat arbitrary.

The exponential smallness of spontaneous wave generation for small strain (i.e. small Rossby number $Ro_L = \delta$) implied by (4.50) has previously been predicted in ‘toy models’ (see Vanneste, 2008, and references therein). The sharp cut-off in wave generation at about $\delta = 0.2$ in figure 4.2 has important consequences for the production of waves in eddy fields which exhibit substantial spatially varying strain fields. Figure 4.2 suggests that we should expect wave generation to be localised to a number of distinct regions of relatively large strain, with exponentially smaller (i.e. negligible) generation outside of these regions. Such behaviour is consistent with numerical studies of spontaneous generation in eddy fields (e.g. Danioux *et al.*, 2012). Equation 4.50 may also provide a theoretical foundation for gravity wave parametrisations in numerical models which often depend on the local strain (Plougonven & Zhang, 2014, and references therein).

Based on the impulse responses displayed in figure 4.3 we can infer some features of the flow at large time during frontogenesis forced by a constant strain — or more generally around any sufficiently sharp, strained front. The GSC and frontal zone will have a fundamental lengthscale, or width, of $2\chi_s(1) = 2Bu/(\pi\delta)$ corresponding to the stagnation point for the fastest propagating mode-one wave. In dimensional units the width is $2NH/(\pi\alpha)$. Stationary gravity waves associated with each vertical mode will appear at or near the stagnation points $\pm Bu/(n\pi\delta)$. The wave amplitudes will grow as frontogenesis proceeds and wave energy

accumulates at these locations. The highest amplitude wave will be associated with the first vertical mode appearing at the stagnation points on the edges of the frontal region. Referring to figure 4.3, this mode will drive a thin band of intense upwelling (since $w = -J \partial_X \psi$) ahead of the front on the warm side (vice versa on the cool side). These mode-one waves can be expected to be visible even for relatively small values of strain, since the GSC response tends to zero at these locations. Waves associated with the higher vertical modes overlay the frontal zone and will, for small strains, tend to add relatively weak ‘fine-scale structure’ to the GSC-dominated fields in this region.

4.4.2 Full solution

Equation (4.33) demonstrates how the full time-dependent solution $\phi(\chi, Z, T)$ may be generated by summation of the impulse responses of infinitesimal elements $d\chi_0$ of buoyancy gradient at that time. The partial time derivative $\partial_T \phi(\chi, Z, T)$ may be similarly generated from its impulse response,

$$\partial_T \phi(\chi, Z, T) = -\delta \int_{-\infty}^{\infty} (\chi - \chi_0) \frac{\partial \phi_I(\chi - \chi_0, Z)}{\partial \chi} \frac{\partial}{\partial \chi_0} b_0(\chi_0 e^{\delta T}) d\chi_0. \quad (4.51)$$

Once $\phi(\chi, Z, T)$ and $\partial_T \phi(\chi, Z, T)$ have been obtained, the along-front velocity, buoyancy and streamfunction fields at time T can be computed by expressing equations (2.27) in coordinate χ :

$$v(\chi, Z, T) = \frac{\partial}{\partial Z} \phi(\chi, Z, T), \quad (4.52a)$$

$$b(\chi, Z, T) = b_0(\chi e^{\delta T}) + F^{-2} Z - Ro F^{-2} \frac{\partial}{\partial \chi} \phi(\chi, Z, T), \quad (4.52b)$$

$$\psi(\chi, Z, T) = -\delta \phi(\chi, Z, T) - \partial_T \phi(\chi, Z, T). \quad (4.52c)$$

Further, we can define the time-dependent generalised secondary circulation (GSC) as

$$\psi_{GSC}(\chi, Z, T) = \int_{-\infty}^{\infty} \psi_{I,GSC}(\chi - \chi_0, Z) \frac{\partial}{\partial \chi_0} b_0(\chi_0 e^{\delta T}) d\chi_0, \quad (4.53)$$

where $\psi_{I,GSC}$ is the GSC impulse response defined in (4.45). The wave streamfunction may then be computed as the difference, $\psi_W = \psi - \psi_{GSC}$. As noted previously, this separation of wave and GSC streamfunctions is not unique. We will now examine the behaviour of these time-dependent fields in detail.

Firstly, it is useful to consider an explicit example of the differences between the generalised and HB models in a parameter regime, δ and Ro both small, where both are expected to be valid. In figure 4.4 we display the vertical velocity fields at late time arising from the generalised model, w , the HB model, w_{HB} , and the difference between the two, $w - w_{HB}$, for parameter values of $\delta = 0.2$ and $Ro = 0.6$, and a buoyancy profile of $b_0(X) = 1/2 \operatorname{erf}(X/\sqrt{2})$. Since all time dependence in the model arises through the straining of the boundary buoyancy profile as per (4.33), initial conditions on the model fields cannot be explicitly set and are instead determined implicitly from relations (2.27) using the field ϕ from (4.33) with $T = 0$. The HB model predicts a single thermally direct overturning cell with upwelling on the warmer (right-hand) side, and downwelling on the cooler side. The generalised model velocity field is broadly similar, dominated by an analogous large scale overturning cell, but contains a number of additional features. The most obvious addition is the formation of distinct lines of intensified vertical flow on the periphery of the frontal region (at $\chi_s(1) = \pm Bu/(\pi\delta) = \pm 2.4$), associated with the mode 1 gravity wave. Similar bands of up/downwelling were observed by Snyder *et al.* (1993, e.g. see their figure 1) and Garner (1989, e.g. see their figure 5) in their numerical simulations, although in those cases it is difficult to determine whether the feature is arising due to waves generated by frontogenesis (as here) or waves arising due to the initial conditions (e.g. as in Chapter 3), since both types of waves stagnate at $\pm\chi_s(1)$. One key difference between the wave types is that the amplitude of the waves associated with initial conditions decay with time due to the action of the strain field (see Chapter 3), whereas the amplitude of the waves associated with frontogenesis amplify with time as the front sharpens. Thus at sufficiently late time, or for a sufficiently sharp front, the frontogenesis waves are expected to dominate.

Figure 4.4 also shows additional fine structure associated with higher vertical modes in the vertical velocity field. For example, note the slight ‘bumps’ in the contours near $x \simeq \pm 0.8$ associated with the third vertical mode. There are also sizeable differences between the HB and generalised models at the location of the front ($x \simeq \pm 0.3$) on the upper and lower boundaries; this ‘updraft-downdraft couplet’ feature was observed by Snyder *et al.* (1993, their figure 2 and footnote 2) when comparing the HB prediction with the output of their numerical model. The feature appears due to the higher along-front velocity magnitudes (v) near the origin in the generalised model (as a result of the strain-imposed limit on wave propagation ensuring more energy remains in the frontal zone, see figure 4.3), which cause the front to slump/slant further as represented by the momentum coordinate transformation, $x = \chi - Ro v$. Consequently, there is an outward shift of the frontal position (and the associated extremum of the vertical velocity) in the generalised model compared with the HB model, giving rise to the couplet feature observed in the difference field.

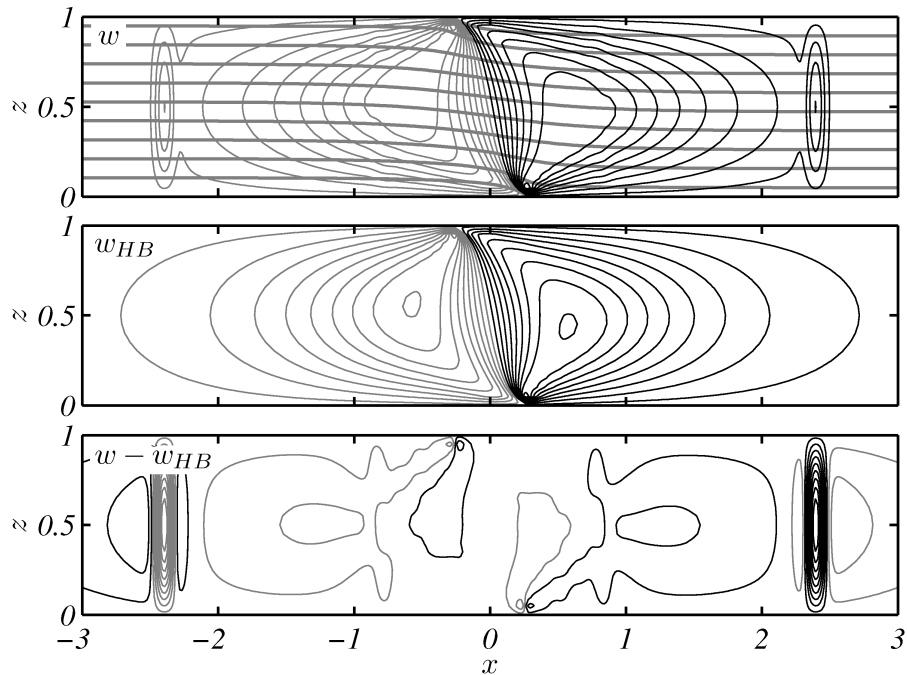


Fig. 4.4 The vertical velocity field from the generalised model w , Hoskins & Bretherton (1972) model w_{HB} , and the difference between the two, evaluated just prior to the critical time for parameter values of $Ro = 0.6$, $Bu = 1.5$, and $\delta = 0.2$. Black denotes positive and grey denotes negative velocities. Contours of buoyancy are overlaid on the top plot (thick grey lines).

In figure 4.5 we consider the time evolution of the system (same parameter values) via a Hovmöller plot of the generalised secondary circulation (GSC) and wave streamfunctions at mid-depth. The GSC at mid-depth is initially squeezed inwards and amplified by the strain, but by $t \sim 10$ it approaches a steady state consistent with the GSC impulse response function (i.e. from figure 4.3a, overlaid in grey). Thus, as argued in the previous section, the impulse response provides a snapshot of the long-time state of the system. The wave streamfunction in figure 4.5 shows the accumulation of wave energy into distinct packets at the stagnation points, consistent with the wave impulse response (overlaid in grey). However, in contrast to the GSC, the convergent strain then acts to continually amplify these wave packets with time. The waves do not propagate owing to the trapping effect of the strain field, and are essentially fixed in space at the stagnation points. Note that the wave streamfunction in figure 4.5 is two orders of magnitude smaller than the GSC. A consequence of this is that distinct wave features (e.g. as in figure 4.4) are only visible at late time, once wave energy has accumulated at the stagnation points.

One of the most important applications of the generalised model is to flows which have order one strains (i.e. order one large scale Rossby numbers), such as frontogenesis in a

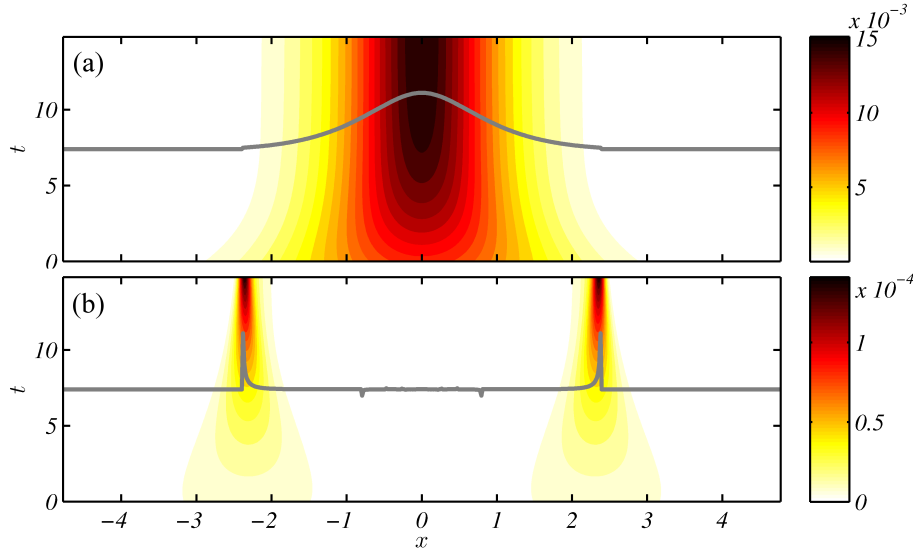


Fig. 4.5 The (a) generalised secondary circulation (ψ_{GSC}) and (b) wave streamfunction (ψ_W), for parameter values of $Ro = 0.6$, $Bu = 1.5$, and $\delta = 0.2$. The GSC and wave impulse response functions from figure 4.3a have been overlaid in grey.

submesoscale eddy field in the ocean mixed layer. As an example, consider a case with parameter values of $\delta = 0.9$, but $Ro = 0.6$ and $Bu = 1.5$ as before. The initial conditions are again implicitly defined through (4.33) and relations (2.27). Figure 4.6 shows the time evolution of the wave and GSC streamfunctions with buoyancy contours overlaid in black at each time-step. In contrast to the previous small-strain example, here the wave and GSC streamfunctions are of the same order of magnitude. Initially both streamfunctions are characterised by a single-cell thermally direct overturning ($t = 0$), which rapidly intensifies as the frontal scale contracts ($t = 1.3$). The GSC remains as a single cell and continues to intensify as time proceeds. However, the wave streamfunction splits into two distinct wave packets ($t = 2$) which then intensify with time. As in the previous example, the waves do not propagate and are essentially fixed in space at the stagnation points, $\chi_s(1) = \pm 0.53$. For a more realistic flow with a temporally or spatially varying strain field (see §4.5) these generated waves tend to be released rather than remaining fixed at the stagnation points and amplifying indefinitely. The structure of the wave and GSC streamfunctions at $t = 2.7$ (i.e. at long-time, $T \gg \delta^{-1}$) is consistent with the impulse responses for the same parameter values shown in figure 4.3b.

Between $t = 0$ and $t = 1.3$ in figure 4.6, the strain rapidly amplifies the horizontal buoyancy gradients, but this amplification is counterbalanced by a flattening of the isopycnals in the frontal zone. It was observed in Chapter 3 that such flattening is indicative of adjustment and wave generation processes, giving credence to the ‘balance adjustment’ theory of Zhang

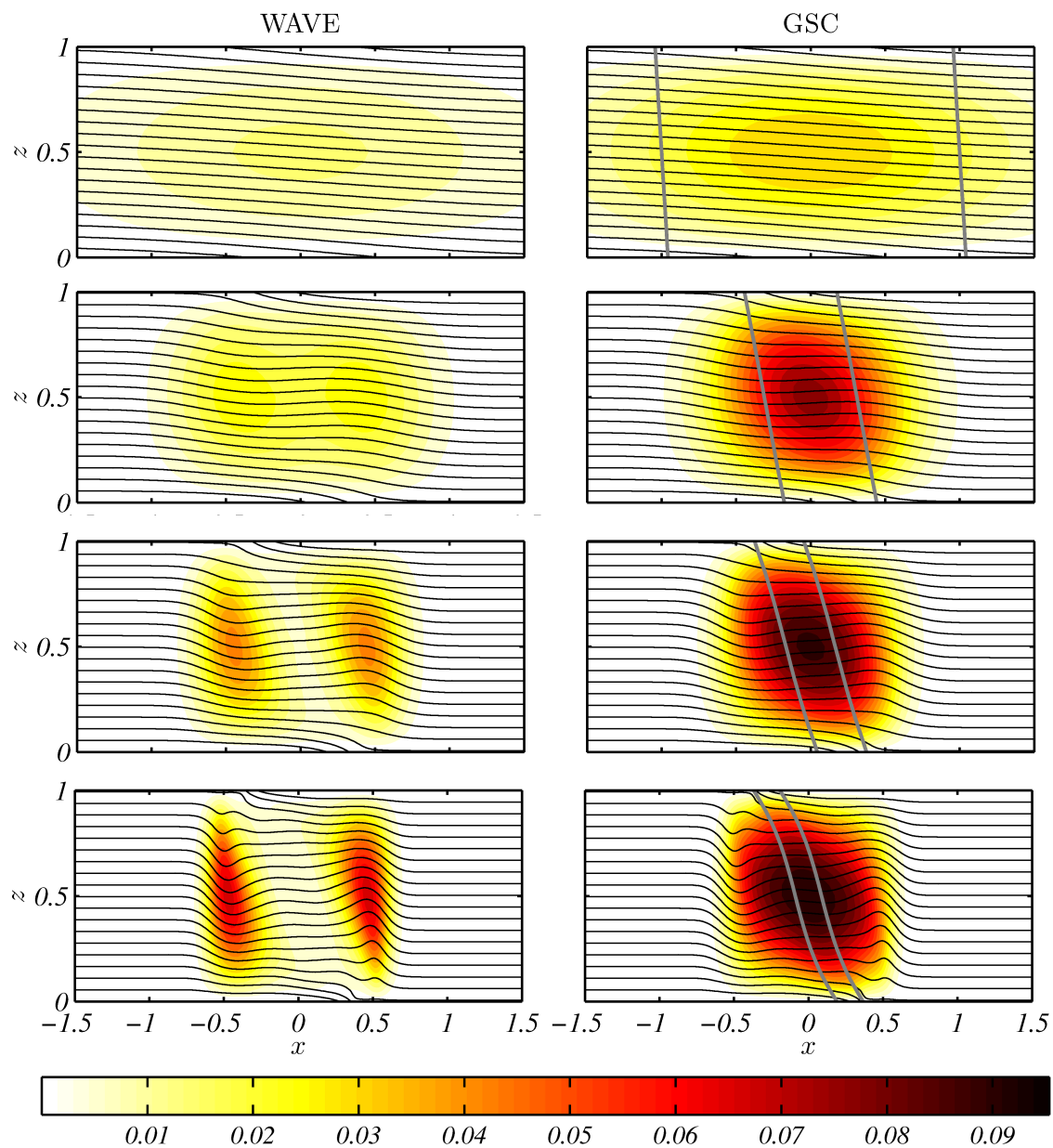


Fig. 4.6 The time evolution of the wave ψ_W (left) and GSC ψ_{GSC} (right) streamfunctions for parameter values of $Ro = 0.6$, $Bu = 1.5$, and $\delta = 0.9$, at times of $t = 0, 1.3, 2$ and 2.7 (just prior to the critical time) with time increasing down the page. Buoyancy contours are overlaid in black in each case. Grey contours enclose the region $|X| \leq 1$, demonstrating the convergent action of the strain field, and the simultaneous slumping of the front.

(2004). Viewed from this perspective, the system adjusts to the strain-generated imbalance in the frontal zone by generating inertia-gravity wave packets ($t = 1.3, 2$). The amplitude of these waves then increases with time as their horizontal scale contracts.

The adjustment process can only occur in the interior since buoyancy conservation requires that $b = b_0(X) + F^{-2}Z$ on the boundaries at all time, leading to the formation of a sharp front on the boundary (see $t = 2.7$ in figure 4.6). A scale for the depth of the frontal feature can be determined based on the impulse solutions above. Taking the GSC ($e^{-|\epsilon|}$) part of the impulse response solution (4.42), we observe that the amplitudes of the vertical modes in this solution decay exponentially with mode number n . Such exponential decay implies that the lowest vertical modes dominate the solution. The solution amplitude (and thus degree of adjustment) near to the boundary, $Z \ll 1/(n\pi)$, must therefore be small, and the front will be sharp in this region. For small χ , where the front is located, (4.42) yields a scale depth for the front of

$$h \sim \frac{1}{n\pi} \sim \frac{\sqrt{1-\delta^2}}{Bu}, \quad (4.54)$$

for $\delta < 1$. Thus, for order one strains we expect frontal features to be concentrated in a very shallow boundary layer near the surface, as figure 4.6 exemplifies. Strong adjustment and wave generation is expected outside the boundary layer.

4.5 Time-dependent strain

Here we return to the more general case of a time-dependent strain field with the objective of describing the response of an initially weak front, as defined by (4.13), that is initially in geostrophic balance, to an imposed strain field. We will employ the pulse-like strain profile from (4.30) to exemplify the situation of a strain field that is smoothly switched on, acts for a finite period of time τ during which it obtains a maximum value of δ_0 , before being smoothly switched off. Such a strain field is expected to be ubiquitous in geophysical flows, particularly in strong eddying regions in the ocean mixed layer. The temporal variation of the strain in the model can be thought of as either (a) representing the lifetime of the eddies responsible for forming the convergent strain field or (b) the time taken for a patch of fluid (comprising the front) to advect through a convergent region within a large scale eddy field. The latter case invokes a temporal variation in the model strain to represent a spatial variation in the physical strain. The numerical solutions presented below proceed by Fourier transforming the PDE (2.29) with $\mathcal{N} \equiv 0$ (noting that the right-hand side forcing term vanishes sufficiently far from the front) and solving the resultant time ODE for each mode, then reconstructing the solution from a summation of the modes.

Consider an explicit example with parameter values representative of a front in a mesoscale eddy field in the ocean mixed layer; $Ro = 0.1$ (initially weak front), $Bu = 1$ (a length scale of the order of the Rossby radius), $\delta_0 = 0.2$ (approximate Rossby number for a mesoscale eddy) and $\tau = 8\pi$ (time scale for the eddy of $2\pi/\delta \sim \tau = 4$ days). Figure 4.7 displays the solution of our model for the above parameter values. The pulse of strain (figure 4.7b) pushes the system out of the initial geostrophic balance and drives a thermally direct secondary circulation (similar to the HB model), which forms the dominant feature of the Hovmöller plot of the streamfunction at mid-depth (figure 4.7a). Note that the contours in this plot are logarithmically spaced from 1% to 100% of the maximum value. The time-varying strain also acts to smoothly sharpen the front as demonstrated by the time series of frontal width shown in figure 4.7d. Consistent with this frontal sharpening, the along-front velocity magnitude (figure 4.7c) increases to maintain the front close to geostrophic balance. The streamfunction (figure 4.7a) exhibits wave generation on the flanks of the secondary circulation (i.e. associated with the first vertical mode) as the front sharpens, similar to the case of constant strain (§4.4). These *frontogenesis waves* are initially trapped by the strain field but begin to propagate as the strain weakens. The time-variation in the strain field also drives the generation of waves. These *transience waves* are visible as a near-inertial oscillation in the frontal zone for $T > \tau$, and slowly propagate outwards with time. Thus, for $T > \tau$ the system consists of near-inertial oscillations about a state of geostrophic balance, plus a propagating wave field. The behaviour of the front for $T > \tau$ is thus identical to the large-time behaviour described in Chapter 3 for an unstrained flow. In that case unbalanced initial conditions were responsible for wave generation, whereas here the dual mechanisms of frontogenesis and acceleration of the large scale strain flow themselves generate IGWs from purely balanced initial conditions.

While the impulse response solution presented in §4.4 is no longer valid for a time-dependent strain field, many of the properties of that solution still apply. The characteristics of the sine transformed generalised model equation (4.20) were derived in §4.2.1 for both time-varying (4.22) and constant (4.23) strains. As noted in that section, the region between the plus (χ_+) and minus (χ_-) characteristics indicates the area over which amplitude/energy associated with vertical mode n , and initially at location χ_0 , has spread by time T . The highest horizontal wavenumbers ($k \rightarrow \infty$) propagate along the lines χ_{\pm} , while the lowest wavenumbers ($k \rightarrow 0$) essentially remain fixed along the centre line, $\chi = \chi_0 e^{-\beta(T)}$. Comparing (4.22) with (4.23), we expect the behaviour of time-dependent strain flows to be similar to the constant strain case, except that the stagnation points will be time-dependent. In both cases, a pair of positive (or negative) characteristics initially separated by a distance $\Delta\chi_0$ will be squeezed together by the convergent strain field, to a separation distance of $\Delta\chi_0 e^{-\beta(T)}$ by

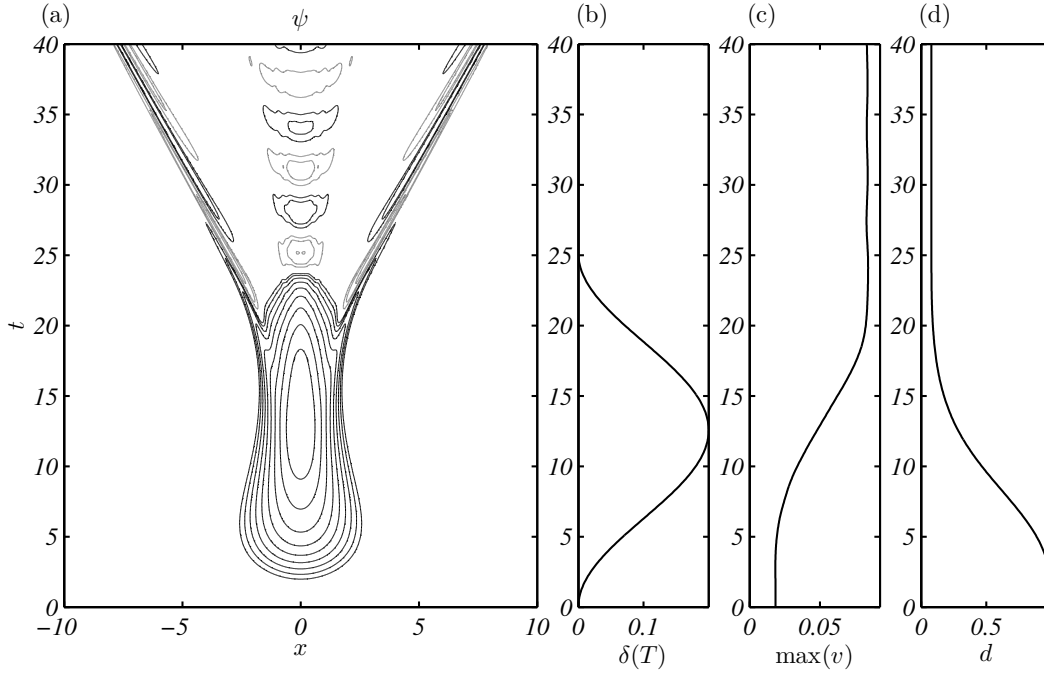


Fig. 4.7 The solution of the time dependent model (2.29) with $\mathcal{N} \equiv 0$, computed numerically, for parameter values of $Ro = 0.1$ and $Bu = 1$. The imposed strain field (b) is defined in (4.30) with $\delta_0 = 0.2$ and $\tau = 8\pi$. The boundary profile of buoyancy is $b_0(X) = 1/2 \operatorname{erf}(X/\sqrt{2})$. (a) Hovmöller of the streamfunction evaluated at mid-depth. Contour spacing is logarithmic from 1% to 100% of the maximum value, with grey contours indicating negative (clockwise) overturning. (c) The maximum value of the along-front velocity v . (d) The frontal width $d = J^{-1}$.

time T . This convergence implies that waves will be concentrated in a small region of width $\Delta\chi_W = e^{-\beta(T)}$ about the stagnation points as time progresses, leading to the formation and amplification of wave packets in these narrow regions as seen in §4.4. The relative amplitude \mathcal{R}_A of the wave streamfunction compared to the generalised secondary circulation may be estimated using the ratio \mathcal{R} derived previously (4.50) for the net integrated amplitudes, and the relative width of the regions in which the streamfunctions are concentrated,

$$\mathcal{R}_A = \mathcal{R} \frac{\Delta\chi_{GSC}}{2\Delta\chi_W} = \mathcal{R} \frac{Bue^{\beta(T)}}{n\pi\delta} \approx \frac{Bue^{\beta(T)}}{n\pi\delta^2} e^{-\frac{\pi}{2\delta}} \text{ for } \delta \leq 0.2, \quad (4.55)$$

where δ is an appropriate mean (or maximum) value of the time-dependent strain. These results will prove useful in interpreting the numerical solution introduced in figure 4.7.

In figure 4.8 we examine the generation and properties of the IGWs in detail by dividing the flow into the secondary circulation and wave components. The generalised secondary circulation (GSC, figure 4.8a,c) is computed as defined in §4.4, but evaluated at each time T

using the value of the strain at that time; that is,

$$\psi_{GSC}(X, Z, T) = \int_{-\infty}^{\infty} \psi_{I,GSC}((X - X_0) e^{-\beta(T)}, Z) b'_0(X_0) dX_0. \quad (4.56)$$

This part of the flow is directly-forced, and only exists during the time $T < \tau$ where the strain is non-zero (see (4.45)). Given the form of the time-dependence in (4.56) it is clear that — as with the general constant strain solution in §4.4 — propagating waves will not be present in the GSC part of the flow. Defining the wave part of flow (subscript W, figure 4.8b,d) as the difference between the GSC and the full flow, $\psi_W = \psi - \psi_{GSC}$, ensures that all propagating signals are contained within this component. In other words, while ψ_W is not a unique separation of the wave field, it is an upper limit. As expected the wave field in figure 4.8 persists when the strain field is switched off. Hovmöller plots of the streamfunction (c,d) and vertical velocity (a,b) fields are displayed in the figure, evaluated at mid-depth. The wave streamfunction is at least an order of a magnitude weaker than the secondary circulation (see the colour bar scales).

We will first consider the frontogenesis waves. The amplitude of the frontogenesis wave streamfunction may be estimated by substitution of the parameter values into (4.55), yielding a relative amplitude $\mathcal{R}_A = 0.04$ in agreement with figure 4.8. The maximum distance from the origin of the frontogenesis wave packet with time is plotted in figure 4.8b as dashed black lines. These ‘stagnation lines’ for the first vertical mode are given by (4.22) with $\chi_0 = 0$ and $n = 1$. Note that these stagnation lines converge between roughly $t = 10$ and $t = 20$ in the figure. During this time wave energy accumulates along these lines (as seen in §4.4), leading to the formation of a wave packet. This behaviour is reinforced by the family of characteristics χ_+ and χ_- for the first vertical mode (defined by 4.22) shown on figure 4.8c as solid black lines. The convergence of the characteristics between $t = 10$ and $t = 20$ indicates the confinement of energy initially spread over a broad region ($\Delta\chi \sim 1$) at $t = 0$ into a region of width $e^{-\beta(t)}$ by time t , leading to the formation of a (relatively) high-amplitude wave packet. Correspondingly, an initial wavenumber of k_0 becomes $k = k_0 e^{\beta(t)}$ after a time t . By time τ the integrated strain is $\beta \sim 2.5$ implying an order of magnitude amplification ($k/k_0 = e^{\beta} \sim 12$) of the initial wave numbers. For $T > \tau$ the wave packet is composed of a narrow band of high wavenumber, high frequency waves which disperse weakly with time as the packet propagates outwards (at or near to the maximum speed of Bu/π). Specifically, the wave packet is composed of only the first vertical mode $n = 1$ and a spread of horizontal mode numbers around $k = e^{\beta(t)}$. Applying the hydrostatic IGW dispersion relation (e.g. Chapter 3), the dominant frequency of a first vertical mode wave packet subjected to integrated strain

β is

$$\omega = \sqrt{1 + \left(\frac{Bu e^\beta}{\pi}\right)^2}. \quad (4.57)$$

For the current example the dominant frequency is thus $\omega \sim 4$, or $4f$ in dimensional units. The result is clearly highly sensitive to the integrated strain β — a smaller β would lead to a wave packet consisting of a broader band of lower wave number, lower frequency, lower amplitude waves that disperses more strongly. For example, an integrated strain of half the present value leads to a dominant frequency of $\omega \sim 1.5$, closer to the inertial frequency.

In contrast to the frontogenesis waves, the transience waves in figure 4.8 are dominated by low wavenumber, near-inertial signals. The transience waves are generated as a result of the time-dependent strain changing the quasi-steady secondary circulation (GSC) that can be supported at the front. For instance, consider impulsively switching off the strain field at some time T_0 . In the absence of strain, for $T > T_0$, the system possesses a steady state corresponding to geostrophic balance with *zero* secondary circulation. Thus, switching off the strain will trigger the geostrophic adjustment of the GSC towards this steady state. Such geostrophic adjustment of a now *unstrained* flow will be associated with the generation of freely propagating IGWs — or transience waves. For a smoothly switched-off strain, as in figure 4.8, the same adjustment process gives rise to transience wave generation, but the wave amplitude will be smaller than in the impulsive case and the waves will be (partially) trapped until the strain vanishes. In either case, the wavenumber spectrum of the waves is controlled by the GSC streamfunction that is undergoing adjustment, implying lower wavenumbers, frequencies and group velocities compared with the frontogenesis waves.

The generation and propagation of waves due to geostrophic adjustment at a front was discussed in Chapter 3. In that case the initial condition considered was an unbalanced buoyancy gradient (or mass imbalance). Here the ‘initial condition’ is the state of the flow when the strain is switched off, and corresponds to an unbalanced streamfunction (or momentum imbalance). However, the dynamics of the adjustment process are unchanged and we can use the results of Chapter 3 to understand the transience wave generation seen in figure 4.8. By approximating the smooth switch-off (over timescale $\tau/2$) of the strain field supporting a frontal secondary circulation of ψ_{GSC} at $\tau/2$ as an impulsive switch-off, we can derive an approximate response streamfunction $\psi_{T,W}$ for the transience wave generation for $T > \tau$. Following Chapter 3, the Fourier mode amplitude of the response is

$$\widehat{\psi_{W,T}}(k, n, T) = \widehat{\psi_0} \cos \left(\sqrt{1 + \left(\frac{Buk}{n\pi}\right)^2} (T - \tau) \right), \quad (4.58)$$

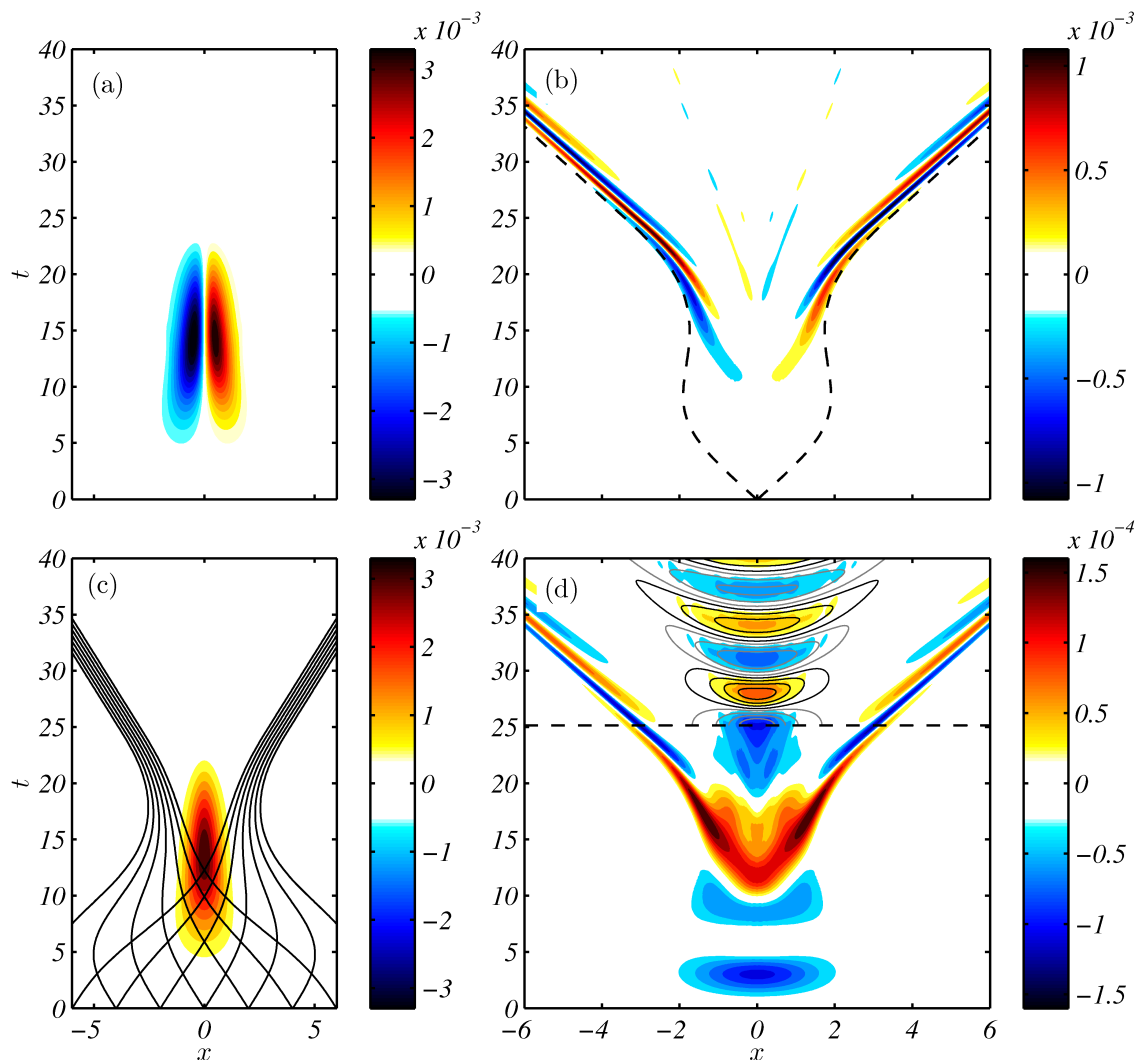


Fig. 4.8 The solution of the time dependent model (2.29) with $\mathcal{N} \equiv 0$, computed numerically, for parameter values of $Ro = 0.1$ and $Bu = 1$, as in figure 4.7. Hovmöller plots of the generalised secondary circulation (GSC) and wave components of the vertical velocity (top) and streamfunction (bottom) are displayed, evaluated at mid-depth ($z = 0.5$). The stagnation lines for the first vertical mode are shown on the top-right plot (black-dashed lines; from (4.22) with $\chi_0 = 0$). The family of characteristics χ_+ and χ_- defined by (4.22) for the first vertical mode are shown on the bottom left plots (solid black lines). Streamfunction contours for the unstrained adjustment of the maximum GSC for $T > \tau = 8\pi$ (shown by a dashed black line) are overlaid on the bottom-left plot, with black denoting positive (anticlockwise) and grey negative (clockwise) overturning.

where k is the wavenumber in momentum coordinates. Contours of the (approximate) transience wave streamfunction $\psi_{W,T}$, computed from (4.58), are overlaid on the wave streamfunction plot in figure 4.8. The initial streamfunction ψ_0 has been taken as the generalised secondary circulation at $T = \tau/2$; that is, $\psi_0 = \psi_{GSC}(X, Z, \tau/2)$. The displayed contours of the approximate transience wave streamfunction closely match the full wave response for $T > \tau$.

Transience waves are also generated by the switching-on of the strain field via an analogous adjustment mechanism to that discussed above. The waves are visible in the Hovmöller plot of ψ_W in figure 4.8 (bottom-right) as near inertial oscillations for $T < \tau/2$. In the limit of an impulsive switching-on of the strain field at $T = 0$, these transience waves are identical to the waves associated with initial conditions that were studied in Chapter 3.

4.6 Discussion

Here we employed the generalised model developed in Chapter 2 as an idealised configuration in which to investigate frontogenesis and the associated spontaneous wave generation occurring in eddy fields in the atmosphere and ocean. Unlike Chapter 3, here we considered appropriately balanced initial conditions such that time-dependence only arises through the strain-driven contraction of the boundary front. We showed that the generalised model is valid for such initial conditions — in the sense that neglected terms are small compared to leading order retained terms — if the product $Ro\delta$ is sufficiently small (as defined by (4.10)). One subset of the generalised model is the weak-strain limit studied by Hoskins & Bretherton (1972), $\alpha^2 \ll f^2$ where α is the strain rate and f is the inertial frequency, in which the along-front velocity remains geostrophically balanced for all time and no wave motions exist. We call this weak-strain limit the ‘HB model’. A second subset of the generalised model is the weak-front limit, as defined by (4.13), where the initial buoyancy gradient on the boundary must be small, but the strain α can be order f . The key feature of the weak-front limit is that the generalised model yields an accurate description of both inertia-gravity wave generation and the large scale secondary circulation. The weak-front limit does not neglect any terms in the rotating fluid equations which are retained in the HB model, but instead retains additional terms relating to wave propagation. The additional terms vanish for sufficiently weak strains, and thus the weak-front limit reduces to the HB model. The time evolution of the system in the generalised and HB models is completely described by the PDEs in field ϕ , (2.29) with $\mathcal{N} \equiv 0$ and (4.18), respectively. The along-front velocity, buoyancy and cross-front streamfunction may then be generated from ϕ for each limit via equations (2.27).

The generalised model was solved analytically in §4.4 for the case of a steady strain field, using a Green's function method. While the model solution breaks down for a sufficiently sharp front (as does the HB model), we are able to make some qualitative statements about the differences between the two models. Firstly, a finite strain field has the effect of confining the frontal circulation within a region of $2NH/(\pi\alpha)$ about the deformation axis — we define a secondary circulation (GSC) which accounts for this effect and generalises the HB secondary circulation to finite strain. Secondly, a steady strain field drives the formation of stationary inertia-gravity waves as the front sharpens. The first vertical mode tends to appear on the periphery of the frontal zone (at a distance of $\pm NH/(\pi\alpha)$ from the centre of the front). For small Ro the front remains largely vertical and this mode is visible as a distinct band of strong vertical flow ahead of the front. As such, this wave feature provides a potential dynamical model for the formation of squall lines ahead of cold fronts in the atmosphere. Ley & Peltier (1978) previously obtained a similar result from an ad-hoc fast-timescale correction to the solution of Hoskins & Bretherton (1972). Stationary waves associated with the higher vertical modes tend to overlay the frontal zone and add fine structure to the fields in this region. We emphasise that the formation of these stationary waves is independent of the initial conditions, suggesting that they should be a ubiquitous feature of fronts, at least for small Rossby numbers. Similar fine structure and squall line type features have been observed in numerical models of frontogenesis such as Snyder *et al.* (1993) and Garner (1989).

Since the generalised model only accurately describes second order flow features in the limit of small Rossby number (4.13), the wave features described above may not be quantitatively valid for larger Rossby numbers. However, even neglecting the wave field, the effect of the strain is important in modifying the first order secondary circulation for all Rossby numbers. Specifically, the generalised secondary circulation (GSC) contains an additional dynamical/physical correction relative to the HB secondary circulation; namely, that spread of energy and momentum during frontogenesis is associated with a *finite* group velocity, which limits the outward spread of the frontal circulation into the oncoming strain flow. As such, this confinement effect is expected to be a ubiquitous feature of fronts for parameter values where the generalised model is applicable (4.10), which includes the weak-strain HB limit.

In our model, spontaneous inertia-gravity wave emission at a front occurs via two mechanisms: large scale flow acceleration (transience waves) and frontal sharpening (frontogenesis waves). The flow acceleration mechanism was isolated in the limit of zero PV flow (§4.3) where inertial waves are generated via a time-varying strain flow independent of the frontal sharpness. In §4.4 it was demonstrated that stationary IGWs evolve naturally from a front

subject to constant strain, as the frontal scale contracts. In the more general situation of an initially weak, balanced front subjected to a time-dependent strain field (as in §4.5) both mechanisms are active. With a time-varying strain flow the frontogenesis IGWs are initially confined by the convergent strain field and wave energy is forced to accumulate at locations set by the vertical mode number, leading to the formation of high-amplitude wave packets as the frontal scale shrinks. As the strain weakens, these wave packets begin to propagate away from the front. The time-dependent strain also generates transience waves. These waves arise since a change in the strain magnitude implies a change in the magnitude of the secondary circulation that can be sustained at a front, thus giving rise to an adjustment process. The transience waves tend to exhibit lower wavenumbers and frequencies than frontogenesis waves, although the propagation of the waves away from the frontal zone can still only occur once the strain field weakens sufficiently. In general it is likely to be difficult to determine which wave generation mechanism is responsible for individual features in the observed flow fields, particularly as waves triggered by initial conditions may also be present.

Using the analytical solutions developed in §4.4 we were able to compute estimates of the relative amplitude of the frontogenesis wave streamfunction compared to the secondary circulation (the ‘mean flow’). A scaling for the relative wave amplitude was given in (4.55). In terms of the physical scales of the problem, this reduces to

$$\mathcal{R}_A = \frac{NHf}{\pi\alpha^2 L_F} e^{-\frac{\pi f}{2\alpha}}. \quad (4.59)$$

The parameter L_F in (4.59) is the minimum frontal width which in our model is given by $L_F = L e^{-\beta(t)}$. A key feature of (4.59) is that it implies exponentially small wave generation for strain rates α smaller than about $0.1f$ to $0.2f$, but finite generation above this threshold. Equation (4.59) may thus provide a theoretical basis for parametrisations of gravity wave emission from frontal zones in numerical models of the atmosphere, which at present are based on largely arbitrary thresholds (Plougonven & Zhang, 2014).

Our results may have important implications for energy loss from balanced flows via IGW emission. Danioux *et al.* (2012) demonstrate that wave generation in an eddy field is highly intermittent in both space and time. In particular, wave packets tend to be emitted in discrete ‘generation events’ from thin filamentary density structures associated with high strain regions. Our model provides a possible explanation for this intermittency. In §4.4 we demonstrated that wave generation via frontal sharpening is exponentially small for small strain (see equation 4.50 and figure 4.2) but becomes first order for larger strain, and consequently we expect a localisation of wave emission to small regions of high strain. Further, as noted above, waves generated via convergent straining across a front remain

trapped in the vicinity of the front while the strain remains large and then begin to propagate as distinct wave packets as the strain weakens — for example, by advection of the frontal feature into a region of weaker strain in an eddy field. Consequently, we expect a tendency for the emission of wave packets to be highly localised in time as well as space. The localisation in time due to trapping by the strain field emphasises that the effect of the large scale strain on the propagation of waves is vitally important in determining the structure of the observed wave field (e.g. Plougonven & Snyder, 2005).

Here we have shown that the generalised model introduced in Chapter 2 is able to describe spontaneous IGW generation at actively strained fronts. It should be noted, however, that the model is only stringently valid for small Rossby numbers, whereas many fronts in the ocean and atmosphere have order one Rossby numbers. The effects of larger Rossby numbers will be examined in the next chapter by directly comparing the model predictions developed here to the observed frontogenesis and IGW generation in a fully non-linear numerical model.

Chapter 5

Spontaneous wave generation during frontogenesis: numerical solutions

In the previous chapter we formulated an analytic ‘forced solution’ to the 2D frontogenesis problem (1.12) that extends the classical Hoskins & Bretherton (1972, HB) model to large strain rates ($\alpha \sim f$). In this chapter we use a numerical model to simulate the fully non-linear problem and compare the results with the analytic solution for a variety of strain rates. Even for weak strains ($\alpha = 0.2f$), the confinement of the secondary circulation and the spontaneous generation of waves, predicted in Chapter 4, are shown to be important corrections to the HB solution. These inviscid predictions are also robust for an equilibrated front where strain-forced frontogenesis is balanced by diffusion. For strong strains the wave field becomes of leading order importance to the solution. In this case the frontal circulation is tightly confined, and the vertical velocity is an order of magnitude larger than in the HB model. The addition of a strain field that weakens with time allows the release and propagation of the spontaneously generated waves. We also consider fronts with both large vorticity and strain rate, beyond the validity of the generalised model.

5.1 Introduction

In Chapter 4 we derived the *forced solution* to the generalised model, defined as the solution that eliminates the propagating waves associated with initial conditions that were studied in Chapter 3. This solution has the special property that time only enters through the strain-driven collapse of the boundary buoyancy gradient (i.e. (4.33)), as in the classical HB model, thus allowing a direct comparison of the predictions of the HB and generalised models for the response of the flow to strain forcing. In both models the strain field sharpens

the front and drives a large scale thermally direct secondary circulation. However, the generalised model includes two important dynamical effects not described by the HB model: confinement and spontaneous wave generation. These effects arise due to the presence of the strain field modifying the propagation of waves in the system. Waves can only spread energy away from the front in the region where their outward propagation speed exceeds the incoming strain flow speed, thus limiting the horizontal extent of the secondary circulation. This *confinement* leads to a secondary circulation that is more localised about the front, and consequently exhibits larger vertical velocities than predicted by the HB model. The confinement effect thus provides a possible explanation for enhanced vertical velocities observed near submesoscale eddies, where the stronger strain (larger α) leads to a more confined secondary circulation, as compared with the mesoscale. The trapping effect of the strain field also leads to the accumulation of wave energy at a certain distance from the front, resulting in the spontaneous generation of distinct ‘frontogenesis wave’ packets. In Chapter 4 we showed that the weakening of a strain field with time leads to the trapped frontogenesis waves being released, and propagating freely away from the front. The time-variation in the strain was also shown to generate additional ‘transience waves’ via an adjustment mechanism. Here we will test the validity of the generalised analytical model by direct comparison with fully non-linear numerical simulations for both constant and time-varying strain flows. As in Chapter 4, here we consider only appropriately balanced initial conditions such that waves are only generated spontaneously.

A large and growing literature examines the ‘spontaneous’ generation of inertia-gravity waves from balanced flows in various idealised and geophysical situations (see Vanneste (2013) and Plougonven & Zhang (2014) for recent reviews on the topic). Previous work includes studies of inertia-gravity waves generated from Couette flow (Vanneste & Yavneh, 2004), stratified vortex dipoles (Viudez, 2007), and baroclinic life cycles (Plougonven & Zhang, 2007; Viudez & Dritschel, 2006). Collectively, these studies demonstrate the ubiquity of wave generation in geophysical settings, and that while spontaneous generation is exponentially weak at small Rossby numbers (near-balanced flows), it can be significant at large Rossby numbers. The generalised model of frontogenesis is a natural extension of this work: it provides a description of the inevitable breakdown of classical frontal semigeostrophic balance (e.g. Hoskins, 1982), and the associated spontaneous wave generation, when the background strain (or Rossby number, Ro_L) is large. Consistent with the aforementioned studies, in the previous chapter we showed that the amplitude of the waves is exponentially small for weak strain fields, $\alpha < 0.2f$, but substantial for larger strains.

Both the HB and generalised analytical models of frontogenesis predict the collapse of the front to a discontinuity in finite time — known as the ‘critical time’. In real flows, frontal

collapse will be arrested either by small scale mixing or instabilities of the front. Previous studies have employed two-dimensional numerical simulations to test HB theory (e.g. Gall *et al.*, 1987; Garner, 1989; Snyder *et al.*, 1993). In these simulations, the front collapses to the grid scale close to the critical time — regardless of resolution — and the numerical solution breaks down. Iterating the numerical solution beyond the point of frontal collapse requires the addition of an explicit diffusion.

The numerical studies noted above (Gall *et al.*, 1987; Garner, 1989; Snyder *et al.*, 1993) focused mostly on the case of very weak strain, $\alpha = 0.1f$, although some studied $\alpha = 0.2f$. Snyder *et al.* (1993) found that differences to the HB solution take the form of (a) higher order corrections to the secondary circulation, and (b) waves that appear at late time, often following frontal collapse. Here we show, using numerical simulations, that the generalised model is able to at least partially capture both of these features.

In order to arrive at analytical solutions, a number of simplifying approximations were made in formulating the generalised model. The setup of the problem follows the original HB model in considering the flow between two rigid horizontal surfaces, neglecting along-front variations, and assuming that the potential vorticity and background strain are both uniform in space. These assumptions restrict the direct applicability of the model results to fronts in the ocean and atmosphere, but we anticipate that the dynamics described by the generalised model will be present in a more realistic setting. The scaling analysis detailed in Chapter 4 also shows that the model solutions will break down when the Rossby number associated with the background strain and the Rossby number associated with the frontal circulation are both order one. Both of these Rossby numbers may be order one for strained submesoscale fronts (Shcherbina *et al.*, 2013). One of the main objectives of this chapter is to use numerical simulations to test the validity of the generalised model when applied to high Rossby number flows. Unlike the HB and generalised analytical models, the numerical simulations retain all non-linear terms. In §5.3.2 we show that the non-linear terms become important as frontogenesis proceeds and are responsible for the formation of intensified vertical jets near surface fronts.

A major challenge arising in previous numerical studies is the presence of so-called ‘spurious’ propagating waves in the solutions. These are due to the initial condition derived from the HB model not being precisely ‘balanced’ (Gall *et al.*, 1987). Here we are able to largely resolve this issue by initialising our numerical model in the state predicted from the generalised model forced solution — rather than the HB model — greatly reducing the spurious wave field. In other words, the initial condition implied by generalised model forced solution is more ‘balanced’ than that from the HB model, in the sense that it reduces the generation of propagating waves associated with adjustment to the initial condition. In

§5.3 we demonstrate this fact by comparison of numerical solutions initialised from the two analytical models.

5.2 Numerical setup

Here we describe the numerical model and configuration used in this chapter (and also in Chapter 7, and previously for the numerical solutions shown in Chapter 3). The equations to be solved numerically are the 2D frontal equations (1.12), but with the addition of horizontal and vertical diffusion/viscosity (assuming a Prandtl number of unity):

$$\frac{Du}{Dt} - fv = \alpha u - \frac{1}{\rho_0} \frac{\partial p}{\partial x} + \kappa_h \frac{\partial^n u}{\partial x^n} + \kappa_v \frac{\partial^n u}{\partial z^n}, \quad (5.1a)$$

$$\frac{Dv}{Dt} + fu = -\alpha v + \kappa_h \frac{\partial^n v}{\partial x^n} + \kappa_v \frac{\partial^n v}{\partial z^n}, \quad (5.1b)$$

$$\frac{Dw}{Dt} = b - \frac{1}{\rho_0} \frac{\partial p}{\partial z} + \kappa_h \frac{\partial^n w}{\partial x^n} + \kappa_v \frac{\partial^n w}{\partial z^n}, \quad (5.1c)$$

$$\frac{Db}{Dt} = \kappa_h \frac{\partial^n b}{\partial x^n} + \kappa_v \frac{\partial^n b}{\partial z^n}, \quad (5.1d)$$

$$\frac{\partial u}{\partial x} + \frac{\partial w}{\partial z} = 0, \quad (5.1e)$$

Variables κ_h and κ_v are the n^{th} order horizontal and vertical (hyper-)diffusivities, respectively, for $n = 2, 4, 6, 8, \dots$, noting that $\kappa_h, \kappa_v < 0$ for $n = 4, 8, \dots$. The non-dimensional form of the above equations — using the same scales as previously (see table 2.1) — is

$$\frac{Du}{Dt} - v = \delta u - Ro \frac{\partial p}{\partial x} + \frac{Ro}{Re_h} \frac{\partial^n u}{\partial x^n} + \frac{Ro}{Re_v} \frac{\partial^n u}{\partial z^n}, \quad (5.2a)$$

$$\frac{Dv}{Dt} + u = -\delta v + \frac{Ro}{Re_h} \frac{\partial^n v}{\partial x^n} + \frac{Ro}{Re_v} \frac{\partial^n v}{\partial z^n}, \quad (5.2b)$$

$$A^{-2} \frac{Dw}{Dt} = Rob - Ro \frac{\partial p}{\partial z} + \frac{A^{-2} Ro}{Re_h} \frac{\partial^n w}{\partial x^n} + \frac{A^{-2} Ro}{Re_v} \frac{\partial^n w}{\partial z^n}, \quad (5.2c)$$

$$\frac{Db}{Dt} = \frac{Ro}{Re_h} \frac{\partial^n b}{\partial x^n} + \frac{Ro}{Re_v} \frac{\partial^n b}{\partial z^n}, \quad (5.2d)$$

$$\frac{\partial u}{\partial x} + \frac{\partial w}{\partial z} = 0. \quad (5.2e)$$

with the non-dimensional material derivative defined as

$$\frac{D}{Dt} \equiv \frac{\partial}{\partial t} + Ro \left(u - \frac{\delta}{Ro} x \right) \frac{\partial}{\partial x} + Row \frac{\partial}{\partial z}. \quad (5.3)$$

All variables are henceforth assumed to be non-dimensional, unless otherwise stated. The horizontal and vertical Reynolds numbers are defined as

$$Re_h = \frac{\sqrt{\Delta b} H L^{(n-1)}}{\kappa_h}, \quad Re_v = Re_h \frac{\kappa_h}{\kappa_v} \left(\frac{H}{L} \right)^n. \quad (5.4)$$

The other non-dimensional numbers are defined as previously (see table 2.1).

The numerical model to be employed is DIABLO (Taylor, 2008) which solves the incompressible, non-hydrostatic Navier-Stokes equations. Here it will be used to solve the non-dimensionalised system of equations (5.2) in a two-dimensional box. The numerical method is pseudo-spectral in the horizontal (x) direction, and periodic boundary conditions are applied in this direction, while finite differences are used in the vertical (z) direction. In this chapter we will mainly focus on ocean applications of the generalised model. Consequently, we choose the upper rigid lid to be at $z = 0$ and the lower lid, representing the thermocline, to be at $z = -1$.¹ The boundary conditions applied in the numerical model on the rigid lids ($z = -1, 0$) are no vertical flow, $w = 0$, free-slip horizontal flow,

$$\frac{\partial u}{\partial z} = \frac{\partial v}{\partial z} = 0, \quad (5.5)$$

and a vertical buoyancy gradient fixed to the value of the background stratification,

$$\frac{\partial b}{\partial z} = F^{-2}. \quad (5.6)$$

These numerical boundary conditions differ from the analytical in that they are inconsistent with conservation of PV on the boundary. The analytical model boundary conditions are determined implicitly from the uniform-PV relations (2.27) — and therefore must satisfy conservation of PV — and the constraint that w and therefore ϕ vanish on the rigid lid boundaries. While it is theoretically possible to apply numerical boundary conditions that agree precisely with the analytical, these would be time dependent and rather complicated, and hard to relate to physical boundary conditions typically used in more sophisticated numerical models. Instead we have chosen to use simple free-slip and constant-flux numerical boundary conditions (5.5, 5.6) that, while minimising the PV boundary layers appearing in the numerical solution, also show that the analytic results are relatively insensitive to a change in the boundary conditions and therefore more robust.

Here, we will describe model runs without explicit (hyper-)diffusion ($\kappa_h = \kappa_v = 0$ in (5.1)) as ‘inviscid numerical solutions’, although there will inevitably be some small amount

¹This shift in the z coordinate relative to prior chapters has no effect on the solution.

of numerical diffusion. For these inviscid model runs the numerical solution will break down once the frontal width becomes comparable to the numerical resolution, $d \sim \Delta x$, where Δx is the horizontal resolution. The numerical simulations are ended upon reaching this threshold. The horizontal resolution is set to $\Delta x = 0.005$, or $1/200$ of the initial frontal width, allowing a contraction in the front of over two orders-of-magnitude before the numerical model breaks down. The vertical resolution is set to $\Delta z = 0.01$ or smaller. For the diffusive simulations in §5.4 we employ a horizontal hyperdiffusion to prevent the collapse of the front to the grid scale. The explicit vertical diffusion is set to zero, $\kappa_v = 0$ or $Re_v \rightarrow \infty$, as the addition of explicit vertical diffusion leads to boundary layers that complicate the comparison of the numerical and analytical solutions.

Given the pseudo-spectral numerical method, care must be taken to ensure that the equations (5.2) are periodic in the horizontal direction. In particular, the material derivative contains a non-periodic operator, $-\alpha x \partial_x$, corresponding to the horizontal advection of the perturbation fields by the background strain flow. However, the perturbation fields are guaranteed to vanish sufficiently far from the front, owing to the trapping effect of the strain field studied in Chapter 4. Thus, selecting a numerical domain of width $L_N \gg 2Bu/\delta$, with the front located in the centre, ensures that the solution vanishes at the edge of the domain, and hence $-\alpha x \partial_x = 0$ there.

5.3 Comparison of numerical and analytical solutions

Here we compare the solution from the generalised analytical model (2.29) with that arising from the fully non-linear numerical solution to the inviscid governing equations (5.2). As noted above, the numerical model is initialised with the constant-strain generalised model forced solution (i.e. (4.33) with $T = 0$), since this is the most ‘balanced’ state available and will minimise any generation of waves associated with adjustment to the initial condition.

As an explicit demonstration of this fact, figure 5.1 compares the numerical model solution when initialised from the generalised (GM) and semigeostrophic (HB) models for parameter values of $Ro = 0.6$, $Bu = 1.5$, and $\delta = 0.2$. The initial streamfunctions from the GM and HB models are shown in figure 5.1(a) and (b), respectively. The difference between the initial conditions is $O(\delta^2)$ and is shown in (c). The initial GM streamfunction is narrower than the HB streamfunction, with increased amplitude in the centre but reduced amplitude on the periphery (owing to the confinement effect discussed in Chapter 4, and below). The numerical model is allowed to evolve freely from these initial conditions, and around $t = 14.5$ approaches a discontinuity on the boundaries. The streamfunctions just prior to this critical time are shown in (b) and (d), and the difference in (f). The large scale

secondary circulation is similar for both model runs, but the HB-initialised run displays an order $\delta^2 \sim 0.04$ transient wave signal that is not present in the GM-initialised run; these are the ‘spurious’ waves reported in previous numerical frontogenesis studies (e.g. Snyder *et al.*, 1993, see their figure 3). The presence of these waves implies that the HB initial condition is *less balanced* than the GM initial condition, due to the neglect of effects at $O(\delta^2)$ in the semigeostrophic model that are included in the generalised model. In other words, the constant-strain generalised model solution (4.33) represents a higher-order balance than semigeostrophy. As seen in the Hovmöller plot in figure 5.1g, the $O(\delta^2)$ imbalance in the HB initial condition gives rise to an adjustment process, and wave emission and trapping by the same mechanism as studied in Chapter 3. Given the above analysis, the numerical simulations presented below will be initialised from the generalised model to minimise wave generation associated with the initial condition.

In figure 5.2, the analytical and numerical solutions are compared for five sets of parameter values with a Burger number $Bu = 1.5$, a range of Rossby numbers Ro , and either weak strain (characterised by $\delta = 0.2$) or strong strain (characterised by $\delta = 0.9$). Figure 5.2 displays time series of the (a) frontal width d and (b) maximum vertical velocity for each of the five cases as derived from the generalised (wide-dash), HB (narrow-dash) and numerical (solid) models. Each case is colour-coded according to the legend in (a). The smaller Rossby number cases ($Ro = 0.6$; green and black) have relatively weak, broad fronts at time zero (i.e. $d \simeq 1$) and only form a discontinuity for time $t \gg \delta^{-1}$. By contrast, larger Rossby numbers correspond to a sharper initial front (smaller d) and thus more rapid formation of a discontinuity on times $t \sim \delta^{-1}$. As expected, the frontal width and maximum vertical velocity derived from the generalised, HB and numerical models are essentially indistinguishable for the small strain cases (black, magenta). The generalised and numerical models also agree for small Rossby number, but strong strain (green). The vertical velocity in this case increases exponentially during the course of frontogenesis, unlike the weak strain cases, and is an order-of-magnitude larger than the HB prediction. Such behaviour indicates that strong strain is a different dynamical regime to weak strain and that these dynamics are well captured by the generalised model. By contrast, for a given Rossby number (e.g. $Ro = 0.6$; green/black, or $Ro = 1.5$; magenta/red), the time evolution of the frontal width, $d(\delta t)$, predicted by the HB model is the same for all strain, and the HB maximum vertical velocity differs only via scaling by a constant.

The numerical results in figure 5.2 depart from the generalised model prediction at late times, for cases with both order one Rossby numbers and order one strains (red, blue), indicating that neglected non-linear effects are becoming important. The most notable difference in the numerical model is the super-exponential increase in the peak vertical

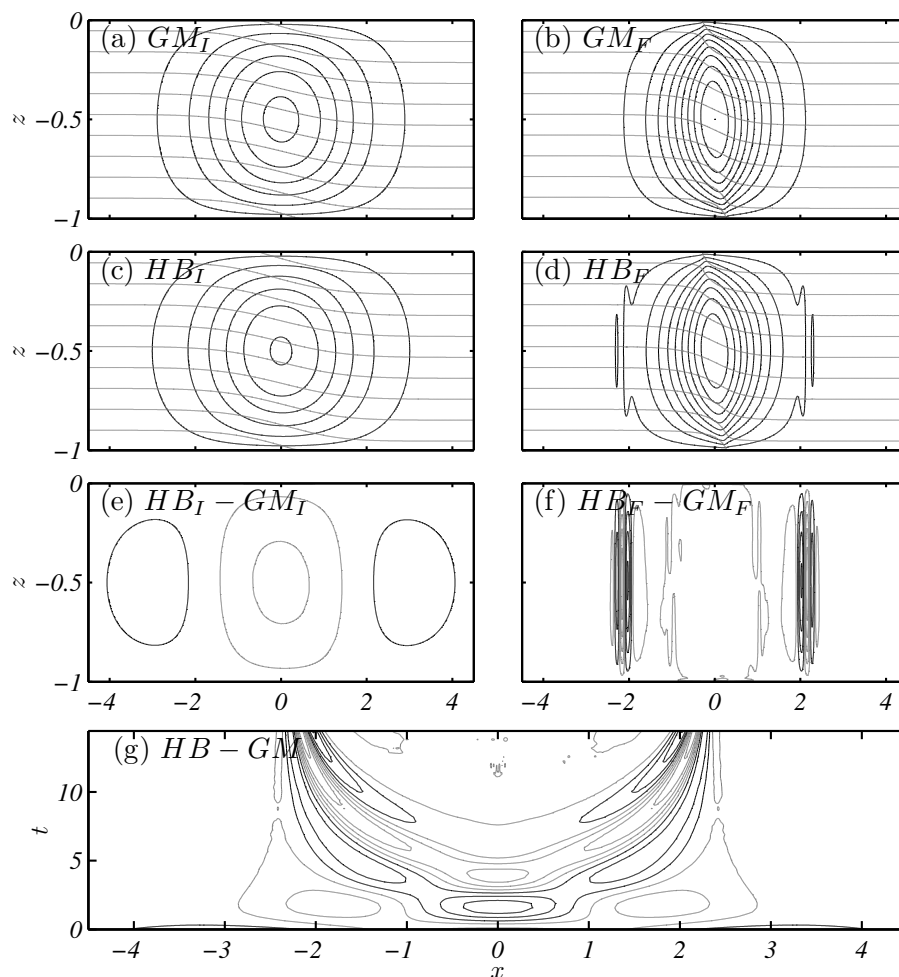


Fig. 5.1 A comparison of the streamfunctions from the numerical model when initialised in the state predicted by the generalised model forced solution, GM, (a: GM_I) and semigeostrophic balance, HB, (c: HB_I) for parameter values $Ro = 0.6$, $Bu = 1.5$, $\delta = 0.2$, and $A = 100$. Buoyancy contours are overlaid in grey. The difference between the initial states is shown in (e). The streamfunctions just prior to the critical time ($t = 14.5$) for the GM- and HB-initialised runs, GM_F and HB_F , are shown in (b) and (d), respectively. The difference between the final states is shown in (f). The time evolution of the difference at mid-depth ($z = -0.5$) is shown in (g). Positive (anticlockwise) values are represented by black contours, and negative by grey. The contour interval in (e-g) is 10% of that in (a-d).

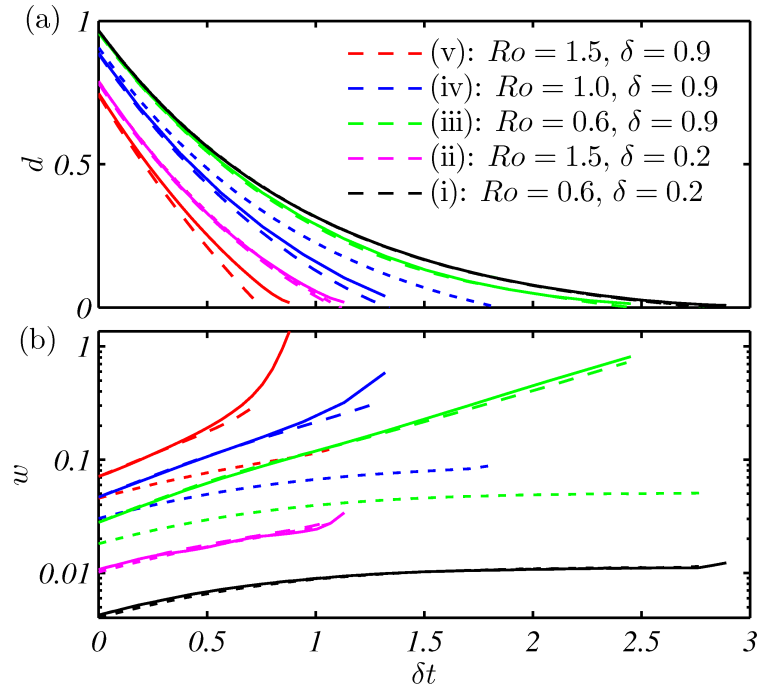


Fig. 5.2 Time series of the (a) frontal width $d = \min J^{-1}$ and (b) maximum vertical velocity w , from the generalised model (wide-dash), HB model (narrow-dash) and numerical model (solid). The colours correspond to different values of Rossby number Ro and uniform strain δ as indicated in (a). The Burger number is $Bu = 1.5$ in each case. The time axis is in units of δt ; that is, time is normalised by the strain rate rather than the inertial frequency. The evolution of the frontal width, $d(\delta t)$, from the HB model is independent of strain, meaning that the red/magenta lines and green/black lines in (a) are overlaid.

velocity as the front collapses (the GM prediction only increases exponentially, not *super*-exponentially). The critical time — that is, the time taken for frontal collapse — is also increased relative to the analytical prediction, particularly for $Ro = 1.5$ (red).

In the next sections (§5.3.1, §5.3.2) we will examine each of the cases shown in figure 5.2 in more detail, beginning with the two weak strain ($\delta = 0.2$) examples. The five cases are also summarised in table 5.1 for reference, along with the estimated and observed errors in the HB and generalised model predictions.

5.3.1 Weak strain

Traditionally, the HB model has been employed for weakly strained fronts, $\delta^2 \ll 1$, and has been found to be accurate at first order (e.g. Snyder *et al.*, 1993). However, the HB model does not include a description of inertia-gravity waves. In contrast, in Chapter 4 we argued that where the Rossby number is small, the generalised model will be able to accurately

Table 5.1 Parameter values for cases (i) to (v) shown in figure 5.2 and discussed in §5.3. The strain is constant in time, and $Bu = 1.5$ for each case. The structure of the generalised, HB and numerical model solutions for each case are shown in the figure listed in the ‘Fig.’ column. The table lists the fractional error expected from scaling arguments for the HB model, $(Ro^2 + 1)\delta^2$, and the GM model, $Ro^2\delta^2$, in addition to the RMS error (in the vertical velocity field) computed from comparison of the analytic solutions at their critical times with the numerical solutions at their critical times, as shown in each of the figures.

	Case			HB error		GM error	
	Ro	δ	Fig.	scaling	RMS	scaling	RMS
(i)	0.6	0.2	5.3	0.05	0.10	0.01	0.06
(ii)	1.5	0.2	5.4	0.13	0.14	0.09	0.12
(iii)	0.6	0.9	5.5	1.1	0.95	0.29	0.34
(iv)	1.0	0.9	5.6	1.6	0.75	0.81	0.43
(v)	1.5	0.9	5.7	2.6	0.64	1.8	0.55

describe the wave field associated with frontogenesis. We also proposed that even at order one Rossby numbers, while not able to accurately describe the wave field, the generalised model is more accurate than the HB model owing to the inclusion of additional $O(\delta^2)$ terms from the governing equations. Here we test these predictions.

Case (i): Consider a front with parameter values of $Ro = 0.6$, $\delta = 0.2$ and $Bu = 1.5$ — the same parameter values used in figures 4.4 and 4.5. Figure 5.3 shows the vertical velocity fields just prior to the critical time arising from the (a) generalised analytical (GM) and (b) numerical models. The fields arising from the two models are remarkably similar. Both are dominated by a large scale, thermally direct circulation, similar to that predicted by the HB model (shown in c). However, the generalised and numerical models also include wave structures — most notably the bands of intensified vertical flow on the periphery of the front. These wave packets form during the course of frontogenesis as the strain shrinks horizontal scales — or increases horizontal wavenumbers $k = k_0 e^{\delta t}$ — meaning all wavenumbers with a given vertical mode number n approach a constant propagation speed, $c = Bu/(n\pi)$ (equal to the maximum group speed of hydrostatic inertia-gravity waves of vertical mode n). Waves of all horizontal scales therefore accumulate at the same location where this outward propagation speed equals the incoming strain-flow speed, or $c = \delta x$. As in Chapter 4, we

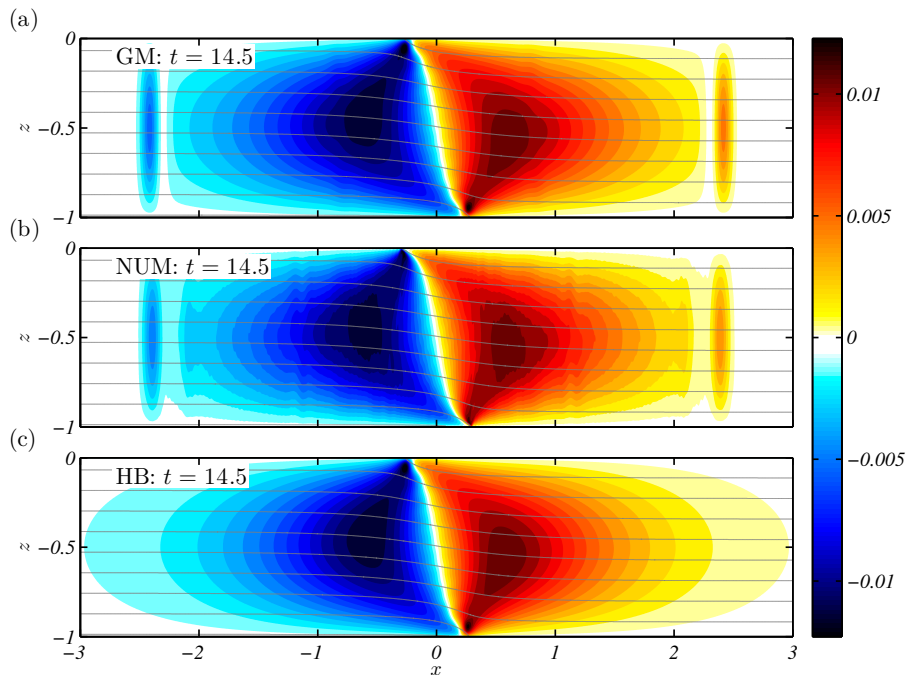


Fig. 5.3 Case (i): The vertical velocity field from the (a) generalised (GM), (b) numerical (NUM), and (c) semigeostrophic (HB) models, just prior to the time of discontinuity formation in each model, for parameter values of $Ro = 0.6$, $Bu = 1.5$, and constant strain $\delta = 0.2$. Contours of buoyancy from each model are overlaid in grey.

call these locations the ‘stagnation points’. The wave signals in figure 5.3a,b appear at the first vertical mode stagnation points, $x = \pm Bu/(\pi\delta) = \pm 2.4$.

Case (ii): Now consider a case with large Rossby number, $Ro = 1.5$, but the same Burger number and strain as employed above (i.e. $Bu = 1.5$, $\delta = 0.2$). This choice of Rossby and Burger number is similar to those employed by Snyder *et al.* (1993) to compare the HB model with numerical solutions. Figure 5.4 shows the vertical velocity fields just prior to the critical time arising from (a) the generalised, (b) numerical, and (c) HB models. The large scale thermally direct secondary circulation is similar in all three models, although the GM and numerical circulations are narrower compared with the HB prediction (similar to figure 5.1a,c,e). The narrower GM/numerical circulation is due to the convergent strain flow confining the spread of energy associated with an element of boundary gradient to the region where the maximum group speed of inertia-gravity waves exceeds the strain flow speed. By contrast, the HB model permits the spread of energy far from the front, giving rise to a broader circulation. While the confinement of the circulation by the convergent strain is an $O(\delta^2)$ effect and is relatively weak in this example, the correction associated with the GM solution is important in preventing the generation of spurious waves in the numerical

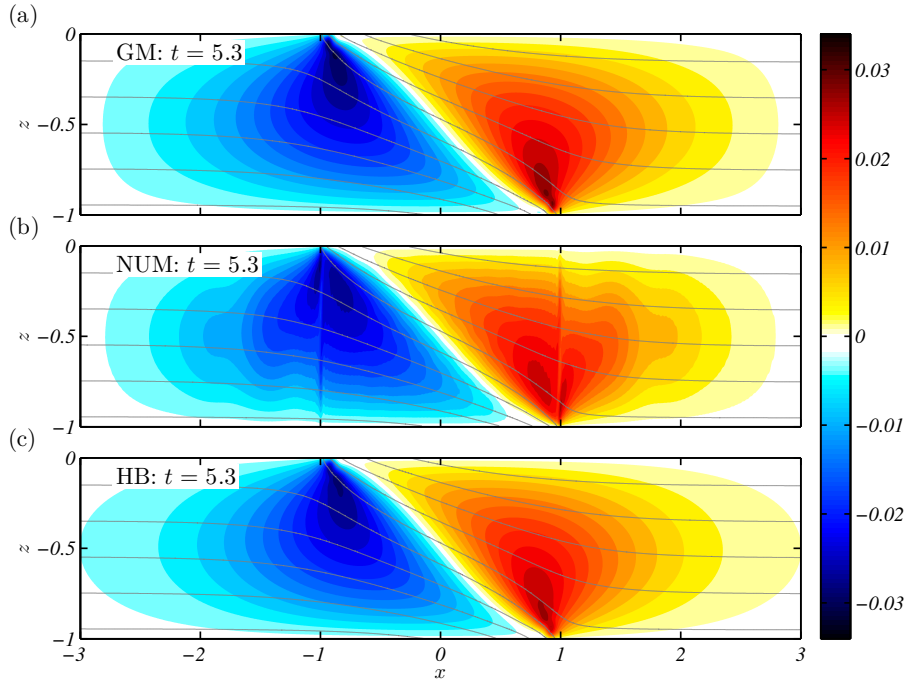


Fig. 5.4 Case (ii): The vertical velocity field from the (a) generalised (GM), (b) numerical (NUM), and (c) semigeostrophic (HB) models, just prior to the time of discontinuity formation in each model, for parameter values of $Ro = 1.5$, $Bu = 1.5$, and constant strain $\delta = 0.2$. Contours of buoyancy from each model are overlaid in grey.

solution, as demonstrated in figure 5.1. In §5.3.2 we will see that confinement becomes of leading order importance for strong strain.

The numerical solution in figure 5.4b displays some notable differences to both the HB and GM predictions. For example, there is a distinct double jet over the surface fronts $x \sim \pm 1$ (also noted by Snyder *et al.*, 1993), not present in either analytical solution, that appears to be associated with a vertical mode-two wave. This mode-two wave becomes particularly prominent if the numerical model is iterated past the critical time through the introduction of explicit diffusion (see §5.4). Figure 5.4b also displays some additional vertical mode-one wave structures, for example near $x \sim \pm 1.75$. These waves are generated in part due to the adjustment of a slight imbalance in the initial conditions, since the non-linear terms \mathcal{N} in (2.29), which are neglected in the generalised model, are not exactly zero at time zero and increase with Rossby number. The behaviour and propagation of such ‘imbalance waves’ in a strain field was examined in Chapter 3.

5.3.2 Strong strain

Here we consider order one values of strain ($\delta \sim 1$), where the wave field becomes of similar order to the secondary circulation. For strong strains the HB model, which omits waves and assumes the cross-front acceleration is small, is not valid even at first order. By contrast, for sufficiently small Rossby number, $Ro^2 \ll \delta^{-2}$, the generalised model is valid. We firstly examine this small Rossby limit, before considering order one Rossby numbers, for which the generalised model is expected to break down.

Case (iii): Consider a front with Rossby number $Ro = 0.6$, strain $\delta = 0.9$, and Burger number $Bu = 1.5$ — the same parameter values employed in figure 4.6, which displayed the analytical prediction for the time evolution of the streamfunction. In figure 5.5 we show the vertical velocity field just prior to the critical time ($t = 2.7$) from the (a) generalised and (b) numerical models. The vertical velocity is dominated by two wave packets located at the first vertical mode stagnation points, $x = \pm Bu/(\pi\delta) = \pm 0.53$. These stagnant waves form by the same mechanism discussed in the weak strain example (i.e. case (i); figure 5.3), although in that case the waves are a small second order correction to the flow. The strain shrinks the horizontal scale of the wave packets indefinitely, giving rise to the exponential increase in the maximum vertical velocity seen in figure 5.2b.

The structure of the solution in this strong strain case is qualitatively different from the previous weak strain cases (figures 5.3, 5.4) where the vertical velocity was dominated by a thermally direct, large scale overturning, and waves appeared as second-order features. To emphasise this distinction, in figure 5.5c we display the vertical velocity from the HB model for the parameter values under consideration, just prior to the critical time predicted by that model, $t = 3.3$. Even at this later time, the HB vertical velocity is an order-of-magnitude weaker than the numerical/generalised models, and displays the broad, thermally direct overturning characteristic of small-strain limit.

Case (iv): Now consider a front with larger Rossby number, $Ro = 1$, but the same Burger number and strain as considered previously ($\delta = 0.9$, $Bu = 1.5$). Since the product $Ro\delta$ is now order one, the scaling arguments of §4.2 suggest that the generalised model will not be valid, even at first order. Figure 5.6 displays the vertical velocity from the (a) generalised and (b) numerical models, just prior to the critical time. Both models predict a thermally direct circulation, strongly confined about the surface front. For comparison, the relatively weak, broad circulation predicted by the HB model is shown in figure 5.6c. The numerical model exhibits intensified vertical jets directly over the surface fronts that are not present in the generalised analytical model. These jets emerge at late time, close to frontal collapse, and are associated with the super-exponential growth in the maximum vertical velocities shown in figure 5.2b. It is difficult to distinguish between the secondary circulation and waves in

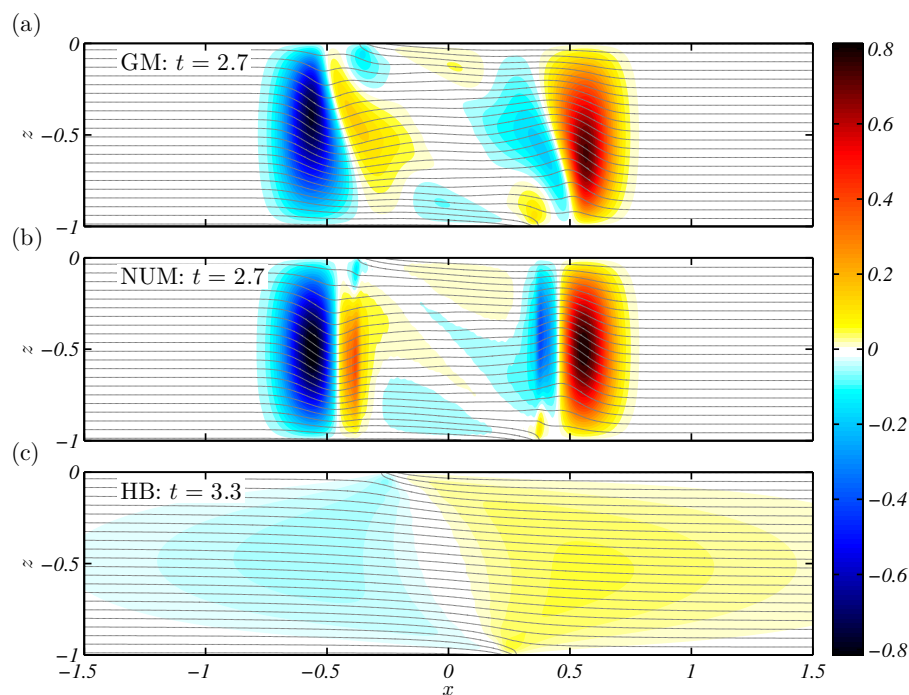


Fig. 5.5 Case (iii): The vertical velocity field from the (a) generalised (GM), (b) numerical (NUM), and (c) semigeostrophic (HB) models, just prior to the time of discontinuity formation in each model, for parameter values of $Ro = 0.6$, $Bu = 1.5$, and constant strain $\delta = 0.9$. Contours of buoyancy from each model are overlaid in grey.

this case. The absence of distinct waves is a result of the larger Rossby number driving more rapid frontal collapse. The front is not strained for a sufficiently long period before frontal collapse to permit the accumulation of energy and formation of the stagnant wave packets seen previously in figure 5.5.

Case (v): As noted above, the generalised model breaks down at late times for order one strain and Rossby number, as strong vertical jets form over the surface fronts. Here we examine this behaviour at an even larger Rossby number, using parameter values of $Ro = 1.5$, $\delta = 0.9$ and $Bu = 1.5$. Figure 5.7 displays three snapshots of the streamfunction from the numerical model at (a) time zero, (b) 50% of the critical time, and (c) just prior to the critical time. The net cross-front velocity vectors, $(u - \delta x/Ro, w)$, are displayed as black arrows. The locations of the surface fronts, defined as the maximum of $\partial_x b$ on the boundary, are denoted by red circles. Three momentum coordinates contours, $\chi = x + Ro v = 0, \pm Bu/(\pi\delta)$, are also displayed on each plot. The outer contours are the ‘stagnation lines’ along which the maximum outward wave group speed *in momentum coordinates* equals the strain-forced

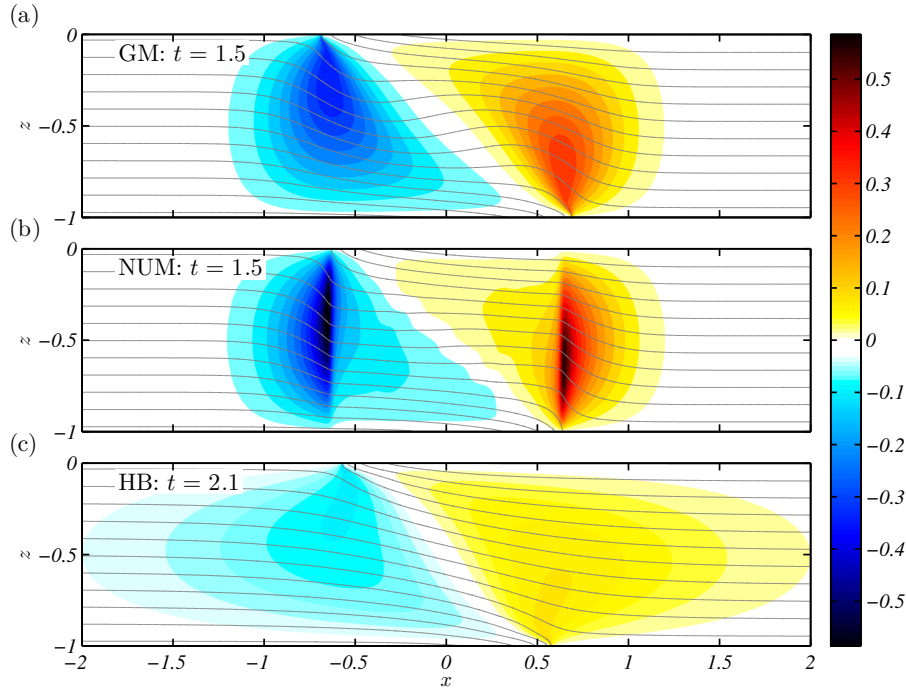


Fig. 5.6 Case (iv): The vertical velocity field from the (a) generalised (GM), (b) numerical (NUM), and (c) semigeostrophic (HB) models, just prior to the time of discontinuity formation in each model, for parameter values of $Ro = 1.0$, $Bu = 1.5$, and constant strain $\delta = 0.9$. Contours of buoyancy from each model are overlaid in grey.

contraction of the coordinate, or

$$\frac{D\chi}{Dt} = -\delta\chi = \pm \max c_g = \pm \frac{Bu}{\pi}. \quad (5.7)$$

The use of momentum coordinates accounts for the effect of the perturbation horizontal flow (u, v) on the propagation of the wave. As can be seen from figure 5.7c, the circulation is largely confined within the outward limits of these contours ($x \sim \pm 1$) by the critical time. Thus, despite the generalised model breaking down, the confinement effect predicted by that model still operates for order one strain and Rossby numbers. For these larger Rossby numbers, the greater buoyancy difference across the front drives a larger along-front velocity v , and thus significant slumping of the $\chi = x + Ro v$ contours, such that a balance is established between buoyancy-driven flow and rotation. Consequently, the circulation is broader for larger Rossby numbers (but the same Burger number and strain), as may be confirmed by comparison of figures 5.5, 5.6 and 5.7.

Figure 5.7a shows the numerical model streamfunction at time zero, initialised from the generalised analytical model. The overturning circulation is relatively broad, and smooth.

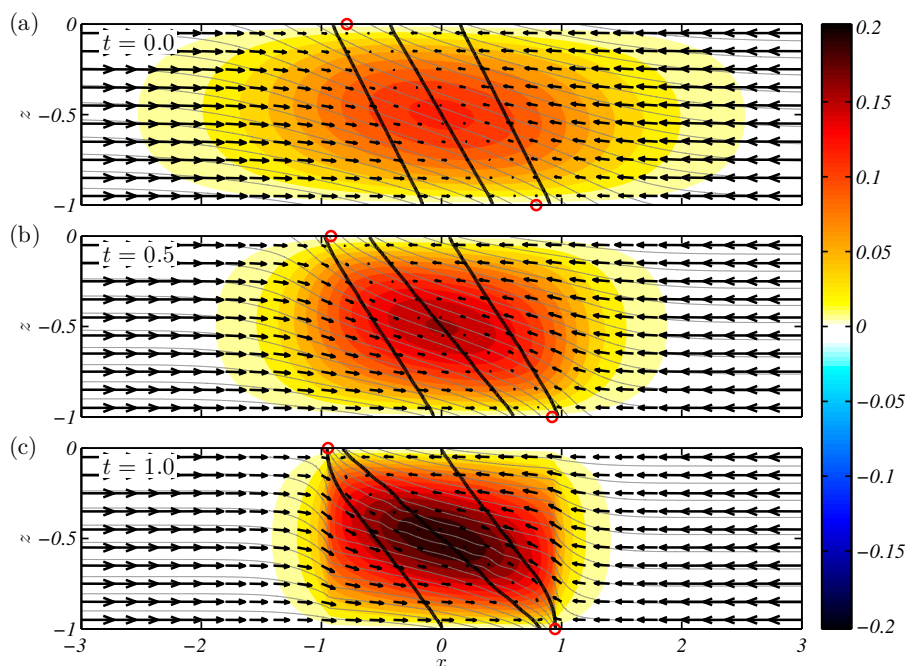


Fig. 5.7 Case (v): The streamfunction, buoyancy field, and net velocity vectors from the numerical model numerical model at times (a) 0, (b) 0.5 and (c) 1.0 (critical time), for parameter values of $Ro = 1.5$, $Bu = 1.5$, and constant strain $\delta = 0.9$. The net cross-front velocity vectors, $(u - \delta x/Ro, w)$, are displayed as black arrows. The locations of the surface fronts, defined as the maximum of $\partial_x b$ on the boundary, are denoted by red circles. Three momentum coordinates contours, $\chi = x + Ro v = 0, \pm Bu / (\pi \delta)$, are displayed on each plot as thick black lines.

As time progresses ($t = 0.5$; figure 5.7b), the surface front (red circle) slumps outward, buoyancy gradients increase, and the circulation becomes narrower and more intense as it is squeezed inward by the strain flow. However, the interior flow and buoyancy contours remain relatively smooth. The time series in figure 5.2 (red curve) indicates good agreement with the generalised model up to this time. Between $t = 0.5$ and $t = 1$ (the critical time; figure 5.7c) sharp ‘kinks’ develop in the interior buoyancy field, directly over the surface fronts, associated with intense vertical jets. The vertical velocity and interior buoyancy gradient grow super-exponentially over this period.

The super-exponential growth in the vertical velocity and interior buoyancy gradient results from a combination of two effects discussed above: the slumping of the front for large Rossby number, and the strong confinement of the circulation for large strain. These two effects lead to the surface front (red circle), associated with large surface and near-surface gradients, becoming coincident with the stagnation lines, associated with large vertical velocities, at late time, as shown in figure 5.7b,c. Consequently, there is strong vertical

advection of the near-surface buoyancy gradient into the interior of the flow (associated with the non-linear terms that are neglected in the analytical model, \mathcal{N} in (2.29)), thereby steepening isopycnal slopes directly above/below the surface fronts. The horizontal strain flow converging across the steepened isopycnals then drives an increased vertical flow at these locations. This result is readily derived from buoyancy conservation,

$$\frac{Db}{Dt} = 0 \Rightarrow w = \frac{-\frac{\partial b}{\partial t} - Ro \left(u - \frac{\delta}{Ro} x \right) \frac{\partial b}{\partial x}}{\frac{\partial b}{\partial z}} \simeq F^2 \delta x \frac{\partial b}{\partial x}, \quad (5.8)$$

where we have, at first approximation, neglected perturbations from the background. Thus, for the upper boundary front at $x \sim -1$, the advection of a positive buoyancy gradient into the interior of the flow will drive an increased downward velocity (and vice versa for lower boundary front). The larger vertical velocity will then lead to even greater advection of the near-surface frontal gradient into the flow interior, giving rise to sharper interior buoyancy gradients, and thus even larger vertical velocities as per (5.8). This positive feedback mechanism drives the formation of the sharp ‘kinks’ in the buoyancy fields in figure 5.7c and the associated vertical jets. The result is the super-exponential growth (exponential on a log scale) in the vertical velocity seen in figure 5.2b. The feedback effect also delays frontogenesis by advecting buoyancy gradient away from the boundary, thereby increasing the *interior* buoyancy gradient, but reducing the *boundary* gradient. This behaviour is shown in figure 5.2a (red curve) where the frontal width in the numerical model is increased relative the generalised model prediction at late time, $\delta t > 0.45$.

Time-varying strain

Ocean fronts typically exist within strain fields with significant temporal and spatial variation. The generalised analytical model only directly incorporates temporal variations in strain, $\delta(t)$. However, we can approximate spatial variations by considering how the strain experienced by a patch of fluid will vary as it is advected in a strain field. For example, a patch of fluid in the ocean mixed-layer initially in a region of convergence between two eddies will ultimately be advected out of that region, implying an effective decrease of the strain with time. As discussed in Chapter 4, this decrease in strain allows waves generated spontaneously by the front and trapped by the strain flow to be released and propagate freely. In Chapter 4 we also showed that time variation in the strain field drives additional wave generation by continually forcing imbalances in the flow. Below we will examine how these analytical predictions compare with the results of the numerical model for a case with strong strain and moderate

Rossby number. The comparison provides insight into the dynamics that are captured by the GM solution, and those features that are missed.

Consider a front subject to large strain ($\delta = 0.9$) with initial Rossby number $Ro = 0.6$ and Burger number $Bu = 1.5$, as in figure 5.5. These parameters are representative of, for example, frontogenesis between submesoscale eddies in the ocean mixed-layer. In the previous example (figure 5.5) the constant strain drove the spontaneous generation of stagnant wave packets, and ultimately the collapse of the surface front to a discontinuity on the boundary. Here, we will consider an *initially* constant strain, leading to the generation of frontogenesis waves as in figure 5.5. We will then decrease the strain smoothly to zero prior to the formation of a discontinuity, permitting the release and propagation of these waves; that is,

$$\delta(T) = \begin{cases} \delta_0 & T < \tau_1 \\ \delta_0 \cos^2\left(\frac{T-\tau_1}{\tau_2-\tau_1} \frac{\pi}{2}\right) & \tau_1 \leq T \leq \tau_2 \\ 0 & T > \tau_2 \end{cases}, \quad (5.9)$$

with $\delta_0 = 0.9$, $\tau_1 = 1.5$ and $\tau_2 = 3$. Figure 5.8 displays Hovmöller plots of the vertical velocity just below the surface ($z = -0.25$) from the (a) generalised and (b) numerical models. The analytical and numerical solutions are very similar; we will first describe the common features before examining the differences. Contours of surface ($z = 0$) buoyancy are overlaid in black on each plot, showing the collapse of the initially broad surface front into a relatively sharp front by time $\tau_2 = 3$. Associated with the surface front collapse, the vertical velocity (and buoyancy gradient) just below the surface is concentrated into two distinct bands on the periphery of the front ($x \sim \pm 0.5$); these are the same frontogenesis wave packets from the constant strain case (figure 5.5). As the strain is decreased to zero, these waves are released and propagate outwards as free inertia-gravity waves. The waves propagate parallel to the characteristics (4.22) for the first vertical mode predicted from the analytical model (overlaid in grey; characteristics for modes two and three also shown). The maximum vertical velocity (the time series of which is overlaid in black) is located at the leading edge of these outward propagating waves. The velocity gradually decreases with time as the horizontal scales in the mode-one wave packets disperse. The propagation of the wave packet in figure 5.8a is indicated by the arrow labelled ‘FG1’. A relatively weak third vertical mode frontogenesis wave packet is also visible propagating outwards in each model, following the mode-three characteristic (labelled ‘FG3’). This wave was visible in the constant strain velocity fields (figure 5.5) at the critical time.

Apart from the frontogenesis wave packets, generated spontaneously during the collapse of the front, there are many other waves visible in figure 5.8 that are generated due to the time variation in the strain (5.9); we call these ‘transience waves’. Specifically, as shown in

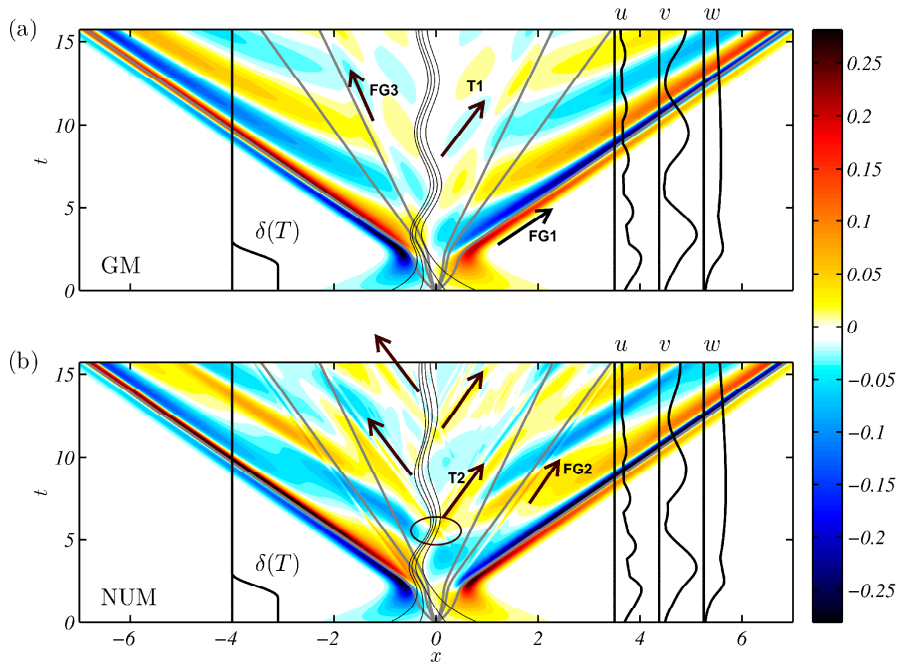


Fig. 5.8 Hovmöller plot of the vertical velocity just below the surface, at $z = -0.25$, from the (a) generalised (GM) and (b) numerical (NUM) models for the time dependent strain defined by (5.9), and parameter values of $Ro = 0.6$, $Bu = 1.5$, $\delta_0 = 0.9$ and $A = 100$. Contours of surface ($z = 0$) buoyancy are overlaid in black, showing the collapse of the front with time. The strain field $\delta(T)$ is overlaid at $x = -4$, and time series of the maximum of the velocities u , v and w near $x = 4$. The characteristics predicted from the analytical model (4.22) for vertical modes $n = 1$ to 3 are overlaid in grey.

Chapter 4, these waves arise due to a change in the strain magnitude altering the secondary circulation that can be supported at the front, thus causing a ‘momentum imbalance’ and driving a continuous adjustment process in response. This adjustment process is analogous to the mass imbalance problem discussed in Chapter 3, and leads to a decaying oscillation in the frontal zone and the continual emission of IGWs as the front adjusts back towards geostrophic balance. Slowly decaying near-inertial oscillations are clearly visible in figure 5.8, both in the surface buoyancy contours and in the time series of maximum horizontal velocities overlaid on figure 5.8. Figure 5.8 shows the production of a near-inertial wave packet associated with this oscillation (indicated by the arrow labelled ‘T1’) which slowly propagates away from the front.

Let us now consider the differences between the numerical and analytical solutions. Firstly, as in the constant strain example (figure 5.5) the numerical mode-one frontogenesis wave packets are intensified compared with the analytical, corresponding to a greater vertical velocity. There are also mode-two wave signals in the numerical model generated both during

frontogenesis (arrow labelled ‘FG2’ in figure 5.8b) and associated with the frontal oscillations once the strain field is turned off (arrow labelled ‘T2’) — by contrast, the generalised model solution has no even modes. The mode-two wave packet generated during frontogenesis can be seen in the vertical velocity field from the constant strain case (figure 5.5), in between the primary mode-one wave packet and the mode-three wave packet. This wave packet propagates outwards along the mode-two characteristic in figure 5.8b, once the strain is turned off. Interestingly, subsequent oscillations of the surface front, as shown in figure 5.8b, generate additional high horizontal wavenumber mode-two wave packets, propagating parallel to the mode-two characteristic. These generation events are indicated by four black arrows in figure 5.8b. The horizontal scale of these waves is much smaller than the other transience waves seen in the solution. Indeed, the waves appear to be generated from a ‘pinching’ of the surface frontal gradient (indicated by the black ellipse in figure 5.8b) that occurs each oscillation in the numerical model — but is not seen in the analytical model. The generation of additional transience waves in the numerical solution leads to more rapid loss of energy from the oscillating front, and hence a more rapid decay in the oscillation amplitude. Despite these differences, the error in the analytical solution remains less than about 20% over the time period shown.

5.4 Equilibrated fronts

As seen in earlier sections, larger Rossby numbers lead to greater slumping of the surface front and more rapid frontal collapse. One consequence of such rapid frontogenesis is that wave energy has insufficient time to accumulate at the wave stagnation points prior to frontal collapse and thus distinct wave features are not readily observed in the flow fields at the critical time for large Rossby numbers (e.g. $Ro = 1.5$, figure 5.4) — in contrast to smaller Rossby numbers (e.g. $Ro = 0.6$, figure 5.3). Since many fronts in the ocean mixed-layer may be characterised by order one Ro , an important question is whether waves will develop after the formation of a sharp front, and whether the generalised analytical model can be of use in predicting the structure of these waves.

We can address this question by adding explicit horizontal diffusion to the numerical model to arrest frontogenesis before the front collapses to the grid scale. For this purpose we use horizontal hyperdiffusion ($n = 4$ in (5.2)) to localise the smoothing to regions of large horizontal gradient (i.e. the front), without substantially affecting the larger scale flow. In this context the hyperdiffusion is intended as a crude representation of the small scale processes that are not captured by the numerical model, but which may arrest frontogenesis. The addition of hyperdiffusion will be unable to realistically represent the often fully

three-dimensional process of frontal equilibration. However, it is sufficient for the present investigation since our focus is on the wave field and not the surface front itself, and in particular, determining whether the wave field is substantially modified by the local dynamics at the surface front.

With horizontal diffusion and a steady, uniform strain the numerical model eventually achieves a steady state where strain-driven advection (and sharpening of the front) is balanced by diffusion. Figure 5.9a displays the steady state vertical velocity field for a front with parameter values of $Ro = 1.5$, $Bu = 1.5$, $\delta = 0.2$, $A = 100$ and $|Re_h| = 10^7$. These are the same parameter values as for the inviscid solution shown in figure 5.4b; we note that waves are not clearly identifiable in that case. The steady state has a large scale thermally direct circulation as would be expected from both the generalised and HB models. It also possesses intense wave packets at the first vertical mode stagnation points ($x = \pm Bu/(\pi\delta) = \pm 2.4$), similar to those observed for smaller Rossby numbers in the inviscid simulations (e.g. $Ro = 0.6$, figure 5.3). However, the largest amplitude features are the pair of mode-two wave packets at the second vertical mode stagnation points ($x = \pm 1.2$). These wave packets were also visible in the inviscid solution prior to frontal collapse (near $x \sim \pm 1$ in figure 5.4b).

Figure 5.9b displays the time evolution of the vertical velocity at mid-depth towards the steady state. The mode-one wave packets near ± 2.4 noted above develop in the solution around $t = 15$. There are also propagating waves that appear to be generated due to a slight imbalance in the initial condition used in the numerical model. The generation of these propagating waves may also be associated with the formation of PV anomalies in the numerical solution, since the numerical boundary conditions (5.5, 5.6) and hyperdiffusion are inconsistent with PV conservation. As shown by the thick grey PV contours in figure 5.9a, the PV anomalies in the numerical solution are largest near the surface fronts, where the propagating waves appear to originate.

In order to better understand the dynamics of the waves in figure 5.9b, it is useful to consider how the generalised model solution would be modified in the presence of diffusion. As described in Chapter 4, the constant strain GM (forced) solution is determined from the convolution of a Green's function with the boundary buoyancy gradient in momentum coordinates as per (4.31). The presence of diffusion will modify the buoyancy on the rigid boundary as per (5.2d) with $w = 0$,

$$\frac{\partial b}{\partial T} - \delta\chi \frac{\partial b}{\partial \chi} = \frac{Ro(-1)^{n/2+1}}{|Re_h|} \frac{\partial^n b}{\partial x^n}, \quad (5.10)$$

where the left hand-side is written in regular momentum coordinates (χ, Z, T) and the right-hand side in Eulerian coordinates (x, z, t) . The inviscid ($|Re_h| \rightarrow \infty$) solution to (5.10) is

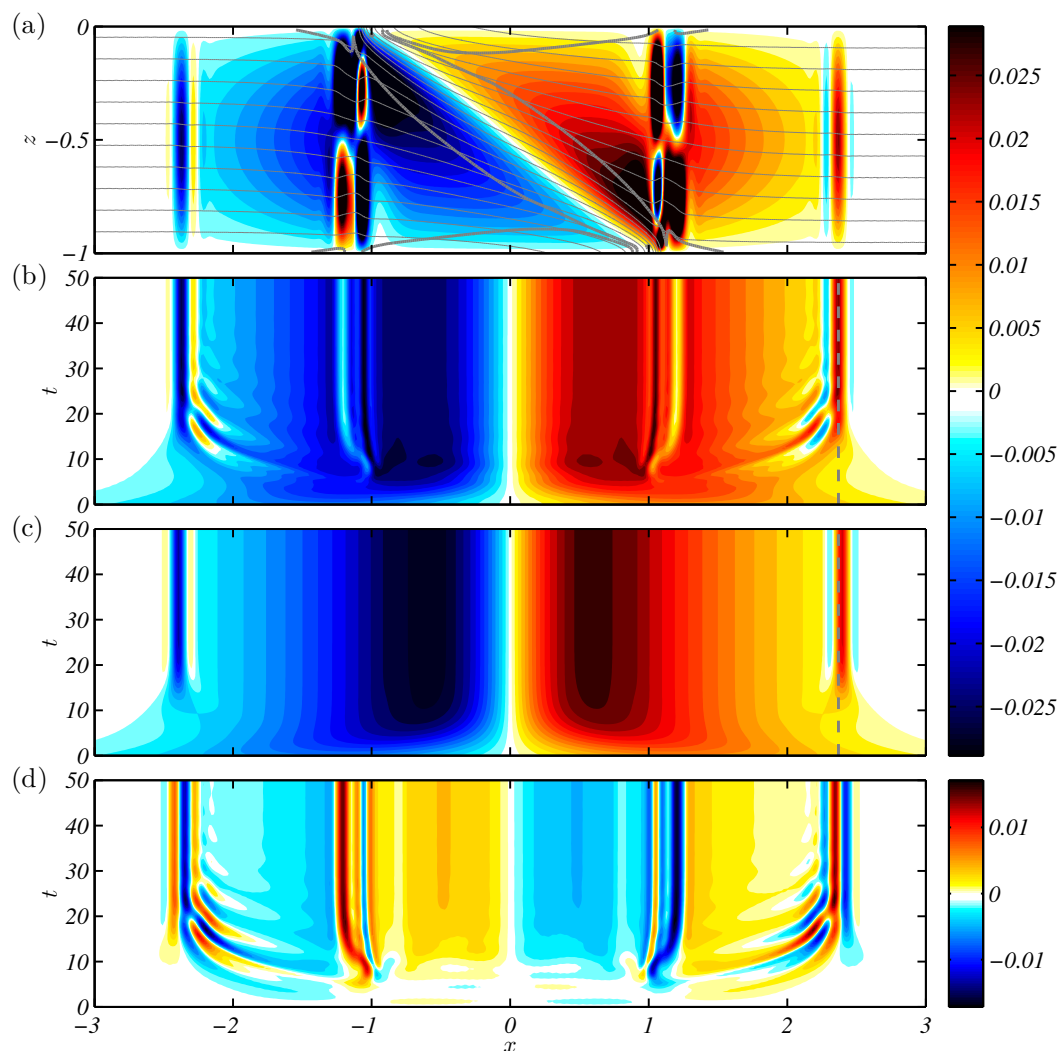


Fig. 5.9 Numerical solution for parameter values of $Ro = 1.5$, $Bu = 1.5$, $\delta = 0.2$ and $A = 100$, as in figure 5.4, but with horizontal hyperdiffusion of $|Re_h| = 10^7$. (a) The steady state vertical velocity field with buoyancy contours overlaid (thin grey lines). The presence of diffusion modifies the PV from the background value of $q = F^{-2}$; the PV contours for 90% and 110% of the background value are displayed (thick grey lines). PV is reduced along the boundary between the fronts and increased in the interior along the frontal axis. (b) Hovmöller of the vertical velocity at mid-depth. (c) The diffusive analytical prediction from (5.12) for the vertical velocity at mid-depth. (d) The difference between (b) and (c).

simply $b = b_0(\chi e^{\delta T})$ for an arbitrary function b_0 , giving rise to the boundary gradient in the GM solution (4.31). We can derive an approximate solution for a finite Re_h by replacing the buoyancy gradient in (4.31) by an approximation to the solution of (5.10) for finite Re_h . To solve (5.10) we assume that the Eulerian derivative on the right-hand side of (5.10) is equivalent to the momentum coordinate derivative, $\partial_x \sim \partial_\chi$, which is true except near the location of the surface front. With this approximation, the solution to (5.10) for the buoyancy gradient $\partial_\chi b$, written in terms of its Fourier transform (denoted by a hat), is

$$\widehat{\partial_\chi b} = \widehat{\partial_\chi b_0}(k e^{-\delta T}) \exp\left(-k^n \frac{Ro}{n \delta |Re_h|} (1 - e^{-n\delta T})\right), \quad (5.11)$$

where k is the horizontal wavenumber. The solution (5.11) satisfies the initial condition $b = b_0$, and boundary conditions $\partial_\chi b(\chi \rightarrow \pm\infty) = 0$. Taking the Fourier transform of the generalised model solution (4.31), and replacing the inviscid boundary buoyancy gradient with our diffusive approximation (5.11), we have an estimate for the diffusive solution of

$$\widehat{\phi}(k, Z, T) = \widehat{\phi}_I(k, Z) \widehat{\partial_\chi b_0}(k e^{-\delta T}) \exp\left(-k^n \frac{Ro}{n \delta |Re_h|} (1 - e^{-n\delta T})\right). \quad (5.12)$$

Equation (5.12) is well-defined in *momentum coordinates* at all times, and collapses to a steady state at late time. The steady state is defined by

$$\widehat{\phi}_{SS}(k, Z) = \widehat{\phi}_I(k, Z) \exp\left(-k^n \frac{Ro}{n \delta |Re_h|}\right), \quad (5.13)$$

assuming an appropriately normalised b_0 . The corresponding (approximate) velocity and buoyancy fields at a given time can be generated from ϕ through the relations (2.27), assuming that the interior flow is essentially inviscid and uniform PV. The solution given by (5.12) will still become multivalued in Eulerian coordinates ($x = \chi - Ro v$) near the locations of the surface fronts, but will be well-defined for all time at mid-depth ($z = -0.5$) where $v = 0$ and hence $x = \chi$.

The time evolution of the vertical velocity at mid-depth predicted from (5.12) is shown in figure 5.9c. The prediction is remarkably similar to the numerical result shown above (figure 5.9b). The prediction captures the overall confinement of the circulation within the first vertical mode stagnation points, $|x| < 2.4$. It also predicts the formation of stagnant wave packets near $x = \pm 2.4$ with the same amplitude and structure as those seen in the numerical solution. The origin of these wave packets is the same accumulation mechanism discussed in the inviscid case that gave rise to the wave packets seen in the inviscid generalised model and numerical solutions at smaller Rossby numbers (e.g. figure 5.3). As noted above, larger

Rossby numbers — as in the present example — lead to more rapid frontal collapse, and hence these wave packets are not visible in the inviscid solution (e.g. figure 5.4) since there is insufficient time for energy to accumulate. Here, with frontal collapse arrested by the introduction of diffusion, energy continues to accumulate beyond the inviscid critical time and the wave packets ultimately develop as seen in figure 5.9. However, the structure of these wave packets is modified by the presence of the diffusion. In the inviscid case, the scale of the wave packets shrinks continually with time, and the amplitude increases. With the addition of diffusion, the wave packet shrinks to the diffusive lengthscale, at which point a steady state is reached. The structure of the steady state wave packet is controlled by the balance between the strain driven sharpening and the diffusive smoothing, as described by the steady state solution (5.13). Since the Green's function ϕ_I is a delta function at the location of the wave packets (see §4.4.1) we have $\widehat{\phi}_I \rightarrow 1$, and thus the steady wave packet structure is defined by the second factor in (5.13) and depends on the type of diffusion (i.e. $n = 2, 4, \dots$). For Laplacian diffusion ($n = 2$) the structure is a simple Gaussian profile. For the hyperdiffusion used in the present example ($n = 4$), the structure has a dominant central maximum, and decaying oscillations to either side — exactly as seen in figure 5.9.

The difference between the numerical vertical velocity at mid-depth and the diffusive approximation (5.12) is shown in figure 5.9d. There is a weak near-inertial oscillation in the region $|x| < 1$ at early times, probably associated with the initial conditions being slightly out of balance, and the subsequent generation of propagating waves (e.g. as discussed in Chapter 3). The stagnant wave packets discussed above also contribute to the difference field in figure 5.9d, due to the fact that they are slightly shifted between the numerical solution (centred on the dashed grey line at $x = \pm 2.37$) and the analytical prediction (centred at $x = \pm 2.4$, outside of the dashed grey line). The shift appears to be due to the analytical prediction (5.12) not including the reduction in propagation speed of the wave packet associated with the fact that it has a diffusion-limited maximum wavenumber (minimum scale), and hence a maximum group speed less than the inviscid maximum of Bu/π that occurs as $k \rightarrow \infty$. The lower group speed results in the wave packet stagnating at a slightly smaller value of $|x|$.

5.5 Discussion

Here we have used fully non-linear numerical simulations to test the generalised model of strain-forced frontogenesis developed in Chapter 2. In particular, here we considered cases with appropriately balanced initial conditions corresponding to the forced solution of the generalised model derived in Chapter 4, which extends the model of Hoskins & Bretherton (1972, HB) to larger values of strain. Consistent with the scaling analysis of §4.2, the

examples considered in §5.3 show that the generalised model is accurate at first order both for small ($\alpha = 0.2f$) and large ($\alpha = 0.9f$) values of strain so long as $Ro^2\delta^2 \ll 1$. Even for small strain, the generalised model represents an improvement on the HB model by correctly describing the confinement of the frontal circulation by the strain field (e.g. figure 5.3). Further, for sufficiently small Rossby number, the examples in §5.3 (particularly figures 5.3 and 5.5) show that the generalised model is capable of accurately describing the spontaneous generation of waves at a strained front. In the case of constant strain these waves takes the form of stationary bands of vertical flow a fixed distance ahead of the surface front.

The generalised model also accurately describes frontogenesis, and the generation and propagation of waves, in a time-varying strain flow. As shown in §5.3.2, the waves generated at constant strain and trapped by the strain field are released when the strain weakens and propagate away from the front. As predicted by the generalised model, the presence of a weakening strain field also drives additional wave generation and oscillations by way of a geostrophic adjustment process (see figure 5.8). These wave dynamics are likely to be relevant to ocean fronts which often exist within strongly time varying strain fields (e.g. Alford *et al.*, 2013).

Furthermore, the dynamics described by the generalised model — including confinement and wave generation — remain relevant beyond the point of discontinuity formation in the inviscid model if some diffusive process is introduced to counteract frontogenesis. In §5.5 we added a horizontal hyperdiffusion to the numerical model in order to allow the front to attain a steady state; the hyperdiffusion can be interpreted as a parameterisation of missing frontolytic processes. We introduced a simple method to expand the generalised analytical model to (approximately) incorporate the effects of diffusion (i.e. (5.12)). As seen in figure 5.9, this approximate solution provides a good estimate of both the secondary circulation and spontaneously generated waves observed in the numerical model, even though these waves are generated beyond the time of discontinuity formation in the generalised model (when it is formally invalid). Thus, the spontaneous generation of wave packets on the periphery of the front appears to be a generic feature of any sharp front that has been subject to a convergent strain for a sufficiently long period of time, $t \gg \alpha^{-1}$, such that wave energy has time to accumulate.

In §5.3.2 we used the numerical model to explore the dynamics of 2D fronts in the limit of large Rossby numbers and large strains ($Ro\delta \sim 1$) where the generalised analytical model is no longer expected to be valid. Even in this parameter regime, numerical simulations produce a frontal circulation that is horizontally confined within the region of possible wave propagation at large time, dimensionally $x + v/f < NH/(\alpha\pi)$, as would be predicted by the generalised model. Hence, the confinement effect appears to be a fundamental constraint

on the system that is independent of approximations made in the generalised model. One important consequence of confinement is increased vertical velocity on the edges of the confinement region. The breakdown of the analytical model for order one Ro and δ is due to the combination of strong confinement (due to large δ), and hence large vertical velocities, and significant outward slumping of the surface front (due to large Ro). As a consequence, the surface front is coincident with the large velocities (e.g. see figure 5.7), and the vertical advection terms neglected in the generalised analytical model (2.29) become important in the numerical solution. The vertical velocities advect the near-surface frontal gradient into the interior of the flow, leading to large interior gradients, whereupon convergence of the strain field across these gradients further amplifies the vertical flow. The positive feedback results in super-exponential growth of the vertical velocity at sharp fronts. This feedback mechanism may provide a dynamical explanation for the exceptionally large vertical velocities directly below submesoscale fronts in the ocean mixed-layer, where Ro and δ may both be order one (Mahadevan & Tandon, 2006).

Here we have shown that the generalised model of frontogenesis provides an accurate description of frontal sharpening and spontaneous wave generation in a simple, idealised theoretical framework. In particular, the validity of the generalised model for order one values of strain, $\alpha \sim f$, makes it applicable to regimes such as the ocean submesoscale. Further, the generalised model includes important dynamical differences — which we have shown here to be robust — compared with the classical Hoskins & Bretherton (1972) model even for relatively small values of strain, $\alpha \sim 0.2f$.

Chapter 6

The linear non-uniform PV model

In this chapter we introduce a generalised *linear* model of frontogenesis valid for arbitrary PV distributions. This model is similar in formulation to the non-linear model developed in Chapter 2 but is derived in regular Eulerian coordinates rather than momentum coordinates — that is, non-linear self-advection associated with the slumping of the surface front is neglected. The linear model thus shares many similarities with the classical QG model of frontogenesis (Williams & Plotkin, 1968), but unlike that model does not assume the strain is weak. In particular, the generalised linear model is able to describe wave generation and non-hydrostatic effects. While less accurate than the uniform PV generalised model, the linear model is more readily applicable to real geophysical fronts which usually have highly variable PV (e.g. figure 1.4c). Furthermore, the inclusion of a non-uniform PV permits us to study the frontogenesis problem in a semi-infinite (i.e. vertically unbounded) domain, without the Davies & Muller (1988) constraint of having flow at infinity. The semi-infinite domain also allows the possibility of wave propagation away from the surface front, and thus allows us to study energy loss from fronts in the ocean and atmosphere boundary layers.

The linear model will be applied to study non-hydrostatic wave generation in Chapter 7 and wave generation in the semi-infinite domain in Chapter 8. Given the focus on applications, we will return to using dimensional equations and variables henceforth, unless otherwise noted.

6.1 Model formulation

The frontogenesis problem has classically been studied in a domain bounded top and bottom by rigid lids (e.g. Hoskins & Bretherton, 1972; Williams & Plotkin, 1968), as examined in previous chapters. Here we wish to generalise the frontogenesis problem to an unbounded domain. Of particular interest is the ‘semi-infinite domain’ consisting of a single rigid

lid at $z = 0$, with a fluid in the region $z \leq 0$. In this configuration, shown in figure 6.1, the rigid lid represents the ocean surface. The configuration can be inverted to obtain an ‘atmosphere model’ with $z = 0$ being the ground, although here it should be assumed we are considering the ocean configuration, unless otherwise noted. We permit the fluid to have some depth dependent stratification, $N^2(z)$, and consider an imposed frontal anomaly with surface signature $b_0(x, 0)$, that will typically decay with depth. Here we consider the situation where the perturbation flow associated with the frontal anomaly, u , is small compared with the background strain, $u \ll \bar{U}$, such that the 2D frontal equations (1.12) become linear, with the material derivative only involving advection by the background flow:

$$\begin{aligned} \frac{D}{Dt} &\equiv \bar{D} = \partial_t + \bar{U} \partial_x \\ &= \partial_t - \alpha x \partial_x \end{aligned} \quad (6.1)$$

As discussed previously, forcing in the equations arises through the geostrophic velocity (pressure gradient) term in (1.12a), and thus the along-front velocity v scales geostrophically, $v \sim \Delta B_0 H / (fL)$. Assuming time scales with the inverse strain rate, $1/\alpha$, (1.12b) implies that $u \sim \alpha / f v$. For the linear model to be strictly valid we require $u \ll \bar{U}$, or substituting the derived scales, $Ro_g = \Delta B_0 H / (f^2 L^2) \ll 1$. Thus, the linearisation is equivalent to the usual quasigeostrophic (QG) assumption that the geostrophic Rossby number is small. However, unlike previous linear QG models (e.g. Williams & Plotkin, 1968, see §1.3.3), we make no assumption about the magnitude of the strain α in comparison to the inertial frequency f . Also unlike previous models, we do not make the hydrostatic assumption.

It is easily shown from the linearised equations that the perturbation potential vorticity (PV) is conserved, or

$$\bar{D}q = 0, \text{ where } q = N^2(z) \frac{\partial}{\partial z} \left(\frac{b'}{N^2(z)} \right) + \frac{N^2(z)}{f} \frac{\partial v}{\partial x}, \quad (6.2)$$

where $b' = b - \int N^2(z) dz$. Note that this perturbation PV is in addition to a background PV of $\bar{Q} = N^2(z)$. Equation (6.2) implies that the PV evolves according to $q = q_0(x e^{\beta(t)}, z)$, where $q_0(x, z)$ is the initial PV distribution and β is the time-integrated strain, as previously (1.11). Thus, the action of the strain flow is to squeeze a PV anomaly with time. Usually such a PV anomaly will be associated with a density front. For consistency with our previous work, here we define the frontal buoyancy anomaly associated with the PV as

$$b_0(x, z) = N^2(z) \int_{-\infty}^z \frac{q_0(x, z')}{N^2(z')} dz', \quad (6.3)$$

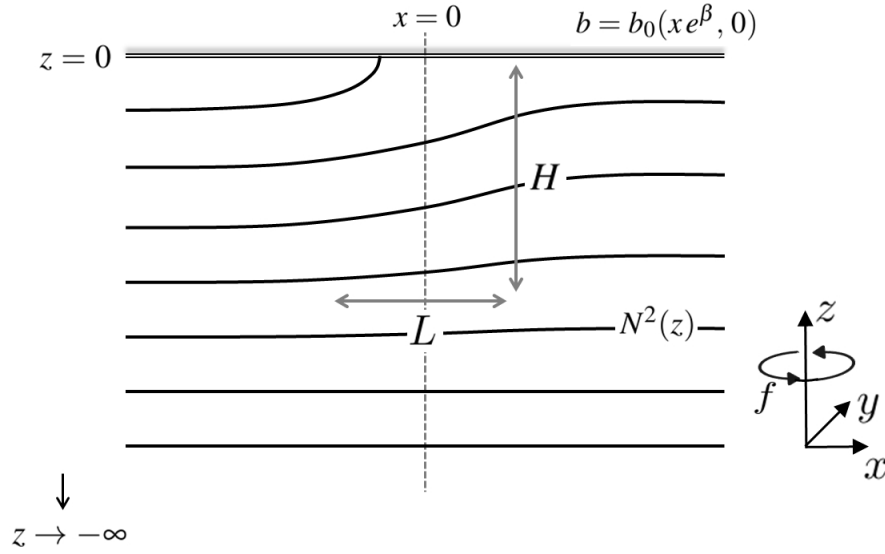


Fig. 6.1 Schematic of the non-uniform PV 2D frontogenesis problem for a semi-infinite domain, $z \leq 0$, with a single rigid lid at the top, representing the ocean surface. The domain is unbounded in the cross-frontal (x) direction, and the front is assumed to be infinitely long into the page (y). The width L and depth scale H of the front are set by the choice of PV anomaly, $q_0(xe^\beta, z)$. The background stratification can be an arbitrary function of depth, $N^2(z)$. The surface buoyancy b_0 is then set by (6.3) and collapses with time in the presence of a confluent background strain flow.

such that the net perturbation buoyancy field, b' , is

$$b'(x, z, t) = b_0(xe^\beta, z) + \Delta b(x, z, t), \quad (6.4)$$

where Δb is the buoyancy response to the imposed PV anomaly. For a rigid lid at $z = 0$ we require that $\Delta b(x, 0, t) = 0$ such that $w = -\bar{D}\Delta b/N^2 = 0$ on the lid. Thus the buoyancy on the rigid lid will be $b_0(xe^\beta, 0)$ at time t as indicated in figure 6.1. Furthermore, the uniform PV frontogenesis formulation studied previously (or at least the linear version thereof) may be recovered by setting N^2 to a constant and considering an infinitely thin layer of surface vorticity; that is,

$$q_0(x, z) = -g(x)\underline{\delta}(z) \implies b_0(x, z) = H(-z)g(x), \quad (6.5)$$

from (6.3) for an arbitrary function g , where $\underline{\delta}$ is the Dirac delta function and H is the Heaviside function. We thus obtain the result that b_0 is a function of x only in the domain of interest, $z \leq 0$, as per the previous model (e.g. equation (2.21)).

Returning to the general non-uniform PV problem, the objective now is to formulate an equation for the evolution of the buoyancy response Δb (6.4), forced by the strain-driven collapse of the frontal anomaly b_0 . The buoyancy response Δb may be related to the along-front velocity, v , by substitution of (6.4) into the PV equation (6.2):

$$\frac{\partial v}{\partial x} = -f \frac{\partial}{\partial z} \left(\frac{\Delta b}{N^2(z)} \right). \quad (6.6)$$

The solution proceeds by taking the material derivative of the y -momentum equation (1.12b), and substituting the x -momentum equation (1.12a), to obtain

$$(\bar{D}^2 + f^2 - \alpha^2 + \partial_t \alpha) v = f^2 v_g. \quad (6.7)$$

Equation (6.7) is the linearised version of the combined horizontal momentum equation seen in our previous solution (2.28). The geostrophic velocity is defined from the vertical momentum balance (1.12c), rewritten here as

$$\begin{aligned} \frac{\partial v_g}{\partial z} &= \frac{1}{f} \frac{\partial}{\partial x} (b' - \bar{D}w), \\ &= \frac{1}{f} \frac{\partial}{\partial x} \left(b_0 + \Delta b + \frac{\bar{D}^2 \Delta b}{N^2(z)} \right), \end{aligned} \quad (6.8)$$

noting that $w = -\bar{D}\Delta b/N^2(z)$ in the linearised framework.

We now take an x and z derivative of (6.7), and substitute $\partial_x v$ from (6.6) and $\partial_z v_g$ from (6.8), yielding an equation for Δb :

$$\left[\underbrace{(\bar{D}^2 - 2\alpha\bar{D}) \frac{\partial^2}{\partial z^2} \frac{1}{N^2(z)}}_{\text{cross-front accel.}} + \underbrace{\frac{1}{N^2(z)} \frac{\partial^2}{\partial x^2} \bar{D}^2}_{\text{vertical accel.}} + \underbrace{\left(\frac{\partial^2}{\partial z^2} \frac{f^2}{N^2(z)} + \frac{\partial^2}{\partial x^2} \right)}_{\text{geostrophic}} \right] \Delta b(x, z, t) = \underbrace{-\frac{\partial^2}{\partial x^2} b_0(x e^\beta, z)}_{\text{strain forcing}}, \quad (6.9)$$

subject to homogeneous boundary conditions at the rigid lid and at infinity. We call (6.9) the *linear generalised model*. Flow is forced via the strain driven collapse of the buoyancy/PV anomaly, as per the right-hand side of (6.9). There are three distinct terms on the left-hand side of (6.9) that control the response of the system to this forcing. The geostrophic term is familiar from the QG frontal model that assumes cross-front geostrophic and hydrostatic

balance (e.g. Williams & Plotkin, 1968). The cross-front acceleration term is associated with $\bar{D}u$ and αu in (1.12a), and scales as $(\alpha/f)^2$ compared to the geostrophic term. The vertical acceleration, or non-hydrostatic term, is associated with $\bar{D}w$ in (1.12c), and scales as $(\alpha H/(fL))^2$ compared to the geostrophic term. While negligible initially, this term can become of first order importance as the front collapses.

Equation (6.9) may be solved numerically for a given choice of initial conditions, buoyancy anomaly b_0 , strain $\alpha(t)$, and stratification $N^2(z)$. The solution procedure is described in Appendix B. Such numerical solutions will be used in §7.4 to investigate the effect of variable stratification profiles on wave trapping.

In the next section we derive an analytic solution for the special case of constant strain and stratification.

6.2 Analytic solution: constant strain and stratification

Here we will first consider an infinite domain in both x and z . As will be described below, the semi-infinite domain solution with a rigid lid at $z = 0$ may be obtained directly from the infinite domain solution. Taking the Fourier transform of (6.9) in x and z (with N^2 and α constant) yields

$$\left[\left(\widehat{D}^2 - 2\alpha\widehat{D} + f^2 \right) \frac{-l^2}{N^2} - \frac{k^2}{N^2} \widehat{D}^2 - k^2 \right] \widehat{\Delta b} = k^2 e^{-\alpha t} \widehat{b}_0(k e^{-\alpha t}, l), \quad (6.10)$$

where k and l are the horizontal and vertical wavenumbers, respectively, hats denote the Fourier transform, and $\widehat{D} = \partial_t + \alpha(1 + k\partial_k)$ is the transformed material derivative. The general solution to the PDE (6.10) for $\{\alpha, l, N\} \neq 0$ is

$$\begin{aligned} \widehat{\Delta b}(k, l, t) = & \underbrace{-\varepsilon^2 \left(G(\varepsilon) \left[e^{-\alpha t} \widehat{b}_0(k e^{-\alpha t}, l) \right] \right)}_{\text{forced}} \\ & + \underbrace{H_+(\varepsilon) \left[e^{-\alpha t} c_1(k e^{-\alpha t}, l) \right] + H_-(\varepsilon) \left[e^{-\alpha t} c_2(k e^{-\alpha t}, l) \right]}_{\text{adjustment waves}}, \end{aligned} \quad (6.11)$$

where the c_i are unknown functions dependent on the choice of initial conditions.¹ The parameter ε in (6.11) is defined as

$$\varepsilon = \frac{Nk}{fl}, \quad (6.12)$$

¹This solution structure emerges due to the form of the material derivative in the linearised system; i.e. $\widehat{D} \left[e^{-\alpha t} \widehat{F}(k e^{-\alpha t}, l) \right] = 0$ for any \widehat{F} , which is the Fourier equivalent of $\bar{D}[F(xe^{\alpha t}, z)] = 0$.

and corresponds to the scaled mode slope, or Burger number, of a given wavenumber (k, l) combination — the significance of this parameter will be described in more detail in §6.2.1 below. The solution (6.11) contains two parts. The ‘forced’ part is defined by the requirement that time dependence only arises through the strain driven collapse of the buoyancy (and PV) anomaly, $b_0(xe^{\alpha t}, z)$, as per the forcing to the right-hand side of (6.9) and (6.10). This part of the solution is equivalent to the ‘forced solution’ derived in §4.4 for the non-linear model. The remaining ‘adjustment wave’ part of (6.11) describes propagating waves generated due to the adjustment of initial conditions that differ from those implied by the forced solution. The unusual form of the wave solutions in (6.11) is due to the fact that the strain field modifies the propagation of, and ultimately traps the waves as described in §3.3.2 for the non-linear but hydrostatic case. In this and following chapters, our focus is on waves generated in response to strain forcing rather than via adjustment of initial conditions, and thus here we will only consider the forced part of the flow.

6.2.1 Green’s Functions

Firstly, let us consider the requirements for the forced solution defined in (6.11) to be physical. A key requirement is that $G(\varepsilon)$ in (6.11) must be finite at $\varepsilon = 0$. To see this, consider that the forced part of the general solution (6.11) can be rewritten in terms of the along-front shear, by Fourier transforming (6.6) to yield

$$\widehat{\partial_z v} = ik \widehat{\Delta b} / (f \varepsilon^2) = f^{-1} G(\varepsilon) \left[-ik e^{-\alpha t} \widehat{b}_0(k e^{-\alpha t}, l) \right]. \quad (6.13)$$

The function $\widehat{\partial_z v}_G = f^{-1} G(\varepsilon)$ in (6.13) is the *Green’s function* for the along-front shear. It contains all the dynamics and structure of the forced response, independent of the details of the buoyancy anomaly b_0 . The Green’s function depends only on the scaled wavenumber, $\varepsilon = kN/(fl)$, which can be thought of as the Burger number, or slope, of a given mode (k, l) . In physical space, the solution (6.13) may be written as a double convolution of the Green’s function with the buoyancy gradient anomaly,

$$\partial_z v(x, z, t) = \int_{-\infty}^{\infty} \int_{-\infty}^{\infty} \partial_z v_G(x - x_0, z - z_0) \frac{\partial}{\partial x_0} b_0(x_0 e^{\alpha t}, z_0) dx_0 dz_0. \quad (6.14)$$

A valid solution for the along-front shear requires that its integral over all x has a finite value. The integral over all x is equal to the $k = \varepsilon = 0$ value of its spectrum, $\widehat{\partial_z v}(0)$ in (6.13). The square bracketed factor in (6.13) corresponds to the buoyancy anomaly gradient. Again, the $k = \varepsilon = 0$ value of this factor is the integral over all x of the buoyancy gradient:

$\int_{-\infty}^{\infty} \partial_x b_0(xe^{\alpha t}, z) dx = \Delta b(z)$, the buoyancy difference across the front, which is finite for all time. For $\widehat{\partial_z v}(0)$ to be finite we thus require that $G(0)$ is finite.

The functions G and H_{\pm} in (6.11) may be obtained by substitution of (6.11) into the PDE (6.10), yielding the ODE:

$$\left[\underbrace{1 + \varepsilon^2}_{\text{geostrophic}} + \underbrace{\frac{\alpha^2}{f^2} \left(\varepsilon^2 \frac{\partial^2}{\partial \varepsilon^2} + 3\varepsilon \frac{\partial}{\partial \varepsilon} \right)}_{\text{cross-front accel.}} + \underbrace{\varepsilon^2 \frac{\alpha^2}{N^2} \left(\varepsilon^2 \frac{\partial^2}{\partial \varepsilon^2} + 5\varepsilon \frac{\partial}{\partial \varepsilon} + 4 \right)}_{\text{vertical accel.}} \right] G(\varepsilon) = -1. \quad (6.15)$$

The functions G and H_{\pm} are, respectively, the particular and homogeneous solutions to (6.15). We observe that (6.15) has one singular point at $\varepsilon = 0$, and moreover this is a *regular singular point* (Boyce *et al.*, 1992, §5.6-5.7 therein). Before solving (6.15) directly we need to examine how the solutions behave near this singular point. The leading order term in the homogeneous solution near the singular point may be determined by substituting $G \sim \varepsilon^p$, and collecting the coefficients of ε^p to form the indicial equation:

$$\delta^2 p(p-1) + 3\delta^2 p + 1 = 0 \implies p = -1 \pm \sigma i, \quad (6.16)$$

where $\delta = \alpha/f$ is the non-dimensional strain and $\sigma = \sqrt{f^2 - \alpha^2}/\alpha$, as previously. Equation (6.16) implies that the homogeneous solutions are infinite at $\varepsilon = 0$; for instance, for $\alpha < f$ and therefore σ real, at leading order the solutions (Boyce *et al.*, 1992) are

$$H_{\pm}(\varepsilon) \sim \frac{1}{\varepsilon} \begin{cases} \sin(\sigma \ln|\varepsilon|) \\ \cos(\sigma \ln|\varepsilon|) \end{cases}, \quad (6.17)$$

near $\varepsilon = 0$. The same is true for $\alpha \geq f$ although the form of the solutions is different. Now consider the forced (rather than homogeneous) equation (6.15). It is immediately apparent that there exists a forced solution that goes like $G(\varepsilon) \sim -1$ near $\varepsilon = 0$ (i.e. $G(0)$ is finite). Since the homogeneous solutions are infinite at $\varepsilon = 0$, there is only one such forced solution. Thus there is a unique *physical* forced solution (6.13) and its properties are entirely controlled by the Green's function $G(\varepsilon)$ as described above.

We now determine the unique Green's function $G(\varepsilon)$ in various limits by directly solving (6.15). Note that the three distinct terms discussed in the context of (6.9) are also labelled in (6.15). The simplest limit is that of small strain, $\alpha \ll f$ and $\alpha \ll N$, where the cross-front and vertical acceleration terms may be neglected, yielding the classical QG model solution,

$$G_{QG}(\varepsilon) = -\frac{1}{1 + \varepsilon^2}. \quad (6.18)$$

We call (6.18) the *quasigeostrophic Green's function*. Now consider higher order solutions of (6.15) involving the derivative terms. Such solutions are most easily obtained by seeking a power series solution, i.e.

$$G(\varepsilon) = -1 + c_1\varepsilon + c_2\varepsilon^2 + c_3\varepsilon^3 + \dots \quad (6.19)$$

which may then be expressed in terms of generalised hypergeometric functions as below. The hydrostatic limit of (6.15) is characterised by $f \ll N$, but unlike QG, does not require the strain to be small. In this limit, the vertical acceleration terms may be neglected to yield

$$G_H(\varepsilon) = -1 + \frac{\varepsilon^2}{1 + 8\delta^2} {}_1F_2\left(1; \mathbf{q}; -\frac{\varepsilon^2}{4\delta^2}\right), \quad (6.20)$$

where ${}_pF_q$ is the generalised hypergeometric function with $\mathbf{q} = \{5/2 - \iota\sigma/2, 5/2 + \iota\sigma/2\}$. The *hydrostatic Green's function* (6.20), and thus the flow dynamics in this limit, depends only on the ratio of the strain and inertial timescales, α/f .² The most general solution to (6.15), including all terms, is

$$G_{NH}(\varepsilon) = -1 + \varepsilon^2 \frac{1 + 4(\alpha/N)^2}{1 + 8(\alpha/f)^2} {}_pF_q\left(\mathbf{p}; \mathbf{q}; -\frac{f^2\varepsilon^2}{N^2}\right), \quad (6.21)$$

where $\mathbf{p} = \{1, 2 - \iota N/(2\alpha), 2 + \iota N/(2\alpha)\}$, and the other parameters are defined as previously. The structure of the *non-hydrostatic Green's function* (6.21) depends on relative sizes of all three timescales in the problem: forcing, α^{-1} , inertial, f^{-1} , and gravitational, N^{-1} .

As shown above, $G(\varepsilon)$ is the Green's function for the along-front shear (6.13). Green's functions for other dynamical fields may also be written as derivatives of $G(\varepsilon)$. For instance, since $u = -f^{-1}(\bar{D} + \alpha)v$ from (1.12b), it may be shown that the Green's function for the cross-front shear is defined by

$$\widehat{\partial_z u}_G = -f^{-1} \delta \left(\varepsilon \frac{\partial}{\partial \varepsilon} + 2 \right) G(\varepsilon). \quad (6.22)$$

Similarly, the Green's function for the divergence may be derived from continuity (1.12e) and satisfies,

$$\widehat{\partial_x u}_G = -\widehat{\partial_z w}_G = -N^{-1} \delta \varepsilon \left(\varepsilon \frac{\partial}{\partial \varepsilon} + 2 \right) G(\varepsilon). \quad (6.23)$$

²This solution (6.20) is identical to the hydrostatic Green's function derived in Chapter 4 (up to scaling by a constant). However here we define the Green's function in Fourier (k) space rather than physical (x) space. Also, here we are using the regular Eulerian coordinate x and not the momentum coordinate χ .

Note that the motivation for using the shear and divergence of the velocity fields in the above expressions, rather than the velocities themselves, is that the former depend only on the mode slope, $\varepsilon = Nk/(fl)$, whereas the latter depend on the individual horizontal and vertical wavenumbers. Nonetheless, the expressions for the Green's functions for any of the velocity fields or streamfunction (e.g. $\widehat{\psi}_G = -\widehat{\partial_z w}_G/(kl) = -\widehat{\partial_z u}_G/l^2$) are readily obtained from the above expressions.

The Green's functions for the along-front shear, cross-front shear and divergence are plotted in figure (6.2) for the three models derived above (QG, hydrostatic, non-hydrostatic) for a relatively small strain, $\alpha = 0.2f$. Panels (a,c,e) display the Green's functions in spectral space as a function of the mode slope $\varepsilon = Nk/(fl)$. Panels (b,d,f) display the horizontal structure (where the scaled horizontal coordinate $x' = xfl/N$) of the Green's function for a single vertical wavenumber l . In the dual rigid lid model studied in previous chapters there is a discrete vertical wavenumber spectrum (i.e. $l = n\pi/H$ for integer n) and thus plots (b,d,f) give the actual horizontal flow structure seen in the solutions. For the (semi-) infinite model there is a continuum of vertical wavenumbers and the actual horizontal structure is an average over all these wavenumbers. Consequently, the horizontal structure of the unbounded domain solutions will be quite different to that shown in the plots (e.g. see §6.3). Nonetheless, the plots provide a useful comparison of the three models developed in this chapter. With reference to figure 6.2, the major points of similarity/difference are:

- There is negligible difference in the along-front shear (panels a, b) between the three models for the small value of strain considered here. Differences will emerge at larger values of strain.
- The cross-front shear and divergence spectra (c, e) for all three models agree for small mode slopes ε (i.e. large horizontal scales and small vertical scales). This behaviour is consistent with the notion that large scale motions are essentially geostrophic. Differences between the unbalanced (hydrostatic/non-hydrostatic) models and the QG model begin appearing for $\varepsilon \sim 1$, or equivalently slopes $k/l \gtrsim f/N$. These differences take the form of oscillations in the spectrum, implying a preferential accumulation of amplitude/energy at certain wavenumber combinations and thus the generation of wave packets of particular frequency and slope (see Chapter 8).
- As expected, differences between the hydrostatic and non-hydrostatic models become significant for mode slopes $k/l \sim 1$ (in this case $\varepsilon \gtrsim 10$) as seen in panels c and e. The non-hydrostatic spectrum has lower amplitude at high wavenumbers than the hydrostatic.

- While non-hydrostatic effects are only important for the smallest horizontal scales and may appear relatively minimal in the spectra (c, e), they cause a significant qualitative difference in the horizontal structure of the vertical velocity (panel f) for a given vertical wavenumber. The sharp cut-off in amplitude seen in the hydrostatic model is no longer present. Instead the amplitude decays smoothly to zero outside of this location. Furthermore, many bands of vertical flow appear, with smaller scales appearing closer to the strain axis ($x = 0$).

We can understand the qualitative behaviour of the Green's functions in terms of the dispersion relations for hydrostatic and non-hydrostatic inertia-gravity waves. For freely propagating waves (i.e. in the absence of a strain flow) the dispersion relation is

$$\omega_{NH}(k, l) = f \sqrt{\frac{1 + \frac{Nk}{fl}}{1 + \frac{k}{l}}}, \quad (6.24)$$

or in the hydrostatic limit, $k \ll l$,

$$\omega_H(k, l) = f \sqrt{1 + \frac{Nk}{fl}}. \quad (6.25)$$

The horizontal velocity of a freely propagating plane wave is $c_p = \omega/k$ in each case. In the hydrostatic limit, $c_p \rightarrow N/l = \max c_g$ for small scales (where $c_g = \partial_k \omega$). In other words, all small scales propagate at the same speed, and therefore will stagnate at the same location in the flow — namely where the maximum group speed equals the strain flow speed, as described in previous chapters — giving rise to the sharp cut-off in amplitude and single wave band seen in the hydrostatic Green's function. The behaviour of waves in the non-hydrostatic model is the same as in the hydrostatic for small horizontal wavenumbers, $k/l \ll 1$. However, wavenumbers larger (or scales smaller) than this propagate more slowly than in the hydrostatic model, and thus tend to be confined closer to the strain axis ($x = 0$). Furthermore, since all the small scales do not stagnate in the same location, there is no sharp cut-off in the amplitude of the Green's function.

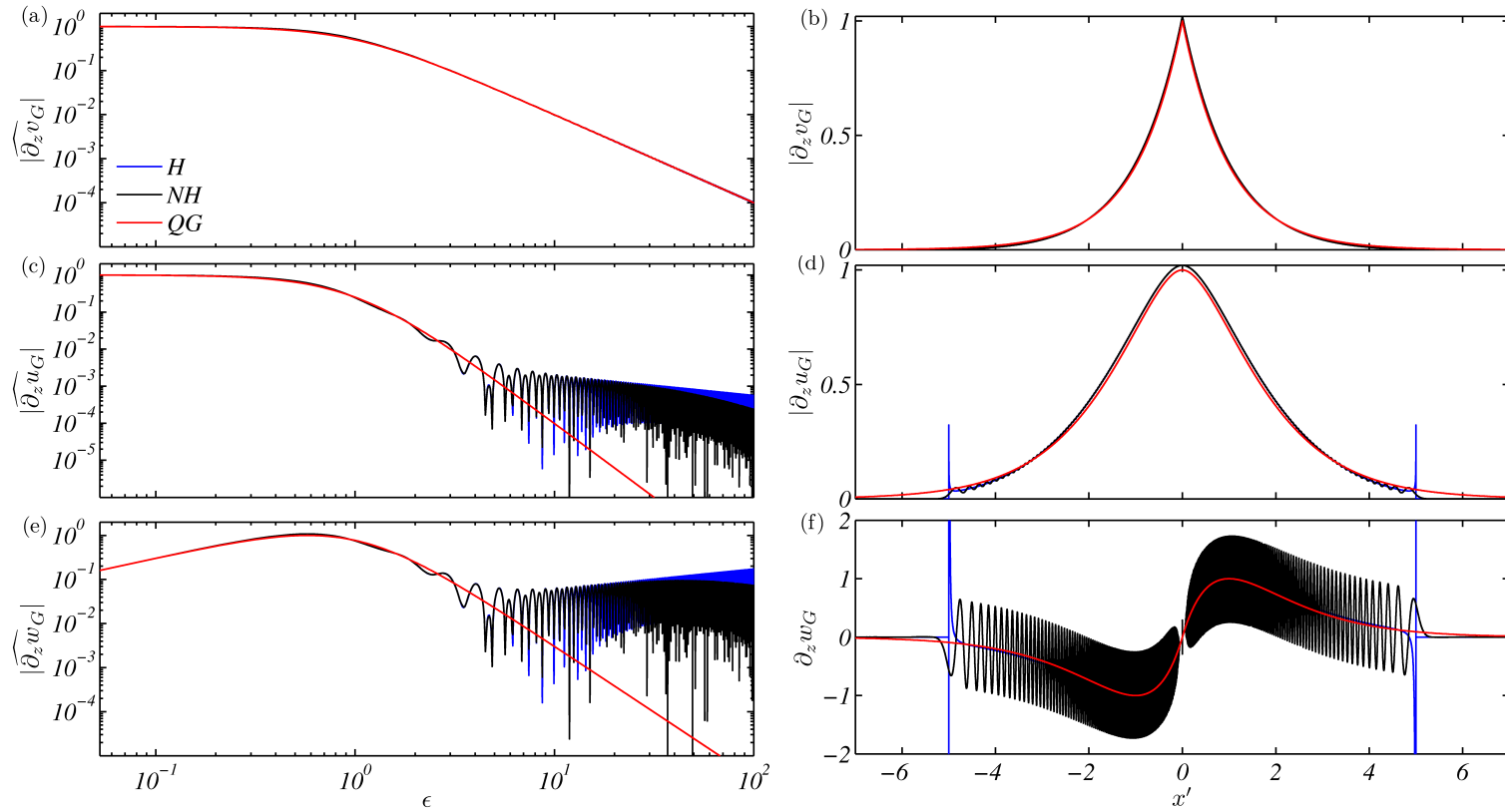


Fig. 6.2 (Normalised) Green's functions from the three limits of the constant strain and stratification linear model: quasigeostrophic (QG, red; (6.18)), hydrostatic (H, blue; (6.20)) and non-hydrostatic (NH, black; (6.21)). The plots are for parameter values of $\alpha/f = 0.2$ and $N/f = 61$. (a,c,e) The modulus of the spectral Green's function for the (a) along-front shear $\widehat{\partial_z v_G}$, (c) cross-front shear/streamfunction $l^2 \widehat{\psi_G} = -\widehat{\partial_z u_G}$ and (e) divergence $\widehat{\partial_z w_G}$, as a function of the mode slope $\epsilon = Nk/(fl)$. The high wavenumber oscillations in the H and NH models are associated with waves. (b,d,f) The cross-frontal structure of the Green's function for a single vertical wavenumber l for (b) along-front shear $\partial_z v_G$, (d) cross-front shear/streamfunction $l^2 \widehat{\psi_G} = -\widehat{\partial_z u_G}$ and (f) divergence $\partial_z w_G$. The non-dimensional horizontal coordinate x' is defined as $x' = flx/N$.

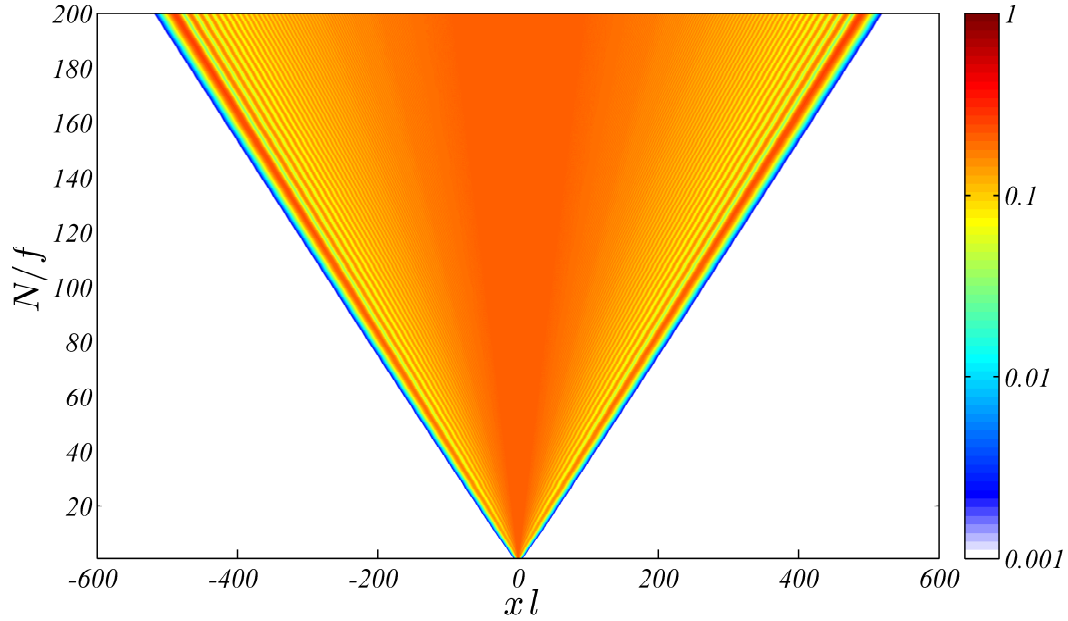


Fig. 6.3 Normalised cross-frontal shear Green's function $|\partial_z u_G|$ as a function of N/f for a strain of $\delta = \alpha/f = 0.4$ and single vertical wavenumber l . The amplitude is almost entirely confined within the region where the maximum hydrostatic group speed, $\max c_g = N/l$, exceeds the strain flow speed, αx , or equivalently the region where $N/f > \delta x l$.

Figure 6.2 displayed the Green's functions for a single value of the stratification ratio N/f . In figure 6.3 we plot the non-hydrostatic cross-frontal shear Green's function $|\partial_z u_G|$ for a single value of strain ($\alpha = 0.4f$) and vertical wavenumber l , as a function of the stratification ratio N/f and cross-frontal position $x l$. This figure emphasises that for any stratification the Green's function amplitude is almost entirely confined within the region where the maximum hydrostatic group speed, $\max c_g = N/l$, exceeds the strain flow speed, αx , or equivalently where $N/f > \delta x l$. Further, figure 6.3 demonstrates how the banded wave structures observed in the previous figure depend on the stratification: as N/f is increased more wave bands develop and existing bands become wider. In the limit $N/f \rightarrow 1$ the bands vanish entirely, since waves are unable to propagate (i.e. $\omega \rightarrow f$ and $c_g \rightarrow 0$ for all scales).

We now detail how the full solutions may be generated from the Green's functions for the various domains of interest.

6.3 Solutions in three domains

6.3.1 Fully infinite domain

Firstly, let us consider the fully infinite domain, $-\infty < z < \infty$, where the solution is defined by the product in Fourier space of the gradient of the imposed buoyancy anomaly ($\partial_x b_0(x, z)$) at some instant in time with the Green's function for the field of interest (e.g. (6.13)). In figure 6.4 we display an example solution for the vertical velocity fields from (a) the QG model and (b) the hydrostatic model for a buoyancy anomaly of $b_0(x, z) = \Delta B_0 \exp(-(z/H)^2 - (x/L_R)^2)$ (where $L_R = NH/f$ is the Rossby radius) and strain $\alpha = 0.4f$. This buoyancy anomaly corresponds to a 'blob' of warm fluid centred on the origin as shown by the buoyancy contours (in blue) on figure 6.4a. The associated perturbation PV, $q_0 = \partial_z b_0$ (6.3), is also shown (black/grey contours). The QG model solution in figure 6.4a demonstrates that the action of the background strain on the PV anomaly drives a secondary flow, which is localised near to the PV anomaly. The hydrostatic model shown in figure 6.4b predicts a similar secondary circulation localised near the PV anomaly, but also predicts the radiation of waves away from the PV anomaly into the far field (note the different vertical axes in figures 6.4a and b).

6.3.2 Semi-infinite domain

While the fully infinite domain solution displayed in figure 6.4 has intriguing structure, it is unclear whether it is particularly relevant to any geophysical situation. However, we can easily generate solutions for the arguably more relevant semi-infinite domain $z \leq 0$ (shown schematically in figure 6.1) from the above theory. Solutions for the semi-infinite domain can be generated using the solutions in the previous section by mirroring the buoyancy anomaly defined for $z \leq 0$ into the region $z > 0$; that is, multiplying b_0 by $-\text{sign}(z)$ (equivalent to changing the vertical Fourier transform to a pure sine transform). This process ensures that the solution contains only odd (sine) vertical modes, and thus enforces the rigid lid boundary condition of $w = 0$ at $z = 0$. Solutions in the semi-infinite domain will be investigated in Chapter 8.

6.3.3 Dual rigid lid domain

The solutions for the dual rigid lid configuration can also be readily obtained for each of the three linear models. As noted above, the only change from the (semi-)infinite problem is the discretisation of the vertical wavenumber spectrum — that is, $l = n\pi/H$ for integer n

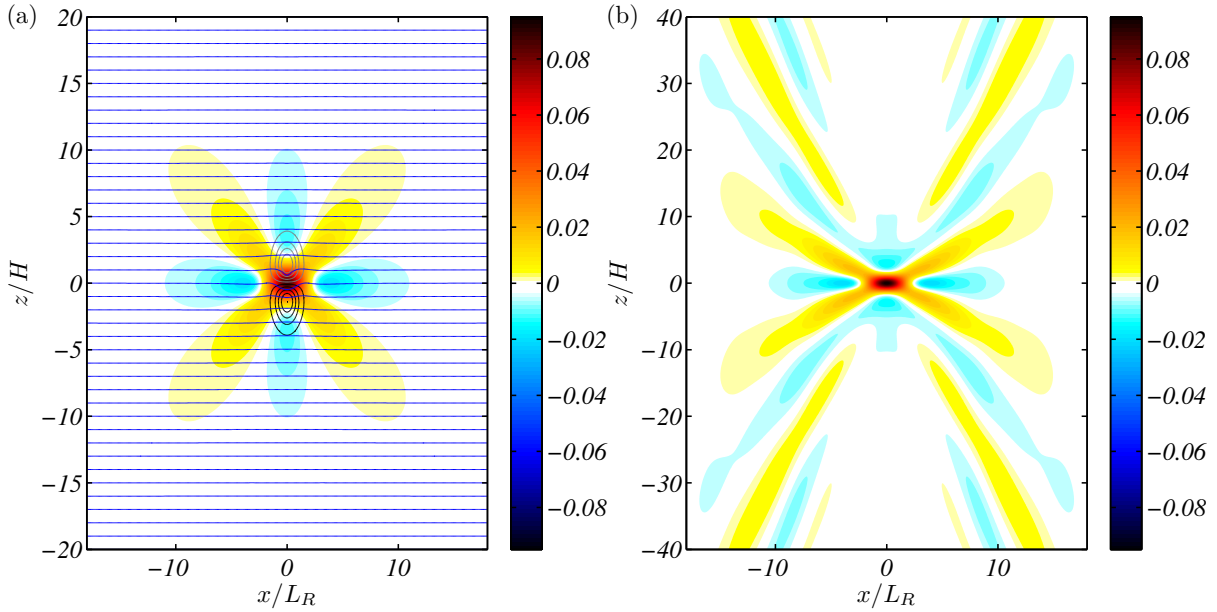


Fig. 6.4 Fully infinite domain solution (vertical velocity field) for a ‘blob’ buoyancy anomaly of $b_0(x, z) = \Delta B_0 \exp(-(z/H)^2 - (x/L_R)^2)$ — where $L_R = NH/f$ is the Rossby radius — and strain $\alpha = 0.4f$ from the (a) QG model and (b) hydrostatic model. The perturbation PV q is contoured on (a) with grey contours implying negative PV and black positive. The buoyancy field is contoured in blue. The action of the background strain on the region of perturbation PV gradient near $z = 0$ and associated ‘blob’ of increased buoyancy drive a secondary flow. The vertical velocity associated with this secondary flow is shown in units of $\Delta B_0 f / N^2$. The hydrostatic model (b) also predicts the radiation of waves away from the PV anomaly. Note the different vertical axes in the two plots.

— in order to satisfy the two rigid lid boundary conditions. For the dual rigid lid model the buoyancy anomaly in spectral space is thus defined by

$$\widehat{b}_0(k, n) = \frac{2}{H} \int_{-\infty}^{\infty} \int_0^H b_0(x, z) \sin \frac{n\pi z}{H} dz e^{ikx} dx, \quad (6.26)$$

$$= -\frac{2(-1 + (-1)^n)}{n\pi} \int_{-\infty}^{\infty} b_0(x) e^{ikx} dx. \quad (6.27)$$

The simplification (6.27) applies in the uniform PV limit (as studied in prior chapters) where the buoyancy anomaly is uniform in z , $b_0 = b_0(x)$. In spectral space the rigid lid solutions are

$$\widehat{\Gamma}(k, n) = \widehat{\Gamma}_G \left(\varepsilon = \frac{NHk}{fn\pi}, n \right) \times \left[-ik e^{-\alpha t} \widehat{b}_0(k e^{-\alpha t}, n) \right], \quad (6.28)$$

for an arbitrary field Γ with Green’s function $\widehat{\Gamma}_G$ as defined in the previous section. In real space the solution is a convolution in x and a sum over the discrete vertical modes (c.f. a

double convolution for the (semi-)infinite case, e.g. (6.14)):

$$\Gamma(x, z, t) = \sum_{n=1}^{\infty} \left\{ \begin{array}{l} \sin \frac{n\pi z}{H} \\ \cos \frac{n\pi z}{H} \end{array} \right\} \int_{-\infty}^{\infty} \Gamma_G(x - x_0, n) \frac{\partial}{\partial x_0} b_0(x_0 e^{\alpha t}, n) dx_0. \quad (6.29)$$

The sin/cos modes must be chosen appropriately depending on the field Γ (e.g. sin for w , ψ or Δb , cos for u or v etc.). The spatial Green's function $\Gamma_G(x, n)$ in (6.29) is exactly what is plotted in figure 6.2b,d,f above. We will employ the dual rigid lid solution to study non-hydrostatic dynamics in the next chapter.

6.4 Summary

In this chapter we have derived a generalised non-hydrostatic linear model for the flow around a strained front. We derived analytic solutions for the special case of constant strain and uniform stratification. The solutions are unique in the sense that they are the only possible solution where time only enters the problem through the strain-driven collapse of the PV anomaly, i.e. $q = q_0(x e^{\alpha t}, z)$. In this way, the model developed here is an extension of the classical quasigeostrophic balance model (Williams & Plotkin, 1968) — which also possesses this property — to situations where the strain may be large, $\alpha/f \sim 1$, or the stratification weak, $N/f \sim 1$. The non-hydrostatic model collapses to the hydrostatic model in the limit $N/f \rightarrow \infty$, and to the quasigeostrophic model in the limit $\alpha/f \rightarrow 0$. The three models — non-hydrostatic, hydrostatic and quasigeostrophic — are summarised in table 6.1 for reference. The solutions developed here can be used to solve the linear strained front problem in any domain of interest whether dual rigid lid, semi-infinite or fully infinite.

In the next two chapters we employ the linear model developed above to study atmospheric and oceanic phenomena. Specifically, in Chapter 7 we investigate the importance of non-hydrostatic dynamics in the formation of finescale cloud bands around sharp atmospheric fronts. Following this, in Chapter 8, we investigate the predictions of the semi-infinite hydrostatic solution with regard to the properties of waves generated at strained submesoscale fronts in the ocean mixed layer.

Description	Eqn.	Definition
Mode slope		$\varepsilon = \frac{Nk}{f\ell}$
Non-Hydrostatic (NH) Green's function	(6.21)	$G(\varepsilon) = -1 + \varepsilon^2 \frac{1+4(\alpha/N)^2}{1+8(\alpha/f)^2} {}_pF_q \left(\mathbf{p}; \mathbf{q}; -\frac{f^2\varepsilon^2}{N^2} \right)$
Hydrostatic (H) Green's function	(6.20)	$G(\varepsilon) = -1 + \frac{\varepsilon^2}{1+8\delta^2} {}_1F_2 \left(1; \mathbf{q}; -\frac{\varepsilon^2}{4\delta^2} \right)$
limit: $N \gg f$		
Quasi-Geostrophic (QG) Green's function	(6.18)	$G(\varepsilon) = -\frac{1}{1+\varepsilon^2}$
limit: $\alpha \ll f$		
Generalised hypergeometric function		$\sigma = \frac{\sqrt{f^2 - \alpha^2}}{f}$
parameters: ${}_pF_q$		$\mathbf{p} = \{1, 2 - iN/(2\alpha), 2 + iN/(2\alpha)\}$
		$\mathbf{q} = \{5/2 - i\sigma/2, 5/2 + i\sigma/2\}$
Along-front shear Green's function	(6.13)	$\widehat{\partial_z v}_G = f^{-1} G(\varepsilon)$
Cross-front shear Green's function	(6.22)	$\widehat{\partial_z u}_G = -f^{-1} \delta \left(\varepsilon \frac{\partial}{\partial \varepsilon} + 2 \right) G(\varepsilon)$
Divergence Green's function	(6.23)	$\widehat{\partial_x u}_G = -\widehat{\partial_z w}_G = -N^{-1} \delta \varepsilon \left(\varepsilon \frac{\partial}{\partial \varepsilon} + 2 \right) G(\varepsilon)$
Forced solution at time t for field Γ		$\widehat{\Gamma}(k, n, t) = \widehat{\Gamma}_G(\varepsilon) \left[\frac{ke^{-\alpha t}}{l} \widehat{q}_0(ke^{-\alpha t}, l) \right]$
PV anomaly at time zero	(6.2)	$q_0(x, z) = \left[\frac{\partial b}{\partial z} + \frac{N^2}{f} \frac{\partial v}{\partial x} \right]_{t=0}$

Table 6.1 Linear forced solutions in spectral space for the flow about a 2D strained front with constant strain α and uniform stratification N^2 from the quasigeostrophic, hydrostatic and non-hydrostatic models. The horizontal and vertical wavenumbers are k and l , respectively. The Coriolis frequency is f and the non-dimensional strain is $\delta = \alpha/f$. The solution at any instant in time can be determined if the PV anomaly at that time $q_0(xe^{\alpha t}, z)$ is known.

Chapter 7

Non-hydrostatic wave generation at a tropospheric front

Here we use the linearised non-hydrostatic model developed in Chapter 6 to describe spontaneous wave generation at a tropospheric front. The generated waves are trapped in the strain field and form steady bands of enhanced vertical flow on either side of the surface front on scales from 1 to 100 km. The model thus provides a potential mechanism for the formation of narrow bands of cloud often observed near fronts. The predictions of the linearised analytic model are confirmed by comparison with fully non-linear numerical simulations.

7.1 Introduction

Frontal regions often exhibit bands of clouds roughly parallel to the surface front. These bands may be hundreds to thousands of kilometres long, but only one to ten kilometres in width, and are often associated with significant precipitation (e.g. Hobbs *et al.*, 1980). However, such finescale features are typically not well resolved in regional or global atmospheric models and hence require parameterisation (Ryan *et al.*, 2000). Unfortunately, the dynamics governing the generation and evolution of these frontal bands are not completely understood (e.g. Houze & Hobbs, 1982; Schultz, 2005).

In this chapter we investigate one potential mechanism for the formation of frontal bands: spontaneous gravity wave generation during frontogenesis and the trapping of these waves in the frontogenetic strain field. In this context, frontogenesis refers to the sharpening of surface gradients by the action of a large scale confluent flow. As observed in previous chapters, a common idealised configuration for the study of frontogenesis is the ‘quasi-2D’ framework of an infinitely long, straight front, subject to a uniform strain flow (e.g.

Griffiths & Reeder, 1996; Hoskins & Bretherton, 1972; Snyder *et al.*, 1993) as defined by (1.12). Most previous analytic models further assume the along-front flow to be in geostrophic balance, such as the semigeostrophic formulation of Hoskins & Bretherton (1972), building on earlier quasigeostrophic models of frontogenesis (Williams & Plotkin, 1968). However, since these balanced models omit waves other methods must be employed to describe wave generation during frontogenesis. For instance, Ley & Peltier (1978) devised an ad-hoc analytical correction to the Hoskins & Bretherton (1972) model where departures from geostrophic balance are assumed to force wave generation; the predicted wave packet creates a banded structure, similar to a squall line, ahead of the surface front. Many authors have also investigated wave generation in the idealised quasi-2D framework by way of numerical solutions to the full primitive equations (e.g. Gall *et al.*, 1988; Garner, 1989; Griffiths & Reeder, 1996; Reeder & Griffiths, 1996; Snyder *et al.*, 1993). Both propagating and stationary waves are observed in these solutions. In many cases, at least part of the propagating wave field is attributable to so-called ‘spurious waves’ associated with the adjustment of a slightly unbalanced initial condition (Snyder *et al.*, 1993). These waves evolve on a much faster timescale than the background strain flow and their propagation can be described via ray-tracing arguments. The key features of the waves are an exponential increase in the wavenumber with time and the ultimate trapping, or capture, of the propagating wave by the background strain flow (e.g. Buhler & McIntyre, 2005; Plougonven & Snyder, 2005). Since these spurious waves are not continually forced, the presence of diffusion in the numerical model leads to the rapid damping of the propagating wave amplitude once the scale contracts sufficiently. Here, we will also observe such spurious propagating waves in our numerical solution in §7.3.

Once spurious waves are filtered from the solutions, Snyder *et al.* (1993) show that additional largely stationary waves are present, both prior to the time at which the semi-geostrophic model predicts the formation of a discontinuity, and often with larger amplitudes after this time, if horizontal diffusion is introduced to prevent the formation of a discontinuity in the numerical model. These stationary waves are observed in a narrow region directly over the surface front. Similar to Ley & Peltier (1978), Snyder *et al.* (1993) describe the waves as a linear response to cross-front accelerations neglected in the semigeostrophic model. In the presence of diffusion, it is argued that the waves adopt a steady state characterised by a forced-dissipative balance. In our numerical model in §7.3 we will observe waves directly over the surface front, analogous to those described by Snyder *et al.* (1993). However, here our focus is on a different class of waves that form stationary bands of intensified vertical flow well ahead of and behind the surface front. We will show that these waves are essentially

independent of the details of the collapse of the surface front and may be described by our generalised linear model of frontogenesis that does not exhibit a finite-time singularity.

In Chapters 2 through 5 we developed a generalised non-linear model of frontogenesis for a quasi-2D strained front, that predicts the spontaneous generation of such stationary wave bands. Unlike the waves described above, which are considered to be linear response to departures from balance, these stationary waves were derived as an intrinsic, non-propagating part of the forced solution. As in Chapter 4, here the ‘forced solution’ is defined as having time purely as a parameter in the solution (or equivalently, time only enters the problem through the boundary condition), as per the classical Hoskins & Bretherton (1972) model. In the limit of very small strain the forced solution reduced to the semigeostrophic balance solution of Hoskins & Bretherton (1972). More generally, in Chapter 4 we showed that for small but finite strain the forced solution contains two components: a generalised secondary circulation that differs at order $(\alpha/f)^2$ (where α is the strain rate) from the Hoskins & Bretherton (1972) solution, and a stationary wave component that is exponentially small, order $e^{-\pi f/(2\alpha)}$. Given this result, the wave generation described by the generalised model is only significant for strains of about $0.2f$ or larger. As seen in Chapter 5, the waves can appear both before and after the collapse of the surface front (if diffusion is introduced to prevent the formation of a discontinuity), dependent on the size of the Rossby number.

The non-linear generalised model (Chapters 2 through 5), like most — if not all — previous analytic models, assumes hydrostatic balance. This assumption is clearly not appropriate in the present context since we seek to describe the formation of frontal bands of widths $\sim 10\text{ km}$, comparable to the height of the troposphere. The hydrostatic waves described in previous chapters are trapped by the frontogenetic strain flow and drive the formation of a single, intense band of vertical flow a fixed distance ahead and behind the surface front. This band contracts in scale and amplifies indefinitely. Here we will show that the introduction of non-hydrostatic dynamics leads to the formation of many stationary bands of vertical flow, of differing horizontal scale, in contrast to the single band observed in the hydrostatic model. Furthermore, unlike the hydrostatic model, these bands exist in a steady state with constant scale and amplitude.

7.2 Analytic solution

Here we again consider the dual rigid lid configuration (e.g. as pictured in figure 2.1) with uniform stratification N^2 . In this case we place a lower rigid lid at $z = 0$ representing the ground and an upper lid at $z = H$ representing the tropopause. We consider a front with initial width $L_0 = 360\text{ km}$, domain height $H = 9\text{ km}$, stratification $N^2 = 3.76 \times 10^{-5}\text{ s}^{-2}$,

buoyancy difference $\Delta B_0 = 0.46 m^2 s^{-1}$ (equivalent to $\sim 14^\circ C$), and strain $\alpha = 0.2f$. Taking the Coriolis parameter as $f = 10^{-4} s^{-1}$, we have $N/f = 61$. The Rossby radius for these parameters is $L_R = NH/(\pi f) = 176 km$, so the initial frontal width L_0 is approximately twice the Rossby radius. This choice of parameters is consistent with figure 7 of Snyder *et al.* (1993). A boundary buoyancy profile of $b_0(x) = \Delta B_0/2 \operatorname{erf}(x/(\sqrt{2}L_0))$ is imposed on the rigid lids at time zero.

Let us firstly consider what the non-linear analytic models of frontogenesis as studied in Chapters 2 through 5 have to say about this configuration. For the above initial conditions, both the generalised (GM) and Hoskins & Bretherton (1972) semigeostrophic (SG) non-linear analytic models predict the formation of a discontinuity on the boundary after 10 hours. The non-linear solutions just prior to this critical time in each of the models are shown in figure 7.1a&b. The vertical velocity fields in the two models are very similar at this time, with both exhibiting the familiar large scale thermally direct circulation associated with frontogenesis (e.g. Hoskins, 1982). The only notable difference between the models is that the generalised model (b) is confined more closely about the strain axis ($x = 0$) compared to the SG model as discussed in previous chapters. Such confinement leads to higher amplitudes near the front and reduced amplitudes on the periphery as shown figure 7.1c, which displays the difference between the generalised and semigeostrophic model solutions. We observe that no waves are visible in the vertical velocity fields in either of the models at the critical time. However, as seen in Chapter 5, we expect that waves will appear at later times if some process — such as small scale mixing — is present that can prevent the collapse of the surface front. The question here is how to describe the system analytically at later times, given that the non-linear solutions become undefined at the surface fronts after only 10 hours. The simplest answer is to use the linear model developed in Chapter 6 which is well-defined everywhere, for all time, keeping in mind that the model will not be valid in regions where the Rossby number is large (e.g. near the surface fronts). However, we will see below that the linear model performs very well away from the surface fronts.

Following the previous chapter (6.28), the vertical velocity field in the rigid lid, uniformly stratified linear model is defined — in spectral space — by

$$\widehat{w}(k, n, t) = \frac{\widehat{\partial_z w_G}(\varepsilon)}{n\pi} \left[-ik e^{-\alpha t} \widehat{b}_0(k e^{-\alpha t}) \frac{-2(-1 + (-1)^n)}{n\pi} \right], \quad (7.1)$$

where $\widehat{\partial_z w_G}$ is the divergence Green's function defined in table 6.1, n the vertical mode number, k the horizontal wavenumber and $\varepsilon = NH/(n\pi f)$ the mode slope. In real space the

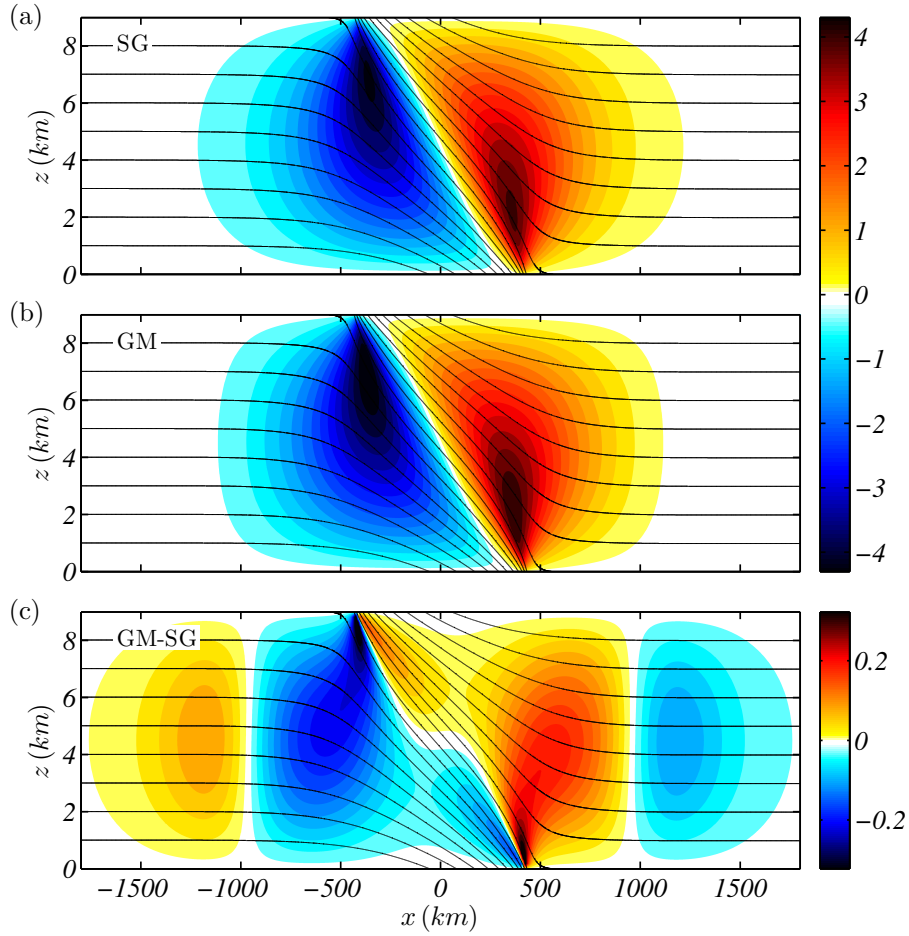


Fig. 7.1 Vertical velocity w (cm s⁻¹) at the critical time, $t = 10$ hrs, from the various non-linear models. (a) Semigeostrophic model (SG) of Hoskins & Bretherton (1972). (b) The hydrostatic generalised model (GM) of Chapters 2 through 5. (c) The difference between the hydrostatic generalised and semigeostrophic models, GM-SG. Contours of buoyancy are overlaid in black in each case.

vertical velocity is a convolution in x and a sum over the discrete vertical modes (6.29):

$$w(x, z, t) = \sum_{n=1}^{\infty} \frac{-2(-1 + (-1)^n)}{n^2 \pi^2} \sin \frac{n\pi z}{H} \int_{-\infty}^{\infty} \partial_z w_G(x - x_0, n) \frac{\partial}{\partial x_0} b_0(x_0 e^{\alpha t}) dx_0. \quad (7.2)$$

The Green's function $\partial_z w_G$ in the above equations was plotted in figure 6.2e,f for each of the quasi-geostrophic (QG), hydrostatic (H) and non-hydrostatic (NH) models for the present parameter values of $N/f = 61$ and $\alpha/f = 0.2$. Equation (7.1) implies that the actual vertical velocity spectrum at a given time is the product of the Green's function spectrum with the boundary gradient spectrum. The boundary gradient spectrum for an error function, $\theta_0(x) = \Delta\theta_0/2 \operatorname{erf}(x/(\sqrt{2}L_0))$, has the form of a low-pass filter with a cut-off wavenumber,

$k_c(t) \sim e^{\alpha t}/L_0$, that increases with time. At small time, there will be minimal difference between the three models, since the spectra shown in figure 6.2 agree for small wavenumbers. As time (and k_c) increases, differences between the balanced (QG) and unbalanced (H, NH) models will begin to appear. As time (and k_c) increases further, non-hydrostatic dynamics will become significant.

Figure 7.2 displays the vertical velocity from the (a) quasigeostrophic (QG), (b) non-hydrostatic (NH) and (d) hydrostatic (H) models after 3 days. As expected, the QG model has the usual large scale thermally direct circulation with no waves. As shown in earlier chapters, the hydrostatic (H) model exhibits a single vertical mode-one wave band of intensified vertical flow on the periphery of the frontal circulation, on both sides of the front. On the warm side, the wave consists of an upwelling band on the outside, and a narrower downwelling band closer to the front (and vice versa for the cool side). Higher vertical modes are also visible closer to the surface front. Instead of a single (vertical mode-one) band on the periphery of the front, the non-hydrostatic (NH) model exhibits many bands of vertical flow on scales of 1 to 60 km. Figure 7.2c,e display Hövmoller plots of the non-hydrostatic and hydrostatic vertical velocities at $z = 4.5\text{ km}$, from time zero up to 3 days, showing the development of the wave bands with time. For both models, the largest scale, most outward band, develops first around 30 hours. The linear model frontal width at this time, $L = L_0 e^{-\alpha t}$, is approximately one quarter of the Rossby radius, L_R . Narrower bands begin to appear in the non-hydrostatic solution around 40 hours (when $L/L_R = 0.1$), closer to the strain axis, with successively narrower bands appearing at later times.

7.3 Numerical solution

We now consider direct numerical solutions to the fully non-linear equations (including diffusion, i.e. (5.1)) and compare the results with the analytic solutions described in the previous section. The details of the numerical model and configuration are as described in Chapter 5. As in that chapter, here we initialise the numerical model fields in the state predicted by the non-linear generalised model (GM) in order to minimise spurious wave generation associated with adjustment to the initial conditions (e.g. see figure 5.1).

Here we employ a purely horizontal Laplacian diffusion in the numerical model; that is, $\kappa_h \neq 0$, $\kappa_v = 0$ and $n = 2$ in (5.1). The diffusion prevents the collapse of the front to grid resolution (which otherwise occurs at $t = 10$ hours as shown in figure 7.2), and allows the system to evolve to a steady state where strain-driven sharpening of the front is balanced by diffusion. The steady state that evolves thus depends on the size of the horizontal diffusivity κ_h . In figure 7.3 we display the steady state vertical velocity fields for (a) 7 km horizontal

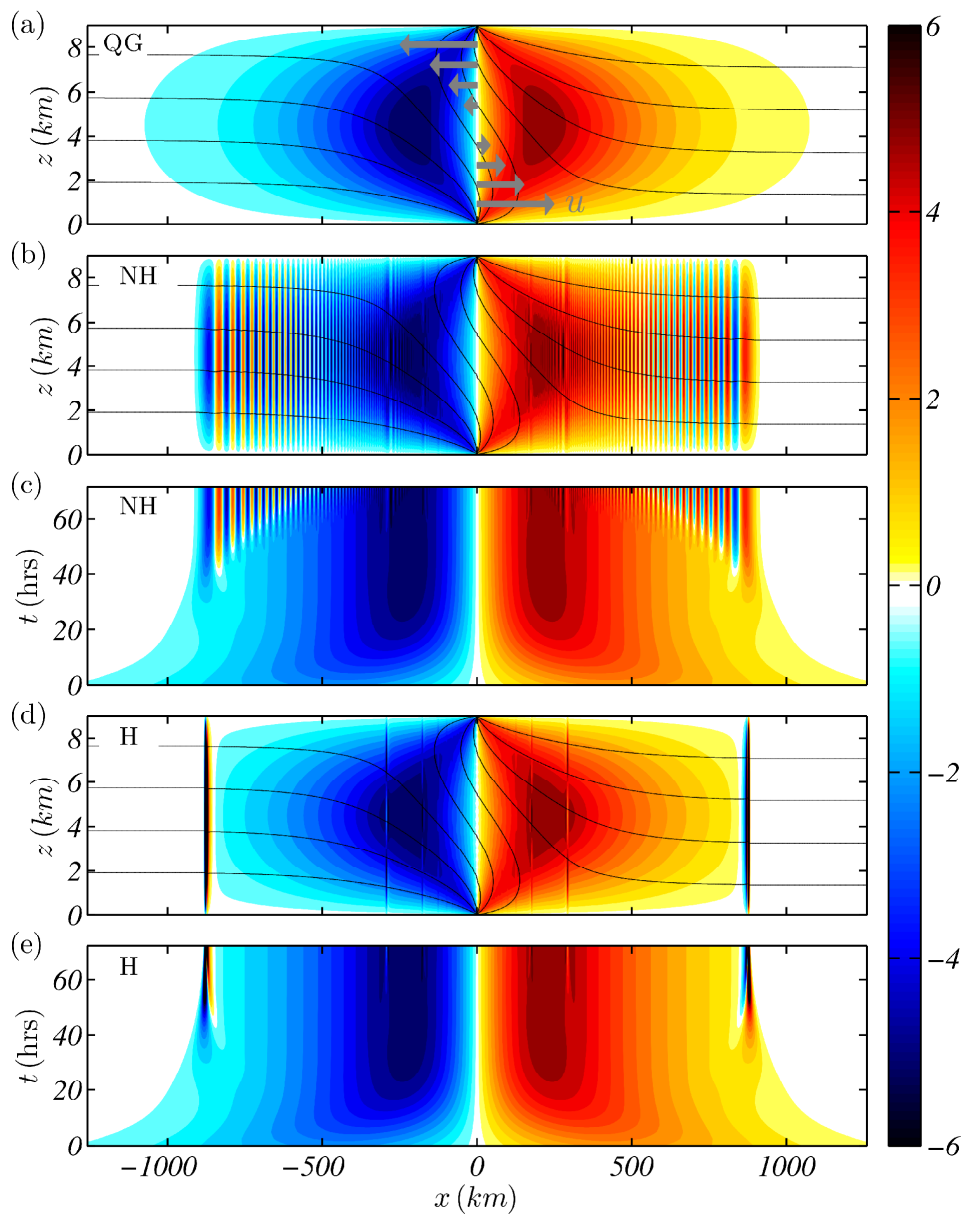


Fig. 7.2 Time evolution of the vertical velocity, w (cm s^{-1}), from the various linear models. (a) The vertical velocity from the QG model at $t = 72$ hours, with isotherms overlaid in black. Cross-front velocity $u(x = 0, z)$ is indicated by grey arrows. If advection by this velocity, $u \partial_x$, is included in the model, the surface front slumps outwards in the direction of the arrows, stabilising the isotherms (as in figure 7.1a). (b) The vertical velocity from the non-hydrostatic (NH) model at $t = 72$ hours, with isotherms overlaid in black. (c) The time evolution of the vertical velocity from the non-hydrostatic (NH) model at $z = 4.5 \text{ km}$, from $t = 0$ up to 72 hours. (d) The vertical velocity from the hydrostatic (H) model at $t = 72$ hours, with isotherms overlaid in black. (e) The time evolution of the vertical velocity from the hydrostatic (H) model at $z = 4.5 \text{ km}$, from $t = 0$ up to 72 hours.

resolution with $\kappa_h = 232 m^2 s^{-1}$ and (b) $0.45 km$ horizontal resolution with $\kappa_h = 58 m^2 s^{-1}$. For the large diffusivity (figure 7.3a), the frontal circulation is relatively smooth and — except near the surface fronts ($|x| < 500 km$) where the Rossby number is large — similar to the hydrostatic (QG, H) models shown in figure 7.2a,d. By contrast, the vertical velocity in figure 7.3b exhibits a strongly banded structure, very similar to the non-hydrostatic (NH) model shown in figure 7.2b. The width of the bands varies from $\sim 5 km$ near the surface fronts to $\sim 50 km$ on the periphery of the circulation, consistent with the NH analytic model prediction. The outermost, largest-scale band also appears very weakly in the low resolution case (figure 7.3a), although all other wave bands are ‘smoothed out’ by the larger diffusion used in that model run.

In addition to the banded wave structures predicted by the analytic theory, there are additional vertical mode-two wave structures in the numerical solution directly over the surface fronts, consistent with those seen in Snyder *et al.* (1993); for example, figure 7 therein, which uses the same parameter values. On the warm side of the front these wave structures consist of a narrow band of ascent in the bottom half of the domain directly above the surface front, and above this, a band of descent in the top half of the domain (and vice versa on the cool side). Such mode-two waves were also observed in the high Rossby number numerical simulations in Chapter 5 both before (figure 5.4) and after (figure 5.9) frontal collapse. As argued by Snyder *et al.* (1993), these waves appear to be forced by non-linear processes associated with the collapse of the surface front and are thus distinct from the banded wave structures that are the focus of the present chapter. Comparison of figure 7.3a&b demonstrates that the amplitude and scale of these stationary mode-two waves is highly diffusion dependent. Unlike the non-hydrostatic banded wave structures, the mode-two waves appear not to have an intrinsic inviscid minimum scale.

The time evolution of the wave field towards the steady state is shown in figure 7.3c,d via a Hovmöller plot at $z = 4.5 km$ for the low and high resolution model runs, respectively. Both runs show a clear propagating wave that is not present in the analytic solutions (figure 7.2), which have only stationary waves. To separate this fast-time propagating wave signal, which evolves at a frequency of order f , from the slow-time forced part of the flow, which evolves at a frequency of order $\alpha = 0.2f$, we apply a filter $F = \exp(-(2\omega/f)^4)$, which has a cut-off frequency of $\omega = 0.5f$, to the vertical velocity field. The slow-time part of the flow for the low and high resolution runs is shown in figure 7.3e,f, and the fast-time part of the flow in figure 7.3g,h. The evolution of the wave bands in figure 7.3f in the slow-time component is broadly consistent with the analytic solution shown in figure 7.2c. The largest-scale waves appear on the periphery of the frontal circulation around $t = 20$ to 30 hours, with successively smaller scales appearing closer to the strain axis as time progresses. Note that unlike the

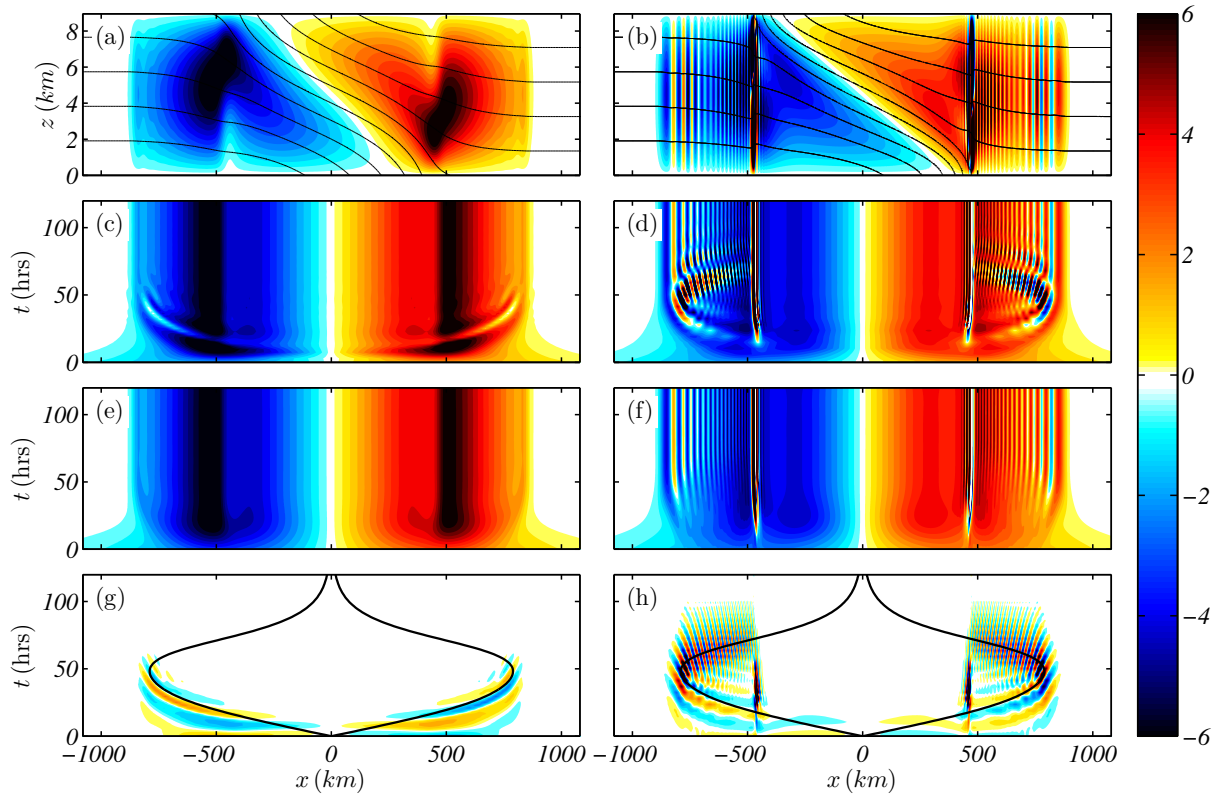


Fig. 7.3 Time evolution of the vertical velocity, w (cm s^{-1}), in the numerical model for the parameter values discussed in the text. Plots (a,c,e,g) correspond to the low resolution run with $\Delta x = 7 \text{ km}$ and diffusivity $\kappa_h = 232 \text{ m}^2 \text{ s}^{-1}$, and (b,d,f,h) to the high resolution run with $\Delta x = 0.45 \text{ km}$ and diffusivity $\kappa_h = 58 \text{ m}^2 \text{ s}^{-1}$. (a,b) The vertical velocity at $t = 72$ hours, with isotherms overlaid in black. (c,d) The time evolution of the vertical velocity at $z = 4.5 \text{ km}$, from $t = 0$ up to 120 hours. (e,f) The time evolution of the slow-time (low-pass filtered) vertical velocity at $z = 4.5 \text{ km}$, from $t = 0$ up to 120 hours. The low-pass filter applied is $F = \exp(-(2\omega/f)^4)$, i.e. a cut-off frequency of $\omega = 0.5f$. (g,h) The time evolution of the residual fast-time vertical velocity at $z = 4.5 \text{ km}$, from $t = 0$ up to 120 hours. The fast time part contains frequencies $\omega > 0.5f$ and thus contains the propagating wave part of the flow. These propagating waves are generated due to an imbalance in the initial condition. The propagating wave packets follow the paths predicted by ray-tracing (7.3), plotted as black lines for parameters of $x_0 = 0$ and $L_0 = \pi/k_0 = 1000 \text{ km}$.

analytic solution, the wave bands appear to form slightly inward of their final steady position, before gradually moving outwards.

We now consider the propagating wave, fast-time part of the flow shown in figure 7.3g,h. These waves are generated via an adjustment process due to the initial condition used in the numerical model (i.e. the generalised model solution) not being a precisely balanced solution to the full non-linear equations. As such, these waves are often described as ‘spurious’ but it is nonetheless useful to briefly consider their dynamics, if only to differentiate them from the spontaneous waves that are the focus of the present chapter. In contrast to the stationary, spontaneously generated waves discussed above, these propagating ‘adjustment waves’ have finite amplitude and horizontal scale at time zero. In Chapter 5 we showed that the fractional error in the GM model scales as $Ro^2(\alpha/f)^2$ (e.g. table 5.1) which yields an error of 0.1 for the current parameter values, consistent with the initial wave amplitude in the figure. As shown in Appendix C, the propagating adjustment waves may be described via classical ray-tracing theory (e.g. Jones, 1969; Plougonven & Zhang, 2014) owing to the timescale separation between the fast-time waves, $\tau \sim f^{-1}$, and slow-time background strain flow, $\tau \sim \alpha^{-1}$. The key result of this timescale separation is that the dispersion relation for the waves is unaffected by the background flow. The ray-tracing theory then proceeds as follows. Suppose a wave packet is located at location x_0 with initial wavenumber k_0 at time zero. The wavenumber of the packet increases in time according to the action of the strain, $k = k_0 e^{\alpha t}$ (e.g. equation 3 of Plougonven & Snyder, 2005). The position of the wave packet then evolves in time according to $\partial_t x(t) = c_g(k_0 e^{\alpha t}) - \alpha x(t)$ where $c_g = \partial_k \omega(k)$ is the group speed with $\omega(k)$ the usual inertia-gravity wave dispersion relation. Rearranging and integrating in time, the location of the wave packet at some later time is

$$x = x_0 e^{-\alpha t} + \frac{1}{\alpha k_0} e^{-\alpha t} (\omega(k_0 e^{\alpha t}) - \omega(k_0)). \quad (7.3)$$

The paths of the adjustment wave packets of initial scale $L_0 = \pi/k_0 = 1000 \text{ km}$ predicted by (7.3) are displayed in figure 7.3g,h, and agree well with the observed behaviour. The initially large scale waves propagate out towards the $x = \pm NH/(\pi\alpha)$ (the hydrostatic model stagnation points), and their scale contracts with time. In the low resolution run (figure 7.3g), further scale contraction is prevented by diffusion, and the waves decay away near the stagnation points around $t = 50$ hours. In the high resolution run (figure 7.3h) the scale of the waves contracts further, and the group speed $c_g = \partial_k \omega$ is reduced, resulting in the waves propagating back inward towards the surface front. The scale contraction is associated with an initial increase in the wave amplitude, before the waves decay around $t = 80$ hours, as their scale decreases sufficiently for diffusion to act to damp the propagating

wave. The dynamics of these propagating adjustment waves thus greatly contrasts with that of the spontaneously generated stationary waves described previously. In particular the spontaneously generated stationary waves evolve on the background flow timescale $\tau \sim \alpha^{-1}$ (i.e. as per (7.2)). Therefore no timescale separation exists and classical ray-tracing (e.g. Jones, 1969) is not applicable in describing these waves (see Appendix C).

7.4 Non-uniform stratification

In the previous sections we examined the wave generation predicted by the numerical and analytical solutions for a domain bounded by rigid lids at the ground ($z = 0$) and the ‘tropopause’ ($z = 9\text{ km}$). Of course, the tropopause in the real atmosphere does not behave like a rigid lid, raising the question of whether the vertically-trapped wave bands seen in the rigid lid solutions would exist in the real atmosphere, or whether these waves would instead propagate freely into the stratosphere. Given the ability of the linear solutions to describe the dynamics of the spontaneously generated waves — as shown in §7.3 above — here we will address these questions via numerical solutions to the generalised linear model (6.9) for arbitrary stratification $N^2(z)$ and time-dependent strain $\alpha(t)$. The method of solution is described in Appendix B. To prevent the generation of spurious waves (as in the numerical model described above) we initialise the linear model in geostrophic balance with a surface-intensified frontal buoyancy anomaly of

$$b_0(x, z) = \Delta B_0 \operatorname{erf}\left(\frac{x}{\sqrt{2}L}\right) e^{-\frac{z^2}{H^2}}. \quad (7.4)$$

That is, the initial buoyancy field is $b = b_0 + \Delta b + \int N^2(z) dz$, where the buoyancy anomaly Δb at time zero is determined from solving

$$\left[\frac{\partial^2}{\partial z^2} \frac{f^2}{N^2(z)} + \frac{\partial^2}{\partial x^2} \right] \Delta b(x, z, 0) = -\frac{\partial^2}{\partial x^2} b_0(x, z), \quad (7.5)$$

subject to homogeneous boundary conditions (see Appendix B). The strain field is then gradually ramped-on with time according to $\alpha(t) = \alpha_0 (1 - \exp(-(t/\tau)^2))$. Here we select a maximum strain value of $\alpha_0 = 0.3 f$ and ramp-on timescale of $\tau = 1$ day. We set the frontal height H to be 3 km , but the depth of the troposphere (defined by the stratification profile $N^2(z)$, see below) will be 9 km as in the previous section. The frontal width L and buoyancy difference ΔB_0 are also chosen as in the previous section.

For the first experiment, consider a buoyancy frequency profile, $N(z)$, that is uniform in the ‘troposphere’ (below 9 km) and then increases linearly at greater height as shown in

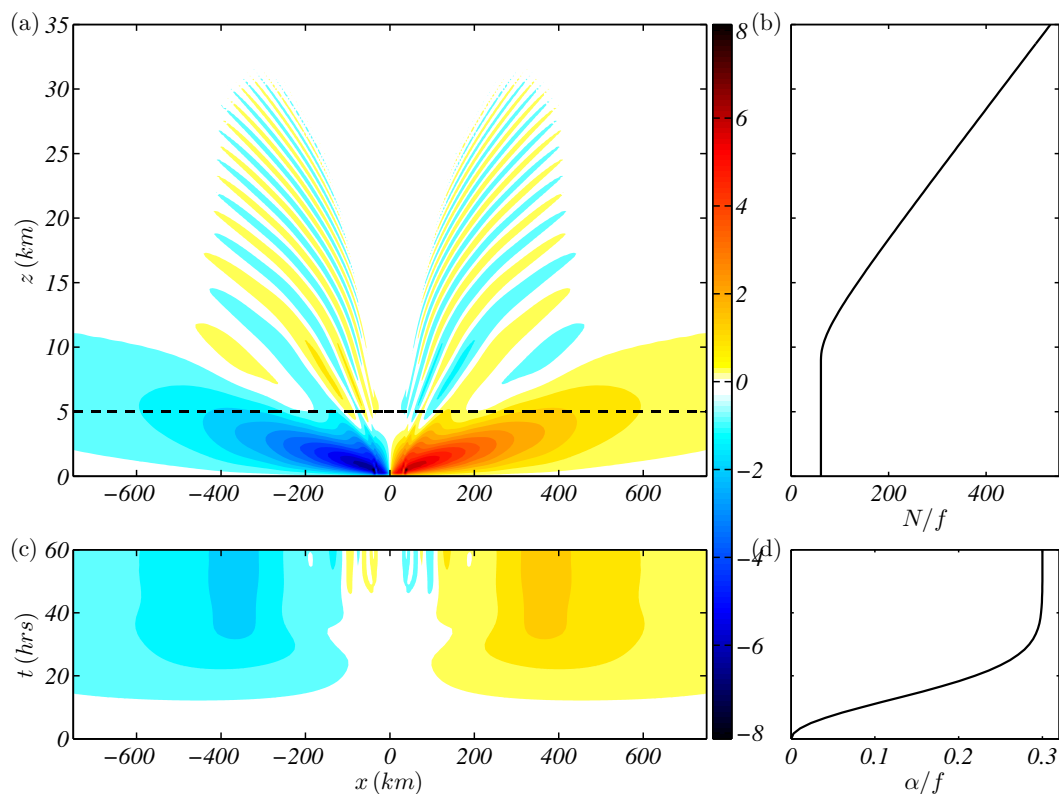


Fig. 7.4 Numerical solution to the non-hydrostatic linear frontal model (6.9) for a variable stratification that increases above 9 km. (a) The vertical velocity (cm s^{-1}) after 60 hours. (b) The vertical profile of stratification ratio $N(z)/f$. (c) Hovmöller plot of the vertical velocity at $z = 5 \text{ km}$ (dashed line in (a)). (d) The strain as a function of time, $\alpha(t)/f$.

figure 7.4b. This profile is chosen to address the question of whether a strong stratification barrier (i.e. the linearly increasing N/f above 9 km) can in any way behave like a rigid lid and confine the frontal circulation. The profile is *not* intended to be a realistic model of the real atmosphere. The tropospheric value of the buoyancy frequency is chosen as $N/f = 61$ as for the experiments in previous sections. The vertical velocity field 60 hours after initialisation is displayed in figure 7.4a. There is a broad thermally direct secondary circulation and strong wave generation. However, these waves show no evidence of trapping beneath the stratification barrier (the ‘tropopause’), and instead propagate through it (into the ‘stratosphere’). Thus, we deduce that a strong stratification barrier does not behave like a rigid lid. Indeed, the solution seen here is very similar to the uniform stratification semi-infinite domain solutions that will be studied analytically in Chapter 8. For reference, the time evolution of the vertical velocity field at $z = 5 \text{ km}$ is shown in figure 7.4c and the strain magnitude in 7.4d.

Now instead consider a buoyancy frequency profile similar to the above, but with reduced stability ($N \sim 20f$) in the upper troposphere as plotted in 7.5b. All other parameters are the same as in the previous example. The vertical velocity field 60 hours after initialisation is displayed in figure 7.5a and the time evolution at $z = 5 \text{ km}$ in figure 7.4c. The reduced stratification in the upper troposphere leads to a secondary circulation that is more confined in the horizontal but deeper in the vertical (occupying the entire depth of the model troposphere) compared with the previous example. Furthermore, there is significant trapping of waves in the vertical, leading to banded structures about the front similar to those seen in the rigid lid models. As in those models, the smaller horizontal scales are trapped closer to the front. The wave bands also attain a steady scale and amplitude as shown in the Hovmöller plot in figure 7.4c. The major difference with the rigid lid models is that the waves with the smallest horizontal scales, rather than being trapped very close to the front, are able to propagate vertically through the region of low stability (into the ‘stratosphere’). Nonetheless, this example suggests that the wave structures seen in the rigid lid solutions could potentially occur in more realistic models in regions with appropriate vertical profiles of stratification.

7.5 Discussion

The generation of gravity waves at fronts has important consequences for precipitation patterns in frontal systems, tropospheric mixing and turbulence, and the vertical transport of momentum (Plougonven & Zhang, 2014). Here we have shown that waves generated spontaneously during frontogenesis are trapped in the frontogenetic strain field, and these wave packets form steady bands of enhanced vertical velocity both ahead and behind the surface front. This banding mechanism is governed by dry dynamics — although the actual formation of clouds and precipitation would require a description of moist effects. The novel feature of our model is the inclusion of both non-hydrostatic and ageostrophic dynamics.

Non-hydrostatic dynamics give rise to substantially different wave behaviour compared with the previous *hydrostatic* model of Chapters 2 through 5. In that (rigid lid) model, a single stationary wave band forms on the periphery of the frontal circulation, and then continually collapses in scale and amplifies with time. The introduction of non-hydrostatic dynamics, as in the present model, gives rise to multiple stationary wave bands of differing scale ahead and behind the surface front, with smaller scales appearing closer to the front. These wave bands add significant fine-scale structure to the vertical velocity field near the surface front, in contrast to the largely smooth thermally direct structure predicted from prior models. Numerical solutions of the linear model developed in Chapter 6 (i.e. figure 7.5) show that the banded structures can persist even in the absence of an artificial rigid lid

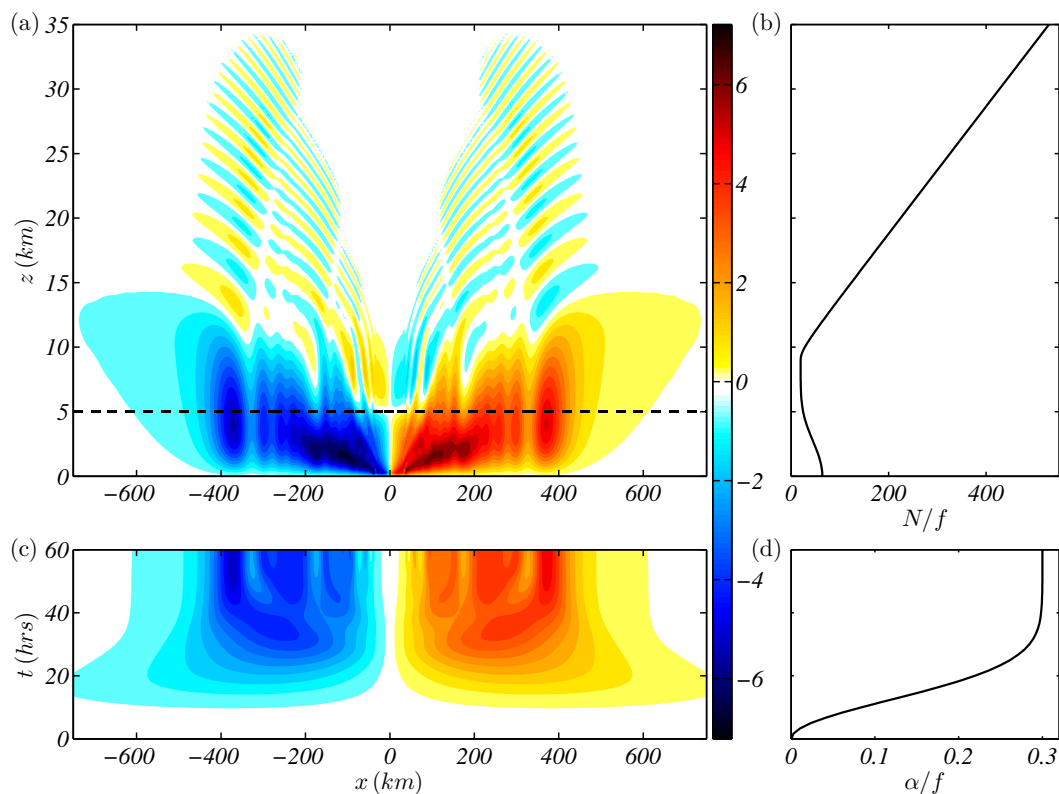


Fig. 7.5 Numerical solution to the non-hydrostatic linear frontal model (6.9) for a variable stratification that initially decreases with height, then increases above 9 km. (a) The vertical velocity (cm s^{-1}) after 60 hours. (b) The vertical profile of stratification ratio $N(z)/f$. (c) Hovmöller plot of the vertical velocity at $z = 5 \text{ km}$ (dashed line in (a)). (d) The strain as a function of time, $\alpha(t)/f$.

upper boundary, if the background density field exhibits a region of reduced stratification at height. Observational evidence suggests that such stratification profiles are quite common in the atmosphere, particularly near fronts (e.g. Schmidt & Cotton, 1990, and references therein). The trapping of waves beneath a layer of reduced static stability has previously been described as ‘wave ducting’ (for example see Lindzen & Tung, 1976), although background vertical shear (not included in our model) is also important to the details of this ducting.

It is significant that the frontal bands are well described by a linear model that does not exhibit a finite-time singularity on the boundary. Thus, unlike the spontaneously generated waves previously considered by Snyder *et al.* (1993) (and also visible directly over the surface front in our numerical solutions; see figure 7.3a,b) that are generated due to non-linear dynamics and forced imbalances at the surface front, the waves considered in the present work are independent of the local non-linear dynamics of the surface front. The exact

mechanism responsible for the formation of the waves is thus an intriguing question and one that will be addressed in Chapter 8.

The precise location, amplitude and structure of the frontal bands depends crucially on the details of the background flow. Since real strain fields exhibit significant spatial and temporal variation, the bands predicted here will move with respect to the front according to variations in the background flow. If the strain weakens with time, we showed in Chapters 4 and 5 that the generated waves can propagate away from the surface front. The amplitude of the predicted bands is also strongly dependent on the magnitude of the strain. As shown in Chapter 4, the amplitude of the spontaneously generated waves has a sharp cut-off, with exponentially small amplitudes for strains less than about $0.2f$. Hence, the mechanism of wave generation and subsequent frontal banding discussed here is likely only significant for fronts that experience relatively strong confluence.

However, despite its limitations, the generalised linear model developed in Chapter 6 provides an analytic description of wave generation and finescale structure at atmospheric fronts that could be of use in, for example, parameterising finescale precipitation and subgrid mixing in large scale atmospheric models (e.g. Plougonven & Zhang, 2014; Ryan *et al.*, 2000).

Chapter 8

Semi-infinite domain solutions with application to the ocean submesoscale

Here we use the linear model developed in Chapter 6 to describe spontaneous generation of inertia-gravity waves at density fronts of arbitrary horizontal and vertical structure in a semi-infinite domain, with a single boundary at the ocean surface. Waves are generated due to the acceleration of the steady uniform strain flow around the density front, analogous to the generation of lee waves via flow over a topographic ridge. Significant wave generation only occurs for sufficiently strong strains, $\alpha > 0.2f$, and sharp fronts, $H/L > 0.5f/N$. The frequencies of the generated waves are entirely determined by the magnitude of the strain, with $\omega = 1.93f$ the lowest frequency distinct wave predicted to be generated via this mechanism. The linear model thus provides a first-order description of wave generation at submesoscale (1 to 10km wide) fronts where large strains are commonplace. The linear model predictions compare well with fully non-linear numerical simulations of the submesoscale regime.

8.1 Introduction

Recent observations and numerical simulations show significant inertia-gravity wave generation at ocean density fronts (e.g. Alford *et al.*, 2013; Danioux *et al.*, 2012). Wave generation at these fronts is associated with an energy transfer from the large scale balanced flow to waves, and from the surface into the deep ocean. The wave energy is ultimately dissipated via breaking in the ocean interior, driving turbulence and mixing, and thus contributing to the maintenance of the global overturning circulation (Polzin, 2010; Wunsch & Ferrari, 2004).

The generation of waves at density fronts occurs through a variety of mechanisms including the action of surface wind stresses and buoyancy fluxes, frontal instabilities, and many other processes occurring at sharp fronts with high Rossby numbers (e.g. Alford *et al.*, 2013; Plougonven & Zhang, 2014; Vanneste, 2013; Viudez & Dritschel, 2006). Here we investigate the specific case of wave generation at fronts subject to strong confluent strain flows, defined by strain magnitudes $\alpha \sim f$. As in previous chapters, here we will use the term ‘strain’ to describe the cross-frontal confluence — that is, $\alpha \equiv -\partial_x u$ for a front oriented along the y -axis — and not the (larger) modulus of the strain rate tensor, which we will call the ‘net strain’. The strain is considered to arise from a larger scale background flow — for example, an eddy field — which then acts on the relatively smaller scale front and drives frontogenesis. Recent observations (e.g. Shcherbina *et al.*, 2013) and numerical simulations (e.g. Rosso *et al.*, 2015) have shown that large strains are commonplace on the ocean submesoscale, which is characterised by horizontal scales of 1 to 10km. Rosso *et al.* (2015) observe large scale (mesoscale) net strains of up to $0.4f$ in their submesoscale resolving numerical model, and show that the vertical velocity on the submesoscale is strongly correlated with the mesoscale strain magnitude (see figure 1.3), suggesting active submesoscale frontogenesis is present. Shcherbina *et al.* (2013) observe very large strains — in places exceeding $2f$ — although this figure is the net strain, including the self-strain associated with the submesoscale fronts (and other phenomena). Nonetheless, these studies make clear that both sharp density fronts and large strains are ubiquitous at small scales in the ocean surface layer. Here we show that the linear model developed in Chapter 6 predicts significant wave generation at such strained fronts, and describe the properties of the generated waves.

The classical quasi- and semi-geostrophic balance frontogenesis models (see §1.3) assume that the strain is small, typically $\alpha \sim 0.1f$. In this limit, the frontal system remains close to geostrophic balance and no wave generation occurs. Wave generation at more strongly strained fronts has been investigated in earlier chapters in the context of the idealised problem of a uniform potential vorticity fluid with rigid lids at the top and bottom of the domain, and fronts on both boundaries. In Chapter 3 we examined the generation of waves in this configuration due to the adjustment of unbalanced initial conditions for weakly strained fronts. In Chapter 4 we examined the same configuration, but for larger strains, and showed that waves are spontaneously generated as the surface front collapses to small scales. The waves did not propagate vertically, owing to the presence of the rigid lids, and were also trapped horizontally by the confluent strain flow. The amplitude of the generated waves was found to be exponentially small for small strain, but substantial for larger strains. In Chapter 5 we confirmed these results by direct comparison with numerical simulations.

Using the linear model developed in Chapter 6, here we investigate a configuration with two important differences to these previous studies. Firstly, we consider a semi-infinite domain with a single boundary at the ocean surface, as pictured in figure 6.1. This domain is more readily applicable to the ocean than previous rigid lid configurations, and in particular, permits the downward propagation of waves generated at the surface front. Secondly, we allow non-uniform potential vorticity, which permits surface intensified fronts where the horizontal density gradient is maximum near the surface and decays with depth, as is typically the case for ocean fronts. As discussed in Chapter 6, the linearised equations are only strictly valid in the limit of small geostrophic Rossby number, $Ro_g = \Delta B_0 H / (f^2 L^2)$, where ΔB_0 is the buoyancy difference across the front, H the frontal height and L the width. This assumption is unlikely to be valid for submesoscale fronts, where Ro_g is often order one (e.g. Shcherbina *et al.*, 2013). However, comparison of the analytical model with a fully non-linear simulation of a submesoscale front (see §8.3) demonstrates that the analytic model is valid at depth, away from the surface front, and in particular, accurately describes the wave field. In other words, the dynamics of waves in the far field are largely unaffected by the locally large Rossby numbers and associated non-linear dynamics at the front itself (as for the waves discussed in Chapter 7).

One objective of this chapter is to investigate the dynamical mechanism responsible for the generation of waves at strained fronts. In §8.2.3 we demonstrate the mathematical similarity of the present frontal wave problem to the classical lee wave problem of Queney (1947). In the Queney (1947) model waves are generated when a uniform background flow passes over a topographic ridge. The background flow is accelerated around the ridge, into the stratified ambient, and for sufficiently sharp ridges (small width L) and strong flow (large \bar{U}), characterised by large Rossby number $Ro = \bar{U} / (fL)$, buoyancy forces give rise to a wave response (Muraki, 2011; Pierrehumbert, 1984; Queney, 1947). Here we show that a density front presents an obstacle to a background strain flow, in the same way a topographic ridge presents an obstacle to a uniform background flow. The background strain flow is accelerated around the density front into the stratified ambient, and for sufficiently sharp fronts and strong strain flows, buoyancy forces drive a wave response. Just like steady lee waves, these ‘frontal waves’ are trapped by the background flow in a distinctive pattern.

The chapter is set out as follows. In §8.2 we discuss the application of the analytic solution derived in Chapter 6 to the present problem. We show how the frequencies and amplitudes of generated waves can be determined directly from this solution, independent of the details of the frontal structure. We then explore the dependence of the wave generation on the magnitude of the strain flow (§8.2.1) and width of the surface front (§8.2.2). The dynamics of wave generation at density fronts is compared to that at topographic obstacles in

§8.2.3. We then investigate the energy budget of the linearised model (§8.2.4). In §8.3 we compare the analytical model predictions with fully non-linear simulations of a submesoscale front. Lastly, in §8.4 we discuss the implications of these results for the generation of inertia-gravity waves in the ocean.

8.2 Analytic model results

Here we employ the linear hydrostatic solution derived in Chapter 6 (see table 6.1), applied to the semi-infinite domain. The full solution for a given field at some time is given by the convolution of a frontal buoyancy gradient (or PV) anomaly at that time, $\partial_x b_0(xe^{\alpha t})$, with the time-independent Green's function for that field, as per (6.13) and (6.14). Before considering a particular frontal structure, we briefly review the structure of the hydrostatic Green's functions.

The Green's function for the hydrostatic model (see table 6.1) depends only on the mode slope $\varepsilon = Nk/(fl)$ — where k and l are the horizontal and vertical wavenumbers, respectively, and N/f is the stratification ratio, as previously — and the non-dimensional strain $\delta = \alpha/f$. The non-dimensional Green's function for the cross-front shear, $f\widehat{\partial_z u}_G$, is shown in figure 8.1. The behaviour of the Green's function depends strongly on the magnitude of the strain. For small strains, $\delta \sim 0.1$, the function decays smoothly to zero with increasing mode slope ε . For larger strain, $\delta \geq 0.2$, the Green's function is smoothly decreasing for small slopes $\varepsilon < 1$ but exhibits high-amplitude oscillations in the region $\varepsilon > 1$, implying the accumulation of energy at certain preferential wavenumber combinations, $\varepsilon = Nk/(fl)$. As will be seen below, in the semi-infinite domain these oscillations correspond to stationary wave packets at slopes of $k/l = f\varepsilon/N$ and frequencies $\omega = f\sqrt{1 + \varepsilon^2}$. The logarithmic colour scale in figure 8.1 indicates that the amplitude of the oscillations (and therefore wave packets) is *exponentially small* at small strain — consistent with the result derived in the rigid lid case in Chapter 4. The differing behaviour at small and large strain is captured by the two asymptotic limits. In the limit of vanishingly small strain, $\delta \rightarrow 0$, the (hydrostatic) Green's function asymptotes to a smoothly decaying profile,

$$G(\varepsilon) = -\frac{1}{1 + \varepsilon^2}, \quad (8.1)$$

and corresponds to an along-front velocity in geostrophic balance with the buoyancy anomaly (i.e. the QG model solution). In contrast, the (hydrostatic) Green's function for large strain,

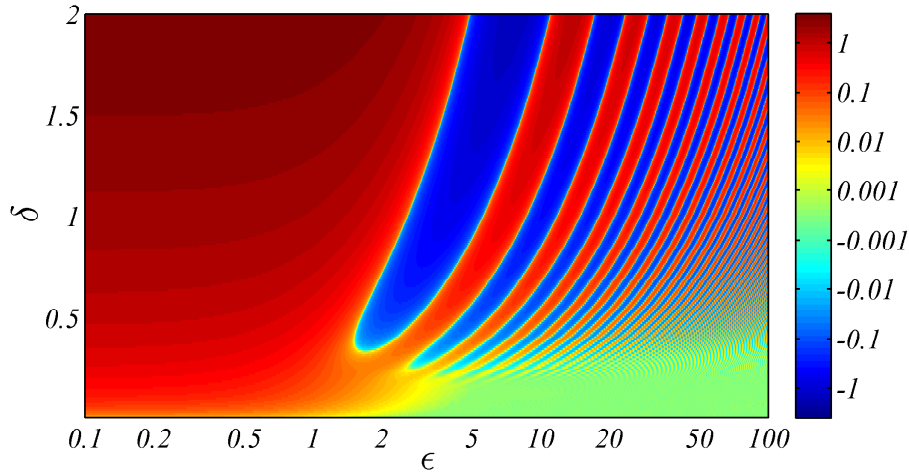


Fig. 8.1 Non-dimensional hydrostatic Green's function for the cross-front shear, $f \widehat{\partial_z u_G}$ (6.22), as a function of slope $\varepsilon = Nk/(fl)$ and strain $\delta = \alpha/f$. Local extrema in the Green's function correspond to wave packets of frequency $\omega = f\sqrt{1 + \varepsilon^2}$.

$\delta \rightarrow \infty$, asymptotes to an oscillation-dominated profile,

$$G(\varepsilon) = -\frac{2\delta}{\varepsilon} J_1\left(\frac{\varepsilon}{\delta}\right), \quad (8.2)$$

where J_1 is the 1st order Bessel function.

8.2.1 Strain dependence

Here we will consider a simple surface-intensified buoyancy anomaly, or front, of the form

$$b_0(x, z) = \frac{\Delta B_0}{2} \exp\left(-\left(\frac{z}{H}\right)^2\right) \operatorname{erf}\left(\varepsilon_F \frac{x}{L_R}\right), \quad (8.3)$$

where H is the height scale of the front, ΔB_0 is the change in buoyancy across the front and $L_R = NH/f$ is the Rossby radius. The parameter $\varepsilon_F = L_R/L$ is the Burger number, or characteristic slope, of the frontal anomaly. As noted in §6.3, solutions for the semi-infinite domain can be generated from the fully infinite domain solutions (6.13, 6.14) by mirroring the buoyancy anomaly defined for $z \leq 0$ into the region $z > 0$; that is, defining an 'effective buoyancy anomaly' in the fully infinite domain ($-\infty < z < \infty$) of

$$b_0^{\text{eff}}(x, z) = \frac{\Delta B_0}{2} \operatorname{sign}(-z) \exp\left(-\left(\frac{z}{H}\right)^2\right) \operatorname{erf}\left(\varepsilon_F \frac{x}{L_R}\right). \quad (8.4)$$

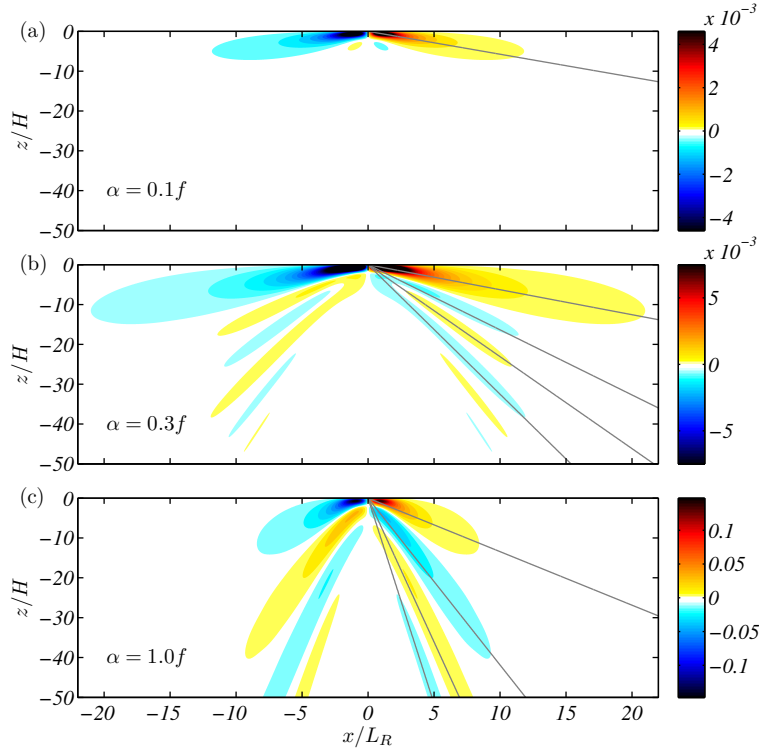


Fig. 8.2 Comparison of vertical velocity field (in units of $\Delta B_0 f / N^2$) for strains of (a) $\alpha = 0.1f$, (b) $\alpha = 0.3f$, and (c) $\alpha = f$, and a frontal anomaly defined by (8.3). Straight grey lines indicate the slopes of secondary circulation and first three wave packets (if they exist), as predicted from the Green's function (see figures 8.3 and 8.4).

The vertical velocity fields for a frontal Burger number (ε_F) of 1 and strains of (a) $0.1f$, (b) $0.3f$ and (c) $1.0f$ are shown in figure 8.2. For the small strain case ($\alpha = 0.1f$, figure 8.2a) the velocity is dominated by an ascending vertical jet on the warmer (right-hand) side of the front, and a descending jet on the cooler side, consistent with the classical paradigm of the thermally direct secondary circulation about a strained front. The larger strains show a similar circulation about the surface front, but the steepness and strength of the jets is increased. In addition the larger strain solutions exhibit banded structures at depth, which correspond to stationary inertia-gravity wave packets. The amplitude of these wave packets is substantially less than the secondary circulation for moderate strain ($\alpha = 0.3f$, figure 8.2b), but of similar order for large strain ($\alpha = 1.0f$, figure 8.2c). Note that the amplitude of the secondary circulation (vertical velocity magnitude) in each case can be significantly larger if non-linear effects are considered, owing to the non-linear collapse of the surface front (see §8.3).

The variation with strain of the strength and steepness of the surface frontal jets — which are associated with a large divergence $\partial_z w$ — can be predicted directly from the divergence

Green's function (table 6.1). The frontal jets correspond to the first extremum (in ε) in the divergence Green's function at each value of strain. The slope of the jets predicted by this method is indicated by grey lines in figure 8.2. More generally, the jet slope as a function of strain is shown in figure 8.3a. The slope is constant for small strain, but increases linearly at large strain. The asymptotic limits (indicated by dashed lines on the figure) may be derived directly from the asymptotic Green's functions. In the limit $\delta \rightarrow 0$ (8.1) the local maxima of the divergence Green's function is located at $\varepsilon = 1/\sqrt{3}$, implying that the jets have a slope of $k/l = f/(N\sqrt{3}) \simeq 0.58 f/N$. In this limit, the scale of the frontal circulation is largely unaffected by the presence of the (weak) strain flow. For large strain, $\delta \rightarrow \infty$, (8.2) the jets are steeper, with slope $k/l \simeq 1.26 \alpha/N$. In this limit, the convergent strain strongly confines the frontal circulation in the horizontal, leading to steeper, intensified jets.

The vertical velocity magnitude (jet strength) may also be estimated from the Green's function as the local maximum value of the divergence, and is plotted in figure 8.3b. The vertical velocity increases linearly at small strain and quadratically at large strain. The linear increase at small strain is predicted from quasi- and semigeostrophic models of frontogenesis (Hoskins & Bretherton, 1972; Williams & Plotkin, 1968) and is merely a requirement of continuity: a larger background strain flow implies a correspondingly larger secondary circulation to conserve volume at the front. The additional (quadratic) increase in vertical velocity at large strain is associated with the linear increase in the slope of the jets, which is due to the strong strain flow confining the secondary circulation around the strain axis, as noted above. While non-linear effects will modify the magnitude of the secondary circulation (see §8.3), the confinement effect of the strain flow will still operate (as shown in Chapter 5), and thus the qualitative dependence of the secondary circulation on the strain described here is expected to be robust. Indeed, figure 8.3b is qualitatively similar to the results of Rosso *et al.* (2015) discussed in Chapter 1 — in particular figure 1.3d which displays the dependence of the vertical velocity on the large scale strain in their submesoscale-resolving numerical model of a sector of the Southern Ocean. The strain dependence of the vertical velocity predicted here may thus have application in parametrising vertical velocities associated with submesoscale fronts in low resolution numerical models.

The slopes and frequencies of the wave packets as a function of strain can also be determined by computing the local extrema of the Green's function for the cross-frontal shear (6.22) shown in figure 8.1. This technique works since the wave packets visible in the solutions (e.g. figure 8.2) are associated with a local maximum in the cross-frontal shear, as well as the vertical velocity and divergence.¹ In figure 8.4 we plot the frequencies and

¹Using the Green's function for the divergence instead of the cross-frontal shear does not produce substantially different results.

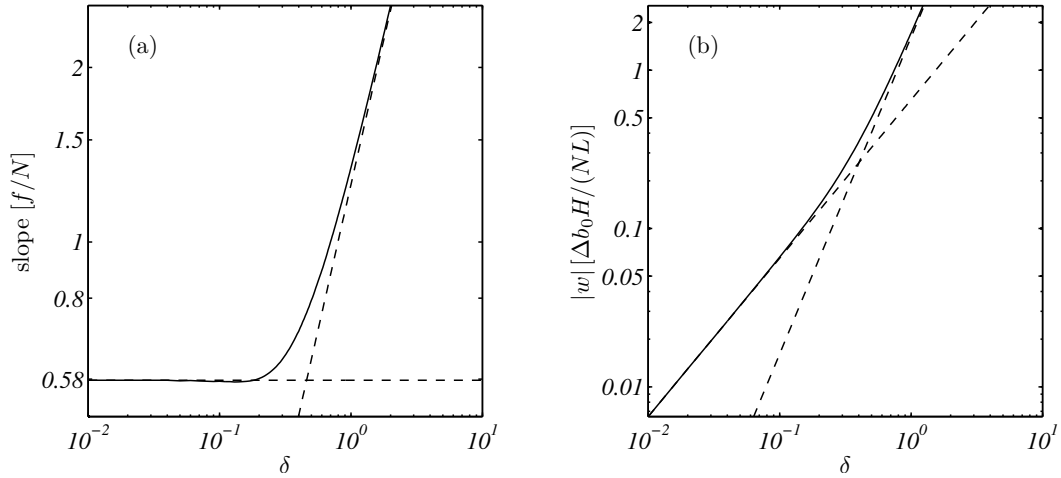


Fig. 8.3 (a) Slope of the frontal jets as a function of strain $\delta = \alpha/f$, in units of f/N . (b) Vertical velocity magnitude as a function of strain, in units of $\Delta B_0 H / (NL)$. The results from the small (8.1) and large (8.2) strain limits are shown as dashed lines. The slope is nearly constant at small strain and increases linearly at large strain. The vertical velocity increases linearly at small strain and quadratically at large strain.

amplitudes of the six lowest frequency wave packets of *significant* amplitude — we cannot rule out the presence of low amplitude, lower frequency wave packets that are obscured by the secondary circulation and which therefore do not generate extrema in the Green's function spectrum. The wave frequency is related to the wave slope via $\omega = f\sqrt{1 + \varepsilon^2}$. The lowest frequency distinct wave packet is $1.93f$ and occurs for a strain of approximately $0.3f$ (the strain used in figure 8.2b). For strains in the range $0.2f < \alpha < f$, the lowest frequency distinct packet has a frequency less than $4f$. The wave packet slopes predicted from figure 8.4 are indicated as grey lines on the vertical velocity plots in figure 8.2b,c. The agreement is excellent.

8.2.2 Frontal scale dependence

In this section we address the question of how the frontal Burger number, or characteristic frontal slope, $\varepsilon_F = L_R/L = NH/(fL)$, affects the solution for a given value of strain. The confluent strain acts to compress the horizontal scale L of the frontal buoyancy gradient anomaly ($\partial_x b_0$) with time as per (6.14). The Burger number of the front will thus increase with time according to $\varepsilon_F = \varepsilon_{F,0} e^{\alpha t}$. In other words, there is a one-to-one relationship between the frontal scale and time. Thus, examining the Burger number dependence of the solution will also tell us about the time evolution of the front.

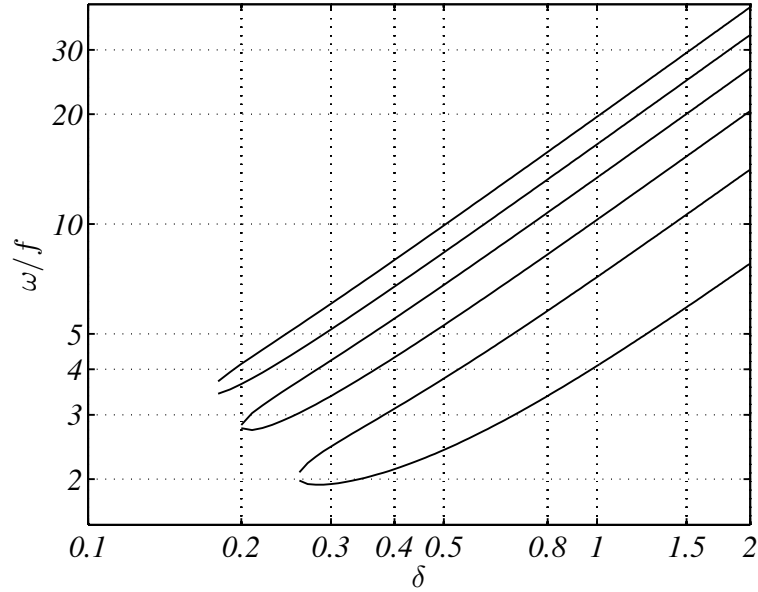


Fig. 8.4 Frequencies of the six lowest frequency distinct wavepackets as a function of strain $\delta = \alpha/f$, derived from computing the local extrema of the non-dimensional cross-front shear Green's function, $f\widehat{\partial_z u_G}$, shown in figure 8.1. The lowest frequency distinct wavepacket is $\omega = 1.93f$, for a strain of $\alpha = 0.29f$.

Figure 8.5 displays the vertical velocity fields for a front subject to strain $\alpha = 0.4f$, for five frontal scales (or time snapshots). The buoyancy anomaly is the same as used previously (8.3). When the frontal width is large compared to the Rossby radius (a, $L = 10L_R$; b, $L = 5L_R$), the secondary circulation is broad and relatively weak.² In particular, for wide fronts ($L \gg L_R$), there are no wave packets present. As the frontal width approaches the Rossby radius (c, $L = 2L_R$), the lowest frequency (primary) wavepacket appears. As the frontal width is reduced further (d, $L = L_R$; e, $L = 0.5L_R$), the primary wave packet amplifies and higher frequency packets appear. We observe that the slopes (indicated on the figure by dashed grey lines) of both the frontal jets and the wave packets are independent of the frontal width, implying that the vertical scale of the flow decreases at the same rate as the horizontal to keep the slope constant. We observe that this behaviour is very different to the dual rigid lid configuration of previous chapters where the vertical wave scale is fixed by the domain height, and does not decrease with time.

This behaviour may be understood by considering the form of the solution, e.g. (6.13). The solution at a given time is defined by the product of the Green's function and the buoyancy gradient anomaly spectra evaluated at that instant in time, as per (6.13). The possible slopes

²Note that the velocities have been non-dimensionalised by $\varepsilon_F \Delta B_0 f / N^2$, so the maximum velocity in (e) is 20 times that in (a) owing to the change in ε_F .

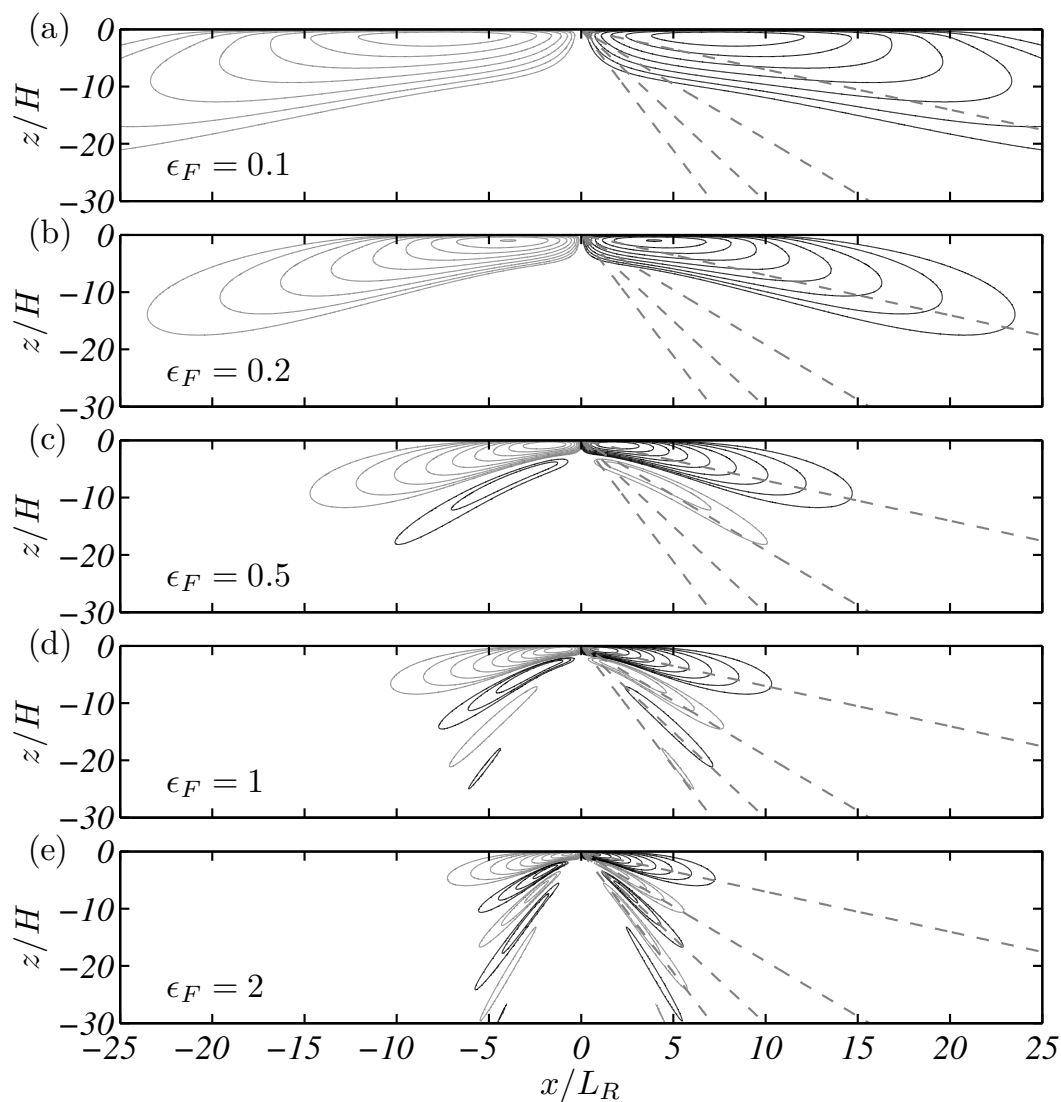


Fig. 8.5 Vertical velocity fields for a strain of $\alpha = 0.4f$ and buoyancy anomaly defined by (8.3), for various frontal Burger numbers $\epsilon_F = L_R/L$. The velocities are in units of $\epsilon_F \Delta B_0 f / N^2$. Contours are logarithmically spaced from 3 to 100% of the maximum value (0.03). Grey-dashed lines indicate the predicted slope of the frontal jets and wave packets. The figure can also be viewed as a sequence of snapshots in time, $\alpha t = \ln(\epsilon_F/0.1)$: (a) $\alpha t = 0$, (b) $\alpha t = 0.69$, (c) $\alpha t = 1.61$, (d) $\alpha t = 2.30$, and (e) $\alpha t = 3$.

of the jets and wave packets are controlled by the structure of the Green's function at a given value of the strain, whereas the amplitude of those features is controlled by the spectral amplitude of the buoyancy gradient anomaly at the corresponding wavenumber combinations. For instance, the amplitude of a wavepacket with a given slope, $\varepsilon = Nk/(fl)$, is determined by the integrated amplitude in the buoyancy gradient spectrum, $\widehat{\partial_x b_0}(k, l)$, along the line $l = Nk/(f\varepsilon)$. As the frontal scale is reduced, the gradient spectrum has more amplitude at larger horizontal wavenumbers k , and therefore more amplitude at larger slopes. Since, as shown in figure 8.1, wavepackets are only present in the region $\varepsilon = Nk/(fl) > 1$, the spontaneous generation of waves can only occur for fronts with significant spectral amplitude at the corresponding wavenumbers. Fronts that satisfy this requirement are characterised by order one Burger numbers, $\varepsilon_F \sim 1$. Thus, as seen in figure 8.5, significant spontaneous wave generation via the present mechanism is only observed for fronts with widths comparable to the Rossby radius, or smaller.

8.2.3 Comparison with lee waves

It is useful to compare the present mechanism of spontaneous generation to other well known mechanisms, specifically 'lee wave' generation associated with flow across topography. The classical lee wave model of Queney (1947) describes the steady state associated with a uniform background flow, $\bar{U} = U_0$, passing over a topographic ridge, $z = h(x)$. The equation for the perturbation buoyancy, $b = B - N^2z$, is

$$\left[\underbrace{(\bar{D}^2 + f^2)}_{\text{accel.}} \underbrace{\frac{1}{N^2} \frac{\partial^2}{\partial z^2} + \frac{\partial^2}{\partial x^2}}_{\text{geostrophic}} \right] b = 0, \quad (8.5)$$

where $\bar{D} = U_0 \partial_x$ is the linearised material derivative at steady state. The equation is composed of two parts: the usual geostrophic scaled Laplace operator familiar from classical QG models, which will yield a smooth large scale flow, and an acceleration term associated with advection by the background flow which is responsible for the generation of small scale stationary waves. The boundary condition on (8.5) is no normal flow at the ridge. Since the flow is inviscid, an equivalent condition is that the ridge is an isopycnal surface; that is, the net buoyancy $B = b + N^2z = 0$ at $z = h(x)$ or the perturbation buoyancy is $b(z = h(x)) = -N^2h(x)$. In the linearised model (valid for small ridge heights) the boundary condition is applied at $z = 0$, and the solution (e.g. Pierrehumbert, 1984; Queney, 1947) is defined by the convolution

$$b(x, z) = -N^2 \int_{-\infty}^{\infty} G_L(x - x_0, z) h(x_0) dx_0, \quad (8.6)$$

where the Fourier transform of the Green's function G_L is

$$\widehat{G}_L(k, z) = \begin{cases} \exp \frac{iNkz}{\sqrt{k^2 U_0^2 - f^2}} & k > \frac{f}{U_0} \\ \exp \frac{-Nk|z|}{\sqrt{f^2 - k^2 U_0^2}} & 0 \leq k \leq \frac{f}{U_0} \end{cases}. \quad (8.7)$$

As with the equation (8.5), the steady solution is thus composed of two parts: a large-scale component that decays with height, and a short-scale wave component that does not. These waves are generated when the background flow is deflected (or accelerated) sufficiently rapidly around the ridge into the stratified ambient, which provides a restoring force. Wave can only propagate for frequencies exceeding f and thus strong wave generation only occurs when the acceleration timescale of $1/(kU_0)$ is of this order, $1/(kU_0) \sim 1/f$, or equivalently the Rossby number is order one, $Ro_L = U_0/(fL) \sim 1$. If the ridge is wide or the flow weak such that $Ro_L \ll 1$, then there are no waves and flow remains in linearised, uniform PV geostrophic balance, defined by $\widehat{G}_L(k, z) = \exp(-Nk|z|/f)$.

Compare these 'lee wave dynamics' to those of the strained front considered in earlier sections. To make the analogy clearer, here we write the governing equation for a strained front with uniform interior PV (see (6.5)). The governing equation is (6.9) with N^2 constant, vertical acceleration neglected, and frontal anomaly b_0 independent of z , or

$$\left[\underbrace{(\bar{D}^2 - 2\alpha\bar{D} + f^2)}_{accel.} \underbrace{\frac{1}{N^2} \frac{\partial^2}{\partial z^2} + \frac{\partial^2}{\partial x^2}}_{geostrophic} \right] b = 0, \quad (8.8)$$

subject to boundary condition $b = b_0(xe^{\alpha t})$. Equation (8.8) describing a strained front is identical in structure to (8.5) describing flow over a ridge — only the form of the acceleration terms differ. The forced solution to (8.8) is defined by the convolution

$$b(x, z, t) = \int_{-\infty}^{\infty} G_F(x - x_0, z) b_0(xe^{\alpha t}) dx_0, \quad (8.9)$$

where the Green's function G_F may be determined via Fourier inversion of the Green's function G defined in table 6.1 (or else from Chapter 4, §4.4). As for lee waves, this solution can be considered to be composed of two parts: a large scale secondary circulation or 'deflection' about the front, and a smaller-scale wave field. Unfortunately, unlike the lee waves, the two parts are not readily separable. As was shown in §8.2.1, if the strain

$\delta = \alpha/f \ll 1$ — analogous to $Ro_L \ll 1$ for the lee waves — then there is negligible generation of waves, and the flow reduces to (quasi-)geostrophic balance with G defined by (8.1). Notably, in this small Rossby number limit, the topographic Green's function is identical to the frontal Green's function, $\widehat{G}_F = \widehat{G}_L = \exp(-Nk|z|/f)$. Comparing (8.6) and (8.9) thus implies that the geostrophic buoyancy field associated with a topographic ridge of profile $h(x)$ is identical to the geostrophic buoyancy field associated with a front with surface buoyancy profile $b_0(x) = -N^2h(x)$ at some instant in time. The secondary circulation around the front/ridge is determined by material conservation of the buoyancy, $w = -\bar{D}b/N^2$, and so will be different for the front and ridge owing to the different material derivative operator \bar{D} . However, in both cases the secondary flow is generated owing to the need to deflect the background flow field along the isopycnals and around the surface obstacle. If this deflection is sufficiently sharp/fast (i.e. Ro_L, δ non-small) then buoyant forces give rise to a wave response.

Figure 8.6 contrasts the linear uniform PV solutions for the action of a uniform flow over a ridge and a strain flow over a front (actually a filament, or double front). The topographic ridge has profile $h(x) = H/(1 + (x/L)^2)$, with the ridge half-width chosen to equal the Rossby radius, $L = L_R = NH/f$, and is placed on the upper boundary for ease of comparison with the frontal case. The front is chosen to have a surface buoyancy profile $b_0(x) = -N^2h(x)$ such that the geostrophic buoyancy fields for front and ridge are identical, as described above. The magnitude of the uniform background flow over the ridge is chosen such that it matches the strain flow magnitude at the edge of the front/ridge, $U_0 = \alpha L$. It follows that the Rossby numbers for the two flows are equal, $\delta = Ro_L = \alpha/f$. Figure 8.6a,b show the vertical velocity and buoyancy fields for the (a) front and (b) ridge for Rossby number $\delta = 0.2$. At this small Rossby number the flow is dominated by the geostrophic part and hence the buoyancy fields are almost identical. The vertical velocity, or secondary circulation, for the ridge and front is similar in magnitude but different in structure. For the front, the circulation has the expected thermally direct structure with upwelling beneath the central warm filament, and downwelling on the flanks. Significantly, no waves are visible in the frontal velocity field, but a weak wave field is evident downstream of the ridge. For the ridge, the wave amplitude is determined by the amplitude in the height profile spectrum, $\widehat{h}(k)$, at wavenumbers $k > f/U_0$ as per (8.6). For the front, as discussed in prior sections, the wave amplitude depends on two factors: (i) the amplitude of the peaks in the Green's function (figure 8.1), which only occur for high wavenumber k and with exponentially small amplitude at small strain; (ii) similar to lee waves, the amplitude in the buoyancy profile spectrum at these wavenumbers. The first effect guarantees that at small Rossby number, except for

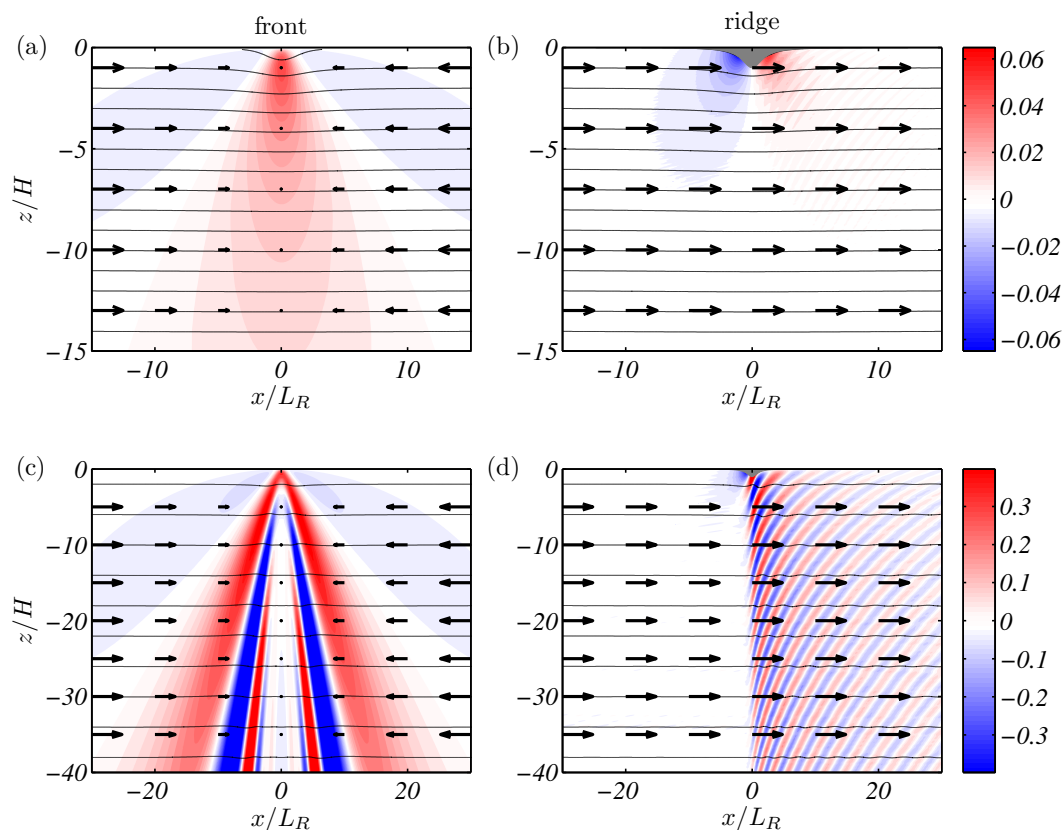


Fig. 8.6 Comparison of perturbation vertical velocity (colour, units of fH) and buoyancy (black contours) fields associated with (a,c) a strain flow, $\bar{U} = -\alpha x$, acting across a front/filament and (b,d) a uniform flow, $U_0 = \alpha L_R$, across a topographic ridge. The topographic ridge has profile $h(x) = H/(1 + (x/L_R)^2)$, and the front has a surface buoyancy profile $b_0(x) = -N^2 h(x)$, such that the geostrophic buoyancy fields are identical for the two flows. Plots (a,b) show the solutions for Rossby number $R_{OL} = \delta = 0.2$, and plots (c,d) for $R_{OL} = \delta = 0.9$. The background flow in each case is indicated by vectors (not to scale).

exceptionally sharp fronts/narrow ridges, the wave amplitude associated with uniform flow across a ridge will greatly exceed that associated with strain flow over a front.

Figure 8.6c,d show the vertical velocity and buoyancy fields for the (c) front/filament and (d) ridge for Rossby number $R_{OL} = \delta = 0.9$. As expected, at this order one Rossby number the wave field dominates over the secondary circulation for both front and ridge flows. The different wave field structure is due to the different background flow (represented by black vectors) trapping differing wave scales in differing locations. In contrast to the small strain scenario, the wave amplitudes for the frontal flow exceed those for the ridge flow. This difference will be exacerbated for sharper fronts/narrower ridges.

8.2.4 Energy budgets

In the previous sections it was shown that the amplitude of the frontal circulation and generated wave packets increases with increasing strain and reducing frontal scale. In this section we investigate the source of the energy associated with this strengthening of the circulation.

Energy budgets can be formed from the horizontal momentum (1.12a, 1.12b) and buoyancy conservation (1.12d) equations. Multiplying (1.12a) — linearised with $D \equiv \bar{D}$ — by u yields

$$\bar{D} \frac{u^2}{2} = fuv + \alpha u^2 - fv_g u. \quad (8.10)$$

We now integrate (8.10) over the entire flow — denoted by angled brackets, $\int \int dx dz = \langle \rangle$. Under the hydrostatic assumption, the integrated pressure term may be rewritten in terms of the vertical velocity, $\langle -fv_g u \rangle = \langle wb \rangle$, via integration by parts and substitution of thermal wind, $f\partial_z v_g = \partial_x b$, and continuity (1.12e). It may also be shown that, due to advection by the strain flow, $\langle \bar{D}\phi \rangle = (\partial_t + \alpha)\langle \phi \rangle$ for any field ϕ . Thus, integration of (8.10) yields an energy budget for the cross-front flow, u ,

$$\frac{\partial}{\partial t} \left\langle \frac{u^2}{2} \right\rangle = \langle fuv \rangle + \left\langle \frac{\alpha}{2} u^2 \right\rangle + \langle wb \rangle. \quad (8.11)$$

Following an analogous procedure for the along-front flow, v , yields,

$$\frac{\partial}{\partial t} \left\langle \frac{v^2}{2} \right\rangle = \langle -fuv \rangle - \left\langle \frac{3\alpha}{2} v^2 \right\rangle. \quad (8.12)$$

To obtain the potential energy budget, the buoyancy equation (1.12d) is multiplied by $\Delta b + b_0$ and integrated over the flow as above, yielding

$$\frac{\partial}{\partial t} \left\langle \frac{\Delta b(\Delta b + 2b_0)}{2N^2} \right\rangle = \left\langle -\frac{\alpha \Delta b(\Delta b + 2b_0)}{2N^2} \right\rangle - \langle wb \rangle. \quad (8.13)$$

Summing equations (8.11, 8.12, 8.13) the net perturbation energy E is

$$E = \left\langle \frac{u^2 + v^2}{2} + \frac{\Delta b(\Delta b + 2b_0)}{2N^2} \right\rangle, \quad (8.14)$$

(up to a constant) and evolves in time according to

$$\frac{\partial E}{\partial t} = \alpha \left\langle \frac{u^2}{2} - \frac{3v^2}{2} - \frac{\Delta b(\Delta b + 2b_0)}{2N^2} \right\rangle. \quad (8.15)$$

Equation (8.15) implies that there exists an energy transfer between the frontal perturbation flow and the background strain for any non-zero strain α . Further, there is the possibility for energy transfer in either direction, depending on the strain magnitude, frontal scale, and other parameters.

The budgets for each of the cross-front kinetic energy (CFKE; 8.11), along-front kinetic energy (AFKE; 8.12) and potential energy (PE; 8.13) reservoirs, and the fluxes between them, are represented diagrammatically in figure 8.7. The directions of the energy fluxes are indicated by the arrows. The cross-front flow gains/loses energy from the potential via the buoyancy flux term $\langle wb \rangle$, loses energy to the along-front flow (or frontal jet) due to Coriolis deflection, $\langle -fuv \rangle$, and gains energy from the strain via the amplification of cross-front velocity perturbations, $\langle \alpha u^2/2 \rangle$. The along-front flow gains energy from cross-front flow, and loses energy to the strain, $\langle 3\alpha v^2/2 \rangle$. Lastly, the potential energy loses/gains energy to the kinetic via $\langle wb \rangle$, and gains/loses energy from the strain via the term $\langle -\alpha \Delta b (\Delta b + 2b_0)/(2N^2) \rangle$. This latter term, describing the energy transfer from the strain to the potential, can be rewritten in a more transparent form in terms of the product of an energy flux with a buoyancy gradient; that is,

$$\left\langle -\frac{\alpha \Delta b (\Delta b + 2b_0)}{2N^2} \right\rangle = \frac{1}{N^2} \left\langle (\bar{U} \Delta b) \frac{\partial b}{\partial x} + (\bar{U} b_0) \frac{\partial \Delta b}{\partial x} \right\rangle, \quad (8.16)$$

where $\bar{U} = -\alpha x$ is the strain flow. Contributions emerge from both the imposed buoyancy anomaly b_0 and the buoyancy response Δb . Whether net potential energy is generated or destroyed by the strain depends on whether the energy flux is up or down the local buoyancy gradient.

Figure 8.8 displays the time evolution of selected energy reservoirs and fluxes for various strains. We use the same buoyancy anomaly as in the previous section (8.3), where the frontal Burger number ε_F in (8.3) is related to time via $\varepsilon_F = L_R/L = 0.1 e^{\alpha t}$. That is, as noted previously, there is a one-to-one relationship between the time and frontal width — both are shown in figure 8.8. Figure 8.8a shows the net energy input to the system, $\partial_t E$ from (8.15). For strains less than about $0.55f$, the energy input is (weakly) negative, implying energy is lost from the perturbation flow to the strain. For larger strains, the energy input is positive, implying a transfer of energy to the perturbation flow from the background strain. In the present model, the background strain is intended to represent a large scale flow such as an eddy field, and thus the strain energy reservoir may be interpreted as the energy associated with the large scale flow. Viewed in this context, for a mesoscale eddy field with strain $\alpha \sim 0.1f$, our model implies an ‘upscale’ energy flux from the small scale frontal circulation to the large scale eddy field. In contrast, for a submesoscale eddy field with strain $\alpha \sim f$, our

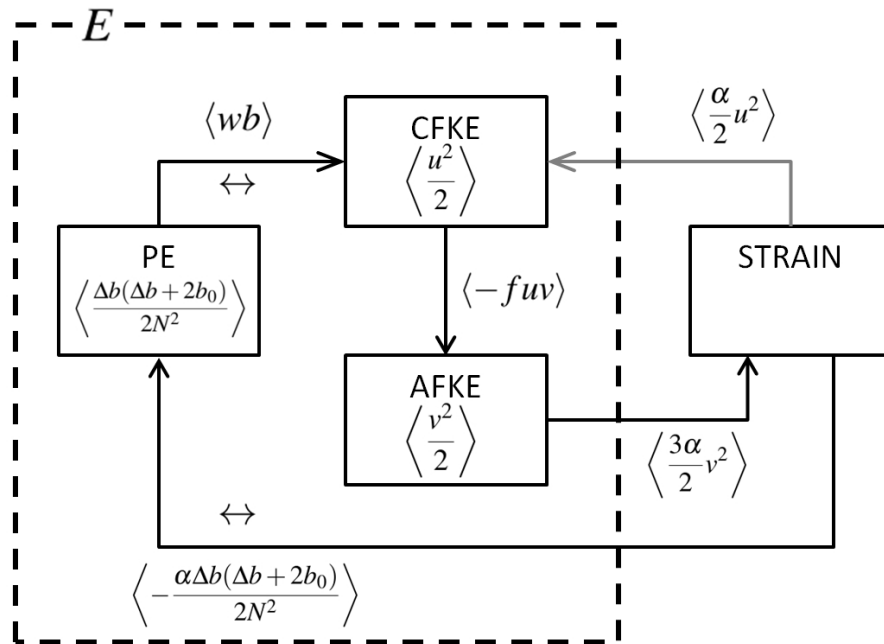


Fig. 8.7 The energy budget for the linearised problem. The four energy reservoirs are the potential energy (PE), cross-front kinetic energy (CFKE), along-front kinetic energy (AFKE) and the strain field (STRAIN). Energy fluxes between the reservoirs are indicated by black/grey arrows. The grey arrow denotes an energy flux that is negligible (order δ^3) for small strains. Double-headed arrows (\leftrightarrow) on some energy pathways indicate that the direction of those fluxes reverse for sufficiently large strains and sharp fronts. The dashed box indicates the total energy E of the perturbation flow.

model implies an ‘downscale’ energy flux from the eddy field to the small scale perturbation flow (and waves).

The net energy input may be divided into the change in the kinetic energy (figure 8.8b) and potential energy (figure 8.8c) of the perturbation flow. The kinetic energy of the flow is always increasing, since the strain always acts to amplify buoyancy gradients, and therefore increase the along- and cross-front velocities. By contrast, the potential energy only increases for very large strains and very narrow fronts. The two fluxes contributing to the change in PE are the loss to kinetic energy, $\langle wb \rangle$, shown in figure 8.8d, and the gain from the strain, shown in figure 8.8f. The $\langle wb \rangle$ term is positive, corresponding to a transfer from potential to kinetic energy, when on average the sense of the perturbation flow is *thermally direct* — that is, warmer fluid rising and cooler fluid descending. The thermally direct circulation associated with the frontal jets dominates the solution for small strain (e.g. see figure 8.2a) and/or broad fronts (e.g. see figure 8.5a,b), and hence $\langle wb \rangle$ is positive for the corresponding region in figure 8.8f. However, for very strong strains and narrow fronts, the buoyancy becomes

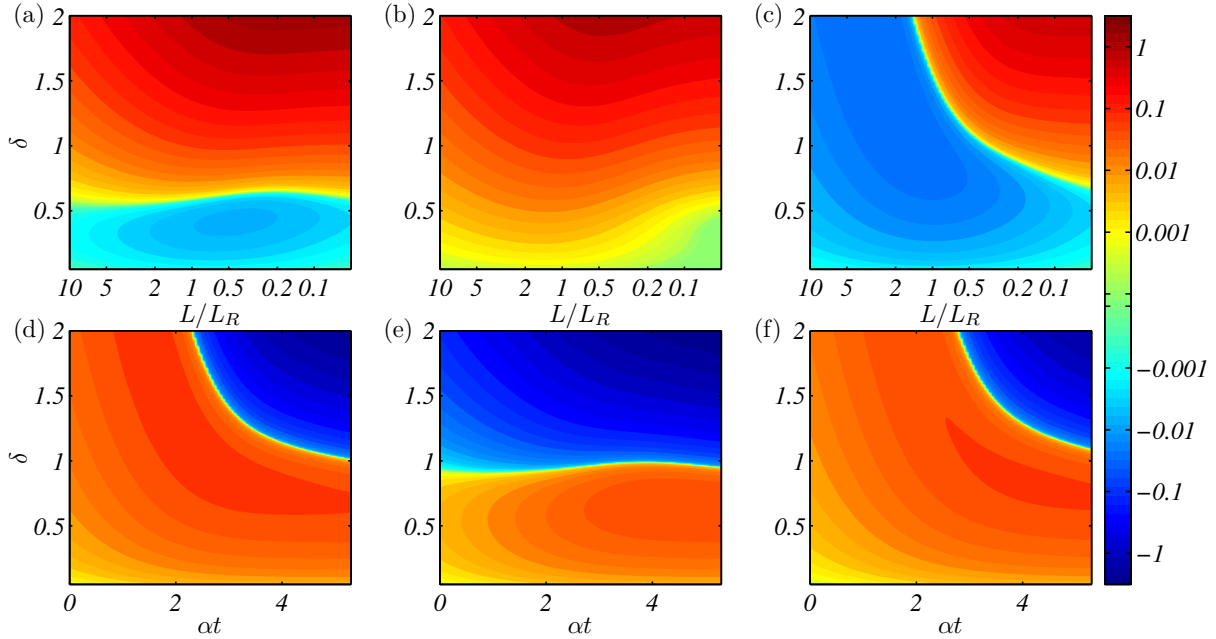


Fig. 8.8 Time evolution of the energy reservoirs and fluxes for various strains, in units of $H^2\Delta B_0^2/N$. The frontal width at a given time is $L/L_R = 10e^{-\alpha t}$ where L_R is the Rossby radius. (a) The net energy input: $\partial_t E$. (b) The change in net kinetic energy with time: $\partial_t \langle (u^2 + v^2)/2 \rangle$. (c) The change in potential energy with time: $\partial_t \langle \Delta b(\Delta b + 2b_0)/(2N^2) \rangle$. (d) Potential energy to kinetic energy flux: $\langle wb \rangle$. (e) Kinetic energy to strain flux: $\alpha \langle -u^2/2 + 3v^2/2 \rangle$. (f) Strain to potential energy flux: $\langle -\alpha \Delta b(\Delta b + 2b_0)/(2N^2) \rangle$.

dominated by the ‘response’ component Δb rather than the background frontal anomaly b_0 , leading to a thermally indirect circulation and $\langle wb \rangle < 0$.³ More generally, even for moderate strains and frontal widths, $\langle wb \rangle > 0$ near the surface ($z > -H$) where $b_0 \sim \exp(-(z/H)^2)$ is large, while $\langle wb \rangle < 0$ at depth, where $\Delta b \gg b_0$ and waves dominate the flow (e.g. figure 8.2b,c). Thus, $\langle wb \rangle < 0$ can be viewed as representing regions where thermally indirect circulation, in this case predominantly stationary waves, dominates over the thermally direct secondary circulation.

Referring to figure 8.8, we note that for sufficiently small strain the time rate-of-change of the energy reservoirs (a, b, c) approaches zero in the limit of infinite time (or infinitely sharp front), implying that the system approaches a steady state.⁴ Correspondingly, the energy fluxes between the reservoirs (d, e, f) become equal at large time. There is a continual cycling of energy between the reservoirs, but no change in the amount of energy in each

³The flux in the limit of very large strain and very narrow front is approximately $\langle wb \rangle \approx -\alpha \langle \Delta b^2 \rangle / (2N^2) - \partial_t \langle \Delta b^2 \rangle / (2N^2)$, both terms of which are negative.

⁴This ‘steady state’ is characterised by a step-like buoyancy profile $b_0(x, z) = H_0(x) \Delta b(z)$, where H_0 is the Heaviside function. This discontinuous state should be considered a limiting state, rather than a true steady state, since the linearised model is almost certainly breaking down in this limit.

reservoir. The ‘energy cycle’ at small strain is indicated by the black arrows on figure 8.7 (the energy associated with the cross-front flow is negligible at small strain). The thermally direct circulation draws energy from the potential. This energy is transferred into the (geostrophic) along-front jet by the Coriolis effect, whereupon it is lost to the strain flow. The strain then returns energy to the potential field by up-gradient advection of the buoyancy perturbation in the background flow, $\langle \bar{U} \Delta b \partial_x b_0 \rangle$ (see equation (8.16)). The amount of energy cycling through the system in the limit of large time may be derived directly from the Green’s function at small strain (8.1). The kinetic energy at large time is

$$\begin{aligned} K_\infty &= \int_0^\infty \int_{-\infty}^\infty \frac{1}{2} |\widehat{v}_\infty|^2 dk dl \\ &= \frac{1}{4\pi} \left(\frac{\Delta B_0}{N} \right)^2 HL_R \int_{-\infty}^\infty G(\varepsilon)^2 d\varepsilon \int_0^\infty \frac{|\widehat{\Delta b}(l')|^2}{|l'|} dl', \end{aligned} \quad (8.17)$$

by application of (6.13) with the Green’s function $G(\varepsilon)$ given by the small strain solution (8.1). In (8.17), $\widehat{\Delta b}$ is the Fourier sine transform of the vertical structure of the front and primes denote non-dimensionalisation, $l' = lH$. In the present example, the vertical structure is $\Delta b(z') = \exp(-z'^2)$, and (8.17) yields a kinetic energy of $K_\infty = 0.036H^2\Delta B_0^2/(Nf)$ per unit length of the front. The rate of energy cycling between reservoirs is then $3\alpha K_\infty$ via (8.12).

The above behaviour at small strain in the limit of large time contrasts with that of large strain where, as shown in figure 8.8, the kinetic and potential energies of the perturbation flow increase indefinitely. The increase is due to the large amplitude oscillations in the cross-front shear Green’s function (e.g. figure 8.1) at large ε and large strain, which are associated with wave packets. As the frontal scale collapses, higher and higher frequency wave packets are generated, continually increasing the energy of the perturbation flow.⁵

8.3 Numerical model comparison

Here we describe a solution to the fully non-linear equations with Laplacian horizontal diffusion ($\kappa_h \neq 0$, $\kappa_v = 0$ and $n = 2$ in (5.1)) for parameter values representative of a submesoscale front. We consider a front with an initial structure of

$$b(x, z, 0) = \frac{\Delta B_0}{2} \left(1 + \operatorname{erf} \left(\frac{x}{L} \right) \right) \exp \left(- \left(\frac{z}{H} \right)^2 \right) + N^2 z, \quad (8.18)$$

⁵Mathematically, the indefinite amplification of the energy is represented by the definite integral of the squared modulus of the cross-front shear Green’s function, i.e. $\int_{-\infty}^\infty |\partial_z \widehat{u}_G|^2 d\varepsilon$, being undefined for the general solution (6.20) — whereas it is well defined for small-strain solution (8.1).

and choose a buoyancy difference of $\Delta B_0 = 5 \times 10^{-3} m^2 s^{-1}$, initial frontal width of $L = 10 km$, depth scale of $H = 100 m$, stratification $N^2 = 1 \times 10^{-5} s^{-1}$ and assume $f = 1 \times 10^{-4} s^{-1}$. These parameters correspond to an initial geostrophic Rossby number — the parameter assumed to be small in the linear model — of $Ro_g = \Delta B_0 H / (f^2 L^2) = 0.5$, although Ro_g increases to $\mathcal{O}(10)$ as the front collapses. To prevent the generation of waves associated with the adjustment of unbalanced initial conditions, we initialise the numerical model with zero strain in a state of geostrophic balance and gradually ramp-on the strain with time according to $\alpha(t) = \alpha_0 (1 - e^{-(t/\tau)^2})$. Here we select a maximum strain value of $\alpha_0 = 0.4 f$ and ramp-on timescale of $\tau = 1$ day.

The numerical model employed is MITgcm (Marshall *et al.*, 1997) configured in hydrostatic, two-dimensional, ocean-only mode with a rigid lid ocean surface. The MITgcm code is modified to include the background strain advection terms in (5.1) as an external forcing to the buoyancy and horizontal momentum equations. The domain width is chosen as $200 km$ with the front in the centre of the domain and a horizontal resolution of $100 m$ at the front. Open boundaries with Orlanski radiation conditions are used at the horizontal edges of the domain. The domain depth is set to $8 km$ with resolution varying from $5 m$ at the surface to $25 m$ at depth. A uniform background horizontal diffusion and viscosity of $10 m^2 s^{-1}$ is introduced to prevent the collapse of the front below the grid-scale. We also add a diffusive sponge in the deep which absorbs downward propagating waves and prevents reflections off the base of the domain. The sponge takes the form of an elevated horizontal diffusion and viscosity in the bottom half of the domain, $\kappa_h(z) = \kappa_\infty (1 + \text{erf}(-(z+6)/1.5))/2$ where $\kappa_\infty = 400 m^2 s^{-1}$ and z is in units of kilometres.

The numerical model ultimately reaches a steady state where strain-driven sharpening of the front is balanced by horizontal diffusion. The time evolution of the model towards this steady state is shown in figure 8.9 via a Hovmöller plot of the surface buoyancy field. The magnitude of the strain as a function of time is also shown. As the front sharpens it moves to the left, with warmer fluid slumping over cooler. The front reaches a steady state after about two days with a steady cross-frontal width of about $700 m$. The vertical velocity field in the steady state is shown in figure 8.10a. The grey lines on the figure are the wave packet and jet slopes predicted from the Green's function derived in the previous section. These predicted slopes show good agreement with the numerical solution.

For comparison, the vertical velocity field predicted from the analytical model is shown in figure 8.10b. This prediction is derived in the following way. First, the frontal anomaly b_0 is determined from the initial buoyancy field $b(x, z, 0)$ used in the numerical model (8.18). This is done by replacing the velocity v in the PV relation (6.6) with the geostrophic velocity, $\partial_z v = f^{-1} \partial_x b$ (since the model is initialised in geostrophic balance), and rearranging to

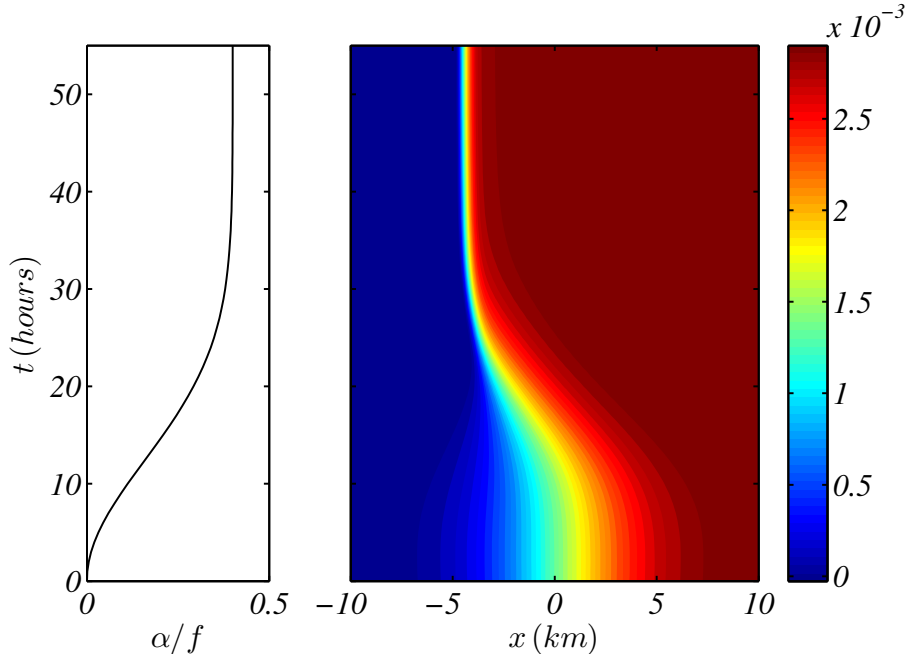


Fig. 8.9 The time evolution of the strain magnitude, $\alpha(t)/f$, and the surface buoyancy field, $b(x,0,t)$, in the numerical model for the initial condition defined by (8.18). A steady state is reached after about 45 hours.

obtain,

$$b_0 = b - \Delta b = b + \left(\frac{N}{f}\right)^2 \int \int \frac{\partial^2 b}{\partial x^2} dz dz. \quad (8.19)$$

In the absence of diffusion the frontal anomaly would collapse continuously in time according to $b_0(xe^{\beta(t)}, z)$ as discussed previously (where $\beta(t) = \int_0^t \alpha(t') dt'$). The inclusion of diffusion will limit the collapse of the front to a finite width. To determine this width, consider that at steady state the dominant balance is between the strain and diffusion, or $-\alpha x \partial_x b \simeq \kappa_h \partial_{xx} b$, which may be solved to obtain $b(x) = \Delta b (1 + \text{erf}(x/L_s))/2$ where the width of the front is $L_s = \sqrt{2\kappa_h/\alpha}$ (as discussed in Chapter 5, see §5.4). For the present values the steady frontal width is $L_s = 707 m$ in agreement with figure 8.9. Thus, the frontal anomaly b_0 will approach $b_0(xL_0/L_s, z)$ at large time, where L_0 is the initial frontal width. This frontal anomaly is convolved with the Green's function to determine the analytical vertical velocity field shown in figure 8.10b. The wave packets seen in this solution compare well in both structure and amplitude with those in the numerical model solution, particularly at depth.

The major differences between the numerical and analytical solutions shown in figure 8.10 occur near the surface front, where the local Rossby number is large. Figure 8.11 shows a magnified view of the steady solutions near the surface front. The local vorticity Rossby number, $Ro = f^{-1} \partial_x v$, from the numerical model (figure 8.11a) peaks at a value of 7.9 at the

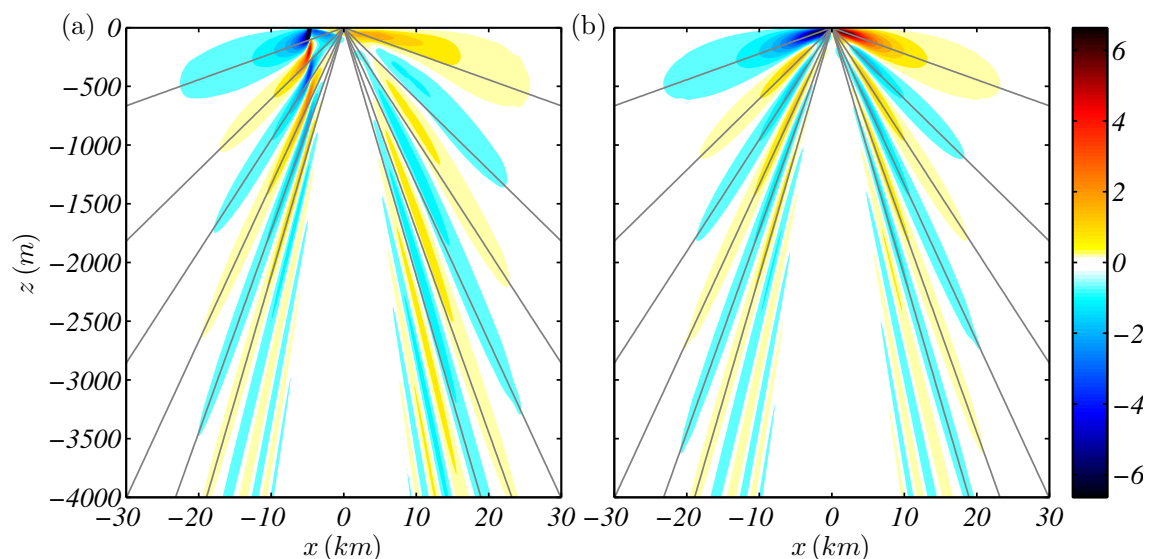


Fig. 8.10 Comparison of the numerical and analytical solutions. (a) The steady state numerical vertical velocity (m day^{-1}) field. (b) The analytical vertical velocity field (m day^{-1}) for the same frontal structure (see text for details). The grey lines on each plot are the wave and jet slopes predicted from the Green's function.

surface front. Associated with this large Rossby number, the surface front in the numerical solution (figure 8.11b) has slumped to the left under the influence of gravity. This slumping has the effect of stabilising the isopycnals compared to the analytic solution (figure 8.11c), which is gravitationally unstable near the surface. Associated with the non-linear leftward slumping of the front, the numerical vertical velocity (figure 8.11b) is weakened on the warm (anticyclonic; right) side of the front, and strengthened on the cool (cyclonic; left) side, relative to the analytic solution. The numerical solution also exhibits an intense downward jet on the cool side of the front, not present in the analytic solution. Similarly, the first few lowest frequency wave packets on the cool side of the front are intensified and steepened directly below the surface front. Furthermore, in the numerical solution the first (lowest frequency) wave packet appears on the cool side of the front around $t = 20$ hours, whereas the corresponding wave packet on the warm side of the front only appears later, around $t = 25$ hours. This behaviour is in contrast to the analytic solution which maintains perfect antisymmetry at all times.

Some of the non-linear dynamics associated with the surface front in the numerical solution can be described by non-linear frontal models (e.g. the generalised model of Chapters 2 through 5) which use the momentum coordinate, $X = x + v/f$, to include the effect of non-linear cross-frontal advection (i.e. $u \partial_x$). The buoyancy b in the non-linear models is described by the same equation as in the linear models, but in the transformed

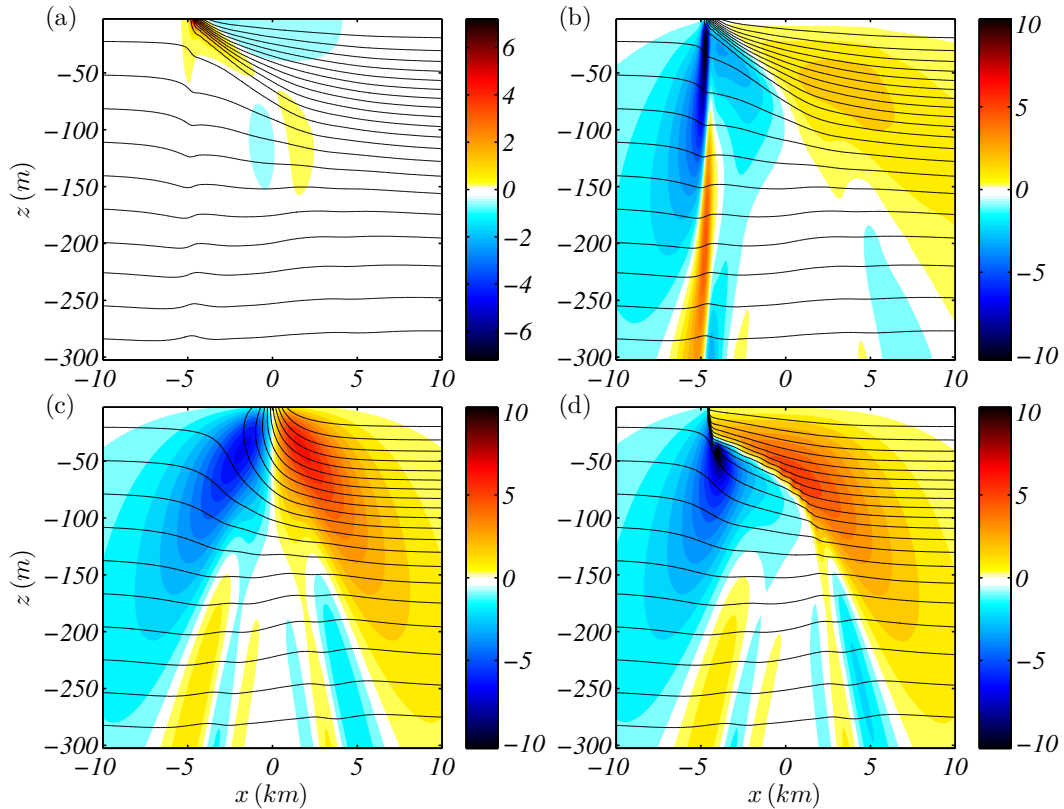


Fig. 8.11 Comparison of the numerical and analytical solutions near the surface front. (a) The vorticity Rossby number $Ro = f^{-1}\partial_x v$ in the numerical model steady state. (b) The vertical velocity field [m day^{-1}] and buoyancy contours in the numerical model steady state. (c) The vertical velocity field (m day^{-1}) and buoyancy contours predicted by the analytical model. (d) The vertical velocity field (m day^{-1}) and buoyancy contours of the ad-hoc non-linear analytical model (see text for detailed description).

coordinate — that is, with x in (6.9) replaced by X . In other words, non-linear models of two-dimensional fronts differ from linear models by the translation $x = X - v(X, z, t)/f$ of the solution, where X is the coordinate appearing in the linear solution. The *magnitude* of the along-front flow v does not change. However, the coordinate contraction associated with the translation $x = X - v(X, z, t)/f$ does imply an amplification of the cross-frontal flow (i.e. u, w) to conserve volume. In particular, the vertical velocity in the non-linear solution is scaled by the absolute vorticity, $\zeta/f = (1 + f^{-1}\partial_x v) = (1 - f^{-1}\partial_X v)^{-1}$, relative to the linear solution (see Chapter 2). We note that this relationship between linear and non-linear models is only strictly valid for the case of uniform interior PV (i.e. as assumed by the non-linear generalised model), whereas here we have a variable PV. Nonetheless, here we apply these transformations to the linear model solution shown in figure 8.11c to obtain the ad-hoc non-linear solution shown in 8.11d. The ad-hoc solution captures some features of the fully

non-linear numerical solution such as the location of the surface front and asymmetry of the vertical velocity field. However, as a result of the very large Rossby number at the front, the ad-hoc solution also exhibits a discontinuity in the buoyancy field at the surface front (down to a depth of about 40 m) and an associated infinity in the vertical velocity, implying that diffusion and other non-linear effects are important in arresting the collapse of the surface front (as discussed in Chapter 5).

8.4 Discussion

Here we have investigated the spontaneous generation of inertia-gravity waves at strongly strained density fronts. We used the linear hydrostatic model derived in Chapter 6 to formulate solutions for the circulation and density fields associated with a background strain flow, $\bar{U} = -\alpha x$, acting across a frontal buoyancy anomaly in a semi-infinite domain. The solutions depend only on the magnitude of the strain and the structure of the frontal anomaly, $b_0(x, z)$, at some instant in time. All information about the amplitude and structure of the frontal circulation, and wave frequencies, is contained with the Green's function for the problem (see figure 8.1). Whether waves are generated at a given front is determined by the Burger number of the front and the magnitude of the strain flow. Here we define the Burger number as $\epsilon_F = NH/(fL)$, where H is the depth of the frontal structure, L the width, and N/f the ratio of buoyancy to inertial frequencies. Wave generation is predicted for Burger numbers exceeding about 0.5 and strains, α , exceeding about $0.2f$. The lowest frequency distinct wave predicted to be generated by the present mechanism has frequency $\omega = 1.93f$ and is generated for a strain of $\alpha = 0.29f$ (see figure 8.4). Wave amplitudes increase with increasing frontal Burger number and background strain.

We also investigated the mechanism responsible for the generation of the frontal waves. In §8.2.3 we showed that wave generation at a strained front is analogous to the classical scenario of 'lee wave' generation associated with a uniform flow over a topographic ridge (e.g. Queney, 1947). Waves are generated in each case whenever the acceleration of the background flow around the front/ridge into the stratified ambient is fast enough that it forces the system away from geostrophic balance. More generally, any structure that presents an obstacle to the background strain flow will tend to generate waves, not only surface density fronts. Indeed, the analytic solution implies that any surface or interior PV anomaly q_0 (i.e. equation (6.3)) with some horizontal structure, whether in a bounded or unbounded domain, will generate waves in a strain flow. This result appears to be closely related to that of recent analytical studies describing the generation of gravity waves by a PV anomaly in a *shear*

flow (Lott *et al.*, 2010, 2012). These studies also employed a similar analytic approach using linearised equations of motion.

The present model is intended as a first-order description of wave generation in regions of the ocean with both sharp horizontal buoyancy gradients (order one frontal Burger numbers) and strong strain flows, such as the ocean submesoscale. Based on the analytic model results, we anticipate strong wave generation at submesoscale fronts. However, submesoscale fronts also typically exhibit large vorticities and Rossby numbers — a parameter that is assumed to be small in the linearised analytical model. Despite this assumption, in §8.3 we showed that the wave field in the analytic solution compares well with a fully non-linear numerical solution to the problem (i.e. equations (5.1)) for parameter values representative of a submesoscale front. The solutions only differ significantly near the surface front, with the numerical solution developing an intense downward jet on the cooler side of the front. The lowest frequency waves on the cooler side of the front are also intensified relative to the analytic prediction, and tend to appear earlier than their counterparts on the warm side. Given these relatively minor differences, we can be confident that the analytic model provides a robust, first-order dynamical description of one mechanism of inertia-gravity wave generation at submesoscale density fronts.

Chapter 9

Conclusion

As argued throughout this thesis, density fronts are ubiquitous and dynamically important features of ocean and atmosphere boundary layers. Fronts occur on a vast range of scales and in many distinct dynamical regimes. Synoptic scale atmospheric fronts form in the regions of convergence between atmospheric high and low pressure systems. The secondary circulation associated with these fronts can be hundreds of kilometres in cross-frontal extent and affect weather on a continental scale. At the other extreme, fronts can form in the ocean mixed layer, in regions of very intense strain between submesoscale eddies. The circulation about these fronts will typically be only hundreds of metres in cross-frontal extent. However, the cumulative impact of the very high vertical velocities at such small scale fronts makes them of vital importance to ocean circulation and biology (Ferrari, 2011). Furthermore, fronts are an important source of non-orographic gravity waves (Plougonven & Zhang, 2014). In the atmosphere, these waves initiate tropospheric mixing and convection (Zhang *et al.*, 2001), and vertically transport energy and momentum (Eliassen & Palm, 1960), thereby affecting the general circulation. Similarly, in the ocean, waves generated at fronts provide a mechanism for energy loss from large scale flows, and drive mixing via breaking in the ocean interior.

In Chapter 1 we introduced a useful idealised configuration for investigating such frontal dynamics: the ‘two-dimensional (2D) strained front’ defined by the inviscid governing equations (1.12). While the dynamics and mathematics of the 2D system are greatly simplified compared with the fully three-dimensional equations, the 2D front remains a challenging problem which has been investigated by many authors over the past four decades. Solutions to the 2D frontal equations in various limits are listed chronologically in table 9.1, from the quasigeostrophic solution of Williams & Plotkin (1968), to the unbalanced frontogenesis solution of Blumen (2000). These solutions have many common properties. In particular, all consider the limit of weak (or zero) strain, $\alpha \ll f$, and omit propagating waves. Given the solutions all arise from the same set of simplified equations (1.12), they should be obtainable

as specific limits of a more general solution. Here we have developed just such a generalised solution that (i) unifies these previous solutions and (ii) incorporates large strains and waves. Our generalised mathematical model is thus capable of describing frontogenesis and wave generation in a wide variety of situations. We developed two versions of the model with different balances of accuracy versus idealisation. The two versions are listed as solutions 6 and 7 in table 9.1.

The first, studied in Chapters 2 through 5, is the non-linear version of the model describing the classical idealised 2D front problem of a strained, uniform potential vorticity fluid, trapped between rigid lids at the top and bottom of the domain. This generalised non-linear model improves upon previous models of this system (i.e. solutions 2, 4 and 5 in table 9.1) in a number of ways. In the first instance it serves to unify various previous studies as limits of the generalised model solution. For instance, the semigeostrophic model of Hoskins & Bretherton (1972) describing strain-forced frontogenesis emerges as the small-strain, balanced limit of the solution. The spontaneous frontogenesis model of Blumen (2000) emerges as the unstrained, unstratified limit of the solution. Furthermore, the steady state solution to the geostrophic adjustment problem derived by Blumen & Wu (1995) emerges as the steady state of the generalised model for vanishing strain. Secondly, the generalised model extends previous work. The generalised model extends the work of Blumen (2000) to describe spontaneous frontogenesis in a stratified flow. It extends the work of Hoskins & Bretherton (1972) to permit large strains, $\alpha \sim f$, rather than being limited to weak strain, $\alpha \ll f$, as in that model. This latter extension is particularly vital in permitting the description of frontogenesis on the ocean submesoscale and the spontaneous generation of inertia-gravity waves.

However, the non-linear uniform PV model, while very accurate, is limited in its direct applicability to geophysical flows owing to the artificiality of some of the assumptions. For instance, geophysical flows often have very non-uniform PV. The constraint of uniform PV in the model results in fronts on both the upper and lower lids, whereas frontal gradients — particularly in the ocean — usually decay with depth. Also, the constraint to dual-rigid lid boundary conditions prevents the vertical propagation of waves and instead traps them around the front. While there are geophysical situations where this occurs (for example, specific stratification profiles as studied in §7.4), there is usually at least some propagation of waves away from the surface layer. We note that it is possible to generalise the non-linear uniform PV model to the semi-infinite domain — that is, with only one rigid lid as Davies & Muller (1988) have done for the semigeostrophic limit (model 3 in table 9.1) — but these solutions have the unfortunate feature of finite magnitude at infinity, and so do not seem to be of significant practical value.

Hence, in Chapters 6 through 8 we developed and described a linear version of the generalised model that removes many of the above limitations. The linear model includes non-hydrostatic dynamics, bounded or unbounded domains, and arbitrary stratification and frontal structure. The trade-off for this increased flexibility is that the linear model is only formally valid for small Rossby numbers, $Ro_g = \Delta B_0 H / (f^2 L^2) \ll 1$. The linear model therefore breaks down near the surface fronts where the Rossby number is large and cannot accurately describe rapid frontogenesis on the boundary. However, the linear model is accurate away from these regions as shown by the numerical simulations in Chapters 7 and 8. In particular, the linear model accurately predicts the frequencies, amplitude and structure of waves generated spontaneously at the front, which are then either trapped around the front (rigid lid domain, Chapter 7) or propagate vertically out of the surface layer (unbounded domains, Chapter 8).

The linear version of the model is of course closely related to the non-linear one. Specifically, the non-linear model is given by the hydrostatic, uniform PV, rigid lid limit of the linear model, but with the regular Eulerian coordinate (x) in that model replaced by the non-linear momentum coordinate ($X = x + Ro v$). The velocities in the cross-frontal plane are correspondingly scaled to satisfy volume conservation. These mathematical differences provide insight into some of the missing non-linear dynamics in the linear model. In particular, larger Rossby numbers (stronger fronts) lead to the slumping of the frontal interface (the region of maximum horizontal buoyancy gradient) towards the cyclonic side. This effect intensifies the vertical flow on that side of the front (which is directed away from the boundary) and weakens and broadens the toward-boundary flow on the anticyclonic side. This non-linear slumping effect can be included *a posteriori* in the linear model in an ad-hoc manner as in §8.3.

In §9.1 we summarise the key results derived from our generalised frontal model and their geophysical significance. We then (§9.2) discuss the limitations of the model and future directions for work on this topic.

Model	Waves	α/f	Ro_g	N/f	Constraints	Domain	Example application
1 Williams & Plotkin (1968) <i>Quasigeostrophic</i>	no	$\ll 1$	$\ll 1$	$\gg 1$		rigid lids	
2 Hoskins & Bretherton (1972) <i>Semigeostrophic</i>	no	$\ll 1$		$\gg 1$	uniform PV [†]	rigid lids	synoptic-scale frontogenesis
3 Davies & Muller (1988) <i>Semigeostrophic</i>	no	$\ll 1$		$\gg 1$	uniform PV, finite at ∞	semi-inf.	
4 Blumen & Wu (1995) <i>Geostrophic</i>	no	0			uniform PV, steady state	rigid lids	geostrophic adjustment energy release
5 Blumen (2000)	inertial	0		0	zero PV	rigid lids	ocean mixed layer frontogenesis
6 Chapter 2 <i>Non-linear generalised model</i>	yes		$\ll (f/\alpha)^2$	$\gg 1$	uniform PV	rigid lids	submesoscale frontogenesis
7 Chapter 6 <i>Linear generalised model</i>	yes		$\ll 1$			any	spontaneous wave generation and vertical propagation

Table 9.1 Solutions of the classical two-dimensional strained front problem defined by (1.12). The front is assumed to infinitely long and straight such that along-front gradients may be neglected. A simple background strain flow $\bar{\Psi} = -\alpha xy$ acts across the front. Models in the table are listed in chronological order. Models 1 through 4 are ‘balance’ models that omit waves, whereas models 5 through 7 include waves. Parameter $Ro_g = \Delta B_0 H / (f^2 L^2)$ is the geostrophic Rossby number, with L the frontal width, H the height, f the Coriolis parameter, and ΔB_0 the buoyancy difference across the front. Parameter N^2 is the buoyancy frequency. [†]The theory of Hoskins & Bretherton (1972) includes non-uniform PV but analytic solutions are only presented for uniform PV.

9.1 Summary of key results

Below we have separated the key results emerging from the generalised model developed herein into three categories: wave generation, frontogenesis and strong strain dynamics.

9.1.1 Wave generation

The generalised model describes the two main types of wave generation at fronts widely discussed in the literature: adjustment and spontaneous generation (Plougonven & Zhang, 2014). Adjustment occurs when the frontal system is not in its ‘balanced state’ for the given value for strain, and therefore releases energy and adjusts towards the balanced state by generating propagating waves. In the limit of zero strain the balanced state corresponds to geostrophic balance, and the process of wave generation is called ‘geostrophic adjustment’. For very weak strain the balanced state is ‘semigeostrophic balance’ as defined by the Hoskins & Bretherton (1972) solution. For larger strain the ‘balanced state’ can be determined from the forced solution of our generalised model. Unbalanced initial states, and thus adjustment wave generation, can occur in the atmosphere and ocean when the fluid is subject to very rapid fluxes of heat, mass or momentum. Here ‘rapid’ implies on a timescale much faster than the wave/adjustment timescale of f^{-1} . Examples in the ocean include storm-driven mixing (e.g. Tandon & Garrett, 1994) and river outflows, and in the atmosphere, differential heating due to variable cloud cover (e.g. Blumen *et al.*, 1996). A further example arising from the present study is an eddy field (i.e. background strain flow) that varies rapidly in time as studied in §4.3.

Of course, the forced solution to the generalised model is not ‘balanced’ in the classical sense since it contains waves (except in the limit of vanishingly weak strain). This brings us to the second mechanism of wave generation at fronts described by the generalised model: spontaneous generation. Regardless of the initial state of a density front, for large enough strains, waves will inevitably be generated due to the action of the strain flow across the collapsing frontal PV anomaly. The inevitability of generation is indicated by the fact that the waves emerge as an intrinsic part of the forced solution — the ‘most balanced state’ of the system. In other words, a true balanced state does not exist for finite strain; this result is sometimes described as the ‘fuzziness of the slow manifold’ (e.g. Vanneste, 2013). Indeed, the idea of ‘balance’ ceases to make sense for large strains or equivalently, large Rossby numbers (McIntyre, 2009). As shown in Chapter 8, the spontaneous wave generation occurs as a result of the acceleration (or deflection) of the strain flow around the front and into the stratified ambient. The generated waves do not propagate but are instead trapped by the strain

flow in a characteristic ‘palm frond’ pattern around the front. The process of frontal wave generation and trapping is thus remarkably similar to that of mountain lee waves (§8.2.3).

The generalised model describes the amplitudes and frequencies of the generated waves. For the adjustment waves, these properties are determined by the scale and amplitude of the initial imbalance. For the spontaneous waves, the properties are entirely controlled by the magnitude of the strain (see §8.2.1). Significantly, the wave amplitude is exponentially small for weak strains, consistent with previous results (Vanneste, 2008), but can be large for strains exceeding about $0.2f$. Such moderate to strong strains are relatively common in both the atmosphere and ocean, implying that spontaneous generation at fronts could be a significant source of inertia-gravity waves.

Furthermore, for particularly sharp fronts non-hydrostatic dynamics can be important in describing the wave field. For sharp enough fronts, even for moderate strain (0.2 to $0.3f$), the trapped wave field can provide an order one contribution to the vertical velocity about the front. In particular, if waves are vertically trapped — for instance by a region of low stability in the upper troposphere — they can give rise to finescale bands of vertical flow that fundamentally change the structure of the frontal circulation. As shown in Chapter 7, these structures can only be observed in very high resolution numerical solutions, and are therefore unlikely to be present in most large scale numerical models. Nonetheless their effects are potentially important to local weather — for instance in the formation of rain bands.

9.1.2 Frontogenesis

As with wave generation, the generalised model describes two mechanisms of frontogenesis. The first is ‘imbalance’ or ‘spontaneous’ frontogenesis associated with the waves generated during the adjustment process described in §9.1.1. As noted above, the unbalanced initial conditions giving rise to these waves occur due to large boundary fluxes of mass, momentum and/or heat. Non-linear self-advection by the generated waves can give rise to a pile-up of wave amplitude and the rapid formation of a discontinuity. The size and scale of the initial imbalance, and thus wave amplitude and frequency, required for such a discontinuity to form was described in Chapter 3 in terms of the Rossby and Froude numbers of the initial state (e.g. figure 3.3). The formation of a discontinuity in the inviscid equations implies that the system will develop instabilities and/or exhibit enhanced mixing at the front. The generalised model also shows that there exists an intriguing dynamical regime where fronts possess geostrophically balanced adjusted states, but these states are not attainable owing to the rapid frontogenesis during the adjustment process.

The second mechanism of frontogenesis is called ‘strain-forced’ — that is, the sharpening of frontal gradients, and ultimate discontinuity in the inviscid fields, associated with the

confluent background flow. This mechanism has historically also been described as ‘balanced frontogenesis’ but we prefer to avoid this terminology since as described above, the solution inevitably includes spontaneously generated waves at finite strain. The action of the confluent strain flow across the front gives rise to a secondary circulation, which intensifies with increasing strain (see §9.1.3 below). As already noted, confluent background flows are very common in the ocean and atmosphere boundary layers on a vast range of scales, due to the ubiquity of eddies generated via baroclinic and barotropic instabilities. While the strain fields associated with these eddies are never precisely uniform, the basic mechanism of strain-forced frontogenesis described by the 2D model should still apply (see §9.2).

Whereas imbalance frontogenesis occurs on the wave timescale (f^{-1} or faster), strain-forced frontogenesis occurs on the (usually slower) strain timescale (α^{-1}). The two mechanisms of frontogenesis can and do occur simultaneously (e.g. Ostdiek & Blumen, 1997), and the generalised model captures these dynamics.

9.1.3 Strong strain dynamics

Perhaps the most important advance made by the generalised model is the inclusion of order f strains, such as occur on the ocean submesoscale. Strong strains have two main consequences in terms of the frontal dynamics: (i) intense spontaneous wave generation as noted above, and (ii) significant changes to the strength and structure of the secondary circulation. Strong strains tend to horizontally confine the secondary circulation, leading to steeper frontal jets (for unbounded domains), or equivalently narrower overturning cells (for bounded domains). Indeed, the scale width of the circulation may be determined as $L \sim 2NH/(\pi\alpha)$ where N^2 is the stratification, α the strain and H an appropriate height scale (see Chapter 4). As a result of this confinement, frontal vertical velocities increase quadratically at large strain, as opposed to linearly at small strains (see §8.2.1). A qualitatively similar non-linear strain dependence of frontal velocities has recently been observed in a submesoscale resolving numerical model (Rosso *et al.*, 2015, also see figure 1.3 herein). As such, the generalised model may provide a basis for parametrisation of submesoscale fronts in mesoscale-resolving numerical models. Non-linear finite Rossby number dynamics, as described by the non-linear generalised model, will also be important in such a parametrisation.

Based on the generalised model, we can make an initial guess as to what form a sub-mesoscale vertical velocity parametrisation might take. Generalising our results to three dimensions, we anticipate that the frontal vertical velocity scales as

$$W \sim fH \zeta(1 + \zeta) S \sqrt{1 + c_1 S^2}, \quad (9.1)$$

or similar, where $S = \sqrt{(\partial_x u - \partial_y v)^2 + (\partial_x u + \partial_y v)^2} / f$ is the (background) net strain magnitude normalised by f (in two dimensions $S = 2\alpha/f$), $\zeta = |\partial_x v - \partial_y u| / f$ is the (background) relative vertical vorticity magnitude normalised by f (in two dimensions $\zeta = f^{-1} |\partial_x v| = Ro_g$) and c_1 is a non-dimensional constant ($c_1 \simeq 1.8$ from a fit to the curve shown in figure 8.3b). Equation (9.1) captures (i) the non-linear strain dependence as described above, (ii) the linear dependence on frontal strength (vorticity) at small Rossby numbers (i.e. in the linear model), and (iii) the non-linear increase in the vertical velocity at large Rossby numbers that is associated with frontal slumping as seen in the non-linear generalised model.¹ Of course, the parametrisation suggested by (9.1) is motivated from an entirely two-dimensional, idealised theory and would require significant investigation and comparison with more sophisticated models to verify (see the discussion of future work below, §9.2). The novel element of (9.1) is the quadratic strain dependence for strong strains. By contrast, the Hoskins & Bretherton (1972) model would yield a vertical velocity scale prediction of $W_{HB} \sim fH \zeta (1 + \zeta) S$ and the Williams & Plotkin (1968) quasigeostrophic model a prediction of $W_{QG} \sim fH \zeta S$.

9.2 Model limitations and future work

The frontal model developed herein provides the most complete solution for the 2D frontal system defined by (1.12) that as yet exists. However, the applicability of the model is limited by the assumptions implicit in this idealised configuration. The main assumptions are that (i) fronts are infinitely long and straight, (ii) the background strain is horizontally uniform, and (iii) the strain is uniform with depth. We now consider in detail what the implications of each of these assumptions and where they may fail in real flows.

In practice assumption (i) requires that the width of fronts is much less than their length, so they appear locally to be infinitely long. This assumption is not particularly limiting, since it is essentially the definition of a front; that is, a elongated feature with large horizontal density gradient in one direction, and minimal gradient in the orthogonal direction. The second part of the assumption requires that these elongated features (fronts) have minimal curvature. This assumption would appear to be valid for many larger (e.g. synoptic) scale fronts, although curvature can sometimes be significant (e.g. Vaughan *et al.*, 2014). We might anticipate that the straightness assumption is more questionable for smaller scale fronts — for example on the ocean submesoscale — since these fronts are rapidly deformed by the eddy field in which they reside. However, we must also consider that the frontal flow and wave generation (which are driven by the strain flow) also evolve on a much faster timescale

¹Specifically, the absolute vertical vorticity factor, $(1 + \zeta)$, appears in (9.1) due to the expression for vertical velocity in the non-linear model; that is, $w = -\partial_x \psi = -(1 + f^{-1} \partial_x v) \partial_x \psi$ as derived in Chapter 2.

for smaller scale fronts (large strains). Thus, for the dynamics described by the 2D model to be locally relevant we only require that some part of a front remain approximately straight for relatively short period of time (order α^{-1} , so a day or less for very small scales). As an example, this approximation would be seen to be reasonable for the submesoscale fronts pictured in figure 1.1b.

As argued in Chapter 1, a horizontally uniform strain (assumption ii) is the first order Taylor approximation for any arbitrarily complex strain flow. Whether this approximation is reasonable depends on the radius of the eddies responsible for generating the strain flow, compared to the frontal width. The approximation will only be reasonable for locations and times where the frontal width is much narrower than the eddy radius. This is likely to be true for most strong fronts, and will become increasingly true with time as the confluent strain narrows the front. In addition, the uniform strain assumption implies that the cross-frontal flow is confluent everywhere, whereas real eddy fields have regions of confluence interspersed between regions of diffluence. One consequence of such spatial variability is that generated waves will be swept along the front out of the region of confluence, and therefore will no longer be horizontally trapped in quite the same manner as in the idealised model. This behaviour could potentially explain the prevalence of waves in jet exit regions (Plougonven & Zhang, 2014), although more investigation is needed.

Requiring that the strain flow is uniform with depth (assumption iii) is equivalent to the statement that the eddy fields responsible for generating the background strain are entirely barotropic. In terms of the front itself, this assumption is reasonable if the depth scale of the eddies is similar or deeper than the front. In that case, we might anticipate that the frontal evolution and wave generation predicted by the generalised model is accurate. However, the propagation of the waves below the eddy field depth will change markedly, since they will no longer be trapped by the strain flow and will instead be able to propagate freely.

In addition to the above assumptions, there are many neglected factors in our model that are likely to prove important in more complicated flows. For example, many fronts exist in a region with both background shear and strain. Shear will affect frontogenesis (e.g. Hoskins & Bretherton, 1972), as well as the generation (e.g. Lott *et al.*, 2010) and trapping (e.g. Griffiths & Reeder, 1996) of the waves. The front may also be unstable to Kelvin-Helmholtz (in the cross-front and/or along-front directions) and baroclinic (e.g. McWilliams & Molemaker, 2009, 2011) instabilities, among others. Further, we have not considered a realistic representation of the processes that act to prevent frontal collapse. Where necessary in our numerical solutions we employed a purely horizontal diffusion to counteract frontogenesis, whereas a vertical diffusion, Rayleigh drag, or more sophisticated boundary layer model may be more appropriate.

Given the above assumptions and limitations, the next stage for the present work is to attempt to apply the generalised model to describe frontogenesis and wave generation in more complex situations. One particular regime of interest is the ocean submesoscale. The applicability of the model in describing submesoscale frontogenesis and wave generation could be examined via idealised baroclinic instability simulations such as those pictured in figure 1.1b. In terms of submesoscale parametrisations, the results of high resolution large scale ocean models such as that of Rosso *et al.* (2015) could be used to further develop and investigate the scaling for vertical velocity implied by the generalised model (i.e. (9.1)). In terms of atmospheric applications, there appears to be scope to investigate applying our predicted spontaneous generation thresholds (which depend on the large scale strain and frontal scale as described in Chapter 8) to improve parametrisations of wave generation at atmospheric jets and fronts (Plougonven & Zhang, 2014). There is also the potential to compare the generalised model predictions with observations of wave generation events in the atmosphere (e.g. Knippertz *et al.*, 2010) and ocean (e.g. Alford *et al.*, 2013).

Thus, despite the limitations of our generalised frontal model, it provides a novel analytical description of frontogenesis in intense strain fields, and the generation of waves during such frontogenesis. As such, the model should be find significant future applications in the study of fronts in the ocean and atmosphere.

References

- ALFORD, M. H., SHCHERBINA, A. Y. & GREGG, M. C. 2013 Observations of near-inertial internal gravity waves radiating from a frontal jet. *J. Phys. Oceanogr.* **43**, 1225–1239.
- BERGERON, T. 1928 Uber die dreidimensional verknupfende Wettranalyse I. *Geofys. Publ.* **5** (6), 1–111.
- BLUMEN, W. 1972 Geostrophic adjustment. *Rev. Geophys. Space Phys.* **10**, 485–528.
- BLUMEN, W. 1997 A model of inertial oscillations with deformation frontogenesis. *J. Atmos. Sci.* **54**, 2681–2692.
- BLUMEN, W. 2000 Inertial oscillations and frontogenesis in a zero potential vorticity model. *J. Phys. Oceanogr.* **30**, 31–39.
- BLUMEN, W., GAMAGE, N., GROSSMAN, R. L., LEMONE, M. A. & MILLER, L. J. 1996 The low-level structure and evolution of a dry Arctic front over the central United States. Part II: Comparison with theory. *Mon. Weather Rev.* **124**, 1676–1691.
- BLUMEN, W. & WILLIAMS, R. T. 2001 Unbalanced frontogenesis. Part I: Zero potential vorticity. *J. Atmos. Sci.* **58**, 2180–2195.
- BLUMEN, W. & WU, R. 1995 Geostrophic adjustment: frontogenesis and energy conversion. *J. Phys. Oceanogr.* **25**, 428–438.
- BOCCALETTI, G., FERRARI, R. & FOX-KEMPER, B. 2007 Mixed layer instabilities and restratification. *J. Phys. Oceanogr.* **37**, 2228–2250.
- BOYCE, W. E., DIPRIMA, R. C. & HAINES, C. W. 1992 *Elementary differential equations and boundary value problems*, vol. 9. Wiley New York.
- BUHLER, O. & MCINTYRE, M. E. 2005 Wave capture and wave-vortex duality. *J. Fluid Mech.* **534**, 67–95.
- CULLEN, M. & PURSER, R. 1984 An extended theory of semigeostrophic frontogenesis. *J. Atmos. Sci.* **41**, 1477–1497.
- DANIOUX, E., VANNESTE, J., KLEIN, P. & SASAKI, H. 2012 Spontaneous inertia-gravity-wave generation by surface-intensified turbulence. *J. Fluid Mech.* **699**, 153–1732.
- DAVIES, H. C. & MULLER, J. C. 1988 Detailed description of deformation-induced semi-geostrophic frontogenesis. *Q. J. Roy. Meteor. Soc.* **114**, 1201–1219.

- ELIASSEN, A. 1962 On the vertical circulation in frontal zones. *Geofys. Publ.* **24** (4), 147–160.
- ELIASSEN, A. & PALM, E. 1960 On the transfer of energy in stationary mountain waves. *Geofys. Publ.* **22**, 1–23.
- FERRARI, R. 2011 A frontal challenge for climate models. *Science* **332** (6027), 316–317.
- FORD, R., MCINTYRE, M. E. & NORTON, W. A. 2000 Balance and the slow quasimanifold: some explicit results. *J. Atmos. Sci.* **57**, 1236–1254.
- GALL, R., WILLIAMS, R. & CLARK, T. 1987 On the minimum scale of surface fronts. *J. Atmos. Sci.* **44**, 2562–2574.
- GALL, R. L., WILLIAMS, R. T. & CLARK, T. L. 1988 Gravity waves generated during frontogenesis. *J. Atmos. Sci.* **45** (15), 2204–2219.
- GARNER, S. T. 1989 Fully lagrangian numerical solutions of unbalanced frontogenesis and frontal collapse. *J. Atmos. Sci.* **46**, 717–739.
- GILL, A. E. 1976 Adjustment under gravity in a rotating channel. *J. Fluid Mech.* **77**, 603–621.
- GRIFFITHS, M. & REEDER, M. J. 1996 Stratospheric inertia-gravity waves generated in a numerical model of frontogenesis. I: Model solutions. *Q. J. Roy. Meteor. Soc.* **122**, 1153–1174.
- HOBBS, P. V., MATEJKA, T. J., HERZEGH, P. H., LOCATELLI, J. D. & HOUZE, R. A. JR. 1980 The mesoscale and microscale structure and organization of clouds and precipitation in the midlatitude cyclones. I: A case study of a cold front. *J. Atmos. Sci.* **37**, 568–596.
- HOSKINS, B. J. 1982 The mathematical theory of frontogenesis. *Annu. Rev. Fluid Mech.* **14**, 131–151.
- HOSKINS, B. J. & BRETHERTON, F. P. 1972 Atmospheric frontogenesis models: mathematical formulation and solution. *J. Atmos. Sci.* **29**, 11–37.
- HOUZE, R. A. JR & HOBBS, P. V. 1982 Organization and structure of precipitating cloud systems. *Adv. Geophys.* **24**, 225–315.
- JONES, W. L. 1969 Ray tracing for internal gravity waves. *J. Geophys. Res.* **74** (8), 2028–2033.
- JUCKES, M. 1994 Quasigeostrophic dynamics of the tropopause. *J. Atmos. Sci.* **51**, 2756–2768.
- KARAN, H., FITZPATRICK, P. J., HILL, C. M., LI, Y., XIAO, Q. & LIM, E. 2010 The formation of multiple squall lines and the impacts of WSR-88D radial winds in a WRF simulation. *J. Atmos. Sci.* **25**, 242–262.
- KNIPPERTZ, P., CHAGNON, J. M., FOSTER, A., LATHOUWERS, L., MARSHAM, J. H., METHVEN, J. & PARKER, D. J. 2010 Research flight observations of a prefrontal gravity wave near the southwestern UK. *Weather* **65** (11), 293–297.

- KUO, A. C. & POLVANI, L. M. 1997 Time-dependent fully nonlinear geostrophic adjustment. *J. Phys. Oceanogr.* **27**, 1614–1634.
- LEVY, M., FERRARI, R., FRANKS, P. J. S., MARTIN, A. P. & RIVIERE, P. 2012 Bringing physics to life at the submesoscale. *Geophys. Res. Lett.* **39**.
- LEY, B. E. & PELTIER, W. R. 1978 Wave generation and frontal collapse. *J. Atmos. Sci.* **35**, 3–17.
- LINDZEN, R. S. & TUNG, K. K. 1976 Banded convective activity and ducted gravity waves. *Mon. Weather. Rev.* **104** (12), 1602–1617.
- LOTT, F., PLOUGONVEN, R. & VANNESTE, J. 2010 Gravity waves generated by sheared potential vorticity anomalies. *J. Atmos. Sci.* **67** (1), 157–170.
- LOTT, F., PLOUGONVEN, R. & VANNESTE, J. 2012 Gravity waves generated by sheared three-dimensional potential vorticity anomalies. *J. Atmos. Sci.* **69** (7), 2134–2151.
- MAHADEVAN, A., D'ASARO, E., LEE, C. & PERRY, M. J. 2012 Eddy-driven stratification initiates North Atlantic spring phytoplankton blooms. *Science* **337** (6090), 54–58.
- MAHADEVAN, A. & TANDON, A. 2006 An analysis of the mechanisms for submesoscale vertical motion at ocean fronts. *Ocean Modell.* **14**, 241–256.
- MARSHALL, J., ADCROFT, A., HILL, C., PERELMAN, L. & HEISEY, C. 1997 A finite-volume, incompressible Navier Stokes model for studies of the ocean on parallel computers. *J. Geophys. Res.* **102** (C3), 5753–5766.
- MCINTYRE, M. E. 2009 Spontaneous imbalance and hybrid vortex-gravity structures. *J. Atmos. Sci.* **66**, 1315–1326.
- MCWILLIAMS, J. C. & MOLEMAKER, M. J. 2009 Linear fluctuation growth during frontogenesis. *J. Phys. Oceanogr.* **39**, 3111–3129.
- MCWILLIAMS, J. C. & MOLEMAKER, M. J. 2011 Baroclinic frontal arrest: A sequel to unstable frontogenesis. *J. Phys. Oceanogr.* **41**, 601–619.
- MURAKI, D. J. 2011 Large-amplitude topographic waves in 2D stratified flow. *J. Fluid Mech.* **681**, 173–192.
- NEVES, A. 1996 Unbalanced frontogenesis with constant potential vorticity. Master's thesis, Naval Postgraduate School, Monterey, California.
- NIKURASHIN, M., FERRARI, R., GRISOUARD, N. & POLZIN, K. 2014 The Impact of Finite-Amplitude Bottom Topography on Internal Wave Generation in the Southern Ocean. *J. Phys. Oceanogr.* **44**, 2938–2950.
- OSTDIEK, V. & BLUMEN, W. 1997 A dynamic trio: inertial oscillation, deformation frontogenesis, and the Ekman-Taylor boundary layer. *J. Atmos. Sci.* **54**, 1490–1502.
- OU, H. W. 1984 Geostrophic adjustment: a mechanism for frontogenesis. *J. Phys. Oceanogr.* **14**, 994–1000.

- PIERREHUMBERT, R. T. 1984 Linear results on the barrier effects of mesoscale mountains. *J. Atmos. Sci.* **41** (8), 1356–1367.
- PLOUGONVEN, R. & SNYDER, C. 2005 Gravity waves excited by jets: propagation versus generation. *Geophys. Res. Lett.* **32**.
- PLOUGONVEN, R. & ZEITLIN, V. 2005 Lagrangian approach to geostrophic adjustment of frontal anomalies in stratified fluid. *Geoph. Astroph. Fluid Dyn.* **9**, 101–135.
- PLOUGONVEN, R. & ZHANG, F. 2007 On the forcing of inertia-gravity waves by synoptic-scale flows. *J. Atmos. Sci.* **64**, 1737–1142.
- PLOUGONVEN, R. & ZHANG, F. 2014 Internal gravity waves from atmospheric jets and fronts. *Rev. Geophys.* **52** (1), 33–76.
- POLZIN, K. L. 2010 Mesoscale eddy-internal wave coupling. Part II: energetics and results from PolyMode. *J. Phys. Oceanogr.* **40**, 789–801.
- QUENEY, P. 1947 *Theory of perturbations in stratified currents with applications to air flow over mountain barriers*. University of Chicago Press.
- REEDER, M. J. & GRIFFITHS, M. 1996 Stratospheric inertia-gravity waves generated in a numerical model of frontogenesis. II: Wave sources, generation mechanisms and momentum fluxes. *Q. J. Roy. Meteor. Soc.* **122**, 1175–1195.
- ROSSBY, C. G. 1938 On the mutual adjustment of pressure and velocity distributions in certain simple current systems, II. *J. Mar. Res.* **1**, 239–263.
- ROSSO, I., HOGG, A. MCC., KISS, A. E. & GAYEN, B. 2015 Topographic influence on sub-mesoscale dynamics in the Southern Ocean. *Geophys. Res. Lett.* **42** (4), 1139–1147.
- RYAN, B. F., KATZFEY, J. J., ABBS, D. J., JAKOB, C., LOHMANN, U., ROCKEL, B., ROTSTAYN, L. D., STEWART, R. E., SZETO, K. K., TSELIODIS, G. *et al.* 2000 Simulations of a cold front by cloud-resolving, limited-area, and large-scale models, and a model evaluation using in situ and satellite observations. *Mon. Weather. Rev.* **128** (9), 3218–3235.
- SAWYER, J. S. 1956 On the vertical circulation at meteorological fronts and its relation to frontogenesis. *Proc. R. Soc. London Ser. A* **234**, 346–362.
- SCHMIDT, J. M. & COTTON, W. R. 1990 Interactions between upper and lower tropospheric gravity waves on squall line structure and maintenance. *J. Atmos. Sci.* **47** (10), 1205–1222.
- SCHULTZ, D. M. 2005 A review of cold fronts with prefrontal troughs and wind shifts. *Mon. Weather. Rev.* **133** (8), 2449–2472.
- SHCHERBINA, A. Y., D'ASARO, E. A., LEE, C. M., KLYMAK, J. M., MOLEMAKER, M. J. & MCWILLIAMS, J. C. 2013 Statistics of vertical vorticity, divergence, and strain in a developed submesoscale turbulence field. *Geophys. Res. Lett.* **40**.
- SNYDER, C., SKAMAROCK, W. & ROTUNNO, R. 1993 Frontal dynamics near and following frontal collapse. *J. Atmos. Sci.* **50**, 3194–3211.

- STONE, P. H. 1966 Frontogenesis by horizontal wind deformation fields. *J. Atmos. Sci.* **23**, 455–565.
- TANDON, A. & GARRETT, C. 1994 Mixed layer restratification due to a horizontal density gradient. *J. Phys. Oceanogr.* **24** (6), 1419–1424.
- TAYLOR, J. R. 2008 Numerical simulations of the stratified oceanic bottom boundary layer. PhD thesis, University of California, San Diego.
- THOMAS, L. N. 2012 On the effects of frontogenetic strain on symmetric instability and inertia-gravity waves. *J. Fluid Mech.* **711**, 620–640.
- THOMAS, L. N., TANDON, A. & MAHADEVAN, A. 2008 Submesoscale processes and dynamics. In *Geophysical Monograph Series 177: Ocean Modeling in an Eddying Regime*. American Geophysical Union.
- VANNESTE, J. 2008 Exponential smallness of inertia-gravity wave generation at small Rossby number. *J. Atmos. Sci.* **65**, 1622–1637.
- VANNESTE, J. 2013 Balance and spontaneous wave generation in geophysical flows. *Annu. Rev. Fluid Mech.* **45**, 147–172.
- VANNESTE, J. & YAVNEH, I. 2004 Exponentially small inertia-gravity waves and the breakdown of quasigeostrophic balance. *J. Atmos. Sci.* **61** (2), 211–223.
- VAUGHAN, G., METHVEN, J., ANDERSON, D., ANTONESCU, B., BAKER, L., BAKER, T. P., BALLARD, S. P., BOWER, K. N., BROWN, P. R. A., CHAGNON, J. *et al.* 2014 Cloud banding and winds in intense European cyclones: Results from the DIAMET project. *Bull. Amer. Meteor. Soc.* .
- VIUDEZ, A. 2007 The origin of the stationary frontal wave packet spontaneously generated in rotating stratified vortex dipoles. *J. Fluid Mech.* **593**, 359–383.
- VIUDEZ, A. & DRITSCHEL, D. G. 2006 Spontaneous generation of inertia-gravity wave packets by balanced geophysical flows. *J. Fluid Mech.* **553**, 107–117.
- WATERMAN, S., POLZIN, K., NAVEIRA-GARABATO, A., SHEEN, K. & FORRYAN, A. 2014 Suppression of internal wave breaking in the Antarctic Circumpolar Current near topography. *J. Phys. Oceanogr.* **44** (5), 1466–1492.
- WILLIAMS, P. D., HAINE, T. W. N. & READ, P. L. 2008 Inertia-gravity waves emitted from balanced flow: observations, properties, and consequences. *J. Atmos. Sci.* **65**, 3543–3556.
- WILLIAMS, R. T. & PLOTKIN, J. 1968 Quasi-geostrophic frontogenesis. *J. Atmos. Sci.* **25**, 201–206.
- WU, R. & BLUMEN, W. 1995 Geostrophic adjustment of a zero potential vorticity flow initiated by a mass imbalance. *J. Phys. Oceanogr.* **25**, 439–445.
- WUNSCH, C. & FERRARI, R. 2004 Vertical mixing, energy and the general circulation of the oceans. *Annu. Rev. Fluid Mech.* **36**, 281–314.

- ZHANG, F. 2004 Generation of mesoscale gravity waves in upper-tropospheric jet-front systems. *J. Atmos. Sci.* **61**, 440–457.
- ZHANG, F., DAVIS, C. A., KAPLAN, M. L. & KOCH, S. E. 2001 Wavelet analysis and the governing dynamics of a large-amplitude mesoscale gravity-wave event along the East Coast of the United States. *Q. J. Roy. Meteor. Soc.* **127** (577), 2209–2245.

Appendix A

Green's function solution of the non-linear generalised model

This appendix relates to the derivation of the real-space impulse response (Green's function) solution of the non-linear generalised model in Chapter 4 of the main text.

A.1 Green's function differential equation

Here we show that, as stated in Chapter 4, the convolution given by (4.31) — with the impulse response defined by (4.34) — is the forced solution to the generalised model (PDE (2.29) with $\mathcal{N} \equiv 0$) when the strain δ is constant. We begin by taking a Fourier transform in X of (2.29) with δ constant to obtain,

$$\left[\frac{\partial^2}{\partial Z^2} \left(\frac{\partial^2}{\partial T^2} + 1 - \delta^2 \right) - k^2 B u^2 e^{2\beta(T)} \right] \hat{\phi}(k, Z, T) = -i k R o e^{\delta T} \hat{b}_0, \quad (\text{A.1})$$

where k is the horizontal wavenumber in generalised momentum coordinates and a hat denotes the Fourier transform. The forced solution is assumed to have the form given by (4.31), the Fourier transform of which is

$$\hat{\phi}(k, Z, T) = -i k \hat{b}_0 e^{\delta T} \hat{\phi}_I(k e^{\delta T}, Z). \quad (\text{A.2})$$

Substituting (A.2) into (A.1) and simplifying yields,

$$\left[\frac{\partial^2}{\partial Z^2} \left(1 + 3\delta^2 \mathcal{K} \frac{\partial}{\partial \mathcal{K}} + \delta^2 \mathcal{K}^2 \frac{\partial^2}{\partial \mathcal{K}^2} \right) - \mathcal{K}^2 B u^2 \right] \hat{\phi}_I(\mathcal{K}, Z) = R o, \quad (\text{A.3})$$

where $\mathcal{K} = k e^{\delta T}$ is the wavenumber in regular momentum coordinates (i.e. $\chi = X e^{-\delta T}$). At this point we make use of the Fourier identities

$$\mathcal{F}^{-1} \left[\mathcal{K}^n \widehat{f}(\mathcal{K}) \right] = i^n \frac{\partial^n}{\partial \chi^n} f(\chi), \quad \mathcal{F}^{-1} \left[\frac{\partial^n}{\partial \mathcal{K}^n} \widehat{f}(\mathcal{K}) \right] = i^n \chi^n f(\chi), \quad (\text{A.4})$$

where $\mathcal{F}^{-1}[\cdot]$ denotes the inverse Fourier transform as defined by (3.19). Inverse Fourier transforming (A.3) with respect to \mathcal{K} , and applying the identities (A.4), yields

$$\left[\frac{\partial^2}{\partial Z^2} \left(\delta^2 \chi^2 \frac{\partial^2}{\partial \chi^2} + \delta^2 \chi \frac{\partial}{\partial \chi} + 1 - \delta^2 \right) + Bu^2 \frac{\partial^2}{\partial \chi^2} \right] \phi_I(\chi, Z) = Ro \underline{\delta}(\chi). \quad (\text{A.5})$$

Equation (A.5) is identical to (4.34) in the main text. Thus, (4.33) with the impulse response defined by (4.34) is the forced solution to the non-linear generalised model at constant strain.

A.2 Boundary conditions on the Green's function

Here we show, using the characteristics of the constant-strain non-linear generalised model (4.23), that (i) the frontal circulation is identically zero for $|\chi| > Bu/(n\pi\delta)$ in the limit of infinite time, and (ii) the appropriate boundary conditions on the Green's function derived in §4.4 are $\widehat{\phi}_I(|\chi| > Bu/(n\pi\delta), n) = 0$.

Consider the *region of dependence* of a point χ_1 just outside of the confinement region for the n^{th} vertical mode (defined as $|\chi| < Bu/(n\pi\delta)$). That is, let

$$\chi_1 = \frac{Bu}{n\pi\delta} + \Delta\chi \quad (\text{A.6})$$

for $\Delta\chi$ a small positive constant. The region of dependence of the point χ_1 at time T_1 is bordered by the positive (χ_+) and negative (χ_-) characteristics (from (4.23)) that intersect at this point. Thus, the region of dependence at time T_1 is $\chi_0 \leq \chi \leq \chi_2$, where

$$\chi_0 = \frac{Bu}{n\pi\delta} + \Delta\chi e^{\delta T_1}, \quad \text{and} \quad \chi_2 = \frac{Bu}{n\pi\delta} \left(2e^{\delta T_1} - 1 \right) + \Delta\chi e^{\delta T_1}. \quad (\text{A.7})$$

Now consider the limit $T_1 \rightarrow \infty$ and define

$$\chi_0^\infty = \lim_{T_1 \rightarrow \infty} \chi_0 = \lim_{T_1 \rightarrow \infty} \left[\frac{Bu}{n\pi\delta} + \Delta\chi e^{\delta T_1} \right]. \quad (\text{A.8})$$

If we apply boundary conditions to ensure that ϕ (and its vertical sine transform $\widehat{\phi}$) vanish infinitely far from the front such that

$$\lim_{|\chi| \rightarrow \infty} \widehat{\phi}(\chi, n, T) = 0 \quad (\text{A.9})$$

for all times, it follows that

$$\widehat{\phi}(\chi > \chi_0^\infty, n, T) = 0. \quad (\text{A.10})$$

In other words, the boundary condition ensures that $\widehat{\phi}$ is everywhere zero in the region of dependence of the point χ_1 : $\widehat{\phi}(\chi_0 \leq \chi \leq \chi_2, n, 0) = 0$. Further, we choose a boundary buoyancy gradient profile $b'_0(X = \chi e^{\delta T})$ such that $b'_0(X > \chi_0^\infty e^{\delta T}) = 0$. The forcing to the model PDE (4.20), $RoA_n e^{\beta(T)} b'_0(X)$, is therefore everywhere zero in the region of dependence. Thus, as $T_1 \rightarrow \infty$, since the initial condition and forcing are zero in the region of dependence, it follows that

$$\widehat{\phi}\left(\chi_1 = \frac{Bu}{n\pi\delta} + \Delta\chi, n, T_1 \rightarrow \infty\right) = 0. \quad (\text{A.11})$$

Since this result applies for any $\Delta\chi$, it follows that

$$\lim_{T \rightarrow \infty} \widehat{\phi}(\chi, n, T) = 0 \text{ for } \chi > \frac{Bu}{n\pi\delta}. \quad (\text{A.12})$$

A similar argument may be made to show that

$$\lim_{T \rightarrow \infty} \widehat{\phi}(\chi, n, T) = 0 \text{ for } \chi < -\frac{Bu}{n\pi\delta}. \quad (\text{A.13})$$

Thus we conclude that the solution to (4.20) is identically zero for $|\chi| > Bu/(n\pi\delta)$ in the limit $T \rightarrow \infty$, and hence the frontal circulation is entirely confined in the region $|\chi| \leq Bu/(n\pi\delta)$. Further, since the n^{th} vertical mode Green's function $\widehat{\phi}_I(\chi, n)$ is the infinite time limit of $\widehat{\phi}(\chi, n, T)$, as per (4.36), the appropriate boundary conditions for the Green's function are $\widehat{\phi}_I(|\chi| > Bu/(n\pi\delta), n) = 0$.

Appendix B

Numerical solution to the linear frontogenesis problem

Here we give describe the procedure used to solve the linear frontogenesis model (6.9) discussed in Chapter 6. The equation (6.9) is second order in time and z , and owing to the non-hydrostatic term, fourth order in x . Equation (6.9) is firstly transformed to the linearly conserved coordinates $(x_0, z_0, t_0) = (x e^\beta, z, t)$, whereupon $\bar{D} = \partial_{t_0}$ and (6.9) reduces to an equation that is only second order in each variable:

$$\left[\left(\frac{\partial^2}{\partial t_0^2} - 2\alpha \frac{\partial}{\partial t_0} + f^2 \right) \frac{\partial^2}{\partial z_0^2} \frac{1}{N^2(z_0)} + \frac{e^{2\beta}}{N^2(z_0)} \frac{\partial^2}{\partial x_0^2} \frac{\partial^2}{\partial t_0^2} + e^{2\beta} \frac{\partial^2}{\partial x_0^2} \right] \Delta b(x_0, z_0, t_0) = -e^{2\beta} \frac{\partial^2}{\partial x_0^2} b_0(x_0, z_0). \quad (\text{B.1})$$

Usually we solve (B.1) beginning from a initial condition of geostrophic balance with zero strain at time zero, $\alpha(0) = \partial_{t_0} \alpha(0) = 0$, such that the initial condition on Δb is defined by

$$\left[\frac{\partial^2}{\partial z_0^2} \frac{f^2}{N^2(z_0)} + \frac{\partial^2}{\partial x_0^2} \right] \Delta b(x_0, z_0, 0) = -\frac{\partial^2}{\partial x_0^2} b_0(x_0, z_0), \quad (\text{B.2})$$

and $\partial_{t_0} \Delta b(x_0, z_0, 0) = 0$. Equation (B.2) is readily solved subject to homogeneous boundary conditions on all edges of the numerical domain. Equation (B.1) may then be stepped forward in time from this initial condition. We use the Crank-Nicholson implicit time-stepping algorithm. An implicit method is necessary due to the use of the conserved (contracting) coordinate which implies the an initial horizontal grid spacing $\Delta x(0)$ in physical (x) space, will shrink to $\Delta x(0) e^{-\beta(t)}$ after time t . As a result, the use of an explicit time-stepping

algorithm would require the time-step to also decrease exponentially with time (which is not practical) so as not to violate the Courant-Friedrichs-Lewy (CFL) condition.

The Matlab code used to solve the problem is available from the author on request.

Appendix C

Ray-tracing in a background strain flow

Here we seek plane wave solutions to the linear dual rigid lid strained front problem studied in Chapter 7. Using this approach we will firstly derive the classical ray-tracing result for the path of a wave packet in the strain flow (i.e. (7.3)) and clarify the assumptions required to obtain it. Secondly, we will show that breakdown of these assumptions for small scales implies that ray theory is not appropriate to describe the small scale stationary waves that are the focus of that chapter.

We begin by seeking homogeneous solutions to the linear governing equation (6.9) with uniform stratification and strain; that is,

$$\left[f^2 \frac{\partial^2}{\partial z^2} + N^2 \frac{\partial^2}{\partial x^2} + (\bar{D}^2 - 2\alpha\bar{D}) \frac{\partial^2}{\partial z^2} + \frac{\partial^2}{\partial x^2} \bar{D}^2 \right] \Delta b = 0. \quad (\text{C.1})$$

We observe that once the homogeneous solutions are known, the forced solutions can (in theory at least) be constructed using the variation of parameters method. As in Chapter 7, we decompose Δb into a sum of vertical sine modes, $\sin n\pi z/H$, whereupon (C.1) becomes

$$\left[1 + \frac{\partial^2}{\partial x'^2} + \frac{1}{f^2} (\bar{D}^2 - 2\alpha\bar{D}) + \frac{1}{N^2} \frac{\partial^2}{\partial x'^2} \bar{D}^2 \right] \Delta b = 0, \quad (\text{C.2})$$

where the scaled horizontal coordinate is $x' = x/L_R$, with $L_R = NH/(n\pi f)$ is the Rossby radius. Equation (C.2) possesses plane wave solutions of the form

$$\Delta b_k(k', x', t) = \exp \left[-i \left(k' X' - \int_0^t \Omega(k', \tau) d\tau \right) \right], \quad (\text{C.3})$$

where $k' = kL_R$ is the scaled wavenumber as previously and X' is the horizontal coordinate following the background flow; that is, $\bar{D}(X') = 0$ or $X' = x' e^{\alpha t}$ in the present case. Thus,

(C.3) defines plane waves in the flow-following coordinate, thereby permitting an exact solution for Ω that is independent of x . Substituting (C.3) into (C.2) it may be shown that the frequency $\Omega(k', t)$ is determined by the solution to the (first order but non-linear) differential equation

$$\begin{aligned} & \frac{\Omega(k', t)^2}{f^2} \left(1 + \frac{f^2}{N^2} k'^2 e^{2\alpha t} \right) - \left(1 - \frac{\alpha^2}{f^2} + k'^2 e^{2\alpha t} \left(1 + \frac{\alpha^2}{N^2} \right) \right) \\ & - \frac{i}{f^2} \left[\frac{\partial \Omega(k', t)}{\partial t} \left(1 + \frac{f^2}{N^2} k'^2 e^{2\alpha t} \right) + 2f \Omega(k', t) \frac{\alpha f}{N^2} k'^2 e^{2\alpha t} \right] = 0. \end{aligned} \quad (\text{C.4})$$

Since k' and t in (C.4) only appear in the combination $K' = k' e^{\alpha t}$ we have the result that $\Omega = \Omega(K')$ and we can rewrite (C.4) as an ordinary differential equation in K' ,

$$\begin{aligned} & \frac{\Omega^2}{f^2} \left(1 + \frac{f^2}{N^2} K'^2 \right) - \left(1 - \frac{\alpha^2}{f^2} + K'^2 \left(1 + \frac{\alpha^2}{N^2} \right) \right) \\ & - \frac{i}{f^2} \left[\alpha K' \frac{d\Omega}{dK'} \left(1 + \frac{f^2}{N^2} K'^2 \right) + 2f \Omega \frac{\alpha f}{N^2} K'^2 \right] = 0. \end{aligned} \quad (\text{C.5})$$

At this point we have made no additional approximations — we have simply rewritten the linearised governing equation (C.1) in terms of plane wave solutions (C.3). In general (C.4) will yield multiple complex solutions for Ω . The general solution to (C.1) for arbitrary initial conditions can be generated by summing over the plane wave solutions (with real part implied) for each Ω ; that is,

$$\Delta b(x', t) = \int_{-\infty}^{\infty} \widehat{A}(k') \Delta b_k(k', x', t) dk', \quad (\text{C.6})$$

such that

$$\Delta b(x', 0) = \int_{-\infty}^{\infty} \widehat{A}(k') e^{-ik'x'} dk' = A(x'). \quad (\text{C.7})$$

Let us firstly derive the classical ray-tracing result regarding the motion of a wave packet in the strain flow. The general dispersion relation is defined by (C.5). To obtain the ‘usual’ (i.e. freely propagating) inertia-gravity wave dispersion relation requires the assumption that the derivative term in (C.5) may be neglected; that is,

$$\Omega^2 \gg \alpha K' \frac{d\Omega}{dK'}, \quad (\text{C.8})$$

or equivalently $|\Omega| \gg \alpha$. That is, we explicitly require the frequency Ω of wave to be much faster than the background strain flow (i.e. a timescale separation). With this assumption,

the frequency Ω defined by (C.5) is purely real and takes the form of the usual dispersion relation,

$$\Omega(K') = \pm f \sqrt{\frac{1 + K'^2}{1 + \frac{f^2}{N^2} K'^2}}, \quad (\text{C.9})$$

also assuming that K' is not too large ($K' < N/f$) and the strain is sufficiently weak, $\alpha \ll f$. This solution for Ω (C.9) breaks down at sufficiently late time (large K'): solving (C.5) for Ω in the limit $K' \rightarrow \infty$ yields the result $\Omega = \pm N + i\alpha$. That is, at late time the waves both oscillate at the buoyancy frequency and decay at rate α . Thus the adjustment waves seen in figure 7.3g,h would be expected to decay even in the absence of diffusion, but this decay would occur at smaller scales and later time (such inviscid decay of plane waves in a strain flow was also noted by Thomas, 2012, and also described in the hydrostatic case in Chapter 3 herein). Nonetheless, for the remainder of this paragraph we assume that Ω is purely real and defined by (C.9). We can use the above general solution (C.6) to describe a wave packet for an appropriate choice of Fourier amplitude $\hat{A}(k)$. In particular we require that $\hat{A}(k)$ is sharply peaked around the dominant wavenumber k_0 of the packet. Since $\hat{A}(k)$ is sharply peaked about k_0 we can approximate Ω via the first two terms in a Taylor expansion about k_0 ,

$$\Omega(k', t) \cong \Omega(k'_0, t) + \frac{\partial \Omega(k'_0, t)}{\partial k'} (k' - k'_0). \quad (\text{C.10})$$

With this approximation (C.6) simplifies to

$$\begin{aligned} \Delta b(x', t) &= \exp\left(i \int_0^t \Omega(k'_0, \tau) - \frac{\partial \Omega(k'_0, \tau)}{\partial k'} k'_0 d\tau\right) \int_{-\infty}^{\infty} \hat{A}(k') e^{ik' \int_0^t \frac{\partial \Omega(k'_0, \tau)}{\partial k'} d\tau} e^{-ik' x' e^{\alpha t}} dk', \\ &= \exp\left(i \int_0^t \Omega(k'_0, \tau) - \frac{\partial \Omega(k'_0, \tau)}{\partial k'} k'_0 d\tau\right) A\left(x' e^{\alpha t} - \int_0^t \frac{\partial \Omega(k'_0, \tau)}{\partial k'} d\tau\right). \end{aligned} \quad (\text{C.11})$$

Equation (C.11) implies that the location of a packet with initial structure $A(x)$, centred about x_0 , will at some later time be

$$x' = x'_0 e^{-\alpha t} + e^{-\alpha t} \int_0^t \frac{\partial \Omega(k'_0, \tau)}{\partial k'} d\tau, \quad (\text{C.12})$$

$$= x'_0 e^{-\alpha t} + \frac{1}{\alpha k'_0} e^{-\alpha t} (\Omega(k'_0 e^{\alpha t}) - \Omega(k'_0)), \quad (\text{C.13})$$

using the result derived above that $\Omega(k'_0, t) = \Omega(K' = k'_0 e^{\alpha t})$. Differentiating (C.13), the speed of the packet is the difference between the strain flow speed and freely propagating

wave group speed,

$$\frac{\partial x'}{\partial t} = -\alpha x' + c_g (k'_0 e^{\alpha t}), \quad (\text{C.14})$$

where $c_g = \partial_{K'} \Omega(K')$ is the group speed of a freely propagating inertia-gravity wave. Equation (C.13) is the same result given in the text (7.3) derived directly from ray-tracing theory. As shown in the text, these solutions accurately describe the paths of the propagating adjustment wave packets considered in §7.3 (e.g. figure 7.3g,h). Hence classical ray-tracing methods provide a valid class of fast-time solutions to (C.1), at least for sufficiently large scales, $K' < N/f$.

However, the classical ray-tracing result associated with real frequencies Ω by no means provides a complete set of solutions to the problem. In particular, the classical result fails in the description of the small scale stationary solutions that are associated with the spontaneously generated waves studied in Chapter 7. To see this, consider the general solution to the homogeneous problem (C.6),

$$\begin{aligned} \Delta b(x', t) &= \int_{-\infty}^{\infty} \widehat{A}(k') \left(c_1 e^{i \int_0^t \Omega_1(ke^{\alpha\tau}) d\tau} + c_2 e^{i \int_0^t \Omega_2(ke^{\alpha\tau}) d\tau} \right) e^{-ik'x' e^{\alpha t}} dk', \\ &= \int_{-\infty}^{\infty} \widehat{A}(K' e^{-\alpha t}) \widehat{G}(K') e^{-iK'x'} e^{-\alpha t} dK', \\ &= \int_{-\infty}^{\infty} A(x_0 e^{\alpha t}) G(x - x_0) dx_0, \end{aligned} \quad (\text{C.15})$$

where Ω_1 and Ω_2 are two independent solutions to the dispersion relation (C.5), c_1 and c_2 are complex constants, and

$$\begin{aligned} \widehat{G}(K') &= \frac{1}{2\pi} \int_{-\infty}^{\infty} G(x) e^{iK'x} dx \\ &= c_1 e^{i \int \frac{\Omega_1(K')}{\alpha K'} dK'} + c_2 e^{i \int \frac{\Omega_2(K')}{\alpha K'} dK'}. \end{aligned} \quad (\text{C.16})$$

The Green's function type solutions defined by (C.15, C.16) are exactly the form of the solutions derived in the text (e.g. (7.1)). The (approximate) propagating wave solutions derived in the previous paragraph can also be written in this form; that is, setting $\Omega_1 = -\Omega_2 = \omega(K')$ from (C.9), and letting $c_1 = c_2 = 1/2$, (C.16) implies that

$$\widehat{G}(K') = \cos \left(\int \frac{\omega(K')}{\alpha K'} dK' \right) \quad (\text{C.17})$$

is the 'propagating wave Green's function'. As seen in the text, the Green's function is associated with the late-time structure of the solution. However as we noted above, the approximate solution for Ω breaks down for small scales, approximately $K' \geq N/f$. At these

scales the dispersion relation Ω contains additional imaginary components; for instance, we noted above that $\Omega = \pm N + i\alpha$ for $K' \rightarrow \infty$ (whereas the approximate solution is merely $\Omega = \pm N$), which from (C.16) implies that the Green's function should scale as

$$\widehat{G}(K') \sim \frac{1}{K'} \cos\left(\frac{N}{\alpha} \ln |K'|\right), \quad (\text{C.18})$$

in the limit $K' \rightarrow \infty$. This result (C.18) differs from the approximation (C.17) by a factor of $1/K'$, implying the small scale structures predicted by the approximation (C.17) will not be correct. Thus even a small imaginary component to the dispersion relation (i.e. in this case $\text{Im}(\Omega) = \alpha \ll N = \text{Re}(\Omega)$) can significantly influence the Green's function and therefore the late-time solution. In reality the differences between the actual Green's function and the approximation (C.17) will be more complicated than just a $1/K'$ factor — this is only the difference in the limit $K' \rightarrow \infty$. More generally, the approximate purely real dispersion relation (C.9) and associated Green's function (C.17) break down for scales $K' > N/f$. These are precisely the scales at which non-hydrostatic effects become significant (e.g. see figure 6.2). It follows that the purely real dispersion relation (C.9) and associated classical dispersive-wave theory cannot be used to quantitatively describe the small scale, steady, non-hydrostatic wave bands that are the focus of Chapter 7.

